UNIVERSIDAD DE GRANADA

TESIS DOCTORAL

PROGRAMA DE DOCTORADO EN FÍSICA Y CIENCIAS DEL ESPACIO

Fenómenos fuera del equilibrio en sistemas de nanopartículas responsivas

José López Molina

Directores

Arturo Moncho Jordá
María Tirado Miranda

Departamento de Física Aplicada, Universidad de Granada

GRUPO DE FÍSICA DE FLUIDOS Y BIOCOLOIDES
DEPARTAMENTO DE FÍSICA APLICADA

—

Granada, 2025

Editor: Universidad de Granada. Tesis Doctorales
Autor: José López Molina
ISBN: 978-84-1195-782-3
URI: https://hdl.handle.net/10481/103700

El doctorando / *The doctoral candidate* José López Molina y los directores de la tesis / *and the tesis supervisors* Arturo Moncho Jordá, Catedrático del Departamento de Física Aplicada de la Universidad de Granada y María Tirado Miranda, Profesora Titular del Departamento de Física Aplicada de la Universidad de Granada.

Garantizamos, al firmar esta tesis doctoral, que el trabajo ha sido realizado por el doctorando bajo la dirección de los directores de la tesis y hasta donde nuestro conocimiento alcanza, en la realización del trabajo, se han respetado los derechos de otros autores a ser citados, cuando se han utilizado sus resultados o publicaciones.

Guarantee, by signing this doctoral thesis, that the work has been done by the doctoral candidate under the direction of the supervisors and, as far as our knowledge reaches, in the performance of the work, the rights of other authors to be cited (when their results or publications have been used) have been respected.

Granada, 12 de Febrero de 2025

Doctorando / *Doctoral candidate*

Fdo: José López Molina

Los Directores de la Tesis / *Thesis supervisors*

Fdo: Arturo Moncho Jordá

Fdo: María Tirado Miranda

A mis padres.

El conocimiento es como el fuego: lo tomamos de otros, pero encendemos nuestra propia llama. Y en ese incendio que devora certezas y alimenta dudas, nos transformamos. El precio del conocimiento es la pérdida de la inocencia, pero la recompensa es la libertad del entendimiento.

Friedrich Nietzsche

Agradecimientos

Me hace gracia pensar en las veces que he dicho que no iba a hacer la tesis y, sin embargo, aquí estoy, escribiendo estas líneas de agradecimiento. Pero quizás sea esto lo mejor de todo el proceso: tener la oportunidad de sentarse y reflexionar sobre todas las personas que han hecho posible que llegue hasta aquí. Porque si algo he aprendido en este camino es que esta tesis, aunque lleve mi nombre, es el resultado de muchas personas que han ido apareciendo, quedándose y, algunas, marchándose a lo largo de estos años.

Por eso, aunque en la portada solo aparezca mi nombre, estas páginas están llenas de las huellas de todos los que han caminado conmigo en este viaje. Y este es el momento de reconocerlo, de dar las gracias, de hacer visible lo invisible.

Me gustaría empezar dando las gracias de corazón a Arturo y María, mis directores de tesis. Gracias por mantener siempre las puertas de vuestro despacho abiertas y por seguir apoyándome incluso cuando yo no lo he puesto nada fácil. Por mostrarme que la ciencia es mucho más humana y enseñarme el valor de la perseverancia. Y a Pepe, por ser quien me introdujo en este mundo de la investigación. Sin vosotros, esta tesis no habría tenido ni tan siquiera un comienzo, y mucho menos un final.

A toda la familia del Departamento de Física Aplicada, especialmente al grupo de Física de Fluidos y Biocoloides. A Ana Belén, por dedicarme tanto tiempo durante mi primer año cuando María no estaba; a Delfi, por su atención y cariño; y a Irene, por ayudarme a espabilar rápido y sacarle el máximo partido a este tiempo de doctorado. A Artur, por ayudarme a encontrar respuestas incluso cuando ni siquiera sabía formular bien las preguntas.

A Miguel Ángel Fernández, por contarnos todas esas cosas que debes saber y nadie te cuenta, y a Laura por recibirnos siempre con una sonrisa que hace que el día empiece mejor.

Y aprovecho para decir, como quien no quiere la cosa, que si eres un lector casual de mi trabajo y tienes la oportunidad de trabajar con alguna de las personas mencionadas hasta ahora, no lo dudes ni un instante. Son no solo grandísimos científicos sino aún más grandes personas. He tenido la suerte de colaborar con ellos en proyectos tanto científicos como solidarios, y puedo dar fe de su calidad humana.

To my Freiburg family - thank you for making the sunniest city in Germany even brighter. Joe and Sebastien, thanks for all your time and help. Sebastian, for teaching me that it's always beer o'clock somewhere. Diptesh, for being my personal happiness

officer, and Nils, for encouraging me to hit the gym at least 60 times per year.

To Anne, for encouraging me to start this PhD and supporting me during all this time. Also for being my travel companion around the world. A Carlos, por ejercer de diplomático en conflictos internacionales, siempre velando por mis intereses como si fueran los suyos. Y a Carmen, por llevar un trocito de hogar allá donde me he encontrado, aunque haya sido en la distancia.

A mis compañeros de la sala PIF, tanto a los que siguen como a los que ya emprendieron otros caminos:

Pablo, por demostrar que es posible llorar y seguir trabajando. Antonio Rubio, por mostrar que el café te da igual, que solo vienes porque nos quieres. Óscar, por... ¡saluda a la gente, anda! Javier, por mostrarme la importancia de estar impoluto todo el día. María, por pese a ir siempre con prisa, sacar siempre un ratito cuando ha hecho falta. Guillermo, por demostrar que se puede hacer una tesis sin perderse ni un solo programa de Juan y Medio. Antonio Ramírez, por acordarte de mí hasta para tu boda. Adri, por tantas conversaciones que han hecho más llevadero este camino. Adrián, por ser mi compañero fiel de expediciones al chino. Sssschooooooon. Fiiiuuuuummm. Ana Cardo y Loli Posoma, por mostrarnos que nosotros somos más simpáticos que los otros grupos de investigación. Martín, por estar desde el principio y ser ese amigo que siempre estuvo para un café. Andrea, por escuchar mis movidas y estar siempre ahí para reliar a la gente.

Y ya que estamos, un recordatorio: los cafés son a las 10:30 y justo después de comer. Los viernes se relía, que es tradición. Y por favor, que no cuesta tanto llegar puntual al café - que ya sois mayorcitos y siempre quedamos a la misma hora. NO ES TAN COMPLICADO.

Marina, por esas cervezas que han sido terapia en los momentos difíciles

A Miguel, por el apoyo incondicional y por ser mi compañero en todas las aventuras docentes en las que nos hemos metido. Por tantas cenas y buenos ratos, y por ser mi consejero astrológico cuando Mercurio está retrógrado.

A Ana, para quien las palabras siempre se quedan cortas. Gracias por ser mi compañera de aventuras, por todos estos años juntos, por tantas historias compartidas y por ser la mejor repartidora de cervezas que uno podría desear. La universidad ha sido un lugar mucho mejor por tenerte como amiga.

A los sapos - Tomás, Rafa, Kevin, Juan, y Cristina (en proceso de sapificación) - y a Chilly, Celia, Dani (hinca rodilla) y Mariajo. Gracias por escuchar todas mis historias y apoyarme en este camino.

A mis kikamigos, en especial a Ana, Juanma, Marta, Loreto, Marta, Juanpa, Pablo, Belén, Balta, Santi, Carmen, Gloria y Ubaldo junto a los brossss, Ricardo, Jesús, Guillermo, Mateos, Manolillo, Luja y a sus satélites Ana y Teresa. Por escucharme y seguir contando conmigo incluso cuando otros no lo hicieron. Gracias

por tantos planes y viajes juntos.

Y finalmente, a mi familia. A mis padres, hermanos, cuñados y sobrinos, por todo el apoyo durante este largo camino. Por aguantar mis ausencias y mis momentos de agobio, y por celebrar mis logros.

A todos los que aparecen en estas páginas y a aquellos que, por estar escribiendo los agradecimientos en el último momento (como debe ser), se me están escapando, solo quiero deciros que esta tesis es tan vuestra como mía, *aunque al final el que se ha comido la parte de escribirla he sido yo*. La próxima vez que hagamos un trabajo entre tantos repensamos el reparto de tareas porque yo prefiero apoyar a redactar. Ha sido un verdadero lujo compartir este camino con vosotros.

A todos, **gracias**.

Financiación

La investigación que ha conducido a la realización de esta tesis doctoral se ha llevado a cabo gracias a la ayuda FPU21/03568 del *Ministerio de Universidades*, al proyecto PY20-00241 financiado por la Junta de Andalucía, y al proyecto PID2022-136540NB-I00, financiado por *Ministerio de Ciencia e Innovación, Plan Estatal de Investigación Científica, Técnica y de Innovación*. Gracias a ellos ha sido posible la asistencia y presentación de comunicaciones en 6 conferencias, así como la participación en 4 artículos científicos de primer autor y la obtención de 1 patente.

La estancia de investigación realizada en el *Institute of Physics de la Universidad de Friburgo, Alemania*, ha sido financiada por el Programa de Ayudas para Realizar Estancias Breves en Centros de Investigación Nacionales y Extranjeros (P10) del Plan Propio de la Universidad de Granada y *Deutsche Forschungsgemeinschaft (DFG)* via the Research Unit FOR 5099 "REDUCING COMPLEXITY OF NONEQUILIBRIUM SYSTEMS" and PROJECT NO. 430195928. The authors also acknowledge support by the state of Baden-Württemberg through bwHPC and the DFG through grant no INST 39/963-1 FUGG (BWFORCLUSTER NEMO).

Resumen

Las suspensiones coloidales, sistemas formados por partículas de tamaño comprendido entre los nanometros y las micras dispersas en un medio continuo, son fundamentales en múltiples campos, desde la industria farmacéutica hasta la ciencia de materiales. Su estudio es crucial para comprender fenómenos como la autoorganización, las transiciones de fase y el comportamiento reológico. Esta tesis se centra en el estudio de las propiedades estructurales y dinámicas de un tipo particular de sistemas coloidales donde las partículas poseen, además del grado de libertad traslacional, un grado de libertad interno: su tamaño. Estas partículas, denominadas responsivas, pueden modificar su tamaño en respuesta a la interacción con otras partículas o campos externos.

Los microgeles representan un ejemplo experimental y teórico de este tipo de sistemas. Son partículas formadas por redes poliméricas entrecruzadas que pueden hincharse o deshincharse en respuesta a cambios en temperatura, pH o fuerza iónica. Esta capacidad de modificar su tamaño introduce nuevas escalas temporales en la dinámica del sistema, asociadas a los procesos de hinchamiento/deshinchamiento, que se acoplan con la difusión traslacional.

En el aspecto teórico, la tesis extiende la Teoría Funcional de la Densidad (DFT) para incluir partículas duras responsivas y estudiar los efectos que posee la blandura de las partículas sobre la estructura del sistema, demostrando fenómenos como la segregación por tamaños bajo campos externos y la compresión inducida por concentración. Se desarrolla también su versión dinámica (DDFT) para estudiar la relajación de coloides responsivos blandos, revelando estados dinámicos transitorios debidos al acoplamiento entre difusión espacial y adaptación del tamaño.

La investigación también aborda la liberación de moléculas desde microgeles colapsados, identificando regímenes limitados por difusión y por reacción, y proporcionando expresiones analíticas para los tiempos de liberación. Estos resultados tienen aplicación directa en el diseño de sistemas de liberación controlada de fármacos.

En cuanto a los avances experimentales, se desarrolla una nueva metodología en Dispersión Dinámica de Luz (DLS) que pemite determinar las velocidades absolutas de deriva de las nanoparticulas cuando el sistema está sometido a interacciones con campos externos o a fenómenos convectivos usando un dispositivo 3D-DLS. La técnica se valida mediante simulaciones de dinámica browniana y dinámica de fluidos, estableciendo su aplicabilidad en sistemas bajo convección térmica. Además, se propone un dispositivo con la capacidad de medir velocidades relativas en un mismo sistema debido a la presencia de campos externos.

Finalmente, se desarrolla una red neuronal convolucional para analizar funciones

de correlación de DLS, superando limitaciones de métodos tradicionales como CONTIN en la determinación de distribuciones de tamaño de partículas. La red demuestra especial robustez en presencia de ruido y en la caracterización de distribuciones multimodales, validada tanto por métricas cuantitativas como por expertos en el campo. Este nuevo procedimiento basado en conceptos de machine learning es también aplicable al estudio de sistemas de nanopartículas responsivas, que son intrínsecamente polidispersas.

Abstract

Colloidal suspensions, systems formed by particles ranging in size from nanometers to microns dispersed in a continuous medium, are fundamental in multiple fields, from the pharmaceutical industry to materials science. Their study is crucial for understanding phenomena such as self-organization, phase transitions, and rheological behavior. This thesis focuses on studying the structural and dynamic properties of a particular type of colloidal system where particles possess, in addition to translational freedom, an internal degree of freedom: their size. These particles, called responsive particles, can modify their size in response to interaction with other particles or external fields.

Microgels represent an experimental and theoretical example of such systems. They are particles formed by crosslinked polymer networks that can swell or de-swell in response to changes in temperature, pH, or ionic strength. This ability to modify their size introduces new time scales in the system's dynamics, associated with swelling/de-swelling processes, which couple with translational diffusion.

On the theoretical aspect, the thesis extends Density Functional Theory (DFT) to include responsive hard particles and study the effects that particle softness has on the system's structure, demonstrating phenomena such as size segregation under external fields and concentration-induced compression. Its dynamic version (DDFT) is also developed to study the relaxation of soft responsive colloids, revealing transient dynamic states due to the coupling between spatial diffusion and size adaptation.

The research also addresses the release of molecules from collapsed microgels, identifying diffusion-limited and reaction-limited regimes, and providing analytical expressions for release times. These results have direct application in the design of controlled drug delivery systems.

Regarding experimental advances, a new Dynamic Light Scattering (DLS) methodology is developed that allows determining the absolute drift velocities of nanoparticles when the system is subjected to interactions with external fields or convective phenomena using a 3D-DLS device. The technique is validated through Brownian dynamics and fluid dynamics simulations, establishing its applicability in systems under thermal convection. Additionally, a device is proposed with the capability to measure relative velocities in the same system due to the presence of external fields.

Finally, a convolutional neural network is developed to analyze DLS correlation functions, overcoming limitations of traditional methods like CONTIN in determining particle size distributions. The network demonstrates particular robustness in the presence of noise and in characterizing multimodal distributions, validated both by quantitative metrics and by experts in the field. This new procedure based on machine

learning concepts is also applicable to the study of responsive nanoparticle systems, which are intrinsically polydisperse.

Contents

Contents **17**

Abbreviations **25**

I Introduction 27

1. Background **29**

1.1. Context 29

1.2. Microgel Fundamentals 30

1.3. Non-Equilibrium Behavior in Responsive Systems 34

1.4. Challenges in Working with Non-Equilibrium Systems 35

Bibliography **39**

2. Motivation and Thesis Outline **49**

2.1. Motivation 49

2.2. Thesis Structure and Outline 50

Bibliography **53**

3. Theoretical Framework **55**

3.1. Classical Density Functional Theory 56

3.2. Dynamic Density Functional Theory 64
3.3. Brownian Dynamics Simulations 66

Bibliography **69**

4. Basis of Dynamic Light Scattering **71**
4.1. Mathematical concepts 72
4.1.1. Time correlation functions 72
4.1.2. Siegert relation 74
4.2. Correlation function derivation 75
4.2.1. Correlation function of monodisperse systems in equilibrium . 75
4.2.2. Correlation function for monodisperse systems under drift velocities 79

Bibliography **81**

II Results **83**

Publication I. Density functional theory for responsive hard-sphere fluids **85**
I.1. Introduction 87
I.2. Theory 89
I.2.1. Basic statistical mechanics relations of inhomogeneous responsive colloids 89
I.2.2. DFT for responsive colloids 92
I.2.3. Free energy functional for responsive hard spheres 94
I.3. Results and discussion 95
I.3.1. Bulk properties of responsive hard spheres 95
I.3.2. Inhomogeneous responsive hard spheres near a hard planar wall 99
I.3.3. Confined responsive hard spheres in a gravitational field . . . 101
I.3.4. Confined responsive hard spheres in a gravitational plus Arquimedes buoyant force 104
I.3.5. Responsive versus conventional polydisperse non-responsive . 106

I.4. Conclusions 108
I.5. Appendix 110
I.5.1. Appendix A. Weight functions and excess chemical potential for a homogeneous (bulk) system 110
I.5.2. Appendix B. Weight functions and excess chemical potential for planar symmetry 110

Bibliography **113**

Publication II. Nonequilibrium relaxation of soft responsive colloids **121**
II.1. Introduction 123
II.2. Theoretical background 125
II.2.1. Theoretical modelling of responsive colloids 125
II.2.2. Dynamical density functional theory for RCs 126
II.2.3. Mean-field responsive DDFT of soft Gaussian responsive colloids confined in planar slits 127
II.3. Brownian Dynamics simulations of RCs 130
II.4. Results and discussion 131
II.4.1. Gravitational potential 133
II.4.2. Osmotic potential 135
II.4.3. Macroscopic Analysis 137
II.4.4. Competition of time scales: the α-study 140
II.5. Concluding remarks 143

Bibliography **147**

Publication III. Diffusion and interaction effects on molecular release kinetics from collapsed microgels **157**
III.1. Introduction 159
III.2. Theoretical methods 162
III.2.1. Model for cargo release from a collapsed microgel 162
III.2.2. Dynamical Density Functional Theory 167
III.3. Results and discussion 170

III.3.1. Spatio-temporal evolution of cargo molecules 171
III.3.2. Time evolution of the fraction of released molecules 172
III.3.3. Effect of the diffusion coefficient and molecule–microgel interaction free energy 173
III.3.4. Effect of the microgel size 175
III.3.5. Analytical expression for the half-release time 176
III.4. Conclusions 178
III.5. Appendix. Calculation of the mean first passage time 180

Bibliography **183**

Publication IV. Measuring Absolute Velocities from Nonequilibrium Oscillations via Single-Detector 3D Dynamic Light Scattering **191**
IV.1. Appendix. Supplementary Material 203
IV.1.1. Two-Laser Single-Detector Correlation Function in Dynamic Light Scattering with One Drift Velocity 203
IV.1.2. Two-Velocity One-Laser Single-Detector Correlation Function in Dynamic Light Scattering 209
IV.1.3. Technical Details of Fluid Dynamics Simulations 210

Bibliography **213**

Publication V. Device and method for characterizing relative drift velocities in colloidal salmples **217**
V.1. Device Description 218
V.2. Applications and Significance 220

Bibliography **223**

Publication VI. Recovery of Size Distributions from Dynamic Light Scattering using Convolutional Neural Networks **225**
VI.1. Introduction 227
VI.2. Methodology 228
VI.2.1. Synthetic Data Generation 229

VI.2.2. Neural Network Architecture and Training 230
VI.2.3. CONTIN Method 233
VI.3. Results 234
VI.3.1. Representative Examples 234
VI.3.2. Quantitative Performance Analysis 236
VI.3.3. Human Expert Validation Study 243
VI.3.4. Computational Performance Analysis 245
VI.4. Conclusions 247
VI.5. Appendix 249

Bibliography **257**

III Conclusions and summary 259

Conclusions and Future Work **261**

Resumen **265**

Bibliography **271**

A colleague asks: "So, what's your thesis about?"

I pause. How do I even begin to explain this?

My mind races through images of papers, light scattering experiments, complex mathematical models dancing across computational simulations. Do I start with the tiny world of microgels? Or jump straight into how they work?

I take a deep breath.

"Well," I begin, drawing an imaginary particle in the air, "imagine a microscopic sponge that you can control. You can make it expand or shrink just by changing things like temperature, pH, or applying a magnetic field. When it's expanded, you can load it with drug molecules, and when you want to release the drugs, you make it collapse – like squeezing a sponge."

I see a glimmer of understanding in her eyes.

"My thesis is about understanding exactly how these particles behave. It's like... we know they work, but we need to understand them better to use them more effectively."

I think about my hours in the lab, wrestling with temperature-sensitive measurements. Should I explain how challenging it is to measure these particles when they're changing with temperature? How the very heat we use to study them creates currents that interfere with our measurements?

"One big part of my work," I continue, warming to the explanation, "was improving how we measure these particles. Traditional techniques struggle when you're studying temperature-sensitive materials because heating creates fluid currents that mess up the measurements. I developed a way to correct for these effects by measuring the exact drift velocity of the system."

Should I dive into the theoretical aspects? Yes, it's crucial to the whole picture.

"But that's just the experimental side. I also used theoretical models to simulate how drugs are released under different conditions. It's like having a virtual laboratory where we can test countless scenarios. And not just drug release – I studied how these soft particles behave under various external forces, trying to understand their dynamic nature."

My colleague nods, following the thread.

"So in essence," I conclude, "my thesis is about developing better ways to understand and characterize these responsive particles. We need to understand how these particles change size, how they move, and how they interact with their environment. I realize I've been gesturing more animatedly as I explain.

"Does that make sense?"

Abbreviations

3D-DLS	Three-Dimensional Dynamic Light Scattering
BD	Brownian Dynamics
cDFT	Classical Density Functional Theory
CONTIN	Constrained Regularization Method for Inverting Data
DDFT	Dynamic Density Functional Theory
DFT	Density Functional Theory
DLS	Dynamic Light Scattering
DoF/DoFs	Degrees of Freedom
FMT	Fundamental Measure Theory
FTCS	Forward-Time Central-Space
HeDLS	Heterodyne Dynamic Light Scattering
HoDLS	Homodyne Dynamic Light Scattering
MF	Mean-Field
PAA	Poly(acrylic acid)
PNIPAM	Poly(N-isopropylacrylamide)
Ra	Rayleigh number
RC/RCs	Responsive Colloid(s)
RC-DDFT	Responsive Colloid Dynamic Density Functional Theory
SM	Supplemental Material
VPTT	Volume-phase transition temperature

Part I

Introduction

Chapter 1

Background

1.1. Context

Colloidal suspensions are fluids containing small particles (from a few nanometers to several micrometers in size) dispersed in a solvent [1.1–1.3]. These suspensions represent a prototypical example of *soft matter*, a class of materials characterized by particles that are hundreds to thousands of times larger than molecular scales while maintaining interaction energies comparable to those between atoms and molecules [1.4]. This unique combination of length and energy scales leads to materials that are easily deformed by thermal or external forces [1.5, 1.6]. Understanding the structural and dynamical properties of colloidal suspensions, both at equilibrium and out of equilibrium, has long been of central interest in physics, chemistry, and materials science [1.7, 1.8]. This interest stems from their ubiquity in nature and industry, where processes such as self-assembly, phase transitions, and complex rheological behavior play pivotal roles in applications ranging from food processing to advanced manufacturing [1.2, 1.9].

Within the broad realm of soft matter, the concepts of *softness* and *responsiveness* are particularly relevant. *Softness* refers to the intrinsic flexibility and adaptability of these materials at the molecular and mesoscopic levels, arising from a delicate balance of entropic and energetic contributions [1.10–1.14]. *Responsiveness*, on the other hand, describes the ability of soft materials to undergo significant, reversible changes in physical properties when exposed to external stimuli such as temperature, pH, ionic strength, light, or mechanical forces [1.15, 1.16]. The internal degrees of freedom of soft materials enable them to reconfigure dynamically, giving rise to a rich set of phenomena that can be harnessed for a wide range of technologies [1.17–1.32].

Responsive colloidal systems include colloids and macromolecules that can sense and adapt to environmental changes by modifying their internal conformation, size, shape, charge density, electric dipole, and orientation [1.33–1.42]. These adjustments affect both single-particle and collective properties, often resulting in complex, multi-relaxation dynamical behaviors [1.8, 1.43]. Such responsiveness is highly appealing in applications where real-time adaptation to external triggers is crucial, for example, in drug delivery (where changes in pH or temperature can trigger drug release), smart coatings (which alter surface properties upon environmental changes), and nanocatalysis (where different reaction pathways can be activated by stimuli) [1.44–1.47].

Microgels constitute a particularly versatile class of responsive colloidal particles [1.48,1.49]. Unlike rigid nanoparticles, a microgel is formed by a *crosslinked polymer network* that retains its integrity as an individual particle [1.16, 1.48]. This crosslinking prevents the polymer network from dissolving, conferring a "sponge-like" character that allows microgels to incorporate a significant amount of solvent within their structure [1.44, 1.49]. A simplified schematic of a microgel is shown in Figure (1.1), where its porous polymeric network can be contrasted with denser, solid nanoparticles [1.1]. One of the hallmark features of microgels is the *volume-phase transition*: the reversible swelling or collapse of the polymer network in response to external stimuli (e.g., temperature, pH, or ionic strength) [1.48]. This unique ability makes microgels ideal candidates for applications such as targeted drug delivery (where microgels can swell to load active molecules and collapse to release them at a specific site), nanocatalysis (where changes in the microgel volume can modulate access to catalytic sites), and biosensing (where particle swelling can alter optical or electrical signals) [1.46, 1.47].

Despite their promising features, most real-world applications of microgels and other responsive materials operate under conditions that deviate significantly from equilibrium [1.8, 1.15, 1.43]. External stimuli often vary in time or space, driving the system out of equilibrium and giving rise to time-dependent structural and dynamical behaviors [1.7, 1.8]. From a fundamental perspective, understanding these **non-equilibrium dynamics** is crucial for designing and optimizing responsive materials that can reliably function in complex environments. This thesis aims to elucidate how the interplay between internal degrees of freedom and external driving forces governs the non-equilibrium behavior of soft, responsive systems, thereby advancing both the fundamental science and practical applications of microgels.

1.2. Microgel Fundamentals

Microgels are cross-linked polymeric networks that swell in a good solvent and collapse in a poor solvent or under unfavorable conditions. Their diameters

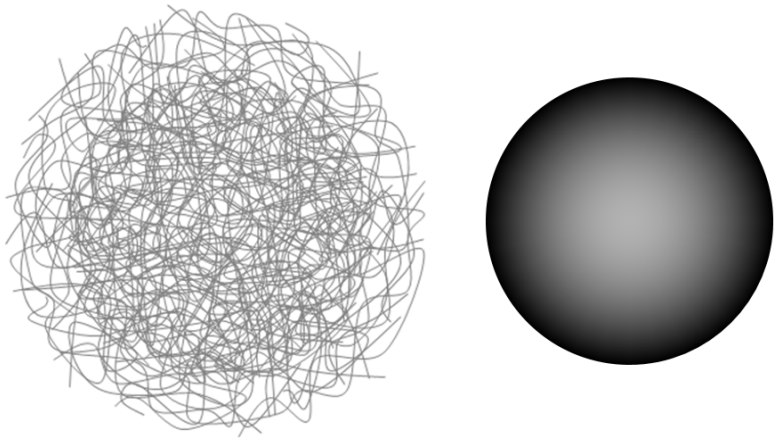

Figure 1.1: Schematic representation of a microgel (left) compared to a solid nanoparticle (right). The crosslinked polymer network in the microgel imbibes solvent and can swell or collapse, whereas a solid nanoparticle lacks such internal porosity.

generally range from tens of nanometers to a few micrometers. Because of their intermediate size, microgels exhibit characteristics typical of both molecular-scale solutions (e.g., polymer–solvent interactions) and colloidal dispersions (e.g., interparticle interactions, stability).

Each microgel particle is a three-dimensional polymer network stabilized by covalent cross-links. The **cross-linking density** typically decreases radially from a denser core to a more loosely cross-linked shell. This gradient creates spatial inhomogeneities within the particle and can lead to distinct swelling behaviors in different regions of the same microgel.

The cross-linked network must balance two opposing tendencies [1.50]:

1. **Polymer–Solvent Interactions**: Favor swelling, especially when polymer chains are hydrophilic or capable of hydrogen bonding with the solvent.
2. **Polymer–Polymer Interactions**: Include various intermolecular forces (such as van der Waals interactions, and in aqueous environments, hydrophobic associations) and elastic forces from the network structure, favoring a collapsed state and thus reducing particle volume.

A higher cross-linking density renders the microgel less deformable and more mechanically robust, whereas a lower cross-linking density enhances responsiveness to external stimuli but may compromise stability.

A defining feature of many microgels is their **volume-phase transition**, where small environmental changes (e.g., temperature, pH, ionic strength) can induce large changes in particle size. Thermodynamically, the swelling of a microgel can be

described by the **Flory–Rehner theory**, which decomposes the total free energy ΔG into two components [1.14, 1.51–1.53]:

$$\Delta G = \Delta G_{\text{mix}} + \Delta G_{\text{elastic}}, \tag{1.1}$$

where ΔG_{mix} represents the mixing entropy and enthalpy between polymer and solvent, and $\Delta G_{\text{elastic}}$ accounts for the elastic free energy of the cross-linked polymer network. When external stimuli shift the balance between polymer–solvent and polymer–polymer interactions, the microgel either **swells** by incorporating more solvent or **collapses** by expelling it.

Microgels can be designed to respond to a variety of external and internal stimuli, making them highly tunable for specific applications. Some common types of responsiveness include:

- **Temperature-responsive microgels.** These systems exhibit significant volume changes in response to temperature variations, where the transition between swollen and collapsed states occurs at specific temperatures determined by the balance between polymer-solvent and polymer-polymer interactions [1.48].
- **pH-responsive systems.** A classic example is poly(acrylic acid) (PAA), whose carboxylic acid groups become ionized under basic conditions, causing electrostatic repulsion within the polymer network and leading to swelling. Under acidic conditions, these groups are protonated and the electrostatic repulsion is reduced, causing the microgel to collapse [1.54, 1.55].
- **Ionic-strength-responsive microgels.** These systems expand or contract depending on the salt concentration in solution. An increase in ionic strength can screen electrostatic repulsions between charged groups, causing the polymer network to shrink; conversely, lowering the ionic strength can lead to swelling [1.56].
- **Solvent-responsive microgels.** When exposed to different solvents or solvent mixtures, microgels may undergo changes in conformation and solvation. For instance, microgels composed of thermoresponsive polymers such as poly(*N*-isopropylacrylamide) (pNIPAM) can change from a swollen, hydrophilic state in water to a more collapsed, hydrophobic state when the solvent composition or temperature is varied [1.48, 1.57].
- **Concentration- or crowding-responsive microgels.** Besides external triggers, microgels can also vary their size due to interactions with neighboring particles in dense suspensions. As the particle concentration rises, volume-exclusion and electrostatic repulsions can force microgels to partially collapse [1.58].

- **External-field-responsive microgels.** External fields such as gravity, electric fields, or magnetic fields can also alter microgel volume and structure. In a gravitational field, for example, microgels near the bottom of a container may experience increased local pressure and compressive forces, leading to a more collapsed state compared to those at the top [1.59].

By adjusting the monomer chemistry, the type of cross-linker, and the network architecture, researchers can tune the **responsiveness** of microgels to meet specific application requirements. Crucially, it is common for a single microgel system to exhibit more than one of these responsiveness mechanisms simultaneously. For example, a pH- and ionic-strength-sensitive microgel may also undergo partial collapse at high particle concentrations or under gravitational sedimentation. Strategic modifications to the polymer composition and cross-link density enable precise control over swelling ratios, collapse transitions, and overall mechanical properties, thereby creating systems optimized for drug delivery, nanocatalysis, biosensing, or other high-impact applications.

The reversible swelling and collapse of microgels underlies their broad utility in various fields. In **biomedicine**, the porous network of microgels enables loading and controlled release of drugs [1.60, 1.61], making them ideal carriers that can respond to local physiological stimuli (e.g., temperature, pH). In **materials science**, microgels are incorporated into coatings, composites, and sensors that require adaptive behavior based on environmental conditions (e.g., humidity, temperature) [1.62, 1.63]. In **environmental technologies**, microgels can be leveraged for pollutant remediation and detection, where their swelling state modulates interactions with contaminants [1.46].

Among the various polymers used in microgels, **poly(N-isopropylacrylamide) (PNIPAM)** exhibits an unusual thermoresponsive behavior. While most thermoresponsive polymers swell with increasing temperature due to enhanced polymer chain mobility, PNIPAM shows the opposite behavior, as illustrated in Figure (1.2). In aqueous solutions, PNIPAM typically has a volume-phase transition temperature (VPTT) near 32–34 °C [1.48, 1.64], although the exact transition temperature depends on the specific synthesis conditions of each microgel system. Because it is very close to body temperature, it is ideal for biomedical applications. This inverse temperature response is due to PNIPAM's amphiphilic nature: below the VPTT, the amide groups form an extensive hydrogen-bonding network with water molecules, overcoming the hydrophobic effects of the isopropyl groups. Above the VPTT, these hydrogen bonds are disrupted by the increased thermal energy of the system, allowing the hydrophobic interactions between isopropyl groups to dominate, causing a **coil-to-globule** transition and resulting in a collapsed microgel, as depicted in Figure (1.2).

This transition is fully reversible: cooling the system reestablishes favorable

polymer–solvent interactions, allowing the microgel to reswell. Because the VPTT is close to physiological temperature, PNIPAM-based microgels have attracted intense interest for biomedical applications such as **targeted drug delivery**, where slight temperature elevations can trigger drug release in specific tissues.

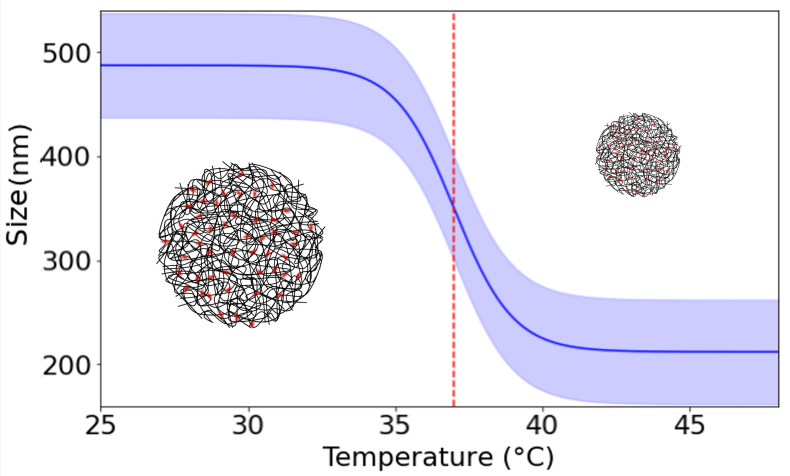

Figure 1.2: Schematic representation of a PNIPAM microgel size in swollen (left) and collapsed (right) states against temperature. Red line indicates VPTT. The blue region accounts for the intrinsic polydispersity of the system. In the swollen state, water molecules are incorporated into the polymer network. Upon heating above the VPTT, hydrophobic interactions dominate, leading to the expulsion of water and a reduced particle size.

1.3. Non-Equilibrium Behavior in Responsive Systems

The dynamic nature of responsive systems is a defining characteristic that underpins their functionality and adaptability. Unlike classical materials, responsive systems undergo continuous and reversible changes in response to external stimuli, making the study of their dynamic processes crucial for several reasons:

- **Enhanced Functional Control:** Understanding the dynamics allows for precise control over the responsiveness of the system, enabling the design of materials that can adapt their properties in real-time to meet specific functional requirements [1.13, 1.14, 1.18–1.28].

- **Optimization of Applications:** In applications such as drug delivery, the kinetics of drug release are critical for therapeutic efficacy. Studying the

dynamic processes helps in optimizing release profiles to ensure that drugs are delivered at the desired rate and location [1.60, 1.61].

- **Fundamental Understanding:** Investigating the non-equilibrium behavior of responsive systems contributes to the fundamental understanding of non-equilibrium thermodynamics and statistical mechanics, providing insights into how systems evolve over time under various conditions [1.65–1.69].
- **Innovative Material Design:** Insights from dynamic studies enable the design of novel materials with tailored properties, enhancing their performance and expanding their range of applications in fields like biotechnology, catalysis, and materials engineering [1.70–1.74].

Microgels serve as an ideal model system for examining non-equilibrium phenomena because of their **reversible volume-phase transitions** [1.44–1.47]. The **transport** of molecules within and across microgels is closely tied to their swelling state. In the collapsed state, hydrophobic interactions dominate, and water is expelled to form a more compact structure. Atomistic simulations suggest that water trapped in collapsed networks can form disconnected, fractal-like clusters, leading to **non-porous membrane** behavior [1.75, 1.76]. For hydrophobic molecules, collapsed microgels may act as reservoirs with enhanced partitioning relative to traditional size-exclusion predictions [1.76–1.80].

These dynamic transport properties are particularly important in drug delivery: as the microgel environment changes (e.g., temperature shifts in tumor tissues), the microgel transitions from collapsed to swollen, releasing its therapeutic cargo in a controlled manner [1.81–1.85].

1.4. Challenges in Working with Non-Equilibrium Systems

Studying non-equilibrium behavior in responsive systems presents several significant challenges that must be addressed to advance the field effectively. Non-equilibrium conditions are inherent in many real-world applications of responsive materials, where continuous and dynamic interactions with the environment dictate system performance. In addition, the ability of these materials to change their properties such as size, shape, or conformation under external stimuli is directly relevant to a variety of applications, including core–shell nano-reactors for selective catalysis [1.15, 1.86] or controlled drug release [1.44, 1.70]. Approaching these challenges requires a combination of computational, theoretical, and experimental strategies, each with its own set of limitations and advantages.

One primary method for investigating non-equilibrium behavior is through computer simulations. A key aspect of computational modeling is the selection of an appropriate level of detail, or degree of coarse-graining, as illustrated in Figure (1.3). This multiscale challenge spans from quantum mechanics at picosecond timescales to continuum mechanics at macroscopic scales. Modern approaches often combine methods across these scales: for instance, atomistic simulations are used to study representative portions of the system to extract effective interactions, which are then employed in coarse-grained models at larger scales to describe collective effects that would be computationally intractable through purely atomistic simulations. This hierarchical approach enables the study of complex phenomena across multiple length and time scales while maintaining computational feasibility.

One primary method for investigating non-equilibrium behavior is through computer simulations. A key aspect of computational modeling is the selection of an appropriate level of detail, or degree of coarse-graining, as illustrated in Figure (1.3). This multiscale challenge spans from quantum mechanics at picosecond timescales to continuum mechanics at macroscopic scales. Molecular dynamics (MD) simulations can be performed at various levels of detail: from fully atomistic representations that capture chemical specificity, to increasingly coarse-grained models where atomic details are systematically eliminated, ultimately reaching effective potential descriptions where entire particles are treated as single units. Each level of coarse-graining represents a trade-off between computational efficiency and molecular detail.

These simulations provide detailed insights into the microscopic mechanisms driving non-equilibrium dynamics, such as particle diffusion, aggregation, and structural transformations. In responsive systems, these mechanisms are often more complex than in non-responsive ones, because the spatial degrees of freedom (e.g., particle positions) couple dynamically with internal degrees of freedom such as particle size, shape, or conformation. As the internal structure changes, it feeds back into the spatial arrangement and vice versa, resulting in a richer, highly coupled dynamical landscape that does not appear in simpler, non-responsive systems.

However, a significant drawback of computational simulations is their high computational cost. Achieving reliable estimations often requires averaging results over a large number of simulation runs to account for the stochastic nature of non-equilibrium processes [1.68, 1.87]. This necessity for extensive averaging increases the time and computational resources required, making it impractical for studying large systems or conducting extensive parameter sweeps. Additionally, capturing long-time-scale phenomena remains challenging due to the inherent limitations of simulation timescales, particularly at the more detailed levels of description.

To overcome some of the limitations associated with computational simulations, theoretical frameworks such as Dynamic Density Functional Theory (DDFT) have been developed. DDFT extends the principles of Density Functional Theory (DFT) to non-equilibrium conditions, allowing for the modeling of time-dependent changes

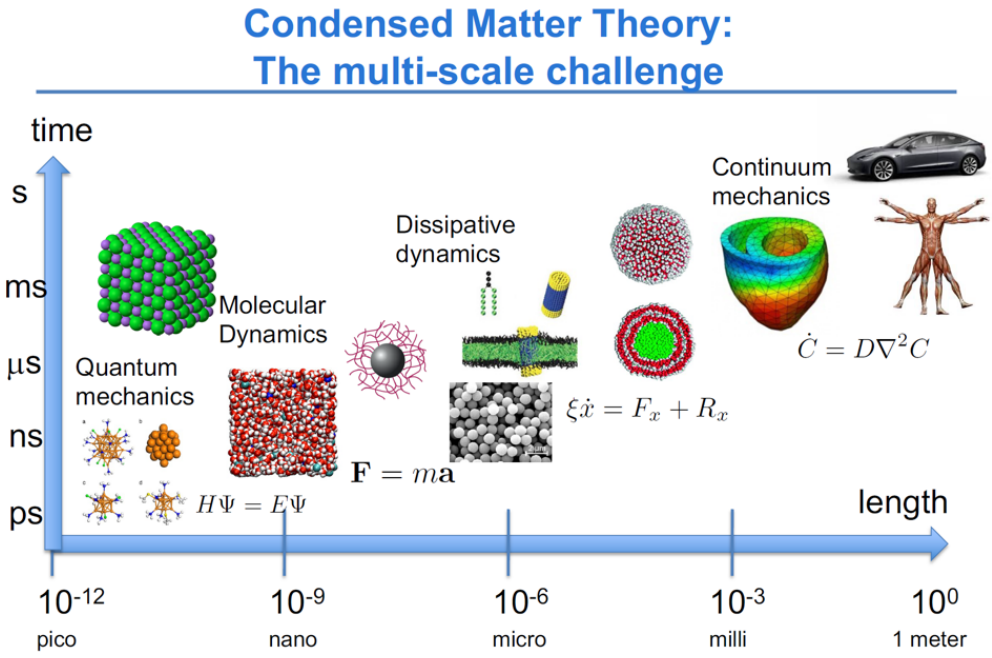

Figure 1.3: Illustration of the multi-scale challenge in condensed matter theory, showing different levels of description from quantum mechanics to continuum mechanics, along with their corresponding length scales and representative equations.

in particle density distributions [1.65, 1.87, 1.88]. This approach provides a more computationally efficient means of studying non-equilibrium dynamics compared to traditional simulations. DDFT is particularly advantageous for modeling soft systems, such as microgels, and can be effectively applied to study phenomena like drug release [1.89, 1.90]. By incorporating interactions and external fields, DDFT enables the prediction of how responsive systems evolve over time, facilitating the design and optimization of materials for specific applications.

Despite its strengths, DDFT relies on certain approximations, such as the adiabatic approximation, which assumes that non-equilibrium correlations resemble those in equilibrium [1.89]. While this simplifies the modeling process, it may limit the accuracy of predictions for systems far from equilibrium or those with strong dynamic interactions.

While computational and theoretical approaches provide valuable insights, experimental measurements remain the most direct method for studying non-equilibrium behavior in responsive systems. Techniques such as Dynamic Light Scattering (DLS) are widely used to characterize the size distribution and dynamic properties of colloidal particles in suspension [1.91–1.93]. DLS measures fluctuations in the intensity of scattered light caused by particle motion, offering real-time information about diffusion coefficients and particle size changes.

However, conducting reliable measurements under non-equilibrium conditions poses significant challenges. In the context of microgels, for example, size-temperature characterization using DLS can be severely affected by convection [1.77, 1.78]. Convection currents induced by temperature gradients introduce additional motions that interfere with the accurate interpretation of DLS data. Traditional DLS analysis assumes a quiescent suspension, and the presence of convection violates this assumption, leading to unreliable measurements [1.94, 1.95].

The difficulties encountered in experimental measurements of non-equilibrium systems necessitate the revision and adaptation of existing techniques. Traditional DLS must be modified to account for the effects of external perturbations like convection. This may involve the implementation of more sophisticated experimental designs, such as using multiple detectors or employing alternative light scattering methods that can distinguish between different types of particle motion.

Bibliography

[1.1] William B. Russel, D. A. Saville, and W. R. Schowalter. *Colloidal Dispersions*. Cambridge University Press, Cambridge, UK, 1989.

[1.2] R. J. Hunter. *Foundations of Colloid Science*. Oxford University Press, Oxford, UK, 2001.

[1.3] P. N. Pusey and W. van Megen. Phase behaviour of concentrated suspensions of nearly hard colloidal spheres. *Nature*, 320(6060):340–342, 1986.

[1.4] Christos N. Likos. Effective interactions in soft condensed matter physics. *Phys. Rep.*, 348(4):267–439, 2001.

[1.5] Ronald G Larson. *The structure and rheology of complex fluids*, volume 150. Oxford university press New York, 1999.

[1.6] Jacob N. Israelachvili. *Intermolecular and Surface Forces, Third Edition*. Academic Press, 3rd edn, 2011.

[1.7] Todd M Squires and Stephen R Quake. Microfluidics: Fluid physics at the nanoliter scale. *Reviews of modern physics*, 77(3):977–1026, 2005.

[1.8] Michael E. Cates and Julien Tailleur. Motility-induced phase separation. *Annu. Rev. Condens. Matter Phys.*, 6(1):219–244, March 2015.

[1.9] Veronique Trappe, V Prasad, Luca Cipelletti, PN Segre, and David A Weitz. Jamming phase diagram for attractive particles. *Nature*, 411(6839):772–775, 2001.

[1.10] José Nelson Onuchic, Zaida Luthey-Schulten, and Peter G. Wolynes. Theory of protein folding: The energy landscape perspective. *Annu. Rev. Phys. Chem.*, 48(1):545–600, 1997.

[1.11] Chi Wu and Xiaohui Wang. Globule-to-coil transition of a single homopolymer chain in solution. *Phys. Rev. Lett.*, 80:4092–4094, May 1998.

[1.12] Samuel S. Cho, Yaakov Levy, and Peter G. Wolynes. *P* versus *Q*: Structural reaction coordinates capture protein folding on smooth landscapes. *Proc. Natl. Acad. Sci. U.S.A.*, 103(3):586–591, 2006.

[1.13] Alan R Denton and Matthias Schmidt. Colloid-induced polymer compression. *J. Phys.-Condes. Matter*, 14(46):12051–12062, nov 2002.

[1.14] Matthew Urich and Alan R. Denton. Swelling, structure, and phase stability of compressible microgels. *Soft Matter*, 12:9086–9094, 2016.

[1.15] Martien A. Cohen Stuart, Wilhelm T. S. Huck, Jan Genzer, Marcus Müller, Christopher Ober, Manfred Stamm, Gleb B. Sukhorukov, Igal Szleifer, Vladimir V. Tsukruk, Marek Urban, Françoise Winnik, Stefan Zauscher, Igor Luzinov, and Sergiy Minko. Emerging applications of stimuli-responsive polymer materials. *Nat. Mater.*, 9(2):101–113, 2010.

[1.16] Matthias Karg and Thomas Hellweg. Smart inorganic/organic hybrid microgels: Synthesis and characterisation. *Journal of Materials Chemistry*, 19(46):8714–8727, 2009.

[1.17] Ucheor B. Choi, James J. McCann, Keith R. Weninger, and Mark E. Bowen. Beyond the random coil: Stochastic conformational switching in intrinsically disordered proteins. *Structure*, 19(4):566 – 576, 2011.

[1.18] J. Brijitta and P. Schurtenberger. Responsive hydrogel colloids: Structure, interactions, phase behavior, and equilibrium and nonequilibrium transitions of microgel dispersions. *Curr. Opin. Colloid Interface Sci.*, 40:87–103, 2019.

[1.19] Upayan Baul and Joachim Dzubiella. Structure and dynamics of responsive colloids with dynamical polydispersity. *J. Phys.-Condes. Matter*, 33(17):174002, apr 2021.

[1.20] Yi-Chen Lin, Benjamin Rotenberg, and Joachim Dzubiella. Structure and position-dependent properties of inhomogeneous suspensions of responsive colloids. *Phys. Rev. E*, 102:042602, Oct 2020.

[1.21] Harper Meng and Guoqiang Li. Reversible switching transitions of stimuli-responsive shape changing polymers. *J. Mater. Chem. A*, 1:7838–7865, 2013.

[1.22] Junhyuk Lee, Kang Hee Ku, Chan Ho Park, Young Jun Lee, Hongseok Yun, and Bumjoon J. Kim. Shape and color switchable block copolymer particles by temperature and ph dual responses. *ACS Nano*, 13(4):4230–4237, April 2019.

[1.23] Wei Kang Lim and Alan R. Denton. Polymer crowding and shape distributions in polymer-nanoparticle mixtures. *J. Chem. Phys.*, 141(11):114909, 2014.

[1.24] Wei Kang Lim and Alan R. Denton. Depletion-induced forces and crowding in polymer-nanoparticle mixtures: Role of polymer shape fluctuations and penetrability. *J. Chem. Phys.*, 144(2):024904, 2016.

[1.25] Wei Kang Lim and Alan R. Denton. Influence of polymer shape on depletion potentials and crowding in colloid–polymer mixtures. *Soft Matter*, 12:2247–2252, 2016.

[1.26] Johannes Harrer, Marcel Rey, Simone Ciarella, Hartmut Löwen, Liesbeth M. C. Janssen, and Nicolas Vogel. Stimuli-responsive behavior of pnipam microgels under interfacial confinement. *Langmuir*, 35(32):10512–10521, August 2019.

[1.27] Giovanni Del Monte and Emanuela Zaccarelli. Numerical study of neutral and charged microgel suspensions: from single-particle to collective behavior. *arXiv preprint arXiv:2404.04032*, 2024.

[1.28] Rajam Elancheliyan, Giovanni Del Monte, Edouard Chauveau, Simona Sennato, Emanuela Zaccarelli, and Domenico Truzzolillo. Role of charge content in the two-step deswelling of poly (n-isopropylacrylamide)-based microgels. *Macromolecules*, 55(17):7526–7539, 2022.

[1.29] Jianshu Cao and B. J. Berne. Theory and simulation of polar and nonpolar polarizable fluids. *J. Chem. Phys.*, 99(9):6998–7011, 1993.

[1.30] Daniel F Calef and Peter G Wolynes. Smoluchowski–vlasov theory of charge solvation dynamics. *J. Chem. Phys.*, 78(6):4145–4153, 1983.

[1.31] Amalendu Chandra and Biman Bagchi. Collective orientational relaxation in a dense liquid of ellipsoidal molecules. *Physica A*, 169(2):246–262, 1990.

[1.32] Amalendu Chandra and Biman Bagchi. The role of translational diffusion in the polarization relaxation in dense polar liquids. *Chem. Phys. Lett.*, 151(1-2):47–53, 1988.

[1.33] Mikhail Motornov, Roman Sheparovych, Robert Lupitskyy, Emily MacWilliams, and Sergiy Minko. Responsive colloidal systems: Reversible aggregation and fabrication of superhydrophobic surfaces. *J. Colloid Interface Sci.*, 310(2):481–488, 2007.

[1.34] Mikhail Motornov, Halyna Royter, Robert Lupitskyy, Yuri Roiter, and Sergiy Minko. Stimuli-responsive hydrogel hollow capsules by material efficient and robust cross-linking-precipitation synthesis revisited. *Langmuir*, 27(24):15305–15311, 2011.

[1.35] Kyriaki Kalaitzidou and Alfred J. Crosby. Adaptive polymer particles. *Appl. Phys. Lett.*, 93(4):041910, 2008.

[1.36] Huan-Xiang Zhou, Germán Rivas, and Allen P. Minton. Macromolecular crowding and confinement: Biochemical, biophysical, and potential physiological consequences. *Annu. Rev. Biophys.*, 37(1):375–397, 2008.

[1.37] Jiang Hong and Lila M. Gierasch. Macromolecular crowding remodels the energy landscape of a protein by favoring a more compact unfolded state. *J. Am. Chem. Soc.*, 132(30):10445–10452, August 2010.

[1.38] Nicholas F. Dupuis, Erik D. Holmstrom, and David J. Nesbitt. Molecular-crowding effects on single-molecule rna folding/unfolding thermodynamics and kinetics. *Proc. Natl. Acad. Sci. U.S.A.*, 111(23):8464–8469, 2014.

[1.39] Jaeoh Shin, Andrey G. Cherstvy, and Ralf Metzler. Kinetics of polymer looping with macromolecular crowding: effects of volume fraction and crowder size. *Soft Matter*, 11:472–488, 2015.

[1.40] Upayan Baul, Nils Götth, Michael Bley, and Joachim Dzubiella. Modulating internal transition kinetics in responsive macromolecules by collective crowding. *J. Chem. Phys.*, 155:244902, 2021.

[1.41] Shilin Huang, Kornelia Gawlitza, Regine von Klitzing, Laurent Gilson, Johannes Nowak, Stefan Odenbach, Werner Steffen, and Gu˜nter K Auernhammer. Microgels at the water/oil interface: In situ observation of structural aging and two-dimensional magnetic bead microrheology. *Langmuir*, 32(3):712–722, 2016.

[1.42] Valeria Garbin, Ian Jenkins, Talid Sinno, John C Crocker, and Kathleen J Stebe. Interactions and stress relaxation in monolayers of soft nanoparticles at fluid-fluid interfaces. *Phys. Rev. Lett.*, 114(10):108301, 2015.

[1.43] Margaret S. Cheung, Dmitri Klimov, and D. Thirumalai. Molecular crowding enhances native state stability and refolding rates of globular proteins. *Proc. Natl. Acad. Sci. U.S.A.*, 102(13):4753–4758, 2005.

[1.44] Shuang Wu, Joachim Dzubiella, Julian Kaiser, Markus Drechsler, Xuhong Guo, Matthias Ballauff, and Yan Lu. Thermosensitive au-pnipa yolk–shell nanoparticles with tunable selectivity for catalysis. *Angew. Chem. - Int. Ed.*, 51(9):2229–2233, 2012.

[1.45] Jian-Tao Zhang, Gang Wei, Thomas F. Keller, Hilary Gallagher, Christian Stötzel, Frank A. Müller, Michael Gottschaldt, Ulrich S. Schubert, and Klaus D. Jandt. Responsive hybrid polymeric/metallic nanoparticles for catalytic applications. *Macromol. Mater. Eng.*, 295(11):1049–1057, 2010.

[1.46] Deepika Parasuraman and Michael J. Serpe. Poly (n-isopropylacrylamide) microgel-based assemblies for organic dye removal from water. *ACS Appl. Mater. Interfaces*, 3(12):4714–4721, 2011.

[1.47] Rakesh Banerjee, Sheetal Parida, Chiranjit Maiti, Mahitosh Mandal, and Dibakar Dhara. ph-degradable and thermoresponsive water-soluble core cross-linked polymeric nanoparticles as potential drug delivery vehicle for doxorubicin. *RSC Adv.*, 5:83565–83575, 2015.

[1.48] Robert Pelton. Temperature-sensitive aqueous microgels. *Adv. Colloid Interface Sci.*, 85(1):1–33, 2000.

[1.49] L Andrew Lyon and Alberto Fernandez-Nieves. The polymer/colloid duality of microgel suspensions. *Annual review of physical chemistry*, 63(1):25–43, 2012.

[1.50] Andrij Pich and Walter Richtering. Microgels by precipitation polymerization: synthesis, characterization, and functionalization. *Chemical design of responsive microgels*, pages 1–37, 2011.

[1.51] P. J. Flory and W. R. Krigbaum. Statistical Mechanics of Dilute Polymer Solutions. II. *J. Chem. Phys.*, 18(8):1086–1094, 12 1950.

[1.52] Tyler J. Weyer and Alan R. Denton. Concentration-dependent swelling and structure of ionic microgels: simulation and theory of a coarse-grained model. *Soft Matter*, 14:4530–4540, 2018.

[1.53] Carlos G. Lopez and Walter Richtering. Does flory–rehner theory quantitatively describe the swelling of thermoresponsive microgels? *Soft Matter*, 13:8271–8280, 2017.

[1.54] Yong Qiu and Kinam Park. Environment-sensitive hydrogels for drug delivery. *Advanced drug delivery reviews*, 53(3):321–339, 2001.

[1.55] Satish Nayak, Daoji Gan, Michael J. Serpe, and L. Andrew Lyon. Hollow thermoresponsive microgels. *Small*, 1(4):416–421, 2005.

[1.56] A. Moncho-Jordá. Effective charge of ionic microgel particles in the swollen and collapsed states: The role of the steric microgel-ion repulsion. *J. Chem. Phys.*, 139(6):064906, 2013.

[1.57] Brian R. Saunders and Brian Vincent. Microgel particles as model colloids: Theory, properties and applications. *Adv. Colloid Interface Sci.*, 80(1):1 – 25, 1999.

[1.58] Valentina Nigro, Roberta Angelini, Monica Bertoldo, Fabio Bruni, Maria Antonietta Ricci, and Barbara Ruzicka. Dynamical behavior of microgels of interpenetrated polymer networks. *Soft Matter*, 13(30):5185–5193, 2017.

[1.59] Arturo Moncho-Jordá, Nils Göth, and Joachim Dzubiella. Liquid structure of bistable responsive macromolecules using mean-field density-functional theory. *Soft Matter*, 19(15):2832–2846, 2023.

[1.60] Allan S. Hoffman. Applications of thermally reversible polymers and hydrogels in therapeutics and diagnostics. *J. Control. Release*, 6(1):297–305, 1987.

[1.61] S. H. Gehrke, J. P. Fisher, M. Palasis, and M. E. Lund. Factors determining hydrogel permeability. *Ann. New York Acad. Sci.*, 831:179–207, 1997.

[1.62] Kunlin Chen, Shuxue Zhou, and Limin Wu. Self-healing underwater superoleophobic and antibiofouling coatings based on the assembly of hierarchical microgel spheres. *ACS Nano*, 10(1):1386–1394, January 2016.

[1.63] Chotiros Dokkhan, Muhamad Z. Mokhtar, Qian Chen, Brian R. Saunders, Nigel W. Hodson, and Bruce Hamilton. Using microgels to control the morphology and optoelectronic properties of hybrid organic–inorganic perovskite films. *Phys. Chem. Chem. Phys.*, 20:27959–27969, 2018.

[1.64] Avraham Halperin, Martin Kröger, and Françoise M. Winnik. Poly(n-isopropylacrylamide) phase diagrams: Fifty years of research. *Angew. Chem. - Int. Ed.*, 54(51):15342–15367, 2015.

[1.65] Michael te Vrugt, Hartmut Löwen, and Raphael Wittkowski. Classical dynamical density functional theory: from fundamentals to applications. *Adv. Phys.*, 69(2):121–247, 2020.

[1.66] Umberto Marini Bettolo Marconi and Pedro Tarazona. Dynamic density functional theory of fluids. *J. Chem. Phys.*, 110(16):8032–8044, 1999.

[1.67] Andrew J Archer and Robert Evans. Dynamical density functional theory and its application to spinodal decomposition. *J. Chem. Phys.*, 121(9):4246–4254, 2004.

[1.68] C Patrick Royall, Joachim Dzubiella, Matthias Schmidt, and Alfons van Blaaderen. Nonequilibrium sedimentation of colloids on the particle scale. *Phys. Rev. Lett.*, 98(18):188304, 2007.

[1.69] Michael te Vrugt, Hartmut Löwen, and Raphael Wittkowski. Classical dynamical density functional theory: from fundamentals to applications. *Adv. Phys.*, 69(2):121–247, 2020.

[1.70] Pablo Hervés, Moisés Pérez-Lorenzo, Luis M. Liz-Marzán, Joachim Dzubiella, Yan Lu, and Matthias Ballauff. Catalysis by metallic nanoparticles in aqueous solution: Model reactions. *Chem. Soc. Rev.*, 41:5577–5587, 2012.

[1.71] Yan Lu, Yu Mei, Markus Drechsler, and Matthias Ballauff. Thermosensitive core–shell particles as carriers for ag nanoparticles: Modulating the catalytic activity by a phase transition in networks. *Angew. Chem. - Int. Ed.*, 45(5):813–816, 2006.

[1.72] Rafael Roa, Won Kyu Kim, Matej Kanduč, Joachim Dzubiella, and Stefano Angioletti-Uberti. Catalyzed bimolecular reactions in responsive nanoreactors. *ACS Catal.*, 7(9):5604–5611, September 2017.

[1.73] Rafael Roa, Stefano Angioletti-Uberti, Yan Lu, Joachim Dzubiella, Francesco Piazza, and Matthias Ballauff. Catalysis by metallic nanoparticles in solution: Thermosensitive microgels as nanoreactors. *Z. Phys. Chem.*, 232(5-6):773–803, 2018.

[1.74] Matej Kanduč, Won Kyu Kim, Rafael Roa, and Joachim Dzubiella. Modeling of stimuli-responsive nanoreactors: rational rate control towards the design of colloidal enzymes. *Mol. Syst. Des. Eng.*, 5:602–619, 2020.

[1.75] Matej Kanduč, Won Kyu Kim, Rafael Roa, and Joachim Dzubiella. Transfer free energies and partitioning of small molecules in collapsed pnipam polymers. *J. Phys. Chem. B*, 123(3):720–728, 2019.

[1.76] Matej Kanduč, Won Kyu Kim, Rafael Roa, and Joachim Dzubiella. How the shape and chemistry of molecular penetrants control responsive hydrogel permeability. *ACS Nano*, 15(1):614–624, 2021.

[1.77] Maria Palasis and Stevin H. Gehrke. Permeability of responsive poly (n-isopropylacrylamide) gel to solutes. *Journal of Controlled Release*, 18(1):1 – 11, 1992.

[1.78] M.A. Molina, C.R. Rivarola, and C.A. Barbero. Study on partition and release of molecules in superabsorbent thermosensitive nanocomposites. *Polymer*, 53(2):445–453, 2012.

[1.79] Matej Kanduc, Won Kyu Kim, Rafael Roa, and Joachim Dzubiella. Selective molecular transport in thermoresponsive polymer membranes: Role of nanoscale hydration and fluctuations. *Macromolecules*, 51(13):4853–4864, 2018.

[1.80] Arturo Moncho-Jordá, Ana B. Jódar-Reyes, Matej Kanduč, Alicia Germán-Bellod, Juan M. López-Romero, Rafael Contreras-Cáceres, Francisco Sarabia, Miguel García-Castro, Héctor A. Pérez-Ramírez, and Gerardo Odriozola. Scaling laws in the diffusive release of neutral cargo from hollow hydrogel nanoparticles: Paclitaxel-loaded poly(4-vinylpyridine). *ACS Nano*, 14(11):15227–15240, 2020.

[1.81] Mehrdad Hamidi, Amir Azadi, and Pedram Rafiei. Hydrogel nanoparticles in drug delivery. *Adv. Drug Deliv. Rev.*, 60(15):1638–1649, 2008. 2008 Editors' Collection.

[1.82] Brian R. Saunders, Nadiah Laajam, Emma Daly, Stephanie Teow, Xinhua Hu, and Robert Stepto. Microgels: From responsive polymer colloids to biomaterials. *Adv. Colloid Interface Sci.*, 147-148:251 – 262, 2009.

[1.83] Serguei V Vinogradov. Nanogels in the race for drug delivery. *Nanomedicine*, 5(2):165–168, 2010.

[1.84] Arturo Moncho-Jordá, Alicia Germán-Bellod, Stefano Angioletti-Uberti, Irene Adroher-Benítez, and Joachim Dzubiella. Nonequilibrium uptake kinetics of molecular cargo into hollow hydrogels tuned by electrosteric interactions. *ACS Nano*, 13(2):1603–1616, February 2019.

[1.85] Arturo Moncho-Jordá, Ana B. Jódar-Reyes, Matej Kanduč, Alicia Germán-Bellod, Juan M. López-Romero, Rafael Contreras-Cáceres, Francisco Sarabia, Miguel García-Castro, Héctor A. Pérez-Ramírez, and Gerardo Odriozola. Scaling laws in the diffusive release of neutral cargo from hollow hydrogel nanoparticles: Paclitaxel-loaded poly(4-vinylpyridine). *ACS Nano*, 14(11):15227–15240, November 2020.

[1.86] A.K. Bajpai, Sandeep K. Shukla, Smitha Bhanu, and Sanjana Kankane. Responsive polymers in controlled drug delivery. *Prog. Polym. Sci.*, 33(11):1088–1118, 2008.

[1.87] Umberto Marini Bettolo Marconi and Pedro Tarazona. Dynamic density functional theory of fluids. *J. Chem. Phys.*, 110(16):8032–8044, 1999.

[1.88] A. J. Archer and R. Evans. Dynamical density functional theory and its application to spinodal decomposition. *J. Chem. Phys.*, 121(9):4246–4254, 2004.

[1.89] Michael te Vrugt, Jens Bickmann, and Raphael Wittkowski. Effects of social distancing and isolation on epidemic spreading modeled via dynamical density functional theory. *Nat. Commun.*, 11(1):5576, 2020.

[1.90] Arturo Moncho-Jordá and Joachim Dzubiella. Controlling the microstructure and phase behavior of confined soft colloids by active interaction switching. *Phys. Rev. Lett.*, 125:078001, Aug 2020.

[1.91] Sebastian Stock, Regine von Klitzing, and Amin Rahimzadeh. Impact of ultrasound on the motion of compact particles and acousto-responsive microgels. *arXiv preprint arXiv:2307.12696*, 2023.

[1.92] Xiaobing Feng, Guiqiong Huang, Jian Qiu, Li Peng, Kaiqing Luo, Dongmei Liu, and Peng Han. Dynamic light scattering in flowing dispersion. *Optics Communications*, 531:129225, 2023.

[1.93] Jonghwan Lee, Weicheng Wu, James Y Jiang, Bo Zhu, and David A Boas. Dynamic light scattering optical coherence tomography. *Optics express*, 20(20):22262–22277, 2012.

[1.94] Robert Pecora. *Dynamic light scattering: applications of photon correlation spectroscopy*. Springer Science & Business Media, 1985.

[1.95] Bruce J Berne and Robert Pecora. *Dynamic light scattering: with applications to chemistry, biology, and physics*. Courier Corporation, 2000.

Chapter 2

Motivation and Thesis Outline

2.1. Motivation

The rapid advancement of nanotechnology has paved the way for the development of sophisticated responsive systems capable of dynamically adapting to varying environmental stimuli. Among these, microgels stand out as highly versatile soft nanoparticles with significant potential in diverse applications, particularly in biomedicine and biotechnology. The intrinsic ability of microgels to undergo reversible volume phase transitions—expanding or collapsing in response to changes in temperature, pH, ionic strength, and other external factors—renders them ideal candidates for applications such as targeted drug delivery, controlled release systems, and responsive coatings [2.1–2.4].

A critical aspect that distinguishes size responsive systems from their static counterparts is their inherent polydispersity. Unlike monodisperse systems, where particles are uniform in size, polydispersity introduces a spectrum of particle sizes within the same system, offering an additional degree of freedom that enhances adaptability and functionality [2.5–2.9]. This size variability is not merely a static characteristic but actively influences the dynamic behavior of the system, especially under non-equilibrium conditions such as the application of external fields or the presence of concentration gradients [2.10]. Understanding and controlling polydispersity is therefore paramount for optimizing the performance of responsive systems in practical applications.

Despite significant progress, several challenges persist in the study and application of responsive microgels:

1. **Coupled Dynamics of Translation and Size Adaptation:** Traditional models often treat translational and internal (size) dynamics separately. However, in responsive systems, these dynamics are intrinsically coupled, especially under non-equilibrium conditions [2.11, 2.12].

2. **Accurate Modeling of Non-Equilibrium Processes:** While Density Functional Theory (DFT) and its dynamic counterpart (DDFT) provide robust frameworks for studying equilibrium and near-equilibrium systems, their extension to fully capture the coupled dynamics of responsive systems remains underexplored [2.13, 2.14].

3. **Advanced Characterization Techniques:** Dynamic Light Scattering (DLS) is a powerful tool for probing the dynamic properties of colloidal systems. However, conventional DLS methods face limitations measuring complex dynamic behaviors, such as drift velocities in non-equilibrium states [2.15–2.17].

4. **Integration of Machine Learning for Enhanced Analysis:** The complexity and high dimensionality of data obtained from techniques like DLS necessitate advanced analytical methods. Machine learning offers promising avenues for improving the accuracy and efficiency of data interpretation in highly polydisperse and dynamic systems.

This doctoral thesis addresses these challenges through a multidisciplinary approach that integrates theoretical modeling, experimental measures, and advanced data analysis methods. Our work aims to bridge the existing gaps by developing and applying extended theoretical frameworks, enhancing experimental methodologies, and leveraging machine learning to achieve a comprehensive understanding of responsive microgels under non-equilibrium conditions.

2.2. Thesis Structure and Outline

This thesis is presented as a compendium of articles, with the Results section structured as a collection of research publications. Each publication is included as an individual chapter, contributing to the overall research objectives. The thesis is organized into four main parts: Introduction, Physical Principles, Results, and Conclusions. Additionally, a patent (in the publication process) related to the developed methodologies is included. The detailed structure is as follows:

Part 1: Introduction

- **Chapter 3: Theory of Classical DFT, DDFT and Brownian Dynamics**

Introduces classical Density Functional Theory (DFT) and Dynamic Density Functional Theory (DDFT). This chapter lays the foundational understanding required to comprehend the extensions and applications presented in the later chapters. It covers the mathematical formulations and assumptions used in DFT and DDFT. It also introduces Brownian Dynamics which will be used as reference in different chapters.

- **Chapter 4: Basis of Dynamic Light Scattering (DLS)**

  Explains the principles and methodologies of Dynamic Light Scattering (DLS), essential for interpreting the theoretical experimental results discussed in subsequent chapters.

Part 2: Results

This part comprises a series of studies presented as individual chapters, each addressing specific aspects of responsive nanoparticles through both theoretical and experimental lenses.

- **Publication I: Density Functional Theory for Responsive Hard-Sphere Fluids**

  Extends classical DFT to hard-sphere fluids by introducing size as a new degree of freedom. This extension allows for the exploration of size-dependent phenomena in polydisperse systems, enhancing the predictive capabilities of DFT for responsive colloidal fluids.

- **Publication II: Nonequilibrium Relaxation of Soft Responsive Colloids**

  Advances classical DDFT by incorporating size as an additional dynamic variable. This chapter investigates the coupled translational and internal (size) dynamics of responsive colloids under various external fields, providing insights into their non-equilibrium behavior.

- **Publication III: Diffusion and Interaction Effects on Molecular Release Kinetics from Collapsed Microgels**

  Utilizes DDFT to model and calculate the release profiles of drugs from collapsed microgels. This study aims to predict release times and optimize drug delivery systems by accounting for diffusion and interaction effects within the densely packed polymeric matrix.

- **Publication IV: Measuring Absolute Velocities from Nonequilibrium Oscillations via Single-Detector 3D Dynamic Light Scattering**

  Extends DLS theory to enhance the capabilities of 3D-DLS setups, enabling the measurement of absolute particle velocities. This chapter provides a formal theoretical justification for the observed oscillatory behavior in

intensity autocorrelation functions and demonstrates the method's application in thermal-convective systems.

- **Publication V: Patent for Measuring Relative Velocities**

  Applies the theoretical advancements from Publication IV to develop a novel device capable of measuring the relative velocities of two colloidal systems within the same volume. This Publication outlines the design, functionality, and potential applications of the device, highlighting its innovation and utility.

- **Publication VI: Improving DLS Analysis Using Machine Learning**

  Integrates machine learning algorithms with traditional DLS analysis methods to enhance the accuracy of size distribution measurements in highly polydisperse systems. This chapter explores various machine learning techniques and their efficacy in complementing methods like CONTIN and cumulant analysis.

Part 3: Conclusions

- Summarizes the key findings and contributions of the thesis, highlighting advancements in theoretical modeling, experimental methodologies, and data analysis techniques for responsive microgels. Discusses the implications of the research presented in this thesis for future applications and suggests potential directions for further investigation.

Bibliography

[2.1] Veronika Kozlovskaya, Jenolyn F. Alexander, Yun Wang, Thomas Kuncewicz, Xuewu Liu, Biana Godin, and Eugenia Kharlampieva. Internalization of red blood cell-mimicking hydrogel capsules with ph-triggered shape responses. *ACS Nano*, 8(6):5725–5737, June 2014.

[2.2] James McMasters, Scott Poh, Jenny B. Lin, and Alyssa Panitch. Delivery of anti-inflammatory peptides from hollow pegylated poly(nipam) nanoparticles reduces inflammation in an ex vivo osteoarthritis model. *J. Controlled Release*, 258:161 – 170, 2017.

[2.3] Yue Qiao, Jian He, Weiyu Chen, Yinhui Yu, Wanlin Li, Zhen Du, Tingting Xie, Yang Ye, Shi Yuan Hua, Danni Zhong, Ke Yao, and Min Zhou. Light-activatable synergistic therapy of drug-resistant bacteria-infected cutaneous chronic wounds and nonhealing keratitis by cupriferous hollow nanoshells. *ACS Nano*, 14(3):3299–3315, March 2020.

[2.4] Takuma Kureha and Daisuke Suzuki. Nanocomposite microgels for the selective separation of halogen compounds from aqueous solution. *Langmuir*, 34(3):837–846, 2018.

[2.5] Alan R Denton and Matthias Schmidt. Colloid-induced polymer compression. *J. Phys.-Condes. Matter*, 14(46):12051–12062, nov 2002.

[2.6] Matthew Urich and Alan R. Denton. Swelling, structure, and phase stability of compressible microgels. *Soft Matter*, 12:9086–9094, 2016.

[2.7] J. Brijitta and P. Schurtenberger. Responsive hydrogel colloids: Structure, interactions, phase behavior, and equilibrium and nonequilibrium transitions of microgel dispersions. *Curr. Opin. Colloid Interface Sci.*, 40:87–103, 2019.

[2.8] Upayan Baul and Joachim Dzubiella. Structure and dynamics of responsive colloids with dynamical polydispersity. *J. Phys.-Condes. Matter*, 33(17):174002, apr 2021.

[2.9] Yi-Chen Lin, Benjamin Rotenberg, and Joachim Dzubiella. Structure and position-dependent properties of inhomogeneous suspensions of responsive colloids. *Phys. Rev. E*, 102:042602, Oct 2020.

[2.10] Valeria Garbin, Ian Jenkins, Talid Sinno, John C Crocker, and Kathleen J Stebe. Interactions and stress relaxation in monolayers of soft nanoparticles at fluid-fluid interfaces. *Phys. Rev. Lett.*, 114(10):108301, 2015.

[2.11] Arturo Moncho-Jordá, Sebastien Groh, and Joachim Dzubiella. External field-driven property localization in liquids of responsive macromolecules. *J. Chem. Phys.*, 160(2):024904, 2024.

[2.12] Arturo Moncho-Jordá, Nils Göth, and Joachim Dzubiella. Liquid structure of bistable responsive macromolecules using mean-field density-functional theory. *Soft Matter*, 19(15):2832–2846, 2023.

[2.13] Michael te Vrugt, Hartmut Löwen, and Raphael Wittkowski. Classical dynamical density functional theory: from fundamentals to applications. *Adv. Phys.*, 69(2):121–247, 2020.

[2.14] Umberto Marini Bettolo Marconi and Pedro Tarazona. Dynamic density functional theory of fluids. *J. Chem. Phys.*, 110(16):8032–8044, 1999.

[2.15] Sebastian Stock, Regine von Klitzing, and Amin Rahimzadeh. Impact of ultrasound on the motion of compact particles and acousto-responsive microgels. *arXiv preprint arXiv:2307.12696*, 2023.

[2.16] Xiaobing Feng, Guiqiong Huang, Jian Qiu, Li Peng, Kaiqing Luo, Dongmei Liu, and Peng Han. Dynamic light scattering in flowing dispersion. *Optics Communications*, 531:129225, 2023.

[2.17] Jonghwan Lee, Weicheng Wu, James Y Jiang, Bo Zhu, and David A Boas. Dynamic light scattering optical coherence tomography. *Optics express*, 20(20):22262–22277, 2012.

Chapter 3

Theoretical Framework

Understanding the behavior of responsive nanoparticle systems, particularly microgels, requires robust theoretical models that can accurately describe both equilibrium and non-equilibrium states. **Density Functional Theory (DFT)** and its dynamic counterpart, **Dynamic Density Functional Theory (DDFT)**, provide essential frameworks for this purpose. These theories, complemented by Brownian Dynamics (BD) simulations, form the theoretical foundation necessary for analyzing responsive colloidal systems studied in subsequent publications.

The theoretical frameworks presented here serve as the basis for several key applications explored in this thesis. In Publication I, we extend Classical DFT using Fundamental Measure Theory combined with effective hard sphere potentials to study the equilibrium properties of responsive particles, focusing on equilibrium density distributions, size-dependent interactions, and packing effects in responsive particle systems. Publication II develops a DDFT framework incorporating mean-field theory with Gaussian interaction potentials to investigate the relaxation dynamics of soft responsive systems, examining time-dependent particle size changes, collective relaxation phenomena, and response to external stimuli. In Publication III, we employ DDFT to model drug release from microgels, where the theory accounts for drug-microgel interactions and spatially-dependent diffusion coefficients, enabling us to study the spatial variation of diffusion coefficients inside and outside the microgel, drug-microgel interactions through appropriate potential terms, and time-dependent density profiles of drug molecules.

Brownian Dynamics simulations provide essential complementary insights throughout this work. In Publication II, BD simulations serve as a benchmark to validate our DDFT extensions for responsive particle dynamics. Additionally, in Publication IV, BD simulations generate correlation functions that verify our

extended Dynamic Light Scattering (DLS) model. This combined approach, utilizing continuum theories (DFT and DDFT) alongside particle-based simulations (BD), offers a comprehensive framework for understanding the complex behavior of responsive colloidal systems.

This chapter begins by establishing the fundamental principles of Classical DFT, proceeds to its dynamic extension in DDFT, and concludes with an overview of Brownian Dynamics simulations. These theoretical tools, while powerful individually, demonstrate their full potential when used in concert to address the diverse challenges presented by responsive colloidal systems.

3.1. Classical Density Functional Theory

Density Functional Theory (DFT) has its roots in quantum mechanics, beginning with the seminal work of Hohenberg and Kohn in 1964 [3.1]. They demonstrated that for an interacting electron gas subject to an external potential, the energy can be uniquely expressed as a functional of the electronic density alone. Shortly thereafter, Kohn and Sham developed a practical method for solving the resulting equations [3.2]. Although these ideas were initially formulated for quantum systems, they inspired a powerful *classical* analog now commonly referred to as Classical Density Functional Theory (Classical DFT or cDFT).

A key milestone in the development of cDFT was provided by Evans in 1979 [3.3], who established the foundational theorems for inhomogeneous classical fluids. An inhomogeneous fluid is one where, even at equilibrium, its thermodynamic properties vary from point to point in space. A familiar example is the variation of pressure with height in a fluid under gravity. The central insight of DFT is that any thermodynamic property of such a system can be expressed in terms of the particle density at each point in space, denoted as $\rho(\mathbf{r})$, where $\mathbf{r}$ represents the position vector in three-dimensional space.

Importantly, due to the inhomogeneous nature of these systems, thermodynamic properties are not expressed as simple functions but as *functionals* of $\rho(\mathbf{r})$. A functional differs from a function in that it depends on the particle density not just at a single point, but on its entire spatial distribution—that is, it depends on $\rho(\mathbf{r})$ at all points $\mathbf{r}$ simultaneously. This mathematical framework allows DFT to capture the rich complexity of inhomogeneous systems while maintaining theoretical elegance.

In parallel with Evans' work, subsequent contributions by Rosenfeld [3.4] and others introduced new ways of approximating the *excess free energy*, broadening the theory's applicability to dense and complex fluids. Today, cDFT is widely recognized as a primary tool for studying equilibrium properties of inhomogeneous fluids ranging from simple hard-sphere liquids to polydisperse colloidal suspensions. The success

of DFT lies in its ability to recast the complex, many-body problem of interacting particles into a variational problem involving density profiles $\rho(\mathbf{r})$. This makes DFT especially suitable for analyzing responsive colloidal systems, such as microgels, where particle interactions and spatial inhomogeneities are essential.

Building upon cDFT, the field has seen dynamic extensions—termed Dynamic Density Functional Theory (DDFT)—primarily through the work of Marconi and Tarazona [3.5, 3.6] and subsequent refinements by Archer, Evans, and coworkers [3.7]. These dynamic approaches incorporate time evolution via a generalized diffusion equation, making them useful for investigating relaxation processes, aging phenomena, and other nonequilibrium effects. In this section, we first present the fundamentals of cDFT, then proceed to discuss two widely used approximations for the excess free energy: the Fundamental Measure Theory (FMT) and a mean-field (MF) approach often used in DDFT formulations. We also illustrate how these approximations are tailored to responsive colloidal systems such as microgels.

Classical DFT provides a framework for describing inhomogeneous systems at equilibrium under external fields. These external fields break spatial symmetry, causing system properties to vary with position. In the absence of external fields, a stable system would maintain uniform density throughout space. However, even without external fields, DFT remains relevant for describing interfaces in phase-separated systems, where density necessarily varies between phases. In the canonical ensemble, the theory minimizes the Helmholtz free energy $F = U - TS$, which balances the competition between minimizing internal energy (U) and maximizing entropy (S) at a fixed temperature (T). The theory's power lies in expressing this free energy as a functional of the local particle density $\rho(\mathbf{r})$, providing a direct route to both structural and thermodynamic properties.

The foundation of Classical DFT rests on two fundamental theorems established by Hohenberg and Kohn:

1. **Existence Theorem:** For any system of interacting particles in an external potential $V_{\text{ext}}(\mathbf{r})$, there exists a unique functional of the particle density $\rho(\mathbf{r})$ that determines the Helmholtz free energy $F[\rho]$. This means that if we know the exact functional form of $F[\rho]$, we can derive all equilibrium properties of the system solely from the density distribution, without needing to solve the full N-body problem.

2. **Variational Principle:** The equilibrium density distribution minimizes the grand potential functional. This provides not just a theoretical foundation but also a practical route to determining the equilibrium properties of the system.

The Helmholtz free energy functional $F[\rho]$ naturally separates into two contributions:

$$F[\rho] = F_{\text{ideal}}[\rho] + F_{\text{ex}}[\rho] \tag{3.1}$$

This separation reflects the distinct physical contributions to the free energy. $F_{\text{ideal}}[\rho]$ represents the free energy of an ideal gas at the same temperature and density distribution. This term is known exactly and captures the entropic contribution from particle positions in the absence of interactions:

$$F_{\text{ideal}}[\rho] = k_B T \int \rho(\mathbf{r}) \left[\ln(\rho(\mathbf{r})\Lambda^3) - 1\right] d\mathbf{r} \tag{3.2}$$

where $\Lambda = h/\sqrt{2\pi m k_B T}$ is the thermal de Broglie wavelength. The logarithmic term arises from the entropy of mixing, while the -1 term ensures the correct dilute gas limit.

$F_{\text{ex}}[\rho]$ accounts for all particle-particle interactions. While its exact form is generally unknown, various approximations have been developed for different types of interactions.

The equilibrium density distribution in the grand canonical ensemble is determined by minimizing the grand potential functional $\Omega[\rho]$:

$$\Omega[\rho] = F[\rho] - \mu \int \rho(\mathbf{r}) d\mathbf{r} + \int \rho(\mathbf{r}) V_{\text{ext}}(\mathbf{r}) d\mathbf{r} \tag{3.3}$$

where μ is the chemical potential. Each term has a clear physical interpretation:

- $F[\rho]$ balances internal energy and entropy
- $-\mu \int \rho(\mathbf{r}) d\mathbf{r}$ represents the energy cost of adding/removing particles
- $\int \rho(\mathbf{r}) V_{\text{ext}}(\mathbf{r}) d\mathbf{r}$ accounts for the interaction with the external potential

The minimization condition leads to the fundamental equation of DFT:

$$\frac{\delta \Omega[\rho]}{\delta \rho(\mathbf{r})} = 0 \tag{3.4}$$

which yields:

$$\frac{\delta F[\rho]}{\delta \rho(\mathbf{r})} + V_{\text{ext}}(\mathbf{r}) = \mu \tag{3.5}$$

The minimization condition can be rewritten by separating the ideal and excess contributions to the free energy:

$$k_B T \ln(\rho(\mathbf{r})\Lambda^3) - c^{(1)}(\mathbf{r}) + V_{\text{ext}}(\mathbf{r}) = \mu \tag{3.6}$$

where we have introduced the single-particle direct correlation function $c^{(1)}(\mathbf{r}) = -\beta\delta F_{\text{ex}}[\rho]/\delta\rho(\mathbf{r})$. This function captures all non-ideal contributions to the chemical potential and plays a central role in the theory. Rearranging this equation provides an explicit expression for the density:

$$\rho(\mathbf{r}) = \frac{1}{\Lambda^3} \exp\left(\beta(\mu - V_{\text{ext}}(\mathbf{r})) + c^{(1)}(\mathbf{r})\right) \tag{3.7}$$

with $\beta = 1/(k_B T)$. The solution of the density profile equation requires careful consideration of its self-consistent nature. Since the direct correlation function depends on the density distribution itself through $c^{(1)}(\mathbf{r})$, we must employ iterative methods to find the equilibrium solution. The standard approach begins with an initial guess for the density profile, from which we calculate the direct correlation function. This allows us to compute a new density profile using the exponential relation derived from the Euler-Lagrange equation. However, direct application of this procedure often leads to numerical instabilities, necessitating the implementation of mixing schemes to achieve convergence.

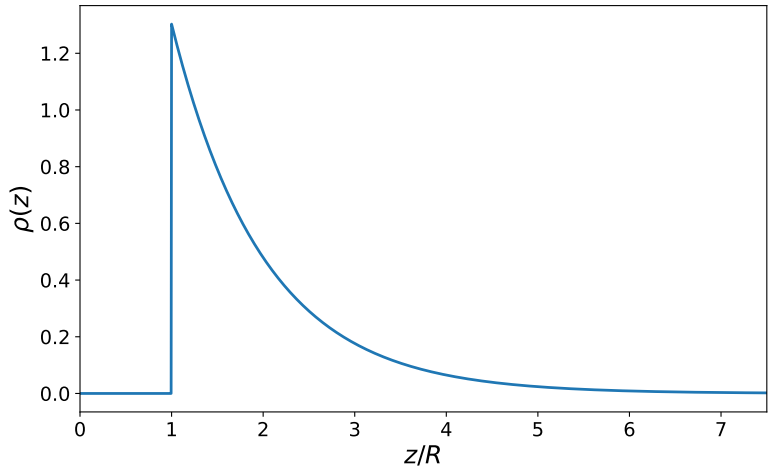

Figure 3.1: Density profile $\rho(z)$ for an ideal gas under a gravitational field. The profile shows the characteristic exponential decay with height due to the gravitational potential $V_{\text{ext}}(z) = z$.

Ideal Gas Approximation

To demonstrate this methodology in practice, let us begin with a simple system: an ideal gas under an external potential $V_{\text{ext}}(z)$. In this case, where particles do not interact with each other, the excess free energy is zero, and the density profile can be obtained analytically. The equilibrium density profile follows a simple exponential law:

$$\rho(z) = \rho_0 \exp(-\beta V_{\text{ext}}(z)) \tag{3.8}$$

where ρ_0 is the density in the absence of external potential. Figure (3.1) shows this behavior for an ideal gas under gravitational field, where $V_{\text{ext}}(z) = z$ for $z > R$ and $V_{\text{ext}}(z) = \infty$ for $z < R$. The exponential decay of density with height is a direct consequence of the competition between entropy and the external potential.

Building upon this foundation, we can examine a more complex system: a hard-sphere fluid near a hard wall. This system, while still relatively simple, introduces particle-particle interactions and captures many essential features of inhomogeneous fluids while remaining mathematically tractable. The external potential in this case takes a particularly simple form, being infinite within the wall ($z < R$) and zero elsewhere. This creates a sharp boundary that the fluid particles cannot penetrate, leading to interesting structural features in the density profile.

Fundamental Measure Theory Approximation

For the excess free energy contribution, we employ the Fundamental Measure Theory (FMT) approximation, which has proven highly successful in describing hard-sphere systems. The FMT provides an expression for the excess free energy functional in terms of weighted densities, which are convolutions of the density profile with geometrically-inspired weight functions. The full derivation of the excess free energy is made in Publication I. From this functional, we can derive the single-particle direct correlation function through functional differentiation:

$$c^{(1)}(z) = -\beta \frac{\delta F_{\text{ex}}^{\text{FMT}}[\rho]}{\delta \rho(z)} \tag{3.9}$$

The numerical solution proceeds iteratively. A reasonable starting point is a simple step function approximation, where the density jumps from zero to the bulk value at a distance of one particle radius from the wall. This initial guess, while crude, respects the basic physical constraint that particles cannot penetrate the wall. At each iteration, we compute a new density profile using the exponential relation:

$$\rho_{i+1}(z) = \rho_{\text{bulk}} \exp\left[c_i^{(1)}(z) - c^{(1)}(\infty)\right] \tag{3.10}$$

for all positions beyond the hard-sphere contact distance. Here, $c^{(1)}(\infty)$ represents the direct correlation function far from the perturbation where the external field is zero ($z \to \infty$), and its subtraction ensures proper normalization to the bulk density. This form explicitly shows how deviations from bulk behavior arise from spatial variations in the direct correlation function.

To stabilize the iteration scheme, we employ a mixing procedure where the new density is combined with the previous iteration:

$$\rho_{\text{new}}(z) = \alpha \rho_{i+1}(z) + (1 - \alpha)\rho_i(z) \tag{3.11}$$

The mixing parameter α plays a crucial role in achieving convergence. Values typically range from 0.01 to 0.1, with smaller values providing more stable iteration at the cost of slower convergence. This trade-off between stability and computational efficiency is a common feature in density functional calculations.

The iteration process continues until the density profile reaches convergence, which we monitor through the integral measure of the density change between successive iterations:

$$\int |\rho_{i+1}(z) - \rho_i(z)| dz < 10^{-8} \tag{3.12}$$

This criterion ensures that the final density profile represents a stable solution to the Euler-Lagrange equation across the entire spatial domain.

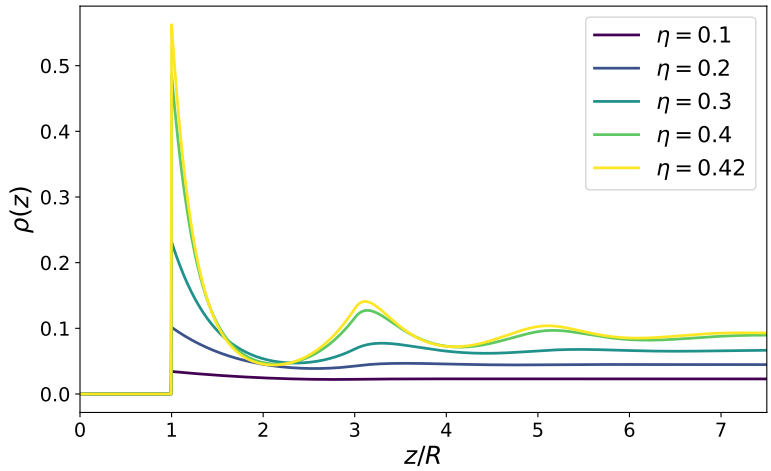

Figure 3.2: Density profiles $\rho(z)$ for hard spheres near a hard wall at different packing fractions η. The profiles show characteristic oscillations reflecting particle layering, with the amplitude of the oscillations increasing with packing fraction. The distance z is measured in units of the particle diameter.

The resulting density profiles for different packing fractions η are shown in Figure (3.2). The packing fraction η is a dimensionless measure of density defined as the fraction of the total volume occupied by the spheres. For monodisperse hard spheres of radius R, it is related to the bulk number density ρ_{bulk} through $\eta = (4\pi/3)R^3\rho_{\text{bulk}}$. This parameter ranges from $\eta = 0$ for an infinitely dilute system to $\eta \approx 0.74$ for close-packed spheres, with fluid-solid coexistence occurring around $\eta \approx 0.49$. This approximation only work for fluids, where $\eta < 0.49$. These profiles reveal rich structural features near the wall. Most notably, we observe oscillations in the fluid density, reflecting the layering of particles near the hard surface. The amplitude of these oscillations increases with packing fraction, demonstrating the enhanced structuring that occurs at higher densities. These oscillations decay to the bulk density over a distance of several particle diameters, showing how the wall's

influence propagates into the fluid through particle-particle correlations. This layering phenomenon is a direct consequence of the interplay between entropy, which favors a uniform distribution, and the geometric constraints imposed by the hard-sphere interactions.

Mean-Field Approximation

In addition to the exact ideal-gas treatment and the highly accurate FMT closure for hard-sphere fluids, a widely used approximation for the excess free energy is provided by the so-called Mean-Field (MF) approach. This approximation treats the interparticle interactions as an averaged or "mean" potential produced by the surrounding fluid, thereby neglecting higher-order correlations. While less accurate than FMT in describing short-range structure, the mean-field approach offers valuable insights into systems where long-range interactions dominate, and it often serves as a tractable starting point for more refined theories.

For a interparticle interaction potential $u(\mathbf{r}-\mathbf{r}')$, the mean-field excess free energy functional can be written as

$$F_{\text{ex}}^{\text{MF}}[\rho] \;=\; \frac{1}{2}\int d\mathbf{r}\int d\mathbf{r}'\,\rho(\mathbf{r})\,\rho(\mathbf{r}')\,u(\mathbf{r}-\mathbf{r}')\,. \tag{3.13}$$

This expression sums the interaction energy over all pairs of particles, with the factor of $\frac{1}{2}$ avoiding double counting. Since this term is a simple quadratic functional of the density, it is more tractable than closures like FMT but lacks their accurate description of excluded-volume effects and short-range correlations.

From the definition $c^{(1)}(\mathbf{r}) = -\beta\frac{\delta F_{\text{ex}}[\rho]}{\delta\rho(\mathbf{r})}$, we see that, for this case, in the mean-field approximation

$$c_{\text{MF}}^{(1)}(\mathbf{r}) \;=\; -\,\frac{\delta}{\delta\rho(\mathbf{r})}\left[\frac{1}{2}\int d\mathbf{r}'\int d\mathbf{r}''\,\rho(\mathbf{r}')\,\rho(\mathbf{r}'')\,\beta u(\mathbf{r}'-\mathbf{r}'')\right]. \tag{3.14}$$

Functionally differentiating and carrying out one of the integrals leads to

$$c_{\text{MF}}^{(1)}(\mathbf{r}) \;=\; -\int d\mathbf{r}'\;\rho(\mathbf{r}')\,\beta u(\mathbf{r}-\mathbf{r}'). \tag{3.15}$$

Combining the ideal and excess contributions to the free energy, and including an external potential $V_{\text{ext}}(\mathbf{r})$, we write the minimization condition

$$\frac{\delta\Omega[\rho]}{\delta\rho(\mathbf{r})} \;=\; \ln\!\big[\rho(\mathbf{r})\Lambda^3\big] \;-\; c^{(1)}(\mathbf{r}) \;+\; \beta\,V_{\text{ext}}(\mathbf{r}) \;-\; \beta\,\mu \;=\; 0, \tag{3.16}$$

where $c^{(1)}(\mathbf{r})$ now includes the mean-field contribution from Eq. (3.15). Solving for $\rho(\mathbf{r})$ then yields

$$\rho(\mathbf{r}) \;=\; \frac{1}{\Lambda^3}\exp\!\Big[\beta\,\mu \;-\; \beta\,V_{\text{ext}}(\mathbf{r}) \;+\; c^{(1)}(\mathbf{r})\Big]. \tag{3.17}$$

Substituting the mean-field form of $c^{(1)}(\mathbf{r})$ from Eq. (3.15) makes the exponential depend on an integral over the density itself,

$$\rho(\mathbf{r}) \;=\; \frac{1}{\Lambda^3}\exp\!\Big[\beta\,\mu \;-\; \beta\,V_{\text{ext}}(\mathbf{r}) \;-\; \beta\int d\mathbf{r}'\,\rho(\mathbf{r}')\,u(\mathbf{r}-\mathbf{r}')\Big]. \tag{3.18}$$

This is the *self-consistent* mean-field equation for the density distribution. As with the more sophisticated FMT closure, solving Eq. (3.18) necessitates an iterative procedure, because $\rho(\mathbf{r})$ appears both inside and outside the integral.

The same iterative techniques described for FMT apply here:

1. Start with an initial guess $\rho_0(\mathbf{r})$.
2. Compute $\rho_{\text{MF},i+1}(\mathbf{r}) \;=\; \frac{1}{\Lambda^3}\exp\!\big[\beta\,\mu-\beta\,V_{\text{ext}}(\mathbf{r})-\beta\int d\mathbf{r}'\,\rho_{\text{MF},i}(\mathbf{r}')\,u(\mathbf{r}-\mathbf{r}')\big]$.
3. Mix the new solution with the previous one: $\rho_{\text{MF,new}}(\mathbf{r}) \;=\; \alpha\,\rho_{\text{MF},i+1}(\mathbf{r}) \;+\; (1-\alpha)\,\rho_{\text{MF},i}(\mathbf{r})$, for a suitably small mixing parameter $\alpha \in [0,1]$.
4. Repeat until convergence, as monitored by the density difference between successive iterations.

In practice, the mean-field approximation can be efficiently implemented for a wide range of interaction potentials, *e.g.* Coulombic or van der Waals interactions, as long as one is mindful of the limitations in describing short-range correlation effects.

Equation (3.18) highlights the essence of the mean-field picture: each point $\mathbf{r}$ in the fluid experiences an average potential generated by all other particles. While this is computationally simpler than treating the full many-body correlations, the approximation becomes less accurate at high densities, where the local structuring of the fluid plays a key role. In such regimes, more refined approaches, such as FMT or other sophisticated density functional approximations, are indispensable for capturing the characteristic layering and excluded-volume effects, as we saw in the hard-sphere system near a hard wall.

Despite these limitations, the mean-field approach remains a valuable theoretical tool. By striking a balance between simplicity and capturing the essential physics of long-range interactions, it serves as a stepping stone to more complex density functional theories and provides qualitative and sometimes semi-quantitative predictions for inhomogeneous fluids where short-range correlations are not dominant.

The hard-wall system serves as a prototype for more complex interfacial phenomena. The same basic framework can be applied to study fluid behavior near structured surfaces, in confined geometries, or at liquid-vapor interfaces. What changes in these cases are the forms of the external potential and the excess free

energy functional, while the fundamental methodology remains the same. This universality is one of the key strengths of classical DFT, allowing us to study a wide range of inhomogeneous systems within a unified theoretical framework.

The theoretical framework of classical Density Functional Theory presented here provides a powerful foundation for studying inhomogeneous fluids. However, the particles we have considered thus far have been characterized by fixed intrinsic properties. In Publication I, we will extend this formalism by introducing a new degree of freedom: particle size. By allowing particles to respond and adapt their size based on their local environment, we open up exciting possibilities for modeling systems with rich emergent behaviors. This extension naturally builds upon the groundwork laid here, while introducing novel mathematical and physical considerations that arise from the particles' internal flexibility.

3.2. Dynamic Density Functional Theory

While Classical DFT effectively captures *equilibrium* properties, many responsive systems are frequently driven out of equilibrium, prompting the need to describe how the density distribution evolves over time. *Dynamic Density Functional Theory* (DDFT) extends the framework of DFT to these time-dependent scenarios, thereby providing an appealing balance between microscopic detail and computational tractability [3.5–3.7]. Over the past two decades, DDFT has become a widely used theoretical tool for studying colloidal suspensions, polymeric fluids, and various soft-matter systems. In this thesis, we employ DDFT to investigate both drug release kinetics (Publication III) and particle relaxation processes in responsive colloids (Publication II).

The starting point for DDFT is the *time-dependent density* $\rho(\mathbf{r}, t)$, which describes the instantaneous distribution of particles in space. Unlike equilibrium DFT, where $\rho(\mathbf{r})$ is time-independent, DDFT seeks to track how $\rho(\mathbf{r}, t)$ evolves under the influence of interactions, external fields, and thermal fluctuations. From a microscopic perspective, DDFT can be viewed as an extension of the *Smoluchowski equation*, which describes the overdamped Brownian dynamics of non-interacting colloidal particles [3.8]. Indeed, in the absence of particle-particle interactions, DDFT reduces to the Smoluchowski equation, making it a natural generalization that incorporates the effects of inter-particle interactions.

A key assumption underlying most DDFT formulations is that *inertia can be neglected* relative to viscous forces, leading to *overdamped* motion. Such an assumption is highly suitable for colloidal suspensions in which the particle mass is large compared to the fluid friction. Another crucial approximation often invoked in DDFT is the *adiabatic approximation* [3.5, 3.7]. This approximation posits that, at any instant in time, the system can be treated as if it were in *quasi-equilibrium*

with respect to the instantaneous density profile. As a result, one can directly employ the same free-energy functionals used in *equilibrium* DFT to derive a time-evolution equation for $\rho(\mathbf{r}, t)$.

The central equation of DDFT is obtained by writing a continuity equation for the density profile, assuming Brownian motion and neglecting inertia. Let us denote by Γ the mobility (or inverse friction) of the colloidal particles. In many treatments, Γ is taken to be a constant, although variations in Γ with density or position can sometimes be considered [3.9]. Γ can also depend on the diffusion coefficient D using $\Gamma = \frac{D}{k_B T}$. The time evolution of $\rho(\mathbf{r}, t)$ can then be written as:

$$\frac{\partial \rho(\mathbf{r}, t)}{\partial t} \;=\; \Gamma \nabla \cdot \left[\rho(\mathbf{r}, t) \, \nabla \frac{\delta \Omega[\rho]}{\delta \rho(\mathbf{r}, t)} \right], \tag{3.19}$$

where $\Omega[\rho]$ is the *grand potential functional*. In a typical grand-canonical setting, $\Omega[\rho]$ splits into the internal free energy of the fluid, the chemical potential term, and the contribution from any external potential $V_{\text{ext}}(\mathbf{r})$.

To connect back to equilibrium DFT, recall that the functional derivative $\frac{\delta \Omega[\rho]}{\delta \rho(\mathbf{r},t)}$ directly relates to the *chemical potential field* experienced by the particles. More explicitly, one often expresses:

$$\frac{\delta \Omega[\rho]}{\delta \rho(\mathbf{r}, t)} \;=\; \frac{\delta F[\rho]}{\delta \rho(\mathbf{r}, t)} \;+\; V_{\text{ext}}(\mathbf{r}) \;-\; \mu, \tag{3.20}$$

where $F[\rho]$ is the Helmholtz free-energy functional, μ is the chemical potential, and $V_{\text{ext}}(\mathbf{r})$ is any external field. Substituting this result into Eq. (3.19) leads to the commonly seen DDFT equation:

$$\frac{\partial \rho(\mathbf{r}, t)}{\partial t} \;=\; \Gamma \nabla \cdot \left[\rho(\mathbf{r}, t) \, \nabla \Big(\frac{\delta F[\rho]}{\delta \rho(\mathbf{r}, t)} \;+\; V_{\text{ext}}(\mathbf{r}) \;-\; \mu \Big) \right]. \tag{3.21}$$

This compact formulation succinctly states that the *diffusive flux* of particles is proportional to the gradient of a generalized chemical potential—composed of the intrinsic (excess) free-energy, external field contributions, and the uniform bulk chemical potential.

The solution of the DDFT equation (Eq. (3.21)) generally requires numerical methods due to its nonlinear nature and the complexity of realistic free-energy functionals. Several numerical approaches have been developed, with the choice of method depending on factors such as the spatial dimensionality, the specific form of the free-energy functional, and the desired accuracy.

A common approach involves discretizing both space and time. The spatial domain is typically divided into a regular grid with spacing Δx, while time is advanced in discrete steps Δt. The spatial derivatives in the DDFT equation are then

approximated using finite-difference schemes. For instance, using a simple forward-time central-space (FTCS) discretization in one dimension, Eq. (3.21) becomes:

$$\frac{\rho_i^{n+1} - \rho_i^n}{\Delta t} = \Gamma \frac{1}{\Delta x^2} \left[\frac{\rho_{i+1}^n + \rho_i^n}{2} \left(\mu_{i+1}^n - \mu_i^n \right) - \frac{\rho_i^n + \rho_{i-1}^n}{2} \left(\mu_i^n - \mu_{i-1}^n \right) \right], \tag{3.22}$$

where ρ_i^n represents the density at grid point i and time step n, and μ_i^n is the local chemical potential including all contributions from Eq. (3.20). For higher dimensions, similar terms are added for each spatial direction.

The stability of this explicit scheme requires that the time step satisfies the condition:

$$\Delta t \leq \frac{\Delta x^2}{2d\Gamma k_B T}, \tag{3.23}$$

where d is the spatial dimensionality. More sophisticated numerical schemes, such as semi-implicit methods or pseudo-spectral approaches, can often use larger time steps while maintaining stability.

A particularly challenging aspect of solving the DDFT equation is the evaluation of the functional derivative $\delta F/\delta \rho$. For simple functionals, such as those describing ideal gases or mean-field interactions, this can be done analytically. However, for more realistic excess free-energy functionals, such as those derived from fundamental measure theory (FMT), the functional derivatives must be evaluated numerically, often involving convolution operations that are most efficiently computed in Fourier space.

In the publications, we will extend this DDFT framework in two significant directions. First, in Publication II, we will adapt the formalism to study soft responsive particles, where the particle size itself can change in response to their environment. Second, in Publication III, we will generalize the theory to handle systems with spatially varying diffusion coefficients, to characterize the drug release from a collapsed microgel. These extensions demonstrate the flexibility of the DDFT framework and its ability to capture increasingly complex physical phenomena in colloidal systems.

3.3. Brownian Dynamics Simulations

Brownian dynamics (BD) simulations provide a particle-based approach to studying colloidal dynamics that complements the continuum description offered by DDFT. In BD simulations, the trajectories of individual colloidal particles are explicitly tracked by solving the overdamped Langevin equation:

$$\gamma \frac{d\mathbf{r}_i}{dt} = \mathbf{F}_i(\{\mathbf{r}_j\}) + \sqrt{2k_B T \gamma}\boldsymbol{\xi}_i(t), \tag{3.24}$$

where γ is the friction coefficient (related to the mobility Γ introduced in the DDFT section through $\Gamma = 1/\gamma$), $\mathbf{r}_i$ is the position of particle i, $\mathbf{F}_i$ represents the total deterministic force acting on particle i (including both interparticle and external forces), and $\boldsymbol{\xi}_i(t)$ is a Gaussian white noise term satisfying $\langle \boldsymbol{\xi}_i(t) \rangle = 0$ and $\langle \xi_{i\alpha}(t)\xi_{j\beta}(t') \rangle = \delta_{ij}\delta_{\alpha\beta}\delta(t-t')$.

The Langevin equation captures two essential aspects of colloidal dynamics: the deterministic forces through F_i, and the random thermal fluctuations through the noise term. While DDFT provides an averaged, field-based description, BD simulations capture the full particle-level dynamics, including fluctuations that are averaged out in DDFT. This makes BD particularly valuable for validating DDFT predictions and for studying phenomena where individual particle trajectories or fluctuations are important.

In subsequent publications, we will employ BD simulations as a benchmark to validate our DDFT calculations in Publication II. Furthermore, in Publication IV, BD simulation results will be compared against dynamic light scattering (DLS) experiments, allowing us to assess the accuracy of these approaches in describing real colloidal systems.

Bibliography

[3.1] Pierre Hohenberg and Walter Kohn. Inhomogeneous electron gas. *Physical review*, 136(3B):B864, 1964.

[3.2] Walter Kohn and Lu Jeu Sham. Self-consistent equations including exchange and correlation effects. *Physical review*, 140(4A):A1133, 1965.

[3.3] R. Evans. The nature of the liquid-vapour interface and other topics in the statistical mechanics of non-uniform, classical fluids. *Advances in Physics*, 28(2):143–200, 1979.

[3.4] Yaakov Rosenfeld. Free-energy model for the inhomogeneous hard-sphere fluid mixture and density-functional theory of freezing. *Physical review letters*, 63(9):980, 1989.

[3.5] Umberto Marini Bettolo Marconi and Pedro Tarazona. Dynamic density functional theory of fluids. *J. Chem. Phys.*, 110(16):8032–8044, 1999.

[3.6] Umberto Marini Bettolo Marconi and Pedro Tarazona. Dynamic density functional theory of fluids. *J. Phys.: Condens. Matter*, 12(8A):A413–A418, feb 2000.

[3.7] A. J. Archer and R. Evans. Dynamical density functional theory and its application to spinodal decomposition. *J. Chem. Phys.*, 121(9):4246–4254, 2004.

[3.8] J.K.G. Dhont. *An Introduction to Dynamics of Colloids*. Elsevier, 1996.

[3.9] A J Archer. Dynamical density functional theory: binary phase-separating colloidal fluid in a cavity. *J. Phys.-Condes. Matter*, 17(10):1405–1427, feb 2005.

Chapter 4

Basis of Dynamic Light Scattering

The aim of this chapter is to provide a comprehensive theoretical framework for analyzing dynamic light scattering (DLS) experiments, with particular focus on systems under drift velocities. This foundation is essential for understanding the collective oscillatory behavior of colloidal particles discussed in Publication IV. To achieve this goal, the section is organized into three main subsections.

The first subsection delves into the concept of correlation functions of the scattered electric field and the scattered intensity. These functions are involved in the description of the statistical properties of the scattered field and in the analysis of our experiments. Furthermore, the Siegert relation is introduced, which allows transforming the scattered intensity correlation function into the scattered electric field correlation function.

The second subsection covers the traditional dynamic light scattering (DLS) theory. The theory is based on the correlation function of the electric field and is derived for systems of particles that do not interact with each other. This model depends on the properties of the medium and the particles, which allows information to be extracted from experimental measurements. By comparing the measured correlation function with the theoretical model, we can gain insight into the dynamics of the particles in the sample.

The final subsection extends the DLS theory to systems that are out of equilibrium. This extension introduces drift velocities into the theoretical model, which is crucial for understanding systems under external forces or showing directed motion. This framework provides the necessary foundation for analyzing the oscillatory phenomena that will be discussed in Publication IV.

4.1. Mathematical concepts

4.1.1. Time correlation functions

Correlation functions provide information about the relationship between two time-dependent properties over a given period of time. To understand these functions, consider a set of particles at a given point in time. The scattered electric field $E_s(t)$ depends on the positions of all the particles in the system. Due to Brownian motion, the particles' positions change continuously over time, causing fluctuations in the value of $E_s(t)$. These random thermal motions result in a noisy pattern in the time dependence of the field $E_s(t)$. To obtain a representative measure of the magnitude of the electric field, we must calculate its time average, as shown in the following equation [4.1, 4.2]:

$$\langle E_s \rangle = \frac{1}{\mathcal{T}} \int_0^{\mathcal{T}} dt E_s(t). \tag{4.1}$$

Here, $\mathcal{T}$ represents the time over which the average is calculated, and we have assumed that the average does not depend on the starting time of the measurement. Additionally, we take $\mathcal{T}$ to be large enough for the average to be representative.

The value of the field at two times t and $t+\tau$ may be different, such that $E_s(t) \neq E_s(t+\tau)$. However, if τ is much smaller than the fluctuation time of E_s, then $E_s(t+\tau)$ will be very close to $E_s(t)$. In this case, we can say that $E_s(t+\tau)$ is correlated with $E_s(t)$ when τ is small and that this correlation is lost for larger values of τ. This can be quantified using the correlation function of the field, defined as follows:

$$G^{(1)}(\tau) = \langle E_s(0) E_s^*(\tau) \rangle = \lim_{\mathcal{T}\to\infty} \frac{1}{\mathcal{T}} \int_0^{\mathcal{T}} dt E_s(t) E_s^*(t+\tau), \tag{4.2}$$

where E_s^* is the complex conjugate of E_s.

In our experiments, we use a detector that counts the number of photons that reach it at each instant Δt. However, Δt, even if very small, will always be finite, so it is useful to discretize this definition. Let's suppose that the time axis is divided into discrete intervals of length Δt, such that $t = j\Delta t$, $\tau = n\Delta t$, and $\mathcal{T} = N\Delta t$ ($N > j > n$). Furthermore, assume that the field changes are small over the interval Δt. With these assumptions, definitions (4.1) and (4.2) can be approximated as follows:

$$\begin{aligned} \langle E_s \rangle &\cong \lim_{N\to\infty} \frac{1}{N} \sum_{j=1}^{N} E_j, \\ \langle E_s(0) E_s^*(\tau) \rangle &\cong \lim_{N\to\infty} \frac{1}{N} \sum_{j=1}^{N} E_j(t) E_{j+n}^*(t+\tau). \end{aligned} \tag{4.3}$$

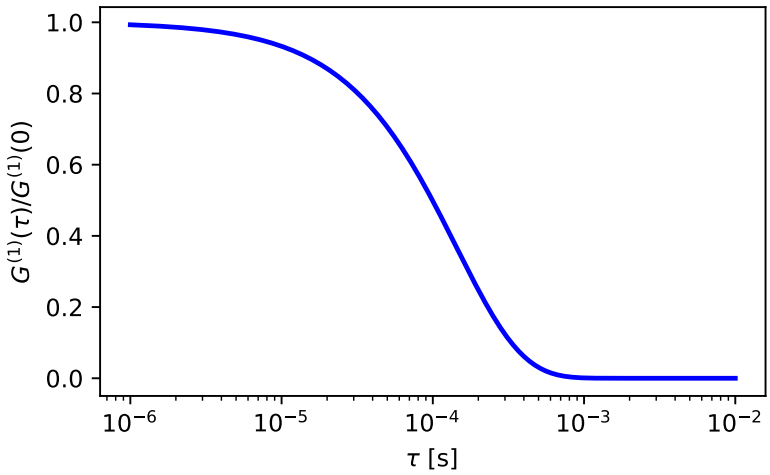

Figure 4.1: Illustration of a typical normalized electric field correlation function.

Here, E_j represents the value of E_s at the beginning of the interval j. Since the field E_s is an oscillating property, it is possible that $E_j E^*_{j+n}$ is negative, which would lead to some level of cancellation in the sum. If we now consider the case $\tau = 0$, or $\langle E_s(0) E^*_s(0) \rangle$, we see that the sum reduces to $\sum_j E_j E^*_j = \sum_j |E_j|^2$. Since $|E_j|^2 \geq 0$, all the terms in the sum are positive, so it is easy to see that

$$\left\langle E_s(0)^2 \right\rangle \geq \langle E_s(0) E^*_s(\tau) \rangle \,. \tag{4.4}$$

In Figure (4.1) we see an example of normalized correlation. As we increase τ, the correlation function decays from its initial value of $\left\langle E^2_s \right\rangle$ to $\langle E_s \rangle^2$:

$$\lim_{\tau \to \infty} \langle E_s(0) E^*_s(\tau) \rangle = \langle E_s(0) \rangle \langle E^*_s(\tau) \rangle = \langle E_s \rangle^2 \,. \tag{4.5}$$

As we noted earlier, the correlation function is defined for infinite times, which is not possible in practice. Therefore, we will assume that for sufficiently long measurement times, a good approximation is achieved.

In our experimental device, the scattered light hits the cathode of the detector directly. The detector generates an instantaneous current proportional to the square of the electric field reaching the detector, $i(t) \propto |E(t)|^2$, which is proportional to the light intensity. We can also calculate the correlation function of the intensity from the detected intensity [4.1–4.3]:

$$\langle i(0)\, i(t) \rangle = B \left\langle |E(0)|^2 |E(t)|^2 \right\rangle , \tag{4.6}$$

where B is a proportionality constant. We work using the homodyne method, in which only the scattered light will strike the photocathode. Therefore, the field $E(t)$

in Equation (4.6) is equal to the scattered field $E_s(t)$. As a result, the correlation function is proportional to the correlation function of the intensity $G^{(2)}(\tau)$ of the scattered field:

$$G^{(2)}(\tau) = \langle I_s(0) I_s(\tau) \rangle = \left\langle |E_s(0)|^2 |E_s(\tau)|^2 \right\rangle , \tag{4.7}$$

where we have used that the intensity $I_s(t) = |E_s(t)|^2$. The normalized correlation functions of the intensity and electric field are often used, respectively:

$$\begin{aligned} g^{(2)}(\tau) &= G^{(2)}(\tau)/G^{(2)}(0) \\ g^{(1)}(\tau) &= G^{(1)}(\tau)/G^{(1)}(0) \end{aligned} \tag{4.8}$$

4.1.2. Siegert relation

In dynamic light scattering (DLS), the detected scattered electric field, $E(t)$ (we omit the subindex s for simplicity), is assumed to be a sum of contributions from many independent scattering centers. Under the assumption of a large number of such independent contributions, the central limit theorem implies that $E(t)$ is a complex Gaussian random variable. This assumption is crucial to deriving the Siegert relation. We express the total scattered field as

$$E(t) = \sum_{n=1}^{N} E_n(t), \tag{4.9}$$

where $E_n(t)$ represents the field scattered by the nth particle (or subregion). If the $E_n(t)$ are statistically independent, then the total scattered field $E(t)$ is Gaussian.

The intensity of the scattered light is given by [4.1, 4.3, 4.4]

$$I(t) = |E(t)|^2 = E(t) E^*(t). \tag{4.10}$$

The normalized intensity autocorrelation function is defined as

$$g^{(2)}(\tau) = \frac{\langle I(t) I(t+\tau) \rangle}{\langle I(t) \rangle^2}. \tag{4.11}$$

Similarly, the normalized field autocorrelation function is

$$g^{(1)}(\tau) = \frac{\langle E(t) E^*(t+\tau) \rangle}{\langle I(t) \rangle}. \tag{4.12}$$

For a Gaussian random process (with zero mean), the fourth-order moment can be factorized using the Gaussian theorem [4.2, 4.3]. In particular,

$$\langle E(t) E^*(t) E(t+\tau) E^*(t+\tau) \rangle = \langle E(t) E^*(t) \rangle \langle E(t+\tau) E^*(t+\tau) \rangle + |\langle E(t) E^*(t+\tau) \rangle|^2 . \tag{4.13}$$

Since $\langle E(t)E^*(t)\rangle = \langle I(t)\rangle$, it follows that

$$\langle I(t)I(t+\tau)\rangle = \langle I(t)\rangle^2 + |\langle E(t)E^*(t+\tau)\rangle|^2 . \tag{4.14}$$

Substituting the above result into the definition of $g^{(2)}(\tau)$ yields

$$\begin{aligned} g^{(2)}(\tau) &= \frac{\langle I(t)I(t+\tau)\rangle}{\langle I(t)\rangle^2} \\ &= \frac{\langle I(t)\rangle^2 + |\langle E(t)E^*(t+\tau)\rangle|^2}{\langle I(t)\rangle^2} \\ &= 1 + \frac{|\langle E(t)E^*(t+\tau)\rangle|^2}{\langle I(t)\rangle^2} \\ &= 1 + \left|g^{(1)}(\tau)\right|^2. \end{aligned} \tag{4.15}$$

Thus, the Siegert relation is

$$g^{(2)}(\tau) = 1 + \left|g^{(1)}(\tau)\right|^2. \tag{4.16}$$

The Equation (4.16) is known as the Siegert relation. In summary, this relation is an equation that relates the normalized correlation function of the intensity, $g^{(2)}(\tau)$, to the normalized correlation function of the electric field, $g^{(1)}(\tau)$. In a real system, this equation may be modified to include a constant β that accounts for experimental factors, so the relationship becomes $g^{(2)}(\tau) = 1 + \beta|g^{(1)}(\tau)|^2$. The value of β can be used to assess the reliability of the measurement.

4.2. Correlation function derivation

4.2.1. Correlation function of monodisperse systems in equilibrium

In this section, we will consider the simplest scenario of dynamic light scattering from a dilute colloidal system in thermal equilibrium: the amplitude of the resulting electric field from a single scattering event. This means that the photons reaching the detector have only been scattered once.

Let's start by considering a flat monochromatic electromagnetic wave, described by the electric field $\mathbf{E}_i(r,t)$ at a point $\mathbf{r}$ and time t. This wave has a wavelength λ_i, frequency ω_i, polarization $\mathbf{n}_i$ perpendicular to the plane, and amplitude E_0. The wave also has a wave vector $\mathbf{k}_i$, which is defined as:

$$\mathbf{k}_i = \left(\frac{\omega_i}{c}\right)\hat{\mathbf{k}}_i$$

where ω_i is the frequency of the incident wave, c is the speed of light, and $\hat{\mathbf{k}}_i$ is the unit vector indicating the direction of propagation of the incident wave.

The electric field of the incident wave is given by:

$$\mathbf{E}_i(r,t) = \mathbf{n}_i E_0 \exp i(\mathbf{k}_i \cdot \mathbf{r} - \omega_i t). \tag{4.17}$$

This wave is incident on a colloidal particle and is scattered. A detector is placed at an angle θ to the incident direction as shown in Figure (4.2). It collects the scattered radiation, which has wave vector $\mathbf{k}_f$ and polarization $\mathbf{n}_f = \mathbf{n}_i$.

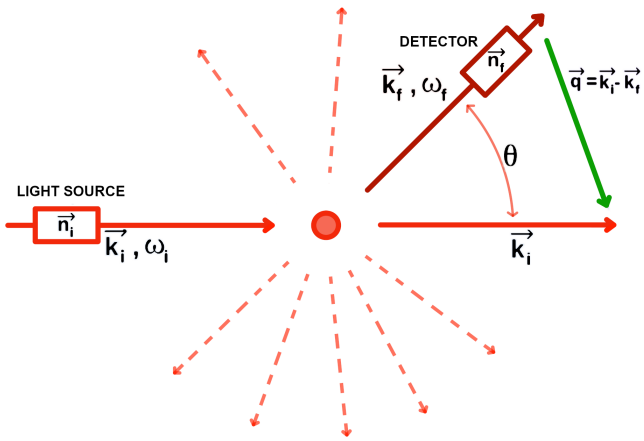

Figure 4.2: Electromagnetic wave with wave vector $\mathbf{k}_i$ strikes a particle and is scattered. At an angle θ, the scattered wave with wave vector $\mathbf{k}_f$ and polarization $\mathbf{n}_f$ reaches the detector.

The particle 1 is placed at position $\mathbf{r}_1(t)$ and the detector is placed at position $\mathbf{R}$, both with respect to the light source. The wave travels from the source to the particle position $\mathbf{r}_1(t)$ with a wave vector $\mathbf{k}_i$, is scattered by the particle, and then travels a distance $\mathbf{R} - \mathbf{r}_1(t)$ to reach the detector with a wave vector $\mathbf{k}_f$.

The field scattered by the particle and arriving at the detector can be expressed as:

$$\mathbf{E}_{s1}(q,t) = \mathbf{n}_i E_{01}(q) \exp i[\mathbf{k}_i \cdot \mathbf{r}_1(t) + \mathbf{k}_f \cdot (\mathbf{R} - \mathbf{r}_1(t)) - \omega_i t], \tag{4.18}$$

where $E_{01}(q)$ is the amplitude of the field scattered by the particle at an angle θ.

The scattering vector $\mathbf{q}$ is defined as $\mathbf{q} = \mathbf{k}_i - \mathbf{k}_f$, where $\mathbf{k}_i$ and $\mathbf{k}_f$ are the wave vectors of the incident and scattered waves, respectively. These wave vectors can be expressed as $k_i = 2\pi n/\lambda_i$ and $k_f = 2\pi n/\lambda_f$, where λ_i and λ_f are the wavelengths of the incident and scattered waves and n is the refractive index of the medium. It is

generally assumed that the wavelength does not undergo significant changes during scattering, so we can approximate $|\mathbf{k}_i| \cong |\mathbf{k}_f|$. This relationship forms an isosceles triangle with $\mathbf{q}$ as the base and the scattering angle θ as the apex (see Figure (4.2)). Using this geometry, we can easily determine the magnitude of $\mathbf{q}$ as:

$$q = 2\left[k_i \sin\left(\frac{\theta}{2}\right)\right] = \frac{4\pi n}{\lambda}\sin\left(\frac{\theta}{2}\right) \tag{4.19}$$

With this expression for $\mathbf{q}$, we can rewrite the equation for the field scattered by a particle (Equation (4.18)) as follows:

$$\mathbf{E}_{s1}(q,t) = \mathbf{n}_i E_{01}(q)\exp i[\mathbf{q}\cdot\mathbf{r}_1(t)]\exp i[\mathbf{k}_f\cdot\mathbf{R} - \omega_i t]. \tag{4.20}$$

Note that the term $\exp\{i[\mathbf{k}_f\cdot\mathbf{R} - \omega_i t]\}$ is a global phase factor common to the scattered field from every particle. Since this phase does not affect the relative interference between the scattered fields, it cancels out in the calculation of correlation functions (e.g., intensity autocorrelations) and is therefore omitted in subsequent analysis. It is thus convenient to work only with the amplitude, retaining the particle-dependent term $\exp\{i[\mathbf{q}\cdot\mathbf{r}_j(t)]\}$.

Once the field scattered by a single colloidal particle is known, it is straightforward to find the field scattered by a system composed of many colloidal particles. Consider a volume V containing a large number of particles N in suspension that do not interfere with each other (that is, their positions $(\mathbf{r}_1, \mathbf{r}_2, ..., \mathbf{r}_N)$ are independent of one another). The total scattered electric field at a given angle θ will be the sum of the fields scattered by each individual particle at that angle. Therefore, the amplitude of the total scattered field can be expressed as:

$$\mathbf{E}_s(q,t) = \sum_{j=1}^{N} E_j(q)\exp i[\mathbf{q}\cdot\mathbf{r}_j(t)]. \tag{4.21}$$

Thus, the temporal fluctuations in the amplitude of the scattered electric field reflect the dynamics of the particles in suspension [4.1, 4.3].

According to Equation (4.8), the correlation function of the scattered electric field at an angle θ can be written as:

$$g^{(1)}(q,\tau) = \frac{\langle E_s(q,0)E_s^*(q,\tau)\rangle}{\langle |E_s(q,0)|^2\rangle}, \tag{4.22}$$

where τ is the correlation time, q is the magnitude of the scattering vector defined in Equation (4.19) and E_s is the amplitude of the scattered field given by Equation (4.21).

In this section, we will focus on monodisperse systems, in which all particles are identical. Therefore, we can set $E_1(q) = E_2(q) = ... = E_N(q) = E(q)$ and rewrite the Equation (4.22) as:

$$g^{(1)}(q,\tau) = \frac{\sum_{i=1}^{N}\sum_{j=1}^{N}\left\langle e^{i\mathbf{q}\cdot(\mathbf{r}_i(0)-\mathbf{r}_j(\tau))}\right\rangle}{\sum_{i=1}^{N}\sum_{j=1}^{N}\left\langle e^{i\mathbf{q}\cdot(\mathbf{r}_i(0)-\mathbf{r}_j(0))}\right\rangle}. \tag{4.23}$$

Note that the amplitudes $E(q)$ cancel out because they are all equal. Recall that we are assuming that the particles do not interact with each other (i.e., their positions are independent), which implies that the cross terms with $i \neq j$ vanish, leaving Equation (4.23) as:

$$g^{(1)}(q,\tau) = \frac{N\left\langle e^{i\mathbf{q}\cdot(\mathbf{r}(0)-\mathbf{r}(\tau))}\right\rangle}{N\left\langle e^{i\mathbf{q}\cdot(\mathbf{r}(0)-\mathbf{r}(0))}\right\rangle} = \left\langle e^{i\mathbf{q}\cdot(\mathbf{r}(0)-\mathbf{r}(\tau))}\right\rangle. \tag{4.24}$$

For non-interacting particles, the only relevant time scale is given by the fluctuation time of the Brownian velocity τ_B, which is assumed to be much smaller than τ. So, we can rewrite Equation (4.24) as:

$$g^{(1)}(q,\tau) = \left\langle e^{-i\mathbf{q}\cdot\Delta\mathbf{r}(\tau)}\right\rangle. \tag{4.25}$$

In this study, the displacement undergoes by a particle at time τ, $\Delta\mathbf{r}(\tau)$, is a Gaussian random variable. Therefore, Equation (4.25) can be rewritten as:

$$g^{(1)}(q,\tau) = \exp\left[-\frac{q^2}{6}\left\langle\Delta r^2(\tau)\right\rangle\right] \tag{4.26}$$

The mean square displacement $\left\langle\Delta r^2(\tau)\right\rangle$ is given by the well-known result of free diffusion [4.1, 4.3].

$$\left\langle\Delta r^2(\tau)\right\rangle = 6D\tau, \tag{4.27}$$

where D is the diffusion coefficient for free particles. It can be related to the radius a of a spherical particle by the Stokes-Einstein relation [4.1]:

$$D = \frac{k_B T}{6\pi\eta a}, \tag{4.28}$$

where k_B is the Boltzmann constant, T is the temperature and η is the viscosity of the medium. By substituting Equation (4.27) into Equation (4.26), we obtain:

$$g^{(1)}(q,\tau) = \exp(-Dq^2\tau). \tag{4.29}$$

This is the expression for the correlation function of the scattered electric field in the case of single scattering and monodisperse systems. From this exponential decay we can obtain the diffusion coefficient of the particles.

4.2.2. Correlation function for monodisperse systems under drift velocities

So far, we have examined systems that are in equilibrium. In this section, we will take a closer look at the behavior of particles in systems that are under an uniform velocity drift. We will be deriving the expression for the correlation function supposing that there is a net particle flow in the direction of the vertical axis, without paying attention to the origin of this drift.

We start from a monodisperse system of spherical particles that are subjected to move with an average velocity $\mathbf{v}$. The particle concentration $c(\mathbf{r}, t)$ will be given by the diffusion equation with a drift term [4.5, 4.6]:

$$\frac{\partial \rho(\mathbf{r}, t)}{\partial t} + \nabla \cdot \mathbf{J} = 0, \tag{4.30}$$

where $\mathbf{J}$ is the flow and is given by a diffusive contribution and an average velocity contribution:

$$\mathbf{J} = \mathbf{v}\rho(\mathbf{r}, t) - D\nabla\rho(\mathbf{r}, t). \tag{4.31}$$

The above equation can be solved to obtain the concentration:

$$\rho(\mathbf{r}, t) = \int F_s(\mathbf{r} - \mathbf{r}', t)\rho(\mathbf{r}', 0)d^3r', \tag{4.32}$$

where $\rho(\mathbf{r}', 0)$ is the initial concentration and $F_s(\mathbf{r}, t)$ is the following expression [4.1, 4.5]:

$$F_s(\mathbf{r}, t) = \frac{1}{(4\pi Dt)^{3/2}} \exp\left(-\frac{(\mathbf{r} - \mathbf{v}t)^2}{4Dt}\right). \tag{4.33}$$

This function is known as the Van-Hove space-time correlation function and represents the probability density of finding a particle at the point $\mathbf{r}$ at time t if it was initially at $\mathbf{r} = 0$. Also, $F_s(\mathbf{r}, t)$ determines the so-called self-intermediate function $F_s(\mathbf{q}, \tau)$ as follows:

$$F_s(\mathbf{q}, \tau) = \int e^{i\mathbf{q}\cdot\mathbf{r}} F_s(\mathbf{r}, t)d^3r. \tag{4.34}$$

This function corresponds to the correlation function of the field $g^{(1)}(\mathbf{q},\tau)$ since we are in the case where the particles do not interact with each other [4.1, 4.3, 4.5]. The expression of $g^{(1)}(\mathbf{q},\tau)$ is obtained by substituting Equation (4.33) into Equation (4.34) and solving the integral:

$$g^{(1)}(\mathbf{q},\tau) = F_s(\mathbf{q},\tau) = \exp(i\mathbf{q}\cdot\mathbf{v}\tau)\cdot\exp(-Dq^2\tau). \tag{4.35}$$

Equation (4.35) allows us to model the correlation function of the electric field of a system of dilute colloidal particles subjected to a drift velocity. However, this has a problem when trying to extract the drift velocity. We can only experimentally measure the correlation function of the intensity $g^{(2)}(\mathbf{q},\tau)$, which is related to that of the electric field by the Siegert relation of the Equation (4.16). The drawback here is that calculating $g^{(2)}(\mathbf{q},\tau)$ from the expression gives the following:

$$g^{(2)}(\mathbf{q},\tau) - 1 = \left|g^{(1)}(\mathbf{q},\tau)\right|^2 = \exp(-2Dq^2\tau). \tag{4.36}$$

As the equation shows, the velocity part is lost, which leaves us with the same expression we derived in the previous section, losing all the information about the drift velocity.

The apparent loss of velocity information in the intensity correlation function presents an intriguing paradox in dynamic light scattering. While theory suggests that drift velocities should be undetectable in standard homodyne setups, our experimental observations have repeatedly hinted at oscillatory behaviors that seem to contradict this limitation. As we will see in Publication IV, this apparent contradiction finds an elegant resolution through an innovative approach using 3D dynamic light scattering with a single detector. By cleverly employing two incident beams, this technique not only preserves the velocity information but also enables precise measurements of drift velocities in nonequilibrium colloidal systems. The theoretical framework and experimental validation of this method open new possibilities for studying systems ranging from thermally-induced convection to particles under external fields, providing a powerful tool for investigating nonequilibrium dynamics at the colloidal scale.

Bibliography

[4.1] Robert Pecora. *Dynamic light scattering: applications of photon correlation spectroscopy*. Springer Science & Business Media, 1985.

[4.2] Jan KG Dhont. *An introduction to dynamics of colloids*. Elsevier, 1996.

[4.3] Bruce J Berne and Robert Pecora. *Dynamic light scattering: with applications to chemistry, biology, and physics*. Courier Corporation, 2000.

[4.4] J.K.G. Dhont. *An Introduction to Dynamics of Colloids*. Elsevier, 1996.

[4.5] Emilie Moulin, Irina A Nyrkova, Nicolas Giuseppone, Alexander N Semenov, and Eric Buhler. Homodyne dynamic light scattering in supramolecular polymer solutions: anomalous oscillations in intensity correlation function. *Soft Matter*, 16(12):2971–2993, 2020.

[4.6] Amit Sehgal and Thomas AP Seery. Anomalous dynamic light scattering from solutions of light absorbing polymers. *Macromolecules*, 32(23):7807–7814, 1999.

Part II

Results

Publication I

Density functional theory for responsive hard-sphere fluids

J. López-Molina[1], M. Tirado-Miranda[1], J. Dzubiella[2] and A. Moncho-Jordá[1,3]

[1]*Departamento de Física Aplicada, Universidad de Granada, Campus Fuentenueva S/N, 18071 Granada, Spain*

[2]*Physikalisches Institut, Albert-Ludwigs-Universität Freiburg, Hermann-Herder Straße 3, D-79104 Freiburg, Germany*

[3]*Institute Carlos I for Theoretical and Computational Physics, Facultad de Ciencias, Universidad de Granada, Campus Fuentenueva S/N, 18071 Granada, Spain*

Published in

Taylor & Francis
Taylor & Francis Group

Molecular Physics, **2024** *122(21-22)*, e2410481.

Abstract

We investigate the equilibrium properties of responsive hard-sphere fluids, where particle size is a coarse-grained property that fluctuates within an internal free-energy landscape, responding to changes in concentration or the application of external fields. For this purpose, we employ a generalized density functional theory for responsive colloids based on the fundamental measure theory for hard-sphere mixtures. We find that increasing particle softness yields a substantial reduction in mean particle size, volume fraction and pressure. We also examine the density profiles and size segregation of responsive hard-sphere fluids subjected to three representative external potentials: a single hard wall, and gravitational and Archimedes buoyant fields. We observe that increasing stiffness or volume fraction enhances density oscillations, converging to the behavior of a monodisperse fluid. Under the gravitational field, size segregation occurs, with smaller particles accumulating at the bottom due to sedimentation. This effect is more pronounced when the Archimedes buoyant force is included, causing larger colloids to accumulate at the top, leading to density oscillations in that region that intensify with particle softness, an effect not observed in monodisperse systems. Finally, we demonstrate that responsiveness leads to distinct behavior compared to conventional polydisperse non-responsive fluids, in which particle compression is not allowed.

I.1. Introduction

Recently, responsive macromolecules and colloids have garnered significant interest in the field of soft matter science due to their capability to undergo substantial conformational changes in response to external fields or environmental stimuli [I.1, I.2, I.3, I.4, I.5].

The concept of responsiveness implies that each individual particle possesses, in addition to the particle location, internal degrees of freedom (DoF) that can be affected by the physico-chemical conditions of the system. These DoFs encompass various features including the particle's conformation [I.6, I.7, I.8, I.9], size [I.10, I.11, I.12], shape [I.4, I.5, I.12, I.13, I.14, I.15, I.16], charge density [I.12, I.17], or electric dipole moment [I.18], among others. They are directly influenced by interactions with other particles or external fields, resulting in particles capable of undergoing significant changes in their internal distributions in response to local potentials.

In many applications involving suspension of soft colloids, the particle size, which we will henceforth denote by R, stands out as the main relevant internal property. This is the case of microgels: particles compressed of crosslinked polymer chains for which R may represent the radius of gyration or hydrodynamic radius of the microgel [I.19, I.20, I.21, I.12, I.22, I.23, I.24, I.25]. It is widely recognized that even minor alterations in temperature or pH can trigger a swollen-to-deswollen transition in the polymer chains, resulting in a significant change in the particle size, often by a factor of at least two from the collapsed to the swollen state. Colloidal size can also be tuned by increasing particle concentration and/or the particle softness, leading to a progressive reduction induced by the excluded volume repulsions with the surrounding particles, with relevant implications on the structural and dynamical properties of the suspension [I.11, I.26, I.27, I.28, I.24, I.12, I.29, I.30, I.25, I.31, I.32, I.33]. In addition, changes in particle size are of great importance in various applications, such as those involving permeable microgels to control the release kinetics in drug delivery [I.34, I.35, I.36, I.37, I.38] and hydrogel-based colloidal nano- or microreactors to tune the reaction rate in selective catalysis [I.39, I.40, I.41].

In this work, we theoretically investigate the homogeneous (bulk) and inhomogeneous equilibrium properties induced by an applied external potential in a specific model system of responsive colloids: the responsive hard-sphere fluid. In this system, particles with varying radius interact through hard sphere potentials but can still adjust their size, R, in response to interactions with other particles or an applied external field that, in general, will be dependent on position and size, $u_{\text{ext}}(\mathbf{r}, R)$. The change in particle size is governed by an intrinsic free energy, $\psi(R)$, which represents the energy cost associated with swelling/deswelling of a single isolated colloid [I.42, I.43]. We will assume that $\psi(R)$ has the form of a potential well. This is precisely the case of the well-known Flory-Rehner theory, which combines an elastic and mixing free energy terms, leading to a size-dependent free energy that shows

a minimum located at a certain reference state with size R_0 [I.44, I.20]. This free energy landscape results in a unimodal polydisperse distribution of sizes, with a peak centered at R_0. The width of this distribution represents the particle softness: softer colloids are more likely to modify their size compared to stiffer ones.

At this point, it is important to highlight two aspects of our model. First, the size polydispersity in this context is a direct result of particle responsiveness. In other words, the system is not composed of a collection of colloids with different sizes; rather, we have identical particles, each capable of existing in different size states, R. Due to their responsiveness, the polydispersity can also be adjusted, for example, by varying the particle concentration of the suspension. This is a significant feature that ordinary polydisperse suspensions do not exhibit in canonical experimental conditions (i.e. closed systems), where the particle size distribution is fixed and cannot be altered by a change of external stimuli. Second, we emphasize that, in our work, softness is strictly related to the particles' ability to change their size. This means tha,t while the particles can be soft, the interparticle interactions remain very stiff because they are governed by hard sphere potentials.

Although responsive hard spheres might initially appear to be an unrealistic model for soft matter systems, they actually provide a good approximation for suspensions of swollen microgel particles. In these systems, the interaction potential between a pair of particles of sizes R and R', separated by a distance r, can be approximated by the coarse-grained Hertzian potential [I.22, I.31]

$$\beta u(r, R, R') = \epsilon \left(1 - \frac{r}{R + R'}\right)^{5/2} \theta(R + R' - r), \tag{I.1}$$

or a combination of them through multi-Hertzian pair potentials [I.45]). In Eq. I.1, $\theta(x)$ is the Heaviside function and $\beta = 1/(k_B T)$ (T is the absolute temperature and k_B the Boltzmann constant). The prefactor of the pair potentials is in general very high, of about $\epsilon = 500$ ($k_B T$ units) or even larger [I.45, I.33]. Given the large elastic repulsion involved in the interpenetration of two swollen microgels, it justifies the mapping of the pair potential into an effective hard-sphere repulsion, with a diameter obtained from the Barker-Henderson model [I.46, I.47, I.48]

$$\sigma_{\text{eff}} = \int_0^\infty (1 - \exp(-\beta u(r, R, R')))dr. \tag{I.2}$$

For the particular case of the Hertzian pair potential, the effective hard sphere diameter is $\alpha(R + R')$, where $\alpha = 0.926$ for $\epsilon = 500$. Therefore, the suspension of responsive Hertzian colloids can be represented by a polydisperse mixture of hard spheres, where the effective radius of the particles is simply given by $R_{\text{eff}} = \alpha R$, and the full system can be regarded as a responsive and additive hard-sphere fluid.

To study the equilibrium inhomogeneous properties of our system we make use of a recently developed generalized clasical density functional theory (DFT) for

responsive colloids [I.42, I.49, I.50], succesfully applied to the description of ultrasoft Gaussian-core particles [I.51, I.52, I.53, I.54]. Here, we adapt this DFT framework to the case of responsive hard spheres by utilizing the polydisperse hard-sphere fluid model developed by Pagonabarraga et al. [I.55, I.56], along with the highly accurate White Bear (Mark II) version of the fundamental measure theory for the excess free energy functional, developed by Hansen-Goos and Roth [I.57]. In particular, we investigate how particle softness and crowding determine the equilibrium size distribution, pressure and volume fraction of homogeneous bulk fluid of responsive hard spheres, and then explore the effect of all these parameters on the inhomogeneous properties of the suspension, namely the density profile and size segregation, when the fluid is affected by three representative external potentials: a single planar hard wall, a gravitational field and a combination of gravitational plus Arquimedes buoyant potential, the last two being of special interest since they are implied in colloidal sedimentation.

The paper is organized as follows. In Sec. I.2, we describe the main statistical mechanics relations, introduce the DFT theoretical framework, and present the excess free energy functional for an inhomogeneous fluid of responsive additive hard spheres. Sec. I.3 presents and discusses the results of our study. Firstly, we apply the DFT method to analyze the effects of particle concentration and softness on the main bulk properties of a homogeneous hard-sphere fluid, including volume fraction, pressure, mean size, and size distribution. Then, we explore the density profiles and size localization effects when the responsive hard spheres are affected by the above mentioned external fields. Finally, we discuss the differences between responsive and conventional polydisperse non-responsive colloidal fluids. We summarize the main conclusions of our work in Sec. I.4.

I.2. Theory

I.2.1. Basic statistical mechanics relations of inhomogeneous responsive colloids

We consider a system composed by N responsive colloids confined in a volume V. In ordinary DFT, the equilibrium properties of a non-responsive colloidal system immersed in an applied external potential, $u_{\text{ext}}(\mathbf{r})$, are determined by the inhomogeneous one-body density profile, $\rho(\mathbf{r})$, where $\mathbf{r}$ is the particle position. Integration over the entire volume V of the system gives the total number of particles, $\int_V \rho(\mathbf{r})d\mathbf{r} = N$. This framework assumes that the particles do not have any additional internal DoF: only the particle's location is relevant. In fact, all the thermodynamic properties of this system can be written in terms of $\rho(\mathbf{r})$.

In the broader context of responsive colloids (RCs), particles can alter their size, R, in response to interactions with other particles or with the applied external potential. Typically, this external field not only depends on position but also on the particle's size, i.e. $u_{\text{ext}}(\mathbf{r}, R)$. Furthermore, the particle size in itself is influenced by its single-particle energy landscape, $\psi(R)$, which represents an intrinsic coarse-grained conformational free energy, reflecting the energy cost incurred when an isolated particle undergoes swelling or shrinking in the absence of any external potential. The so-called *parent* size distribution is given by

$$p(R) = p_0 e^{-\beta\psi(R)}, \tag{I.3}$$

where p_0 is a normalization constant (units of lenght^{-1}) to fulfill normalization, i.e. $\int p(R)dR = 1$.

As common in the theory of liquids, we assume a (isotropic) distance-dependent pair potential for the RC liquid. For RCs, however, the particle-particle pair potential not only depends on the positions $\mathbf{r}_i$ and $\mathbf{r}_j$ of both particles i and j, but also has explicit dependence on the size of both interacting particles, R_i and R_j, namely $u(|\mathbf{r}_i - \mathbf{r}_j|, R_i, R_j)$. The total potential energy of N responsive particles can be expressed as [I.42]

$$U = \sum_{i=1}^{N} \psi(R_i) + \frac{1}{2}\sum_{i=1}^{N}\sum_{j\neq i}^{N} u(|\mathbf{r}_i - \mathbf{r}_j|, R_i, R_j) + \sum_{i=1}^{N} u_{\text{ext}}(\mathbf{r}_i, R_i). \tag{I.4}$$

The presence of $u_{\text{ext}}(\mathbf{r}, R)$ and $\psi(R)$ renders the colloidal system inhomogeneous in both position and size. Consequently, the one-body density profile traditionally utilized in classical DFT now evolves to become dependent on both position and size, $\rho(\mathbf{r}, R)$. Integration over the four coordinates provides the total number of particles,

$$\int_V d\mathbf{r} \int dR \rho(\mathbf{r}, R) = N, \tag{I.5}$$

so $\rho(\mathbf{r}, R)$ is measured in units of length^{-4}. In the absence of applied external field and in the limit of infinite dilution, the one-body density simplifies to

$$\lim_{\rho_0\to 0} \lim_{u_{\text{ext}}\to 0} \rho(\mathbf{r}, R) = \rho_0 p(R), \tag{I.6}$$

where $\rho_0 = N/V$ is the bulk number density. If the particle concentration is increased beyond the dilute regime, interactions with the surrounding particles will affect this single-particle property distribution. We denote by $f(R) = N(R)/N$ the *emergent* probability distribution, where $N(R)dR$ is the number of particles in the system with internal property within $[R, R + dR]$. In particular, in the absence of any external field (i.e. for a bulk homogeneous fluid), we have

$$\lim_{u_{\text{ext}}\to 0} \rho(\mathbf{r}, R) = \rho_{\text{bulk}}(\mathbf{r}, R) = \rho_0 f(R). \tag{I.7}$$

Integrating over the R-space provides the number density distribution of the RC liquid,

$$\rho(\mathbf{r}) = \int dR\rho(\mathbf{r}, R). \tag{I.8}$$

The position dependent mean size is given by

$$\langle R(\mathbf{r})\rangle = \frac{1}{\rho(\mathbf{r})}\int dR\rho(\mathbf{r}, R)R. \tag{I.9}$$

In a similar way, integrating over ,the volume V we obtain the emergent size distribution

$$f(R) = \int_V d\mathbf{r}\rho(\mathbf{r}, R). \tag{I.10}$$

In this work we aim to investigate the bulk and inhomogeneous properties of colloidal systems composed of responsive additive hard spheres, for which the particle-particle interactions are represented by the hard sphere potential:

$$u(|\mathbf{r}-\mathbf{r}'|, R, R') = \begin{cases}\infty & |\mathbf{r}-\mathbf{r}'| < R+R' \\ 0 & |\mathbf{r}-\mathbf{r}'| \geq R+R',\end{cases} \tag{I.11}$$

where $\mathbf{r}$ and $\mathbf{r}'$ are the spatial locations of the center of each particle, while R and R' represent their corresponding radius.

Responsivity implies that each individual particle can modify its radius in response to mutual interactions with other particles or aplied external fields. In order to predict this response, we need to make a choice regarding the shape of the free energy landscape, $\psi(R)$. We select the following FENE-like expression

$$\beta\psi(R) = -\frac{R_0^2}{8\tau^2}\ln\left[1-4\left(\frac{R-R_0}{R_0}\right)^2\right]. \tag{I.12}$$

Here, R_0 denotes a characteristic size, where $\psi(R)$ attains a minimum. For small fluctuations around R_0, $\psi(R)$ mimics an elastic harmonic potential, i.e., $\psi(R) \approx (1/2)k(R-R_0)^2$, with $k = 1/(\beta\tau^2)$ serving as spring constant. Fig. I.1(a) illustrates $\psi(R)$ together with its harmonic approximation for $\tau/R_0 = 0.05$, 0.1 and 0.2. As observed, when R approaches either $0.5R_0$ or $1.5R_0$, the free energy diverges, marking the limits of particle collapse or swelling. Although the harmonic approximations works well in the near vicinity of R_0, it strongly underestimates the free energy when the particle size departs from R_0. The resulting parent size distribution, $p(R)$ (depicted in Fig. I.1(b)) shows a maximum located at $R = R_0$. The width of the maximum increases with τ, which can be regarded as an estimate of the particle softness: small τ lead to very narrow size distributions, and in the limit of $\tau \to 0$ the system behaves as a monodisperse hard-sphere fluid with particles of radius

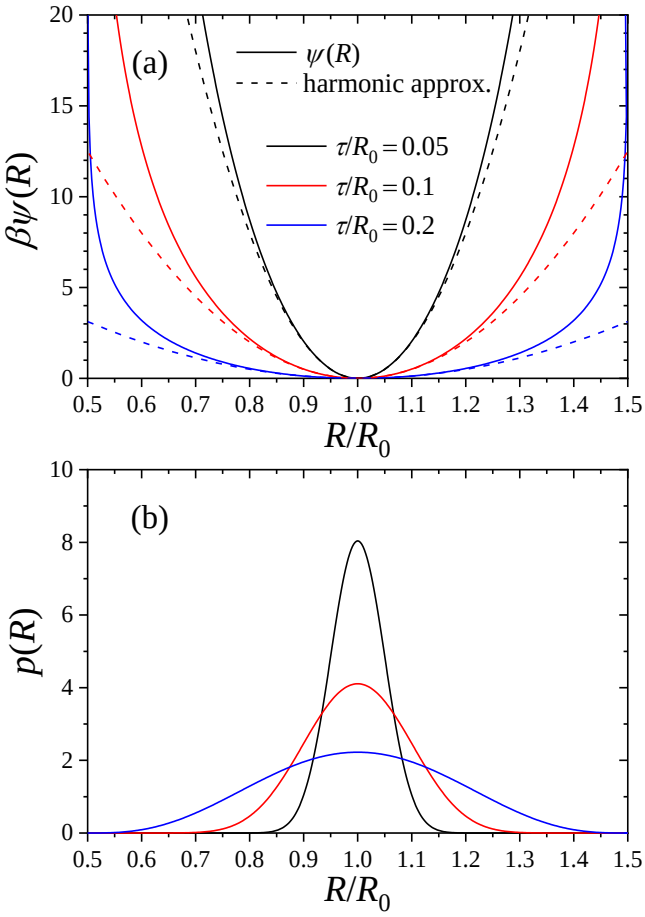

Figure I.1: (a) Free energy ladscape in the R-space, $\psi(R)$, for different values of the particle softness: $\tau/R_0 = 0.05$, 0.1 and 0.2. (a) Parent distribution of size, $p(R)$, evaluated for the same values of τ.

R_0. Since this is only size allowed by the colloids in this limit, the monodisperse system is also intrinsically non-responsive. Conversely, for large τ, colloids becomes softer in the sense that the free energy cost of swelling or deswelling the particle beyond R_0 is very small, leading to a broader size distribution. This also implies a higher polidispersity in the system.

I.2.2. DFT for responsive colloids

DFT for responsive colloids start from the definition of the funcional $\Omega\left[\rho(\mathbf{r}, R)\right]$, which depends on the inhomogeneous density profile, $\rho(\mathbf{r}, R)$, and fulfills a very important property: the equilibrium density profile, $\rho_{\text{eq}}(\mathbf{r}, R)$, is the one that

minimizes Ω, i.e. $\delta\Omega/\delta\rho(\mathbf{r},R) = 0$. In addition, evaluating $\Omega\left[\rho_{\text{eq}}(\mathbf{r},R)\right]$ leads to the grand potential of the system [I.58, I.55, I.56]. $\Omega\left[\rho(\mathbf{r},R)\right]$ can be written in terms of the intrinsic Helmholtz free energy funcional, $F\left[\rho(\mathbf{r},R)\right]$:

$$\Omega\left[\rho(\mathbf{r},R)\right] = F[\rho(\mathbf{r},R)] - \iint d\mathbf{r}dR\rho(\mathbf{r},R)\big(u_{\text{ext}}(\mathbf{r},R) + \psi(R) - \mu_0\big), \quad \text{(I.13)}$$

where μ_0 is the (constant) chemical potential of the RC liquid. Please note that $u_{\text{ext}}(\mathbf{r},R) + \psi(R)$ plays the role of the total external potential applied to the colloids. $F\left[\rho(\mathbf{r},R)\right]$ can be decomposed as

$$F = k_BT \iint d\mathbf{r}dR\rho(\mathbf{r},R)\left[\ln\left(\frac{\rho(\mathbf{r},R)\Lambda^3}{p_0}\right) - 1\right] + F_{\text{ex}}, \quad \text{(I.14)}$$

where $\Lambda = h/(2\pi m k_BT)^{1/2}$ is the thermal wavelength. The first term of Eq. I.14 accounts for the ideal contribution to the Helmholtz free energy functional, while the second term, $F_{\text{ex}}(\mathbf{r},R)$, represents the excess part arising exclusively from interparticle interactions.

Applying functional differentiation to Eq. I.13, using Eq. I.14 and defining the excess chemical potential as $\mu_{\text{ex}}(\mathbf{r},R) = \delta F_{\text{ex}}/\delta\rho(\mathbf{r},R)$ leads to the following Euler-Lagrange equation

$$k_BT\ln\left(\rho(\mathbf{r},R)\Lambda^3/p_0\right) + u_{\text{ext}}(\mathbf{r},R) + \psi(R) + \mu_{\text{ex}}(\mathbf{r},R) - \mu_0 = 0. \quad \text{(I.15)}$$

Solving Eq. I.15 for the particle density, $\rho(\mathbf{r},R)$, and using Eq. I.3, yields

$$\rho(\mathbf{r},R) = qp(R)\exp\big(-\beta u_{\text{ext}}(\mathbf{r},R) - \beta\mu_{\text{ex}}(\mathbf{r},R)\big), \quad \text{(I.16)}$$

where $q \equiv e^{\beta\mu_0}/\Lambda^3$ is a constant prefactor with dimensions of length^{-3}. The value of q is obtained coupling the system to a bulk homogeneous reservoir far away from the external perturbation ($\mathbf{r}\to\infty$), where the fluid is not affected by the applied external potential. The one body density profile in this reservoir is given by

$$\rho_{\text{bulk}}(\mathbf{r},R) = \rho_0 f(R) = qp(R)\exp\big(-\beta\mu_{\text{ex}}(\infty,R)\big). \quad \text{(I.17)}$$

We emphasize that, even though the reservoir is not influenced by the external field, still its emergent distribution, $f(R)$, is in general different to the parent distribution, $p(R)$. Combining Eqs. I.16 and I.17 we finally find

$$\rho(\mathbf{r},R) = \rho_0 f(R)\exp\big(-\beta u_{\text{ext}}(\mathbf{r},R) - \beta\mu_{\text{ex}}(\mathbf{r},R) + \mu_{\text{ex}}(\infty,R)\big) \quad \text{(I.18)}$$

In order to solve this equation, the emergent size distribution of a homogeneous bulk fluid of responsive hard spheres must be previously determined. Once $f(R)$ is known, Eq. I.18 is solved iteratively until convergence is achieved, leading to

the equilibrium position and size distribution of the fluid immersed in the external potential, $\rho_{\text{eq}}(\mathbf{r}, R)$.

We emphasize that this equation is identical to the one proposed by Pagonabarraga et al. to describe the one-body density profile of a polydisperse hard spheres [I.55, I.56]. Therefore, formally in the grand-canonical ensemble with appropriate chosen chemical potentials, our responsive system is fully equivalent to a non-responsive polydisperse hard-sphere fluid having a size distribution in bulk provided by $f(R)$.

I.2.3. Free energy functional for responsive hard spheres

Finding out the explicit expression of $F_{\text{ex}}[\rho(\mathbf{r}, R)]$ for an arbitrary interacting system is in general a difficul task. However, for the particular case of polydisperse hard spheres, there exist a very accurate free energy functional that has even been further improved to achieve consistency with an exact scaled-particle theory for the monodisperse fluid: the White Bear version (mark II) of the Fundamental Measure Theory developed by Hansen-Goos and Roth [I.57]. In this framework, the excess free energy functional reads as

$$F_{\text{ex}}\rho(\mathbf{r}, R) = \int d\mathbf{r}\ \Phi(\{n_\alpha(\mathbf{r})\}). \tag{I.19}$$

Here, Φ is the excess free energy density, given by

$$\begin{aligned}\Phi =& -n_0 \ln(1-n_3) + \Big(1 + \frac{1}{9}n_3^2\phi_2(n_3)\Big)\frac{n_1 n_2 - \mathbf{n}_{\text{V1}}\cdot\mathbf{n}_{\text{V2}}}{1-n_3} \\ &+ \Big(1 - \frac{4}{9}n_3\phi(n_3)\Big)\frac{n_2^2 - \mathbf{n}_{\text{V1}}\cdot\mathbf{n}_{\text{V2}}}{24\pi(1-n_3)^2},\end{aligned} \tag{I.20}$$

where

$$\begin{aligned}\phi_2(n_3) =& \big(6n_3 - 3n_3^2 + 6(1-n_3)\ln(1-n_3)\big)/n_3^3 \\ \phi_3(n_3) =& \big(6n_3 - 9n_3^2 + 6n_3^3 + 6(1-n_3)^2\ln(1-n_3)\big)/(4n_3^3).\end{aligned} \tag{I.21}$$

The functions $\{n_\alpha(\mathrm{r})\}$, with $\alpha = 0, 1, 2, 3, \mathrm{V1}$ and V2 are six weigthed functions of the particle density. For a polidisperse system of hard spheres, they are given by the following convolution integrals

$$n_\alpha(\mathbf{r}) = \int d\mathbf{r} \int dR\ \rho(\mathbf{r}, R)\omega_\alpha(\mathbf{r} - \mathbf{r}', R), \tag{I.22}$$

where $\omega_\alpha(\mathbf{r}-\mathbf{r}',R)$ are the corresponding weight functions:

$$\begin{aligned}
\omega_2(\mathbf{r},R) =& \delta(R-|\mathbf{r}|) & \omega_3(\mathbf{r},R) =& \theta(R-|\mathbf{r}|)\\
\omega_1(\mathbf{r},R) =& \frac{\omega_2(\mathbf{r},R)}{4\pi R} & \omega_0(\mathbf{r},R) =& \frac{\omega_2(\mathbf{r},R)}{4\pi R^2}\\
\omega_{\mathrm{V}2}(\mathbf{r},R) =& \frac{\mathbf{r}}{|\mathbf{r}|}\delta(R-|\mathbf{r}|) & \omega_{\mathrm{V}1}(\mathbf{r},R) =& \frac{\omega_{\mathrm{V}2}(\mathbf{r},R)}{4\pi R}
\end{aligned} \tag{I.23}$$

with $\theta(x)$ the Heaviside function and $\delta(x)$ the Dirac's delta. The resulting excess chemical potential appearing in Eq. I.18 is

$$\mu_{\mathrm{ex}}(\mathbf{r},R) = \sum_\alpha \int d\mathbf{r}' \frac{\partial \Phi}{\partial n_\alpha}(\mathbf{r}')\omega_\alpha(\mathbf{r}'-\mathbf{r},R). \tag{I.24}$$

I.3. Results and discussion

I.3.1. Bulk properties of responsive hard spheres

We begin our study by considering a homogeneous bulk suspension of responsive hard spheres (without any applied external field) at a fixed particle density $\rho_0 = N/V$, where the free energy landscape $\psi(R)$ is given by Eq. I.12. Under this situation, the system becomes a homogeneous polidisperse suspension of hard spheres. For bulk suspensions, the one-body density profile reduces to $\rho(\mathbf{r},R) = \rho_0 f(R)$, and the weighted densities become independent on $\mathbf{r}$, i.e. $n_\alpha(\mathbf{r}) = n_\alpha$. The explicit expressions of $\{n_\alpha\}$ in terms of weigthed integrals of $f(R)$ are given in Eq. I.31 of Appendix A.

We remark again that, due to the squeezing of particles induced by the interparticle hard sphere repulsions, $f(R)$ can significantly differ from $p(R)$ when ρ_0 increases. To calculate $f(R)$, we make use of Eq. I.17, which has to be solved iteratively until convergence is achieved. The constant prefactor q is determined imposing the normalization condition of the distribution, i.e., $\int dR f(R) = 1$. The explicit expression of $\mu_{\mathrm{ex}}(\infty,R)$ for a homogeneous fluid is provided in Eq. I.32 of Appendix A.

In order to characterize the particle compression we make use of the *real* particle volume fraction, defined from the emergent size distribution through

$$\eta = \frac{4\pi}{3}\rho_0 \int dR f(R) R^3. \tag{I.25}$$

Alternatively, we can also use the so-called generalized volume fraction, ζ, defined as the volume fraction of the responsive particles assuming that they do

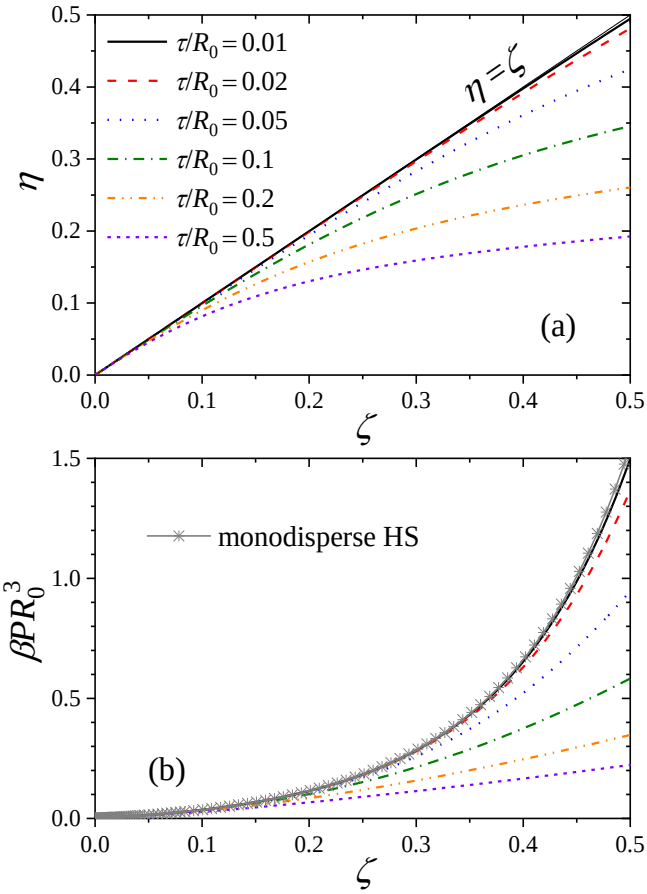

Figure I.2: (a) Real particle volume fraction (η) of an homogeneous hard-sphere fluid versus the generalized volume fraction (ζ), evaluated for $\tau/R_0 = 0.01$, 0.02, 0.05, 0.1, 0.2 and 0.5. The line $\eta = \zeta$ shows the behavior for a monodisperse (non-responsive) fluid. (b) Pressure of the hard-sphere fluid evaluated for the same values of τ. The corresponding pressure for a monodisperse hard-sphere fluid is also included as a reference.

not interact with each other (i.e. having the isolated particle size distribution, $p(R)$), usually employed to feature the particle concentration in soft colloidal systems [I.59, I.60, I.11, I.61]

$$\zeta = \frac{4\pi}{3}\rho_0 \int dR p(R) R^3. \tag{I.26}$$

Fig. I.2(a) shows $\eta(\zeta)$ for increasing values of the softness parameter, ranging from $\tau/R_0 = 0.01$ (stiff colloids) to $\tau/R_0 = 0.5$ (super soft colloids). In all cases, in the limit of high dilution ($\zeta \to 0$), particle interactions are negligible, resulting in no particle compression, and thus $\eta \approx \zeta$. As concentration increases, the squeezing of the colloids leads to $\eta < \zeta$. This reduction in particle volume becomes

more pronounced for increasing particle softness. Indeed, for large τ, the elastic free energy cost of deforming the colloids is very small, resulting in a significant reduction of η. Conversely, for very stiff colloids (small τ), the particles are unable to be compressed, even at relatively high particle densities, aproaching the limiting behavior of a monodisperse fluid of hard spheres, namely $\eta = \zeta$.

Another interesting property to report is the total pressure of the reponsive mixture of hard spheres, P. In the context of the fundamental measure theory, the equation of state is provided by [I.62, I.57]

$$\beta P = \frac{\partial \Phi}{\partial n_3}, \tag{I.27}$$

where $n_3 = (4\pi/3)\rho_0 \int dR f(R) R^3 \equiv \eta$, and Φ is the Helmholtz free energy density, defined in Eq. I.20. Expression I.27 provides excellent agreement with a very accurate equation of state of the additive mixture of hard spheres [I.63, I.57]. Fig. I.2(b) shows $P(\zeta)$ for increasing values of τ. The pressure of a pure monodisperse hard-sphere fluid is also plotted as reference (line with symbols).

As observed, the pressure of the fluid strongly depends on the particle softness. Stiff colloids exhibit a pressure very similar to that of a monodisperse hard-sphere fluid. However, for larger values of τ, there is a progressive deviation from this behavior, resulting in a significant decrease in pressure. This effect arises from the additional internal degree of freedom (size) of the particles, allowing them to adapt to environmental conditions. Specifically, as the system of responsive soft colloids is compressed by increasing ρ_0, individual particles deswell to minimize interparticle repulsion, leading to lower pressure values compared to the monodisperse case.

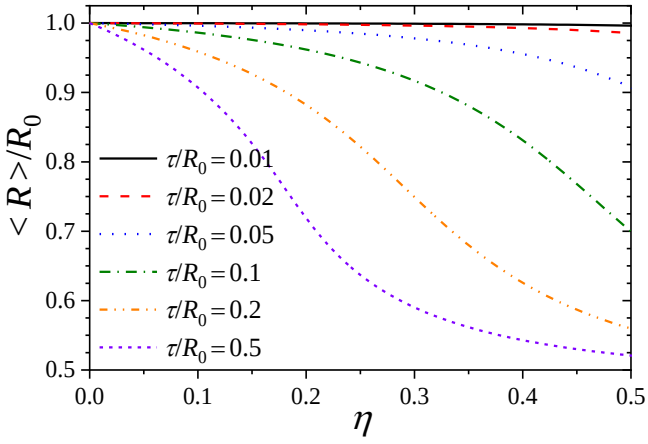

Figure I.3: Mean particle size of a homogeneous responsive hard-sphere fluid, $\langle R \rangle$, as a function of the real volume fraction, η, for $\tau/R_0 = 0.01$, 0.2, 0.05, 0.1, 0.2 and 0.5.

The squeezing of the colloids upon increasing the density is clearly illustrated in Fig. I.3, where the mean particle size, $\langle R \rangle = \int dR f(R) R$, is plotted against η for

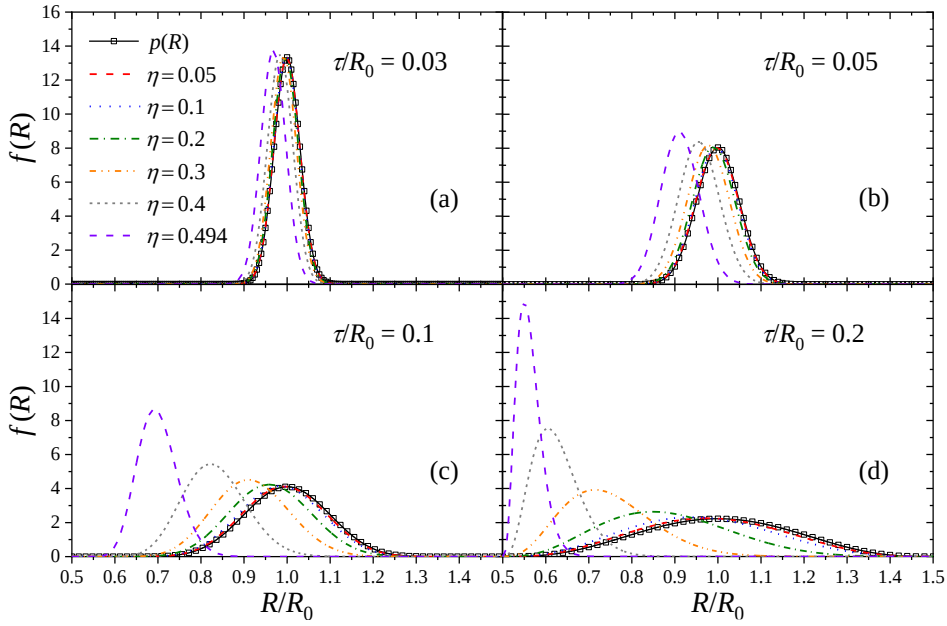

Figure I.4: Emergent size distribution, $f(R)$, for increasing values of the volume fraction, η. Plots (a) to (d) show the results for $\tau/R_0 = 0.03$, 0.05, 0.1 and 0.2, respectively.

various values of τ. We restrict our study to the regime $\eta \leq 0.494$ to assure that our hard-sphere system remains in the fluid phase even in the limit of very stiff colloids. The study of the solid phases formed by responsive hard spheres is out of the scope of this work. For $\tau/R_0 = 0.01$, the particles are so stiff that they remain uncompressed as the volume fraction increases. In stark contrast, for $\tau/R_0 = 0.5$, the ultra-soft nature of these colloids leads to a dramatic reduction in $\langle R \rangle$, which approaches the minimum permissible size ($\langle R \rangle \to 0.5R_0$) at high η. Intermediate values of τ produce a smooth transition between these two extremes.

These results are further corroborated in Fig. I.4, where $f(R)$ is plotted against η for four different values of particle softness: $\tau/R_0 = 0.03$, 0.05, 0.1, and 0.2. The parent distribution, $p(R)$, is also shown as a reference (line with squared symbols). For $\tau/R_0 = 0.03$ (plot (a)), the narrow size distribution is minimally affected by system compression; only at the limit of $\eta = 0.494$ (corresponding to the onset of fluid-solid phase coexistence in a monodisperse hard-sphere fluid) do the particles begin to slightly reduce their size. The effect of compression becomes more relevant for increasing the particle softness, as seen in plots (b) and (c). For $\tau/R_0 = 0.2$ (plot (d)), $f(R)$ exhibits a very broad peak in the dilute regime that significantly shifts to smaller sizes as η increases, while the distribution becomes strongly narrowed. At $\eta = 0.494$, only small colloids remain in the system, causing the responsive fluid to converge to an almost monodisperse system with a size of approximately $R \approx 0.56R_0$.

I.3.2. Inhomogeneous responsive hard spheres near a hard planar wall

In this section we go beyond the bulk properties and explore the behavior of a responsive hard-sphere fluid in the presence of a single planar hard wall. Under this symmetry, the only relevant spatial coordinate is the distance to the wall, z, so $n_\alpha(\mathbf{r}) = n_\alpha(z)$. The external potential is given by

$$u_{\text{ext}}(z, R) = \begin{cases} \infty & z < R \\ 0 & z \geq R \end{cases} \tag{I.28}$$

Please note that the minimum distance of the particle center to the wall is R, which means that smaller colloids will be able to approach more to the wall than larger ones. For $z \to \infty$ the system is not perturbed anymore by the wall. In other words, for $z \to \infty$ the system is coupled to an homogeneous (bulk) reservoir with density ρ_0 and size distribution given by $f(R)$. The equilibrium density profile is obtained solving Eq. I.18, using the function $f(R)$ calculated for an homogeneous system as an input. The explicit expressions of the six weigth functions and excess chemical potential for planar symmetry ($\{n_\alpha(z)\}$ and $\mu_{\text{ex}}(z, R)$, respectively) are given by Eqs. I.33 and I.34 of Appendix B.

In a first step, we analyze the effect of the softness on the structure of the responsive hard-sphere fluid near the wall. Fig. I.5(a) shows the mean local density, $\rho(z)$ (obtained from Eq. I.8), for τ/R_0 from 0.03 to 0.5, for a fixed bulk number density given by $\rho_0 R_0^3 = 0.1$. The density profile for a monodisperse hard-sphere system at the same bulk density is also depicted as a reference (gray line with symbols). The volume fraction of this reference fluid is $\eta = 0.419$, which is quite close to the fluid-solid transition, and large enough to provoke the appearance of a very large adsorption peak in contact to the hard wall, followed by density oscillations normal to the wall that extend to large distances.

As evident, particle softness significantly alters the liquid structure, leading to a notable reduction in the adsorption peak and mitigating the layering of the density. For $\tau/R_0 > 0.2$, the resulting density profile becomes nearly flat, displaying only a small maximum proximate to the wall. This attenuation can be attributed to the combination of two factors. On the one hand, increased particle softness enhances size-polydispersity, diminishing local ordering near the wall. This effect leads to structural disordering effects caused by the ability of small colloids to fill the gaps between large ones, which disrupts the excluded volume effects responsible for the density oscillations observed in monodisperse systems near a hard wall, as reported in Refs. [I.55, I.56]. Furthermore, polydispersity strongly influences the fluid-solid transition observed in hard-sphere systems, impeding particle allocation within a crystalline structure. Experiments [I.64], theory [I.65, I.66, I.67] and computer simulations [I.68, I.69] show that polydispersity broadens the fluid phase and even

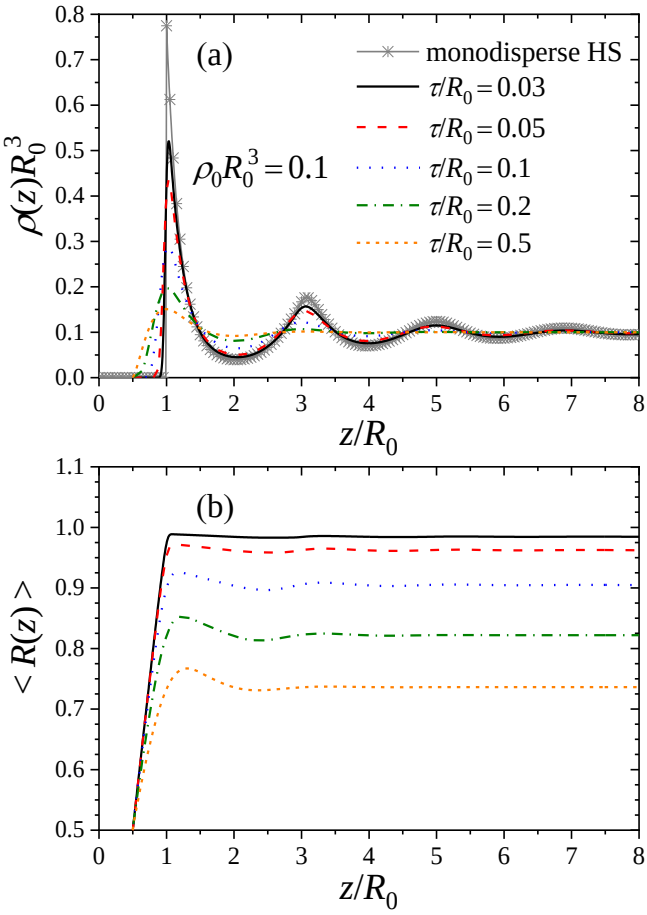

Figure I.5: (a) Density profile of a responsive hard-sphere fluid near a planar hard wall, $\rho(z)$, evaluated for increasing values of the particle softness, from $\tau/R_0 = 0.03$ to 0.5. The density profile of the monodisperse hard-sphere fluid at the same bulk number density with particle size R_0 is also included as a reference. (b) Mean particle size as a function of the separation to the wall, $\langle R(z)\rangle$, calculated for the same values of τ. In all cases, the bulk number density is $\rho_0 R_0^3 = 0.1$.

supresses crystalization above a terminal polydispersity. On the other hand, increasing the particle softness also implies that colloids are more likely to reduce their size at a given concentration in response to interparticle repulsions, which in turn reduces the effective volume fraction of the responsive hard-sphere fluid, as shown in Fig. I.2(a), giving rise to a weaker structuring near the wall.

Decreasing the particle softness makes the fluid less responsive until the density profile gradually converges to the behavior of a monodisperse hard-sphere fluid for $\tau \to 0$.

Fig. I.5(b) presents the mean local radius of the particles, $\langle R(z)\rangle$, for the same τ

values. Far from the wall, $\langle R(z)\rangle$ converges to the value characteristic of a uniform bulk solution (see Fig. I.3). As expected, for very stiff colloids ($\tau/R_0 = 0.03$), particles experience only minimal compression, maintaining a mean radius close to R_0. Increasing particle softness results in greater compression, progressively reducing the mean size. Surprisingly, $\langle R(z)\rangle$ shows a weak dependence on z beyond $z > 2R_0$, despite the oscillatory behavior of particle density near the wall. Only for soft colloids does the mean size exhibit a maximum at $z_{\max} \approx 1.2R_0$, indicating that larger particles are more likely to be accommodated in this region. This effect, also obsersed in responsive Gaussian-core colloids [I.50], can be explained by the conditions near the hard wall: unlike in the bulk, where colloids are completely surrounded by other particles, proximity to the wall reduces the number of neighboring particles, which entails an increase of the mean particle size compared to the bulk. Within the region $0.5R_0 < z < 1.2R_0$, the mean size of the particles decreases monotonically as they approach the wall. This is because larger colloids cannot remain near the wall due to overlap constraints, allowing only smaller colloids to occupy this space.

Having studied the effect of softness, we now turn to examine the influence of particle concentration. Figs.I.6(a) and (b) respectively show the normalized density profile near a planar hard wall, $\rho(z)/\rho_0$, and the local mean particle size, as the volume fraction increases from the dilute regime ($\eta = 0.05$) to the limit of a very dense fluid ($\eta = 0.494$). In all cases, $\tau/R_0 = 0.2$. In the dilute regime, the resulting density profile is almost uniform, as expected, and only approaches zero for $z < 1.2R_0$ due to the steric constraints induced by the wall. Increasing the particle concentration leads to the formation of layering around the wall, which are accompanied by fluctuations in $\langle R(z)\rangle$. The shift of the size distribution to smaller sizes due to particle compression causes the main peak of the density profile to gradually move towards smaller z-values. For $\eta = 0.494$, the mean particle size decreases to $\langle R\rangle \approx 0.56R_0$, and the density profile closely resembles that of monodisperse hard spheres at the same packing fraction, depicted as a gray line with symbols in Fig.I.6(a). In other words, under sufficient compression, the responsive fluid tends to behave like a monodisperse fluid of (non-responsive) hard spheres because the particle size distribution becomes very narrow and close to $R = 0.5R_0$.

I.3.3. Confined responsive hard spheres in a gravitational field

In this section we explore again the effect of the particle softness, but for a hard-sphere fluid immersed in the gravitational potential $u_{\text{ext}}(z) = mgz$ and confined between two hard walls. We select $\beta mg = 1/R_0$ so that $u_{\text{ext}}(z) = z/R_0$. Left and right flat planes ($z = 0$ and $z = L$, respectively) play the role of bottom and upper walls of the container.

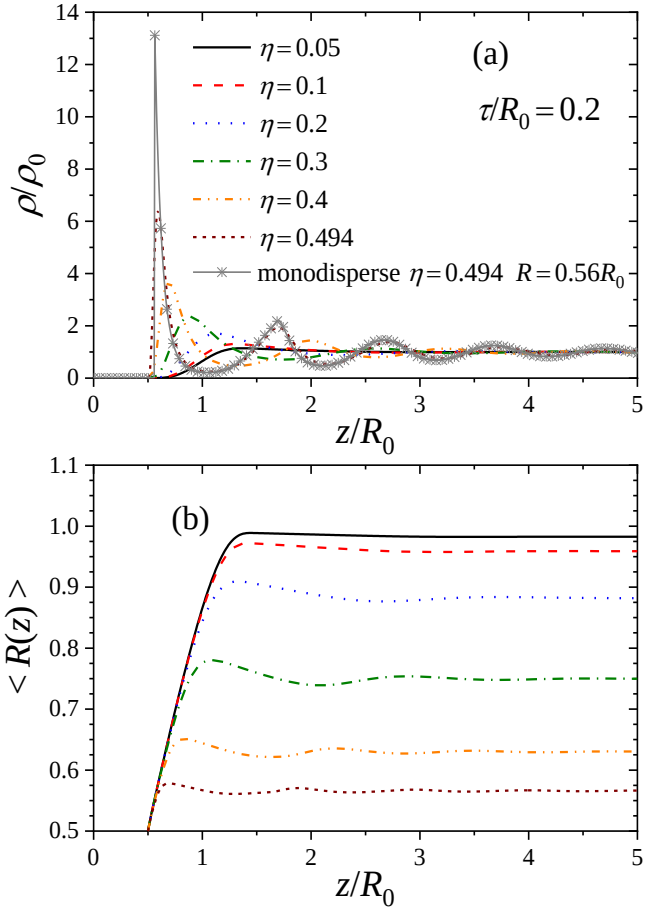

Figure I.6: (a) Normalized density profile of a responsive hard-sphere fluid near a planar hard wall, $\rho(z)/\rho_0$, obtained for increasing values of the volume fraction, from $\eta = 0.05$ to 0.494. The corresponding density profile of a monodisperse hard-sphere fluid with particle size $R = 0.56R_0$ and volume fraction $\eta = 0.494$ is also included as a reference. (b) Mean particle size as a function of the separation to the wall, $\langle R(z) \rangle$, calculated for the same values of η. In all cases, $\tau/R_0 = 0.2$.

We assume in this geometry mass conservation. Although DFT is usually designed in the grand-canonical ensemble, where the system is connected to an external reservoir so that the chemical potential μ_0 appearing in Eq. I.16 is constant, we instead must fix the total surface density of colloids N/S inside the planar slit, and treat μ_0 as a Lagrange multiplier to satisfy this constraint. Therefore, the iterative solution to Eq. I.16 must be assisted with and the additional normalization condition $\int dR \int_0^L dz \rho(z, R) = N/S$ to determine the constant prefactor q. Fig. I.7(a) and (b) respectively show the resulting $\rho(z)$ and $\langle R(z) \rangle$ for increasing values of the particle softness. In all cases, the distance between both walls is $L = 15R_0$ and $N/S = 1.5R_0^{-2}$.

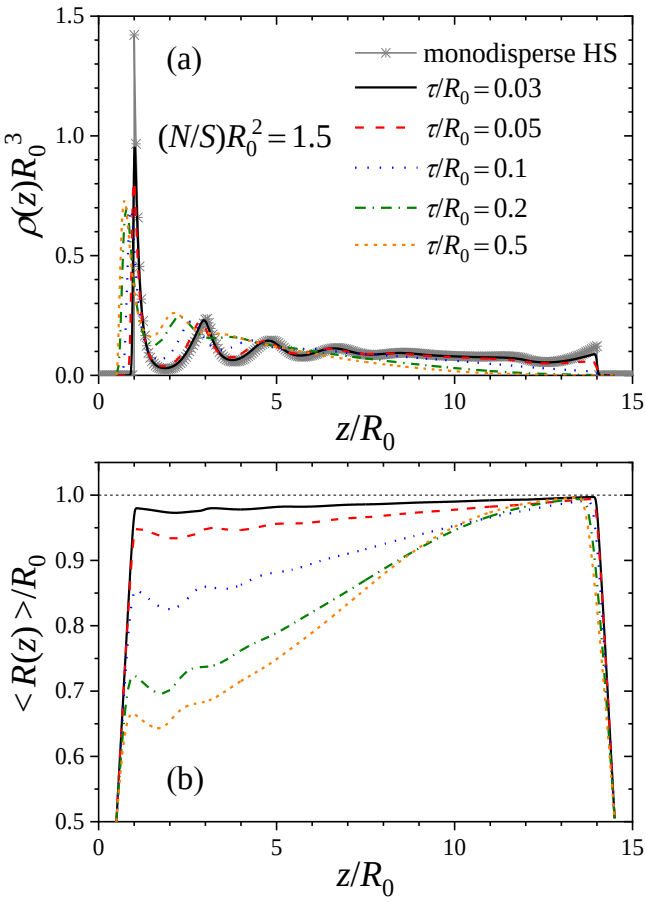

Figure I.7: (a) $\rho(z)$ of a confined fluid of responsive hard spheres immersed in the gravitational external potential $u_{\text{ext}}(z, R) = z/R_0$, for increasing values of the particle softness, from $\tau/R_0 = 0.03$ to 0.5. The density profile of a monodisperse hard-sphere fluid with particle size R_0 is also included as a reference. (b) $\langle R(z) \rangle$, calculated for the same values of τ. In all cases, the surface density is $(N/S)R_0^2 = 1.5$.

We start analyzing the density profile of the reference monodisperse (non-responsive) hard-sphere fluid, with particle radius R_0 and volume fraction of $\eta = 0.419$ (gray line with symbols in Fig. I.7(a)). Clearly, particles accumulate near the left wall (bottom region) due to the influence of the applied gravitational field. The particle concentration in this region is so high that this accumulation leads to an enhanced structuring of the density into coordination layers around the left wall, with a very large contact density $\rho(z = R_0)R_0^3 = 1.42$. These oscillations decay as we move away from the left wall. Close to the right wall, another adsorption peak is observed in contact with the wall, although with much lower intensity, because the local density in this region is very small. It is noteworthy that this density profile is significantly different from the exponential barometric distribution

($\rho(z) \sim \exp(-z/R_0)$) due to the strong interparticle excluded-volume interactions arising in this dense system.

The remaining curves in Fig. I.7(a) correspond to the density profiles of the responsive system for different values of τ. As observed, increasing particle stiffness (decreasing τ) causes the profile to converge to the behavior of the monodisperse case. Conversely, increasing softness reduces the density oscillations and shifts the adsorption peak to smaller distances from the wall. Integration of the density profile (not shown) indicates that softer hard spheres tend to concentrate more in the bottom region than stiffer ones because they are able to further decrease their size upon compression, reducing the volume exclusion and allowing larger particle accumulation. Consequently, softness also enhances the depletion of colloids at the top region. This effect is confirmed in Fig.I.7(b): indeed, increasing softness leads to a significant decrease in $\langle R(z)\rangle$ when approaching the bottom region. For $\tau/R_0 = 0.5$, particles reach a mean particle size around $\langle R(z)\rangle \approx 0.65R_0$ in the bottom region, while it tends to $\langle R(z)\rangle = R_0$ in the upper zone. In other words, the application of the external field produces an important localization of the particle size, also reported is similar systems of ultrasoft responsive colloids [I.50]. Additionally, the high particle concentration in the bottom region also leads to size modulation, showing a local maximum followed by a local minimum that roughly corresponds to regions with lower and higher local concentration. In the regions very close to both walls, the mean size rapidly decreases to $0.5R_0$ due to the steric exclusion exerted by the hard walls, as discussed before.

I.3.4. Confined responsive hard spheres in a gravitational plus Arquimedes buoyant force

In this application we consider an external field that combines gravity and Arquimedes buoyancy. The corresponding force for a spherical particle of mass m and radius R is given by

$$f_{\text{ext}} = -mg + \rho_s g \frac{4}{3}\pi R^3, \tag{I.29}$$

where ρ_s is density of the solvent. We make here the particular choice $\rho_s = 3m/(4\pi R_0^3)$ to achieve $f_{\text{ext}} = 0$ when $R = R_0$. Selecting $\beta mg = 1/R_0$, and integrating the force, the resulting external potential reads as

$$\beta u_{\text{ext}}(z, R) = \frac{z}{R_0}\left[1 - \left(\frac{R}{R_0}\right)^3\right]. \tag{I.30}$$

Unlike the gravitational field, this external potential also explicitly depends on particle size. In particular, colloids with $z < R_0$ will tend to settle down whereas colloids with $z > R_0$ will ascend towards the upper wall due to buoyancy.

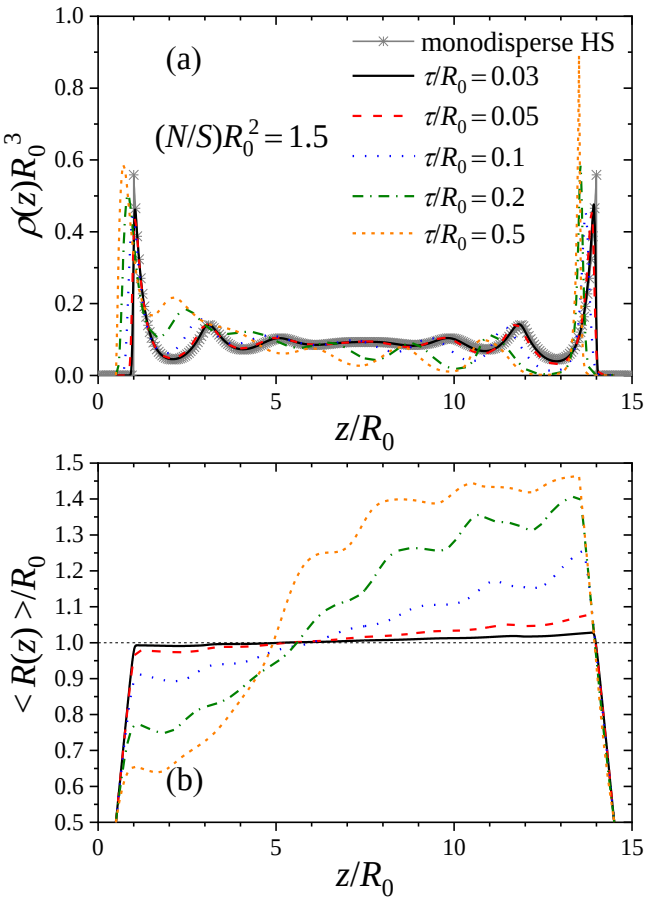

Figure I.8: (a) $\rho(z)$ of a confined fluid of responsive hard spheres immersed in the gravitational plus Arquimedes buoyant external potential $u_{\text{ext}}(z, R) = (1 - (R/R_0)^3)z/R_0$, for increasing values of the particle softness, from $\tau/R_0 = 0.03$ to 0.5. The density profile of the monidisperse hard-sphere fluid with particle size R_0 is also included as a reference. (b) $\langle R(z) \rangle$, calculated for the same values of τ. In all cases, the surface density is $(N/S)R_0^2 = 1.5$.

Fig. I.8(a) and (b) respectively depict the resulting $\rho(z)$ and $\langle R(z) \rangle$ for a confined fluid of responsive hard spheres between two walls with $(N/S)R_0^2 = 1.5$, and for increasing values of the particle softness from $\tau/R_0 = 0.03$ to 0.5. Fig. I.8(a) also includes the results for a monodisperse non-responsive hard-sphere fluid with particle size R_0 at the same surface density, for which $u_{\text{ext}}(z, R_0) = 0$. This monodisperse system shows a flat density profile in the central region of the slit. Near the walls, however, the density exhibits symmetric oscillations with high adsorption peaks. These oscillations and peaks are due to the formation of coordination layers, which are induced by strong excluded volume effects resulting from the high surface density selected in this illustrative example.

For very soft colloids ($\tau/R_0 \geq 0.1$) $\rho(z)$ becomes tilted due to the accumulation of small colloids at the bottom. However, in the region close to the upper wall the density profile does not decreases as occured for the responsive system under the gravitational field. In this case, buoyancy makes the large colloids to emigrate upwards, leading to a remarkably different qualitative behavior. Indeed, since large particles exclude more volume than small ones, this accummulation of colloids at the top gives rise to a very high adsorption peak, followed by well-defined density oscillation in the region nearby the upper wall. The enhanced size segregation arising under this external field is clearly appreciated in Fig. I.8(b). As observed, small colloids accumulate at the bottom, while particles of large radius are preferently located in the middle top region of the slit.

Ths size segregation is predominant in responsive systems having larger softness parameter (τ), as they are able to easily modify their size, adapting it to the conditions imposed by $u_{\text{ext}}(z, R)$. Increasing the particle stiffness (decreasing τ) impedes the deformation of the responsive colloids, flatening the size segregation and approaching the monodisperse case in the limit $\tau \to 0$.

I.3.5. Responsive versus conventional polydisperse non-responsive

Finally, we recall that a fluid of responsive colloids can be considered a polydisperse system with a homogeneous bulk size distribution given by the emergent distribution, $f(R)$. As previously mentioned, $f(R)$ differs from the parent distribution, $p(R)$, which is strictly defined only for one isolated particle. This difference arises because the responsiveness of the particles allows them to reduce their size in bulk when particle density increases.

At this juncture, it is insightful to compare the behavior of the responsive system with that of a polydisperse but non-responsive fluid. We can also refer to this as a "conventional polydisperse" system [I.43], where an initially fixed size distribution of particles is maintained regardless of any changes in density or external fields, as relevant in experiments. We can construct the conventional non-responsive polydisperse system by fixing the appropriate chemical potential in the DFT, such that a pre-fixed distribution (for example, given by the single particle distribution $p(R)$) remains constant and does not change with particle concentration. Therefore, the chemical potential of the reservoir for the responsive system is $\mu(R) = \mu_0 - k_B T \ln(f(R)/p_0)$, whereas for the non-responsive one $\mu(R) = \mu_0 - k_B T \ln(p(R)/p_0)$.

From a practical point of view, Eq. I.18 holds in both situations, but replacing $f(R)$ by $p(R)$ when considering the conventional polydisperse non-responsive case. From a grand-canonical point of view, we are thus comparing systems with different

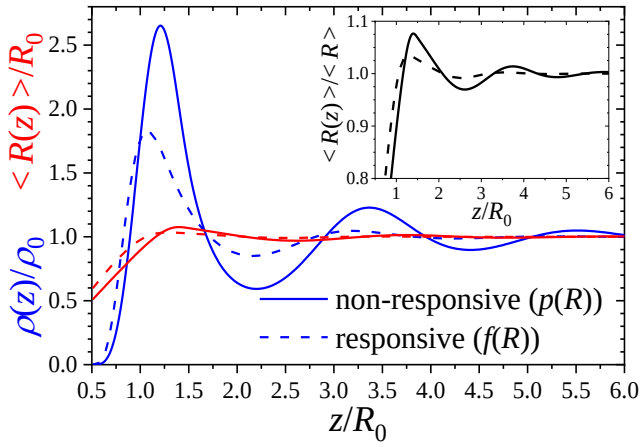

Figure I.9: Normalized density profile and mean particle size ($\rho(z)/R_0$ and $\langle R(z)\rangle$, respectively) for a responsive and a convebtional polydisperse non-responsive hard-sphere fluid. Inset: normalized mean particle size, $\langle R(z)\rangle/\langle R\rangle$ for a responsive and a polydisperse non-responsive fluid. In both cases $\rho_0 R_0^3 = 0.08$ and $\tau/R_0 = 0.2$.

chemical potentials and naturally differences are expected. From an experimental or computer simulation perspective [I.43], however, it corresponds to synthesizing conventional polydisperse systems with the single-particle distribution, $p(R)$, and then investigating the structural response for different densities or under the action of an external potential. The structure will be different between responsive and conventional polydisperse systems because of the explicit response of the RCs. Hence, such a comparison is meaningful, although from a grand canonical statistical physics perspective naturally inconsistent.

Fig. I.9 compares the role of responsiveness by examining the inhomogeneous properties of a fluid in contact with a single planar hard wall. Specifically, it depicts $\rho(z)/\rho_0$ (blue lines) and $\langle R(z)\rangle$ (red lines) for both the responsive system (dashed lines) and for the conventional polydisperse non-responsive fluid (solid lines), for which the bulk size distribution is given by $p(R)$. In both cases, $\rho_0 R_0^3 = 0.08$ and $\tau/R_0 = 0.2$. As observed, the density profile of the non-responsive polydisperse system exhibits enhanced oscillations compared to the explicitly responsive one because the individual colloids cannot reduce their size in response to particle interactions, resulting in a larger volume fraction, η.

Additionally, $\langle R(z)\rangle$ shows more pronounced oscillations in the non-responsive case. This is clearly seen in the inset of Fig.I.9, where the normalized mean size, $\langle R(z)\rangle/\langle R(\infty)\rangle$, is plotted for both situations. Significant size modulations appear for non-responsive polydisperse hard spheres, which become significantly damped in responsive systems due to the compression of the particles. Similar observations for such a comparison have been reported for homogeneous bulk systems [I.43]. Interestingly, this behavior can also be observed for RCs, for which the

size relaxations are infinitely slow. Hence, this comparison between responsive and conventional polydisperse has also a relevance from a dynamic point of view when relaxation time scales are different.

I.4. Conclusions

In this work, we employ a generalized DFT for responsive colloids to characterize the homogeneous (bulk) and inhomogeneous equilibrium properties of a fluid composed of responsive hard spheres, where the particle size (R) is explicitly resolved and fluctuates according to a unimodal distribution. This model represents the first attempt to describe the equilibrium behavior of swollen microgels subjected to confinement and external fields using classical DFT, taking into account that particles can not only distribute themselves within the available space but also modify their internal conformation in response to changes in concentration and external interactions.

Our results demonstrate that particle softness, defined as the ability of particles to vary their size, has a significant impact on the size distribution of bulk systems, allowing a considerable reduction of the mean colloidal size upon increasing the particle concentration. For microgels, the softness can be controlled varying the crosslinker concentration inside the particle. This effect results in lower particle volume fraction, pressure, and mean size for soft colloids compared to stiff ones under identical concentration conditions.

We also systematically investigate the inhomogeneous equilibrium properties, such as density profile and size segregation, of responsive hard-sphere fluids under three representative external potentials. First, we examine the system in contact with a planar hard wall and connected to a bulk reservoir far from the wall. The second example involves a system confined between two parallel hard walls and subjected to a gravitational field. The final example is similar to the second, but also includes the Archimedes buoyancy force. These last two cases provide realistic scenarios related to the sedimentation of colloids.

The results show that increasing particle softness dampens the structural density oscillations of the responsive system near a planar wall, which are induced by the inherent hard-sphere interparticle repulsions. Increasing the volume fraction for a fixed softness enhances the structuring of the hard-sphere fluid, converging to the behavior of a monodisperse (intrinsically non-responsive) system with smaller particle sizes. However, despite the significant oscillations observed in $\rho(z)$ at high volume fractions, the mean local particle size, $\langle R(z)\rangle$, does not exhibit such strong oscillatory behavior. Nonetheless, it experiences a significant decrease near the wall due to the steric constraint imposed by the hard wall, which only allows smaller colloids to approach it.

For a confined hard-sphere fluid subjected to a size-independent gravitational external field, colloids tend to accumulate at the bottom due to sedimentation. In soft systems, the increased concentration results in a substantial decrease in particle size, leading to local size segregation. This effect is even more pronounced when a size-dependent Archimedes buoyant external field is included. This field causes significant structuring near the upper wall too, due to the accumulation of larger colloids in this region. This effect leads to a pronounced size segregation, especially for high values of the softness parameter, τ.

Finally, we show that, although responsiveness leads to a polydisperse distribution of sizes, the behavior of a responsive system differs from that of a conventional polydisperse non-responsive fluid, where particle compression is not permitted.

Future work could focus on modeling responsive colloids that interact through more complex size-dependent pair potentials, where mapping using the effective Barker-Henderson radius may result in a non-additive responsive hard-sphere fluid. Another intriguing topic to explore is the inhomogeneous properties of responsive hard spheres at very high volume fractions, where solid structures are likely to emerge. Additionally, investigating the emergence of transient dynamic states when the responsive hard-sphere fluid is subjected to a sudden change in environmental conditions or applied external field would be highly interesting. This could be achieved by using dynamical density functional theory [I.70, I.38, I.71] or other sophisticated frameworks that incorporate heat dissipation [I.72].

Acknowledgements

This work was supported by the Deutsche Forschungsgemeinschaft (DFG) via the Research Unit FOR 5099 “Reducing complexity of nonequilibrium systems” and Project No. 430195928. The authors also acknowledge support by the state of Baden-Württemberg through bwHPC and the DFG through grant no INST 39/963-1 FUGG (bwForCluster NEMO). Further support was provided by grant PID2022-136540NB-I00 funded by MCIN/AEI/10.13039/501100011033, ERDF *A way of making Europe*, the Spanish Ministerio de Ciencia e Innovación, Programa Estatal de Investigación Científica, Técnica y de Innovación 2021–2023 (Project No. PID2022-136540NB-00) and program Visiting Scholars funded by the Plan Propio of the University of Granada (Project No. PPVS2018-08). J.L.M. thanks the Ph.D. student fellowship (FPU21/03568) supported by the Spanish *Ministerio de Universidades*.

Finally, the authors of this work would like to express our gratitude to Professor Luis Rull Fernández, whom we will always remember fondly, not only as a scientist but also for his human qualities. May he rest in peace.

I.5. Appendix

I.5.1. Appendix A. Weight functions and excess chemical potential for a homogeneous (bulk) system

For the homogeneous case (i.e. in the absence of applied external potential) the weight functions $\{n_\alpha\}$ become independent of $\mathbf{r}$. They can be written as integrals of the actual size distribution, $f(R)$

$$\begin{aligned} n_0 =&\rho_0 \int dR f(R), \quad n_1 = \rho_0 \int dR f(R) R, \quad n_2 = \rho_0 4\pi \int dR f(R) R^2 \\ n_3 =&\rho_0 \frac{4}{3}\pi \int dR f(R) R^3, \quad \mathbf{n}_{\mathrm{V}1} = \mathbf{n}_{\mathrm{V}2} = 0. \end{aligned} \tag{I.31}$$

Performing the partial derivatives of the free energy density, the resulting excess chemical potential is given by

$$\begin{aligned} \mu_{\mathrm{ex}}(\infty, R) = &- \ln(1-n_3) + n_2\phi_2(n_3)R \\ &+ \big(n_1\phi_2(n_3) + 3n_2^2\phi_3(n_3)\big)4\pi R^2 \\ &+ \big(\frac{n_0}{1-n^3} + n_1 n_2 \frac{d\phi_2}{dn_3} + n_2^3 \frac{d\phi_3}{dn_3}\big)\frac{4}{3}\pi R^3. \end{aligned} \tag{I.32}$$

I.5.2. Appendix B. Weight functions and excess chemical potential for planar symmetry

For the particular case of planar symmetry, the one-body density profile can be expressed as $\rho(\mathbf{r}, R) = \rho(z, R)$, where z is the distance measured from the left wall, located at $z = 0$. The other two coordinates vary along $x, y \in]-\infty, \infty[$. This allows to simplify the convolution integrals involved in the calculation of $\{n_\alpha\}$, which only

depend on z. They finally become

$$\begin{aligned}
n_0(z) &= \int dR\, \frac{1}{2R} \int_{z-R}^{z+R} dz' \rho(z', R) \\
n_1(z) &= \int dR\, \frac{1}{2} \int_{z-R}^{z+R} dz' \rho(z', R) \\
n_2(z) &= \int dR\, 2\pi R \int_{z-R}^{z+R} dz' \rho(z', R) \\
n_3(z) &= \int dR \int_{z-R}^{z+R} dz' \rho(z', R) \pi [R^2 - (z - z')^2] \\
\mathbf{n}_{\mathrm{V}1}(z) &= n_{\mathrm{V}1}(z)\hat{\mathbf{k}} = \int dR\, \frac{1}{2R} \int_{z-R}^{z+R} dz' \rho(z', R)(z - z')\hat{\mathbf{k}} \\
\mathbf{n}_{\mathrm{V}2}(z) &= n_{\mathrm{V}2}(z)\hat{\mathbf{k}} = \int dR\, 2\pi \int_{z-R}^{z+R} dz' \rho(z', R)(z - z')\hat{\mathbf{k}},
\end{aligned} \tag{I.33}$$

where $\hat{\mathbf{k}}$ is the unitary vector pointing in the direction of the z axis. The resulting excess chemical potential (Eq. I.24) for this particular symmetry is given by

$$\begin{aligned}
\mu_{\mathrm{ex}}(z, R) = \int_{z-R}^{z+R} dz' \Big[& \frac{1}{2R} \frac{\partial \Phi}{\partial n_0}(z') + \frac{1}{2} \frac{\partial \Phi}{\partial n_1}(z') \\
& + 2\pi R \frac{\partial \Phi}{\partial n_2}(z') + \pi [R^2 - (z - z')^2] \frac{\partial \Phi}{\partial n_2}(z') \\
& + \frac{1}{2R}(z' - z) \frac{\partial \Phi}{\partial n_{\mathrm{V}1}}(z') + 2\pi (z' - z) \frac{\partial \Phi}{\partial n_{\mathrm{V}2}}(z') \Big].
\end{aligned} \tag{I.34}$$

Bibliography

[I.1] Mikhail Motornov, Roman Sheparovych, Robert Lupitskyy, Emily MacWilliams, and Sergiy Minko. Responsive colloidal systems: Reversible aggregation and fabrication of superhydrophobic surfaces. *J. Colloid Interface Sci.*, 310(2):481–488, 2007.

[I.2] Mikhail Motornov, Halyna Royter, Robert Lupitskyy, Yuri Roiter, and Sergiy Minko. Stimuli-responsive hydrogel hollow capsules by material efficient and robust cross-linking-precipitation synthesis revisited. *Langmuir*, 27(24):15305–15311, 2011.

[I.3] Kyriaki Kalaitzidou and Alfred J. Crosby. Adaptive polymer particles. *Appl. Phys. Lett.*, 93(4):041910, 2008.

[I.4] Harper Meng and Guoqiang Li. Reversible switching transitions of stimuli-responsive shape changing polymers. *J. Mater. Chem. A*, 1:7838–7865, 2013.

[I.5] Junhyuk Lee, Kang Hee Ku, Chan Ho Park, Young Jun Lee, Hongseok Yun, and Bumjoon J. Kim. Shape and color switchable block copolymer particles by temperature and ph dual responses. *ACS Nano*, 13(4):4230–4237, April 2019.

[I.6] José Nelson Onuchic, Zaida Luthey-Schulten, and Peter G. Wolynes. Theory of protein folding: The energy landscape perspective. *Annu. Rev. Phys. Chem.*, 48(1):545–600, 1997.

[I.7] Chi Wu and Xiaohui Wang. Globule-to-coil transition of a single homopolymer chain in solution. *Phys. Rev. Lett.*, 80:4092–4094, May 1998.

[I.8] Samuel S. Cho, Yaakov Levy, and Peter G. Wolynes. P versus Q: Structural reaction coordinates capture protein folding on smooth landscapes. *Proc. Natl. Acad. Sci. U.S.A.*, 103(3):586–591, 2006.

[I.9] Ucheor B. Choi, James J. McCann, Keith R. Weninger, and Mark E. Bowen. Beyond the random coil: Stochastic conformational switching in intrinsically disordered proteins. *Structure*, 19(4):566 – 576, 2011.

[I.10] Alan R Denton and Matthias Schmidt. Colloid-induced polymer compression. *J. Phys.-Condes. Matter*, 14(46):12051–12062, nov 2002.

[I.11] Matthew Urich and Alan R. Denton. Swelling, structure, and phase stability of compressible microgels. *Soft Matter*, 12:9086–9094, 2016.

[I.12] J. Brijitta and P. Schurtenberger. Responsive hydrogel colloids: Structure, interactions, phase behavior, and equilibrium and nonequilibrium transitions of microgel dispersions. *Curr. Opin. Colloid Interface Sci.*, 40:87–103, 2019.

[I.13] Wei Kang Lim and Alan R. Denton. Polymer crowding and shape distributions in polymer-nanoparticle mixtures. *J. Chem. Phys.*, 141(11):114909, 2014.

[I.14] Wei Kang Lim and Alan R. Denton. Depletion-induced forces and crowding in polymer-nanoparticle mixtures: Role of polymer shape fluctuations and penetrability. *J. Chem. Phys.*, 144(2):024904, 2016.

[I.15] Wei Kang Lim and Alan R. Denton. Influence of polymer shape on depletion potentials and crowding in colloid–polymer mixtures. *Soft Matter*, 12:2247–2252, 2016.

[I.16] Johannes Harrer, Marcel Rey, Simone Ciarella, Hartmut Löwen, Liesbeth M. C. Janssen, and Nicolas Vogel. Stimuli-responsive behavior of pnipam microgels under interfacial confinement. *Langmuir*, 35(32):10512–10521, August 2019.

[I.17] Tyler J. Weyer and Alan R. Denton. Concentration-dependent swelling and structure of ionic microgels: simulation and theory of a coarse-grained model. *Soft Matter*, 14:4530–4540, 2018.

[I.18] Jianshu Cao and B. J. Berne. Theory and simulation of polar and nonpolar polarizable fluids. *J. Chem. Phys.*, 99(9):6998–7011, 1993.

[I.19] Roland G. Winkler, Dmitry A. Fedosov, and Gerhard Gompper. Dynamical and rheological properties of soft colloid suspensions. *Curr. Opin. Colloid Interface Sci.*, 19(6):594–610, 2014.

[I.20] Arturo Moncho-Jordá and Joachim Dzubiella. Swelling of ionic microgel particles in the presence of excluded-volume interactions: a density functional approach. *Phys. Chem. Chem. Phys.*, 18(7):5372–5385, 2016.

[I.21] Matthias Karg, Andrij Pich, Thomas Hellweg, Todd Hoare, L. Andrew Lyon, J. J. Crassous, Daisuke Suzuki, Rustam A. Gumerov, Stefanie Schneider, Igor. I.

Potemkin, and Walter Richtering. Nanogels and microgels: From model colloids to applications, recent developments, and future trends. *Langmuir*, 35(19):6231–6255, May 2019.

[I.22] Lorenzo Rovigatti, Nicoletta Gnan, Andrea Ninarello, and Emanuela Zaccarelli. Connecting elasticity and effective interactions of neutral microgels: The validity of the hertzian model. *Macromolecules*, 52(13):4895–4906, July 2019.

[I.23] A. Scotti, S. Bochenek, M. Brugnoni, M. A. Fernandez-Rodriguez, M. F. Schulte, J. E. Houston, A. P. H. Gelissen, I. I. Potemkin, L. Isa, and W. Richtering. Exploring the colloid-to-polymer transition for ultra-low crosslinked microgels from three to two dimensions. *Nat. Commun.*, 10(1):1418, 2019.

[I.24] Andrea Scotti, Alan R. Denton, Monia Brugnoni, Judith E. Houston, Ralf Schweins, Igor I. Potemkin, and Walter Richtering. Deswelling of microgels in crowded suspensions depends on cross-link density and architecture. *Macromolecules*, 52(11):3995–4007, June 2019.

[I.25] Andrea Scotti. Characterization of the volume fraction of soft deformable microgels by means of small-angle neutron scattering with contrast variation. *Soft Matter*, 17:5548–5559, 2021.

[I.26] I. Bouhid de Aguiar, T. van de Laar, M. Meireles, A. Bouchoux, J. Sprakel, and K. Schroën. Deswelling and deformation of microgels in concentrated packings. *Sci. Rep.*, 7(1):10223, 2017.

[I.27] Gaurasundar M. Conley, Philippe Aebischer, Sofi Nöjd, Peter Schurtenberger, and Frank Scheffold. Jamming and overpacking fuzzy microgels: Deformation, interpenetration, and compression. *Sci. Adv.*, 3(10):e1700969, 2017.

[I.28] Nicoletta Gnan and Emanuela Zaccarelli. The microscopic role of deformation in the dynamics of soft colloids. *Nat. Phys.*, 15(7):683–688, 2019.

[I.29] Svetoslav V. Nikolov, Alberto Fernandez-Nieves, and Alexander Alexeev. Behavior and mechanics of dense microgel suspensions. *Proc. Natl. Acad. Sci. U.S.A.*, 117(44):27096–27103, 2020.

[I.30] Giovanni Del Monte, Domenico Truzzolillo, Fabrizio Camerin, Andrea Ninarello, Edouard Chauveau, Letizia Tavagnacco, Nicoletta Gnan, Lorenzo Rovigatti, Simona Sennato, and Emanuela Zaccarelli. Two-step deswelling in the volume phase transition of thermoresponsive microgels. *Proc. Natl. Acad. Sci.*, 118(37):e2109560118, 2021.

[I.31] Andrea Scotti, M. Friederike Schulte, Carlos G. Lopez, Jérôme J. Crassous, Steffen Bochenek, and Walter Richtering. How softness matters in soft nanogels and nanogel assemblies. *Chem. Rev.*, 122(13):11675–11700, July 2022.

[I.32] Rajam Elancheliyan, Giovanni Del Monte, Edouard Chauveau, Simona Sennato, Emanuela Zaccarelli, and Domenico Truzzolillo. Role of charge content in the two-step deswelling of poly(n-isopropylacrylamide)-based microgels. *Macromolecules*, 55(17):7526–7539, September 2022.

[I.33] Giovanni Del Monte and Emanuela Zaccarelli. *arXiv:2404.04032*, 2024.

[I.34] Mehrdad Hamidi, Amir Azadi, and Pedram Rafiei. Hydrogel nanoparticles in drug delivery. *Adv. Drug Deliv. Rev.*, 60(15):1638–1649, 2008. 2008 Editors' Collection.

[I.35] Brian R. Saunders, Nadiah Laajam, Emma Daly, Stephanie Teow, Xinhua Hu, and Robert Stepto. Microgels: From responsive polymer colloids to biomaterials. *Adv. Colloid Interface Sci.*, 147-148:251 – 262, 2009.

[I.36] Serguei V Vinogradov. Nanogels in the race for drug delivery. *Nanomedicine*, 5(2):165–168, 2010.

[I.37] Arturo Moncho-Jordá, Alicia Germán-Bellod, Stefano Angioletti-Uberti, Irene Adroher-Benítez, and Joachim Dzubiella. Nonequilibrium uptake kinetics of molecular cargo into hollow hydrogels tuned by electrosteric interactions. *ACS Nano*, 13(2):1603–1616, February 2019.

[I.38] Arturo Moncho-Jordá and Joachim Dzubiella. Controlling the microstructure and phase behavior of confined soft colloids by active interaction switching. *Phys. Rev. Lett.*, 125:078001, Aug 2020.

[I.39] Rafael Roa, Won Kyu Kim, Matej Kanduč, Joachim Dzubiella, and Stefano Angioletti-Uberti. Catalyzed bimolecular reactions in responsive nanoreactors. *ACS Catal.*, 7(9):5604–5611, September 2017.

[I.40] Rafael Roa, Stefano Angioletti-Uberti, Yan Lu, Joachim Dzubiella, Francesco Piazza, and Matthias Ballauff. Catalysis by metallic nanoparticles in solution: Thermosensitive microgels as nanoreactors. *Z. Phys. Chem.*, 232(5-6):773–803, 2018.

[I.41] Matej Kanduč, Won Kyu Kim, Rafael Roa, and Joachim Dzubiella. Modeling of stimuli-responsive nanoreactors: rational rate control towards the design of colloidal enzymes. *Mol. Syst. Des. Eng.*, 5:602–619, 2020.

[I.42] Yi-Chen Lin, Benjamin Rotenberg, and Joachim Dzubiella. Structure and position-dependent properties of inhomogeneous suspensions of responsive colloids. *Phys. Rev. E*, 102:042602, Oct 2020.

[I.43] Upayan Baul and Joachim Dzubiella. Structure and dynamics of responsive colloids with dynamical polydispersity. *J. Phys.-Condes. Matter*, 33(17):174002, apr 2021.

[I.44] Paul J. Flory and Jr. Rehner, John. Statistical Mechanics of Cross-Linked Polymer Networks II. Swelling. *J. Chem. Phys.*, 11(11):521–526, 11 1943.

[I.45] Maxime J. Bergman, Nicoletta Gnan, Marc Obiols-Rabasa, Janne-Mieke Meijer, Lorenzo Rovigatti, Emanuela Zaccarelli, and Peter Schurtenberger. A new look at effective interactions between microgel particles. *Nat. Comm.*, 9(1):5039, 2018.

[I.46] J. A. Barker and D. Henderson. Perturbation Theory and Equation of State for Fluids. II. A Successful Theory of Liquids. *J. Chem. Phys.*, 47(11):4714–4721, 12 1967.

[I.47] Yiping Tang. Role of the Barker–Henderson diameter in thermodynamics. *J. Chem. Phys.*, 116(15):6694–6700, 04 2002.

[I.48] Douglas Henderson. Rowlinson's concept of an effective hard sphere diameter. *J. Chem. Eng. Data*, 55(10):4507–4508, October 2010.

[I.49] Arturo Moncho-Jordá, Nils Göth, and Joachim Dzubiella. Liquid structure of bistable responsive macromolecules using mean-field density-functional theory. *Soft Matter*, 19:2832–2846, 2023.

[I.50] Arturo Moncho-Jordá, Sebastien Groh, and Joachim Dzubiella. External field-driven property localization in liquids of responsive macromolecules. *J. Chem. Phys.*, 160(2):024904, 01 2024.

[I.51] C. N. Likos, A. Lang, M. Watzlawek, and H. Löwen. Criterion for determining clustering versus reentrant melting behavior for bounded interaction potentials. *Phys. Rev. E*, 63:031206, Feb 2001.

[I.52] A. A. Louis, P. G. Bolhuis, and J. P. Hansen. Mean-field fluid behavior of the gaussian core model. *Phys. Rev. E*, 62:7961–7972, Dec 2000.

[I.53] A. A. Louis, P. G. Bolhuis, J. P. Hansen, and E. J. Meijer. Can polymer coils be modeled as "soft colloids"? *Phys. Rev. Lett.*, 85:2522–2525, 2000.

[I.54] P. G. Bolhuis, A. A. Louis, J. P. Hansen, and E. J. Meijer. Accurate effective pair potentials for polymer solutions. *J. Chem. Phys.*, 114(9):4296–4311, 2001.

[I.55] I. Pagonabarraga, M. E. Cates, and G. J. Ackland. Local size segregation in polydisperse hard sphere fluids. *Phys. Rev. Lett.*, 84:911–914, Jan 2000.

[I.56] Matteo Buzzacchi, Ignacio Pagonabarraga, and Nigel B. Wilding. Polydisperse hard spheres at a hard wall. *J. Chem. Phys.*, 121(22):11362–11373, 12 2004.

[I.57] Hendrik Hansen-Goos and Roland Roth. Density functional theory for hard-sphere mixtures: the white bear version mark ii. *J. Phys.-Condes. Matter*, 18(37):8413, aug 2006.

[I.58] J-P. Hansen and I.R. McDonald. *Theory of Simple Liquids, Fourth Edition*. Academic Press, 4th edn, 2013.

[I.59] H. Senff and W. Richtering. Temperature sensitive microgel suspensions: Colloidal phase behavior and rheology of soft spheres. *J. Chem. Phys.*, 111(4):1705–1711, 1999.

[I.60] M. Pelaez-Fernandez, Anton Souslov, L. A. Lyon, P. M. Goldbart, and A. Fernandez-Nieves. Impact of single-particle compressibility on the fluid-solid phase transition for ionic microgel suspensions. *Phys. Rev. Lett.*, 114:098303, Mar 2015.

[I.61] A. Scotti, U. Gasser, E. S. Herman, Jun Han, A. Menzel, L. A. Lyon, and A. Fernandez-Nieves. Phase behavior of binary and polydisperse suspensions of compressible microgels controlled by selective particle deswelling. *Phys. Rev. E*, 96:032609, Sep 2017.

[I.62] R Roth, R Evans, A Lang, and G Kahl. Fundamental measure theory for hard-sphere mixtures revisited: the white bear version. *J. Phys.-Condes. Matter*, 14(46):12063, nov 2002.

[I.63] Hendrik Hansen-Goos and Roland Roth. A new generalization of the Carnahan-Starling equation of state to additive mixtures of hard spheres. *J. Chem. Phys.*, 124(15):154506, 04 2006.

[I.64] P. N. Pusey and W. van Megen. Phase behaviour of concentrated suspensions of nearly hard colloidal spheres. *Nature*, 320(6060):340–342, 1986.

[I.65] J. L. Barrat and J. P. Hansen. On the stability of polydisperse colloidal crystals. *J. Physique*, 47:1547–1553, 1986.

[I.66] Robin McRae and A. D. J. Haymet. Freezing of polydisperse hard spheres. *J. Chem. Phys.*, 88(2):1114–1125, 01 1988.

[I.67] Moreno Fasolo and Peter Sollich. Equilibrium phase behavior of polydisperse hard spheres. *Phys. Rev. Lett.*, 91:068301, Aug 2003.

[I.68] Peter G. Bolhuis and David A. Kofke. Monte carlo study of freezing of polydisperse hard spheres. *Phys. Rev. E*, 54:634–643, Jul 1996.

[I.69] See-Eng Phan, William B. Russel, Jixiang Zhu, and Paul M. Chaikin. Effects of polydispersity on hard sphere crystals. *J. Chem. Phys.*, 108(23):9789–9795, 06 1998.

[I.70] Michael te Vrugt, Hartmut Löwen, and Raphael Wittkowski. Classical dynamical density functional theory: from fundamentals to applications. *Adv. Phys.*, 69(2):121–247, 2020.

[I.71] Michael Bley, Joachim Dzubiella, and Arturo Moncho-Jordá. Active binary switching of soft colloids: stability and structural properties. *Soft Matter*, 17:7682–7696, 2021.

[I.72] Matthias Schmidt. Power functional theory for many-body dynamics. *Rev. Mod. Phys.*, 94:015007, Mar 2022.

Publication II

Nonequilibrium relaxation of soft responsive colloids

J. López-Molina[1], S. Groh[2], J. Dzubiella[2, 3] and A. Moncho-Jordá[1,4]

[1]*Departamento de Física Aplicada, Universidad de Granada, Campus Fuentenueva S/N, 18071 Granada, Spain*

[2]*Physikalisches Institut, Albert-Ludwigs-Universität Freiburg, Hermann-Herder Straße 3, D-79104 Freiburg, Germany*

[3]*Cluster of Excellence livMatS @ FIT - Freiburg Center for Interactive Materials and Bioinspired Technologies, Albert-Ludwigs-Universität Freiburg, D-79110 Freiburg, Germany*

[4]*Institute Carlos I for Theoretical and Computational Physics, Facultad de Ciencias, Universidad de Granada, Campus Fuentenueva S/N, 18071 Granada, Spain*

Published in

AIP | The Journal of Chemical Physics

The Journal of Chemical Physics, **2024**, *161(9)*.

Abstract

Stimuli-responsive macromolecules display large conformational changes during their dynamics, sometimes switching states, and are an integral property for the development of soft functional materials. Here, we introduce a mean-field dynamical density functional theory (DDFT) for a model of responsive colloids (RCs) to study the nonequilibrium dynamics of a colloidal dispersion in time-dependent external fields, with a focus on the coupling of translational and conformational dynamics during their relaxation. Specifically, we consider soft Gaussian particles with a bimodal size distribution between two confining walls with time-dependent (switching-on and off) external gravitational and osmotic fields. We find a rich relaxation behavior of the systems in excellent agreement with particle-based Brownian dynamics (BD) computer simulations. In particular, we find time-asymmetric relaxations of integrated observables (wall pressures, mean size, liquid center-of-mass) for activation/deactivation of external potentials, respectively, which are tuneable by the ratio of translational and conformational diffusion time scales. Our work paves thus the way for studying the nonequilibrium relaxation dynamics of complex soft matter with multiple degrees of freedom and hierarchical relaxations.

II.1. Introduction

Responsive systems have garnered considerable interest in the realm of soft matter science due to their dynamic nature and the ability to adapt to external stimuli [II.1]. These systems, comprising responsive colloids and macromolecules, exhibit remarkable adaptability, controlling their properties—such as the internal conformation of the particle [II.2, II.3, II.4, II.5], size [II.6, II.7, II.8, II.9, II.10, II.11], shape [II.12, II.13, II.8, II.14, II.15, II.16, II.17, II.18, II.19], charge density [II.8, II.20], electric dipole [II.21] and orientation [II.22, II.23, II.24], among others - in response to environmental changes. Such responsiveness, originating from their internal degrees of freedom (DoFs), allows for a nuanced interaction with surrounding particles and external fields, leading to significant alterations in their internal and collective dynamical properties [II.25, II.26, II.27, II.1, II.21, II.28, II.29, II.30, II.31, II.32, II.33, II.34], even leading to multi-relaxation time scales [II.35].

An important system of RCs is the one for which the particle size (that could represent the radius of gyration of a linear polymer coil [II.6, II.36], or the diameter of a microgel particle [II.37, II.38, II.39, II.8, II.40, II.41, II.42, II.43]) is the internal property that couples to the center of mass translational degrees of freedom: particles not only move, but also are able to swell/shrink in response to external stimuli such as changes in the solvent pH, salt concentration and temperature [II.44, II.45, II.46, II.47, II.48]. In addition, particle concentration can also provoke the squeezing of the particles, leading to interpenetration, deformation and compression [II.49, II.50]. Precise control over the interplay between size localization and dynamics is paramount for achieving targeted functionality at specific locations and rates. Notable examples are the local modulation of uptake and release kinetics in soft polymer-based nanocarriers, such as microgels for local control of catalysis [II.51, II.52, II.53] or drug release [II.54, II.55, II.56, II.57, II.58].

Our understanding of soft colloids has been significantly enhanced through developments in equilibrium Density Functional Theory (DFT), which has provided a solid framework for studying the structure and phase behavior of soft materials under external potentials. Classical DFT has been successfully extended to explicitly include varying particle sizes as dynamic variables, describing how microscopic interactions and external potentials affect the equilibrium properties of these systems and enabling the exploration of size-dependent phenomena within polydisperse systems [II.59, II.60, II.6, II.61]. Recently, we demonstrated explicitly for a model of responsive colloids (RC)s with size polydispersity [II.7, II.9, II.10, II.11] how to employ DFT functionals (in RC-DFT) to study and control the localization of the (size) property in space by external fields [II.62, II.63].

However, many interesting behaviors of responsive systems occur out of equilibrium. The dynamical nature of these systems is not only a testament to their adaptability but also to their potential in real applications. In this context,

dynamical density functional theory (DDFT) serves as a powerful tool for exploring non-equilibrium processes by modeling the time evolution of the particle density distribution, $\rho(\mathbf{r}, t)$, driven by diffusive, overdamped Brownian dynamics in the presence of external fields and particle interactions [II.64, II.65, II.66, II.67, II.68]. The theory can also be modified to incorporate reactions or switching [II.69, II.70, II.71, II.72] Crucially, it leverages the adiabatic approximation, assuming that the correlations in a non-equilibrium state are akin to those in equilibrium [II.64]. This theory adapts the equilibrium concepts of DFT to non-equilibrium scenarios, predicting how responsive systems evolve over time. In contrast to conventional polydisperse systems [II.59,II.60], internal degrees of freedom are also able to change during the nonequilibrium process. A systematic study on the coupled dynamics of translation and internal dynamics in the relaxation of a colloidal system as well as the appropriate DDFT is still missing in literature.

In this work, we present an extension of classical DDFT to responsive systems (denoted by RC-DDFT) that allows us to efficiently investigate the dynamical relaxation in the presence of coupled DoFs under applied external potentials. In particular, we consider soft responsive colloids (RC), for which the size of the particles (σ) changes in response to the interactions with the rest of particles or with an applied external potential. This external potential depends on the position and also the size of the particle, i.e. $u_{\text{ext}}(\mathbf{r}, \sigma)$, making the colloidal system inhomogeneous in terms of position and size. In addition to the external potential, this system of responsive colloids also requires the knowledge of the free energy landscape for the particle size, $\psi(\sigma) = -kT \ln p(\sigma)$ (where $p(\sigma)$ represents the parent size-distribution of a single RC), which acts as an additional external potential controlling the size fluctuations [II.11]. Here, we focus on a system formed by bistable particles for which $p(\sigma)$ is described by a generic Landau-like bimodal size distribution [II.73, II.74], so particle size fluctuate between two states (big and small) separated by an energy barrier. This particular two-states behavior is relevant in the conformation of many biological or functional macromolecules, such as folded/unfolded or globule/coil transitions of proteins and polymers [II.75,II.76,II.77,II.78,II.79,II.31,II.80]. For this system, we analyse the time evolution of the one-body density profile, $\rho(\mathbf{r}, \sigma; t)$, after sudden activation/deactivation of the external field, and explore the non-equilibrium transient dynamics resulting of the interplay between structural relaxation and size relaxation.

This paper is organized as follows. In Sec. II.2 we describe the main statistical mechanics equations, discuss DFT and generalize its dynamical counterpart to deal with non-equilibrium systems of responsive colloids under external potentials (RC-DDFT). We also introduce in this Section a mean field model for soft Gaussian colloids with a bimodal distribution of states. Brownian dynamic simulations of RCs are explained in Sec. II.3. Sec. II.4 presents the results and discussion of the non-equilibrium dynamics of RCs under the activation/deactivation non-equilibrium processes for two representative external potentials: gravitation and osmotic. We

specially focus on investigating the appearance of non-equilibrium transient dynamics states that arise due to the interplay between translational diffusion and particle swelling/shrinking. Finally, in Sec. II.5 we present the main conclusions of our work.

II.2. Theoretical background

II.2.1. Theoretical modelling of responsive colloids

In the following, we briefly recall the most basic statistical relations between distributions and averages for the RC model [II.11,II.81]. As common in the theory of liquids, we assume a (isotropic) distance-dependent pair potential for the RC liquid. For RCs, however, the particle-particle pair potential not only depends on the positions $\mathbf{r}_i$ and $\mathbf{r}_j$ of both particles i and j, but also has explicit dependence on the size of both interacting particles, σ_i and σ_j, that is $u(|\mathbf{r}_i - \mathbf{r}_j|; \sigma_i, \sigma_j)$. The external potential can be expressed as $u_{\text{ext}}(\mathbf{r}_i, \sigma_i)$. Hence, the total potential energy of N responsive particles, can be expressed as

$$U = \sum_i \psi(\sigma_i) + \frac{1}{2} \sum_i \sum_{j \neq i} u(|\mathbf{r}_i - \mathbf{r}_j|, \sigma_i, \sigma_j) + \sum_i u_{\text{ext}}(\mathbf{r}_i, \sigma_i), \tag{II.1}$$

where ψ is the energy landscape for the size σ of an isolated particle. The inhomogeneous properties of an RC fluid immersed in a external potential are fully described by the particle density distribution, $\rho(\mathbf{r}, \sigma)$ [II.11, II.81], defined in such a way that integration over the 4 coordinates (3 translational ones and the size) provides the total number of particles in the system,

$$\int_V d\mathbf{r} \int d\sigma \rho(\mathbf{r}, \sigma) = N, \tag{II.2}$$

so $\rho(\mathbf{r}, \sigma)$ is measured in units of length^{-4}.

In the limit of very low particle concentrations and negligible external potential, the one-body density converges to $\lim_{\rho_0 \to 0} \lim_{u_{\text{ext}} \to 0} \rho(\mathbf{r}, \sigma) = \rho_0 p(\sigma)$, where $\rho_0 = N/V$ is the bulk particle density, and $p(\sigma)$ is the so called *parent* distribution, defined as the size distribution of a single isolated responsive particle that does not interact with external forces or with another particles, which is normalized to unity, $\int p(\sigma) d\sigma = 1$. We can express $p(\sigma)$ in terms of the free energy landscape as

$$p(\sigma) = p_0 e^{-\beta \psi(\sigma)}, \tag{II.3}$$

where $\beta = 1/(k_B T)$ (T is the absolute temperature and k_B the Boltzmann constant), and p_0 is a constant prefactor to fulfill the normalization of $p(\sigma)$. For higher particle concentrations or in the presence of external fields, the single-particle property

distribution will change: We denote by $f(\sigma) = N(\sigma)/N$ the *emergent* probability distribution, where $N(\sigma)d\sigma$ is the number of particles with internal property within $[\sigma, \sigma + d\sigma]$ in the system, and N the total number of particles. In particular, in the absence of any external field, the one-body particle density may be expressed as $\lim_{u_{\text{ext}}\to 0} \rho(\mathbf{r}, \sigma) = \rho_0 f(\sigma)$.

II.2.2. Dynamical density functional theory for RCs

Equilibrium DFT prerequisites

Let us recall first the treatment of the RC model in the framework of equilibrium DFT. The inhomogeneous free energy functional of a RC fluid immersed in the external potential $u_{\text{ext}}(\mathrm{r}, \sigma)$ is given by [II.59, II.11, II.81]

$$\begin{aligned} F[\rho(\mathbf{r},\sigma)] &= k_B T \int d\mathbf{r} \int d\sigma \rho(\mathbf{r},\sigma)\big[\ln(\rho(\mathbf{r},\sigma)\Lambda^3/p_0) - 1\big] \\ &+ \int d\mathbf{r} \int d\sigma \rho(\mathbf{r},\sigma)[u_{\text{ext}}(\mathbf{r},\sigma) + \psi(\sigma)] \\ &+ F_{\text{ex}}[\rho(\mathbf{r},\sigma)], \end{aligned} \tag{II.4}$$

where $\Lambda = h/(2\pi m k_B T)^{1/2}$ is the thermal wavelength. The first term of Eq. (II.4) is the ideal gas free-energy functional. The second term takes into account the interaction of the RC fluid with the external potential. Note that $\psi(\sigma)$ also plays the role of an external potential for the particle size, i.e., it represents the energy cost implied in the swelling/shrinking of each responsive colloid. Finally, the third contribution is the excess free energy of the fluid that arises due to the existence of particle-particle interactions.

The grand canonical potential energy functional of a RC fluid is

$$\Omega[\rho(\mathbf{r},\sigma)] = F[\rho(\mathbf{r},\sigma)] - \mu_0 \int d\mathbf{r} \int d\sigma \rho(\mathbf{r},\sigma), \tag{II.5}$$

where μ_0 is the (constant) chemical potential of the RC fluid. The equilibrium density profile is the one that minimizes the grand canonical functional, $\delta\Omega/\delta\rho(\mathbf{r},\sigma) = 0$. Applying this functional differentiation to Eq. (II.5) with Eq. (II.4) and solving the resulting Euler-Lagrange equation for the particle density $\rho(\mathbf{r},\sigma)$, we find

$$\rho(\mathbf{r},\sigma) = q \exp\big(-\beta\psi(\sigma) - \beta u_{\text{ext}}(\mathbf{r},\sigma) - \beta\mu_{\text{ex}}(\mathbf{r},\sigma)\big), \tag{II.6}$$

where $\mu_{\text{ex}}(\mathbf{r},\sigma)$ is the excess chemical potential, given by the functional differentiation of the excess free energy, $\mu_{\text{ex}}(\mathbf{r},\sigma) = \delta F_{\text{ex}}/\delta\rho(\mathbf{r},\sigma)$, and q is a normalization constant that is obtained imposing conservation of the total number of particles, namely Eq. (II.2). Solutions of Eqs. (II.6) and (II.2) lead to the equilibrium position and size distribution $\rho_{\text{eq}}(\mathbf{r},\sigma)$.

Dynamical DFT for a RC fluid

In non-equilibrium conditions, the one-body density distribution becomes also time-dependent, $\rho(\mathbf{r}, \sigma; t)$. For the case of responsive colloids, particles in the system do not only diffuse in the space, but can also can modify their their size in response to external interactions. To describe their dynamics we make the assumption that the property σ of each particle also follows an overdamped diffusive dynamics. Following the prescription given in the work by Baul et al. [II.9], we denote D_{T} as the translational diffusion coefficient, and D_σ the diffusion coefficient in the σ-space. It is important to emphasize that D_{T} depends in general on the particle size (as for Stokes-Einstein), so $D_{\mathrm{T}}(\sigma)$ is a function of σ.

The DDFT can be extended to RCs by defining a 4-dimensional vector $\mathbf{x} = (x, y, z, \sigma) \equiv (\mathbf{r}, \sigma)$, and a 4-dimensional current $\mathbf{J} = (J_x, J_y, J_z, J_\sigma) \equiv (\mathbf{J}_\mathbf{r}, J_\sigma)$ (note that this current has dimensions of length^{-3}time^{-1}). Analogously, we can write a 4-component *nabla* operator $\nabla_\mathbf{x} = (\partial/\partial x, \partial/\partial y, \partial/\partial z, \partial/\partial\sigma) \equiv (\nabla_\mathbf{r}, \nabla_\sigma)$. The time evolution of the density profile is given by

$$\frac{\partial \rho(\mathbf{x}, t)}{\partial t} = -\nabla_\mathbf{x} \cdot \mathbf{J}(\mathbf{x}, t) = -\nabla_r \cdot \mathbf{J}_\mathbf{r} - \frac{\partial J_\sigma}{\partial \sigma} \tag{II.7}$$

The components of the current $\mathbf{J}$ are

$$\begin{cases} \mathbf{J}_\mathbf{r} = -D_{\mathrm{T}}(\sigma)\rho(\mathbf{r}, \sigma; t)\nabla_\mathbf{r}[\beta\mu(\mathbf{r}, \sigma; t)] \\ J_\sigma = -D_\sigma \rho(\mathbf{r}, \sigma; t)\frac{\partial \beta\mu(\mathbf{r}, \sigma; t)}{\partial \sigma} \end{cases} \tag{II.8}$$

where $\mu(\mathbf{r}, \sigma; t)$ is the non-equilibrium chemical potential. In order to calculate it, we make use of the adiabatic approximation, and assume that $\mu(\mathbf{r}, \sigma; t)$ is given by the functional derivative of the equilibrium free energy functional, $\mu = \delta F/\delta\rho$. Using Eq. (II.4), it leads to [II.62]

$$\begin{aligned} \mu(\mathbf{r}, \sigma; t) &= k_B T \ln\left(\rho(\mathbf{r}, \sigma; t)\Lambda^3/p_0\right) + u_{\mathrm{ext}}(\mathbf{r}, \sigma) + \psi(\sigma) \\ &+ \mu_{\mathrm{ex}}(\mathbf{r}, \sigma; t), \end{aligned} \tag{II.9}$$

where $\mu_{\mathrm{ex}} = \delta F_{\mathrm{ex}}/\delta\rho$. Eqs. (II.7)-(II.9) define the new generalized dynamical density functional theory designed for responsive colloids (RC-DDFT).

II.2.3. Mean-field responsive DDFT of soft Gaussian responsive colloids confined in planar slits

In this section, we specify our particular system of responsive colloids, and the corresponding excess free energy model for it to be used in the RC-DDFT framework. In this work we focus on systems composed by soft interpenetrable RCs. We consider

the following size-dependent Gaussian-core pair potential for the particle-particle interaction

$$\beta u(|\mathbf{r}-\mathbf{r}'|,\sigma,\sigma') = \epsilon \exp\Big(-4|\mathbf{r}-\mathbf{r}'|^2/(\sigma+\sigma')^2\Big), \tag{II.10}$$

where $\epsilon > 0$ is the (repulsive) interaction strength (in k_BT units), . It represents an estimate of the particle hardness: for small values of ϵ colloids are able to interpenetrate each other. On the contrary, large values of ϵ correspond to harder colloids, for which the energy penalty of overlapping is very high. Here, $(\sigma+\sigma')/2$ plays the role of the interaction range. In fact, in this interaction model σ represents the effective radius of the each RC.

The Gaussian-core interaction model is a well established coarse-grained description of polymer solutions [II.82], as it has been shown to accurately describe the interaction between two isolated polymers immersed in a good solvent, for polymer of identical [II.83] and different length [II.84], both in homogeneous and the inhomogeneous conditions [II.85]. For different choices of the interaction parameters one can obtain either a mixture exhibiting bulk fluid–fluid (macro)phase separation [II.86, II.87, II.88, II.89] similarly to polymer blends, or alternatively, a mixture exhibiting microphase separation [II.90].

We assume that $\epsilon = 2$ (in k_BT units) for the interparticle interaction strength. This value represents fairly well the soft repulsion existing between linear polymers [II.85, II.87]. The equilibrium properties of such soft Gaussian particles described by Eq. (II.10) are well represented by a weakly correlated mean-field fluid over a surprisingly wide density and temperature range [II.85]. This justifies the use of the mean-field approximation for the excess free-energy of the interacting RC fluid, given by

$$F_{\text{ex}} = \frac{1}{2}\iint_V d\mathbf{r}d\mathbf{r}' \iint d\sigma d\sigma' \rho(\mathbf{r},\sigma)\rho(\mathbf{r}',\sigma')u(|\mathbf{r}-\mathbf{r}'|,\sigma,\sigma') \tag{II.11}$$

This approximation has been successfully used to reproduce the equilibrium and non-equilibrium properties of passive [II.88, II.91] and active switching Gaussian colloids [II.70, II.71, II.71, II.72].

Performing the functional differentiation and introducing it into Eq. (II.9) leads to the explicit expression for the non-equilibrium chemical potential of a mean-field RC fluid

$$\begin{aligned}\mu(\mathbf{r},\sigma;t) &= k_BT\ln\big(\rho(\mathbf{r},\sigma;t)\Lambda^3/p_0\big) + u_{\text{ext}}(\mathbf{r},\sigma) + \psi(\sigma) \\ &+ \int d\mathbf{r}' \int d\sigma' \rho(\mathbf{r}',\sigma';t)u(|\mathbf{r}-\mathbf{r}'|,\sigma,\sigma'),\end{aligned} \tag{II.12}$$

which involves a convolution integral in the $\mathbf{r}$ coordinate.

In our work, we consider RC dispersions confined between two parallel hard walls separated by a distance L and subjected to one-dimensional external potentials,

$u_{\text{ext}}(z,\sigma)$, where $z \in [0, L]$ is the distance from the left wall. The rest of coordinates are assumed to run over the full range, $x, y \in]-\infty, \infty[$ (infinite slit). In this case the density profiles are homogeneous in lateral directions and can be expressed as $\rho(\mathbf{r}, \sigma; t) = \rho(z, \sigma; t)$, with the normalization

$$\int_0^L dz \int d\sigma \rho(z, \sigma; t) = N/S, \tag{II.13}$$

where N/S is the prefixed number density per area S, and the normalization is valid for every time t.

Exploiting the planar symmetry to simplify the convolution integral involved in Eq. (II.12), we find the following equation for the non-equilibrium chemical potential [II.62]

$$\begin{aligned} \mu(z,\sigma;t) \quad &= k_B T \ln\left(\rho(z,\sigma;t)\Lambda^3/p_0\right) + u_{ext}(z,\sigma) + \psi(\sigma) \\ + \quad &\tfrac{\pi\epsilon}{4} \int d\sigma'(\sigma+\sigma')^2 \int_0^L dz' \rho(z',\sigma';t) e^{-\frac{4(z-z')^2}{(\sigma+\sigma')^2}}. \end{aligned} \tag{II.14}$$

In addition to the interparticle interaction potential, we need to specify the parent distribution of the RC, $p(\sigma)$. In this work we consider bistable particles, for which the size fluctuates between two states of size σ_1 and σ_2, that can be referred as small and big. This implies considering a bimodal parent size distribution, with both peaks centered around these two states. To model this behavior, we choose a generic bimodal form using a symmetric double-Gaussian function

$$p(\sigma) = \frac{p_0}{2\sqrt{2\pi\tau^2}} \Big[\exp\Big(-\frac{(\sigma-\sigma_1)^2}{2\tau^2} \Big) + \exp\Big(-\frac{(\sigma-\sigma_2)^2}{2\tau^2} \Big) \Big] \tag{II.15}$$

with $\sigma_1 = 0.63\sigma_0$, $\sigma_2 = 1.37\sigma_0$ (σ_0 represents a reference particle size that will be used as unit length for the rest of sizes and distances). In order to avoid nonphysical negative values and extremely large values of the particle size, the range of σ has been limited to be $\sigma \in [0.1\sigma_0, 2\sigma_0]$.

The parameter τ appearing in Eq. (II.15) provides the thickness of the size distribution around both peaks, and can be interpreted as the particle softness (conversely, τ^{-1} represents the stiffness of the RC). In this work we use $\tau = 0.2\sigma_0$. With this choice, the free energy barrier required to overcome to switch from one state to other is $\Delta\psi \approx 1 k_B T$.

In our system, the σ-dependence of the translational diffusion coefficient will be of the type of Stokes, $D_{\text{T}}(\sigma) = D_0\sigma_0/\sigma$, where D_0 is the diffusion coefficient of a particle of radius σ_0. In addition, a parameter α is introduced to control the ratio between σ-diffusion and translational diffusion, $D_\sigma = \alpha D_0$. We also define our diffusion time for either translation or size relaxation as $\tau_{\text{B}} = \sigma_0^2/D_0$.

From $\rho(z,\sigma;t)$ and integrating over the σ-coordinate we obtain the one-body number density distribution of the RC fluid in our quasi-1D system, namely

$$\rho(z;t) = \int d\sigma \rho(z,\sigma;t). \tag{II.16}$$

We analyze in our work a few integrated properties and monitor their time evolution: The center of mass location of the RC fluid is given by

$$\langle z(t)\rangle = \frac{S}{N}\int_0^L z dz \int d\sigma \rho(z,\sigma;t). \tag{II.17}$$

The mean size of the RC at position z is given by the normalized first moment of the distribution

$$\langle \sigma(z;t)\rangle = \frac{1}{\rho(z;t)}\int d\sigma \rho(z,\sigma;t)\sigma. \tag{II.18}$$

The (global) mean size of the RC is given by

$$\langle \sigma(t)\rangle = \frac{S}{N}\int_0^L dz \int d\sigma \rho(z,\sigma;t)\sigma. \tag{II.19}$$

The pressure exerted on the left and right wall are given respectively by

$$P_{\text{left}}(t) = \rho(0;t)k_BT \;\text{ and }\; P_{\text{right}}(t) = \rho(L;t)k_BT. \tag{II.20}$$

II.3. Brownian Dynamics simulations of RCs

Brownian dynamics (BD) calculations are performed in the framework of the RC model [II.11]. The discretized form of the BD equations for the translational degrees of freedom and for the internal property are given by:

$$\begin{cases} \mathbf{r}_i(t+\Delta t) = \mathbf{r}_i(t) + \frac{D_{\text{T}}}{k_BT}\mathbf{F}_{\text{T}}^{(i)}(t)\Delta t + \boldsymbol{\xi}_{\text{T}} \\ \sigma_i(t+\Delta t) = \sigma_i(t) + \frac{D_\sigma}{k_BT}F_\sigma^{(i)}(t)\Delta t + \xi_\sigma \end{cases} \tag{II.21}$$

where Δt is the simulation time step. While $\mathbf{F}_{\text{T}}^{(i)}(t) = -\boldsymbol{\nabla}_{\boldsymbol{r}_i}u_{\text{ext}}(\sigma_i,z;t) - \sum_{j\neq i}^N \boldsymbol{\nabla}_{\boldsymbol{r}_i}u(\mathbf{r}_i-\mathbf{r}_j,\sigma_i,\sigma_j)$ is the translational force acting on colloid i from both the external field and the pairwise interactions with the other colloids, $F_\sigma^{(i)}(t) = -\nabla_{\sigma_i}\psi(\sigma_i) - \nabla_{\sigma_i}u_{\text{ext}}(\sigma_i,z;t) - \sum_{j\neq i}^N \nabla_{\sigma_i}u(\mathbf{r}_i-\mathbf{r}_j,\sigma_i,\sigma_j)$ is the property force acting on colloid i resulting from its own free-energy landscape $\psi(\sigma)$, and its interaction with both the external field and the pairwise interactions with the other

colloids. Finally, $\boldsymbol{\xi}_T$ and ξ_σ are random vector and random scalar, respectively. Both $\boldsymbol{\xi}_T$ and ξ_σ are drawn from a normal distribution with zero mean and variance $\langle \xi_{T,\alpha}\xi_{T,\beta}\rangle = 2D_{\mathrm{T}}\Delta t\delta_{\alpha\beta}$ and $\langle \xi_\sigma^2\rangle = 2D_\sigma\Delta t$, respectively, with $\alpha, \beta = x, y, z$ being the Cartesian components, and $\delta_{\alpha\beta}$ being the Kronecker delta function.

Simulations were performed using the same geometry and potential parameters as the ones used in RC-DDFT. To avoid non vanishing, non-physical negative values, and extremely large values of the colloid size, the range of σ was limited to $[0.1, 2]\sigma_0$ by simply rejecting (Monte-Carlo like) moves that would lead to $\sigma < 0.1\sigma_0$ or $\sigma > 2\sigma_0$. The same procedure was used to respect the hard walls. Starting with an equilibrium configuration made of 432 responsive colloids (see Fig. II.1(a)), the system was perturbed by either switching on or off ϕ_{G} or ϕ_{O}, prior to a relaxation run of $30\tau_{\mathrm{B}}$ during which the system reached a new equilibrium state (see Fig. II.1(c)). To obtain the time-dependent density, $\rho(z;t)$, and mean size, $\langle\sigma(t)\rangle$, $N_{run} = 4000$ independent runs were performed. The density profile and the mean size were then averaged over all configurations for a fixed time t.

II.4. Results and discussion

For our non-equilibrium relaxation study, our methodology consists on applying an external potential,

$$u_{\mathrm{ext}}(z;\sigma;t) = u_{\mathrm{walls}}(z) + \phi(z,\sigma;t), \tag{II.22}$$

where u_{walls} accounts for the confinement effects, and ϕ represents additional external potentials such as osmotic or gravitational potentials, defined further below. In particular, the wall potential is

$$u_{\mathrm{walls}}(z) = \begin{cases} 0 & \text{for} \quad 0 \le z \le L \\ \infty & \text{for} \quad z < 0 \ \text{ or } \ z > L \end{cases}$$

We initiate our system at equilibrium and consider two time-dependent protocols. In the first one, the external potential ϕ is absent for $t < 0$, and is activated for $t > 0$ (*switch on*) to observe the ensuing relaxation towards the new equilibrium stated (reached in the limit $t \to \infty$) (cf. Fig. II.1 as a representative illustration). In the second protocol we follow the inverse process: the field is already activated for $t < 0$, and it is *switched off* for $t > 0$. Comparison between both procedures will allow to examine whether the system shows a different relaxation dynamics during the switching on and switching off processes.

This bidirectional exploration is conducted for two external potentials, namely gravitational (ϕ_{G}) and osmotic (ϕ_{O}) potentials:

(*i*) The gravitational external potential is linear in 'height' z and reads as

$$\phi_{\mathrm{G}}(z) = Az \quad \text{for} \quad 0 \leq z \leq L, \tag{II.23}$$

with $\beta A \sigma_0 = 1$. Note that the gravitational potential is just a function of position z, not of size. Still, density inhomogeneities will also affect the compressible particle sizes and their distributions in time and space.

(*ii*) The osmotic potential, $\phi_{\mathrm{O}}(z, \sigma)$ is given by

$$\phi_{\mathrm{O}}(z, \sigma) = Bz\sigma^3 \quad \text{for} \quad 0 \leq z \leq L, \tag{II.24}$$

where $\beta B \sigma_0^4 = 1$. This equation introduces a dependence on particle size through the σ^3 volume term, aiming to replicate the volumetric effects exerted by osmotic pressure in environments with varying cosolute concentrations with a constant concentration gradient. As such, σ^3 represents the volume exclusion effect of particles within this gradient [II.6, II.11].

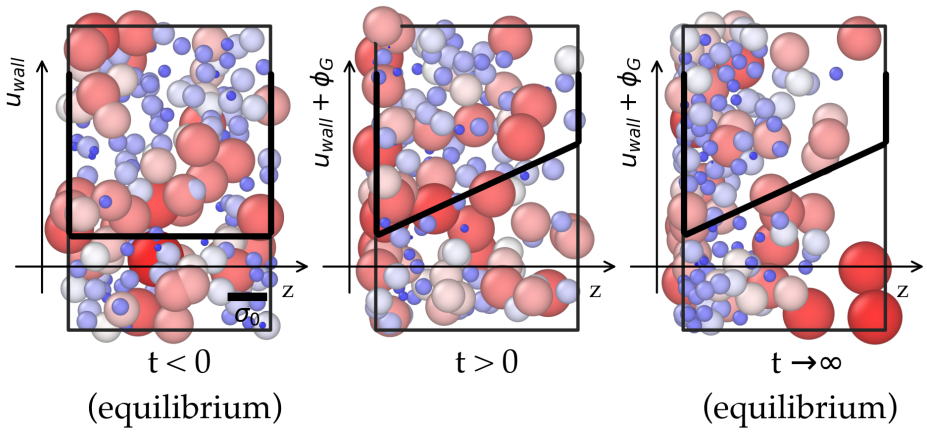

Figure II.1: Representative snapshots of system configurations made of responsive colloids obtained at different times from Brownian dynamics simulations. For $t < 0$, the system is in equilibrium with hard walls on the left and on the right (solid line). At $t = 0$, the system is perturbed by switching on ϕ_{G} (solid line) and relaxes (for $t > 0$) before reaching the new equilibrium at $t \to \infty$. The color gradient from blue (small sizes) to red (large sizes) visualizes the magnitude of the sizes of the colloids.

To validate the theoretical predictions of our extended DDFT, they are compared to BD simulations results. Through this comparison, we analyze macroscopic quantities such as the mean position $\langle z(t) \rangle$, mean size $\langle \sigma(t) \rangle$, and the pressure exerted on the hard walls. Moreover, we delve into a parametric study focusing on the dynamics of these responsive systems, governed by the parameter α. For $\alpha < 1$ the swelling/deswelling of the responsive colloid is slower than the translational diffusion, which means that the change of particle size happens later than the structural relation.

The opposite occurs for $\alpha > 1$. This dissimilar time relaxation is expected to lead to transient dynamic states, that will be explored in the following section.

Fig. II.1 provides a representative illustration of the activation protocol for the particular case of the gravitational external potential. Big and small particles are depicted as red and blue spheres, respectively. The rest of intermediate sizes are represents by a continuous graduation of colors between red and blue. At time $t < 0$ (left panel) the responsive system is in the equilibrium state, confined between two planar hard walls. After activation of the external field (central panel) at $t = 0$, particles dynamically relax in the new potential field and migrate towards the left to lower the external potential energy. Their sizes are also affected subjected to the changes in the local particle concentration. For $t \to \infty$ (right panel) the system finally reaches the final equilibrium state in presence of the external potential, with a very different profile and size distribution compared to the original state.

II.4.1. Gravitational potential

We start analyzing the relaxation dynamics of a responsive colloidal system immersed in the gravitational external potential given by Eq. (II.23) under the two protocols (switching on and off) outlined in the preceding section. For this case, we select $\alpha = 0.1$ and $N/S = 1.2\sigma_0^{-2}$. Fig. II.2 depicts the time evolution of the mean local density ($\rho(z;t)$) and local mean size ($\langle\sigma(z;t)\rangle$) from $t = 0$ to $3\tau_{\mathrm{B}}$ at $\Delta t = 0.5\tau_{\mathrm{B}}$ intervals. Panels (a) and (c) show the results following the activation ('switch on') of the gravitational field, while panels (b) and (d) depict the outcomes subsequent to its deactivation ('switch off') .

The analysis of $\rho(z)$, depicted in panels (a) and (b), reveals a significant alignment between the BD and RC-DDFT methods throughout the dynamic process. These panels also indicate that the system has reached nearly the final equilibrium state already for $t \approx 3\tau_{\mathrm{B}}$. Conversely, the evaluation of $\langle\sigma(z;t)\rangle$ in panels (c) and (d) demonstrates consistent conformity between the methods, albeit with notable differences, particularly a consistent disparity of approximately 5% throughout the dynamic sequence. This deviation in $\langle\sigma(z;t)\rangle$ arises not only in this confined geometry but also in bulk systems (without external potentials and walls). We attribute this discrepancy to the inherent limitations of the mean-field approximation employed in RC-DDFT. To facilitate clearer comparison in the figures, this difference has been rectified in the RC-DDFT data by a scaling factor of 1.05. Following this adjustment, the temporal evolution described by both techniques closely corresponds.

In the initial stage ($t = 0$) of the activation state, depicted in panel (a) of Fig. II.2, we observe a nearly flat density profile, $\rho(z)$, with the exception of regions near the walls where particle adsorption effects become prominent. This accumulation near the hard walls occurs because particles are pushed from the bulk to the walls due to

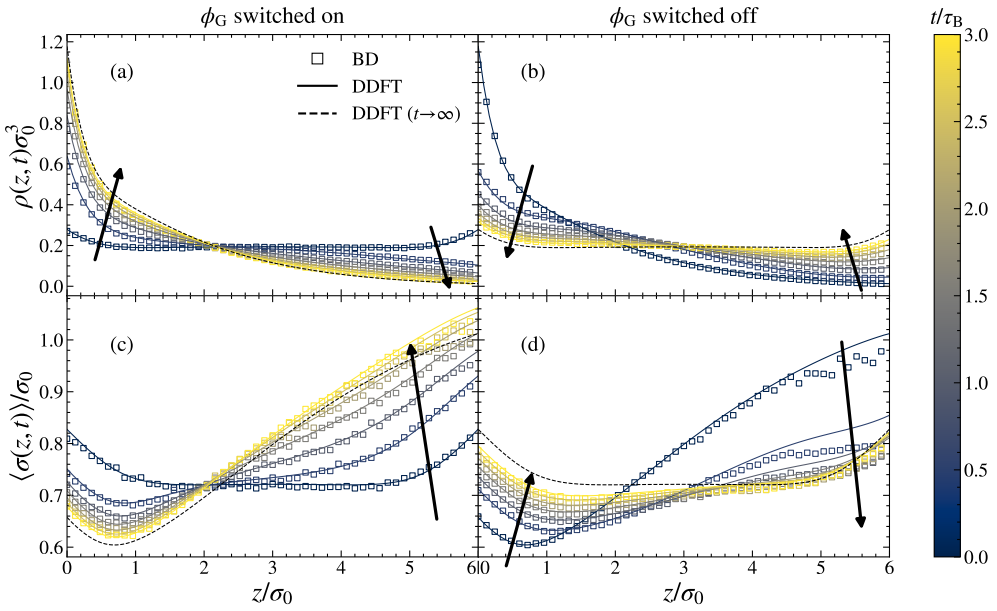

Figure II.2: Time evolution of the density $\rho(z;t)$ and size $\langle\sigma(z;t)\rangle$ of the RCs in the gravitational field, $\phi_G(z)$, plotted at different times ranging from $t = 0$ (dark blue) to $3\tau_B$ (yellow), with a time interval of $\Delta t = 0.5\tau_B$. Lines represent the theoretical predictions obtained with RC-DDFT, whereas symbols correspond to BD simulations. Panels (a) and (c) show, respectively, the local density ($\rho(z;t)$) and the local mean size ($\langle\sigma(z;t)\rangle$) obtained when the external potential is switched on for $t > 0$. Similarly, panels (b) and (d) show the same quantities, but for the deactivation process ('switched off'). In this case, $\langle\sigma(z)\rangle$ data of RC-DDFT is multiplied by a factor 1.05 for a clearer comparison. All calculations are performed considering $\alpha = 0.1$ and a surface density $N/S = 1.2\sigma_0^{-2}$.

the interparticle repulsive interactions. In addition, the local mean size, $\langle\sigma(z)\rangle$, as shown in Fig.II.2(c), exhibits intriguing behavior near the wall. Typically, in the bulk, the mean size is expected to decrease as ρ increases [II.9]. However, near the walls, an increase in $\langle\sigma\rangle$ is observed as ρ increases, a phenomenon also noted in equilibrium configurations [II.62]. This behavior can be explained by the conditions faced by colloids near a hard boundary. Unlike in the bulk, where colloids are fully surrounded by other particles, being near a wall reduces the number of neighboring particles by half. This reduction in surrounding particles diminishes the overall repulsive forces acting on the colloids, allowing them to expand.

Upon activation of the gravitational field $\phi_G(z)$ at time $t > 0$, the system is subjected to a reordering as particles migrate towards the region with lower external field, located on the left side of the slit. This process, depicted in the dynamic sequence in Figs. II.2(a) and (c) is not instantaneous; thus, we plot the density and mean size at various times to capture the evolution. It is interesting to remark the strong change of $\langle\sigma(z)\rangle$ during the first stages of the evolution ($0.5\tau_B$), compared

to the evolution of $\rho(z;t)$. Given that $\alpha = 0.1$ implies that size diffusion should be significantly slower than spatial diffusion, the observed rapid change in size must be necessarily caused by Stokes-type diffusion, $D_{\mathrm{T}} \sim 1/\sigma$: Smaller particles, having a higher diffusion coefficient, move faster towards the left, leaving behind larger particles and thus increasing the average size on the right side of the system. Additionally, a decrease in density favors more expanded states for the particles.

The system keeps evolving, and we illustrate these dynamics only up to $3\tau_{\mathrm{B}}$ because the changes become exceedingly slow thereafter. By $10\tau_{\mathrm{B}}$, the system reaches a state indistinguishable from the equilibrium state achieved under the gravitational field. In this final equilibrium state, which is also the starting point for the deactivation process (Figs. II.2(b) and (d)), the density ρ decays from the left wall. In an ideal, non-interacting system, this decay would be purely exponential. However, due to the existent repulsive interactions between colloids, the actual final equilibrium density profile departs from this ideal behavior. Excluding the near-wall effects previously discussed, regions with higher particle concentration correspond to smaller mean sizes, indicating compression due to increased density. Interestingly, near the right wall, where ρ is nearly zero, the mean size is maximal and very close to one, suggesting negligible interparticle interactions as the size distribution aligns with the parent distribution, $p(\sigma)$. The complete dynamics of the activation process depicted in Fig. II.1 are illustrated through representative snapshots obtained from Brownian Dynamics (BD) simulations, capturing the initial, intermediate, and final states. As depicted, upon activation of $\phi_{\mathrm{G}}(z)$, responsive particles undergo noticeable diffusion towards the left wall. This results in compression, leading to a significant localization effect in particle size when compared to the less compressed region near the right wall.

Figs. II.2(b) and (d) show again $\rho(z;t)$ and $\langle\sigma(z;t)\rangle$ for the deactivation process, respectively. In this case, we find that the migration towards the new equilibrium state is not symmetrical compared to the activation process. During activation, particle movement is driven by the external gravitational force, whereas upon deactivation, particle movement is driven by the gradient of concentration, which pushes the particle from the more dense region (left) to the more dilute one (right). This asymmetry results in differing dynamics between activation and deactivation phases, with the gravitational field's application appearing to accelerate the dynamic process as it will be discussed later.

II.4.2. Osmotic potential

Next, we turn to examine the dynamics of the RC fluid when the osmotic potential is activated and deactivated (Eq. II.24). This external potential varies linearly with z, akin to gravitational force, but its pronounced σ^3-dependency gives rise to a markedly distinct qualitative dynamic behavior. Fig. II.3(a) and (c) illustrate the mean particle

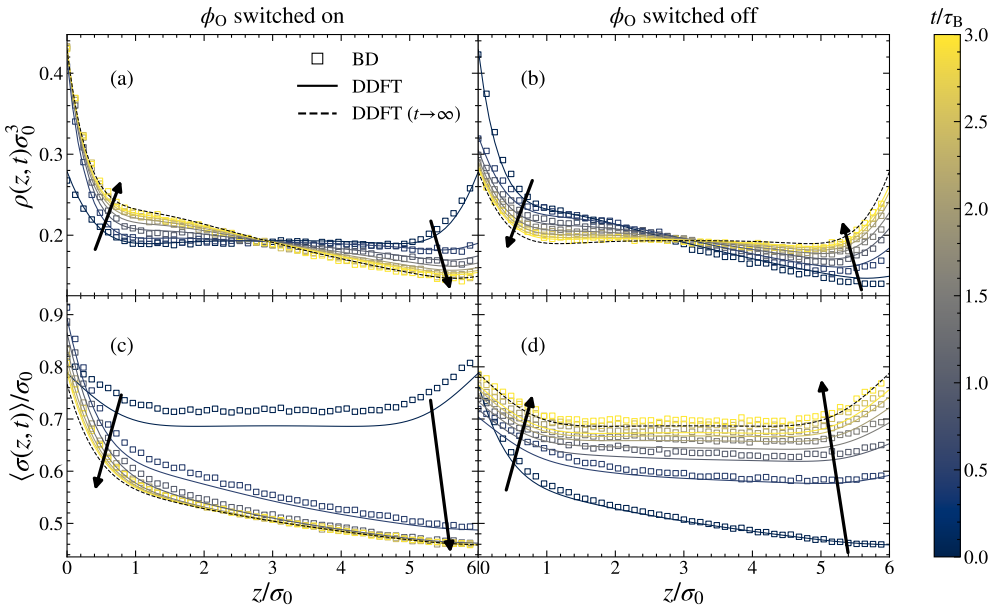

Figure II.3: Time evolution of the RCs in the osmotic field, $\phi_O(z,\sigma)$, plotted at different times ranging from $t = 0$ (dark blue) to $3\tau_B$ (yellow), with a time interval of $\Delta t = 0.5\tau_B$. Lines represent the theoretical predictions obtained with RC-DDFT, whereas symbols correspond to BD simulations. Panels (a) and (c) show respectively the local density ($\rho(z;t)$) and the local mean size ($\langle\sigma(z;t)\rangle$) obtained when the external potential is switched on for $t > 0$. Similarly, panels (b) and (d) show the same quantities, but for the deactivation process. All calculations are performed considering $\alpha = 0.1$ and a surface density $N/S = 1.2\sigma_0^{-2}$.

density and mean size within the planar slit during the activation process, respectively, while plots (b) and (d) delineate the same quantities during deactivation. We maintain $\alpha = 0.1$ and $N/S = 1.2\sigma_0^{-2}$.

Upon activation of $\phi_O(z,\sigma)$, particles tend to migrate globally towards the left, mitigating the energy contribution induced by the external potential, expressed as $\int \rho\phi_O dz d\sigma$. Analogous to gravitational effects, this results in a notable increase in particle density near the left wall over time.

However, $\langle\sigma(z;t)\rangle$ exhibits contrasting behavior, with larger particle sizes accompanying high-density regions, as depicted in Fig. II.3(c). This occurs despite the compression near the left wall. The phenomenon can be elucidated by the strong dependence of $\phi_O(z,\sigma)$ on σ: the energetic penalty for larger colloids near the right wall prompts smaller colloids to prevail in that region. Additionally, $\langle\sigma(z;t)\rangle$ experiences rapid decline in early stages of evolution ($t < 0.5\tau_B$), not attributable to RC shrinkage, given that calculations are conducted with a deswelling diffusion 10 times smaller than spatial diffusion. This effect stems from the migration of larger colloids towards the left wall, propelled by the applied external force, $f_{ext} =$

$-d\phi_{\mathrm{O}}/dz = -A\sigma^3$.

Distinct dynamical behavior emerges upon deactivating the osmotic potential. Remarkably, convergence is achieved within $3\tau_{\mathrm{B}}$ in both scenarios. However, activating the osmotic potential leads to markedly faster dynamics compared to its deactivation. This acceleration is particularly pronounced when examining the size distribution, with temporal profiles nearly coinciding after just $t \approx \tau_{\mathrm{B}}$.

Furthermore, transient behavior is observed upon activation of $\phi_{\mathrm{O}}(z, \sigma)$. Indeed, after activation, there is a rapid migration of colloids towards the left wall, resulting in a significant concentration increase at very short times in this region. Concurrently, the mean particle size of colloids near the left wall initially increases, followed by a decay over longer times. This clearly indicates that particles first move to the left and then decreases their size.

Conversely, deactivating $\phi_{\mathrm{O}}(z, \sigma)$ yields the opposite trend, with ρ and σ increasing on the left and decreasing on the right until equilibrium is attained.

In both scenarios (activation and deactivation), the comparison between theoretical predictions from RC-DDFT and BD simulations demonstrates very good agreement.

II.4.3. Macroscopic Analysis

To validate the agreement between RC-DDFT and BD beyond the local density and size profiles, we examine three interesting macroscopic, integrated quantities. These quantities not only offer insights into the global behavior of the system but also facilitate a comparison of the time scales on which dynamical processes occur. The quantities of interest are the center of mass position $\langle z \rangle$ of the suspension (Eq. (II.17)), the global mean particle size $\langle \sigma(t) \rangle$ (Eq. (II.19)), and the pressures exerted by the RC fluid on the left and right hard walls, given by $P_{\text{left}}(t)$ and $P_{\text{right}}(t)$ (Eq. (II.20)), respectively.

The time evolution of these quantities is illustrated in Fig. II.4 for $\alpha = 0.1$ and $N/S = 1.2\sigma_0^{-2}$. Each panel presents results obtained from RC-DDFT for activated (solid lines) and deactivated (dashed lines) gravitational and osmotic external potentials, distinguished by orange and blue lines, respectively. Corresponding BD simulations are represented by squared and circled symbols. Remarkable congruence between macroscopic quantities derived from both RC-DDFT and BD, not only in shape but also in indicative time scales (the values of DDFT-σ under gravitational field has been multiplied again by a factor 1.05).

The analysis of these curves reveals several features of the relaxation process. Primarily, it is evident that relaxation during the activation of the external field is consistently faster than during deactivation. We attribute this behavior to the

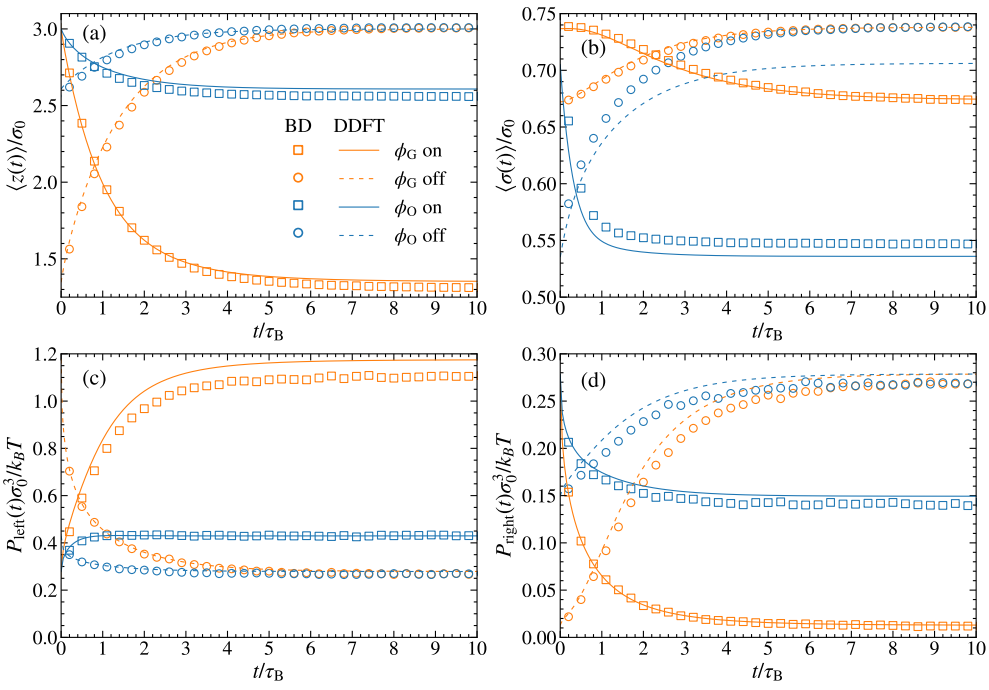

Figure II.4: Time evolution of (a) the center of mass position ($\langle z(t)\rangle$), (b) the mean particle size of the system ($\langle \sigma(t)\rangle$, with gravitational RC-DDFT data multiplied by 1.05), (c) the pressure applied by the fluid on the left wall ($P_{\text{left}}(t)$), and (d) on the right wall $P_{right}(t)$, obtained for the activation (solid lines) and deactivation (dashed lines) processes. Orange and blue colors represents the results for the gravitational and osmotic potentials, respectively. Lines denote RC-DDFT predictions, whereas symbols BD simulations. In all cases $\alpha = 0.1$ and a surface density $N/S = 1.2\sigma_0^{-2}$.

supplementary driving force induced by the activated external potential, intensifying the motion of confined colloids. Conversely, during the deactivation process, this external force is absent, resulting in colloids relying solely on diffusion for movement, thereby leading to a slower evolution towards equilibrium.

With our system's inherent two degrees of freedom, we employ a double exponential function to fit these macroscopic quantities, facilitating the extraction of time scales:

$$\psi(t) = A_1 e^{-t/\tau_1} + A_2 e^{-t/\tau_2} + c, \tag{II.25}$$

being $\psi(t) = \{\langle z(t)\rangle, \langle \sigma(t)\rangle, P_L(t), P_L(t)\}$. The relaxation times, τ_1 and τ_2, obtained from these fits, are summarized in Table II.1, presenting a comparison of the time scales predicted by RC-DDFT and observed through BD (between parenthesis) under the scenarios studied.

In every scenario, we observe two distinct time scales that are similar within

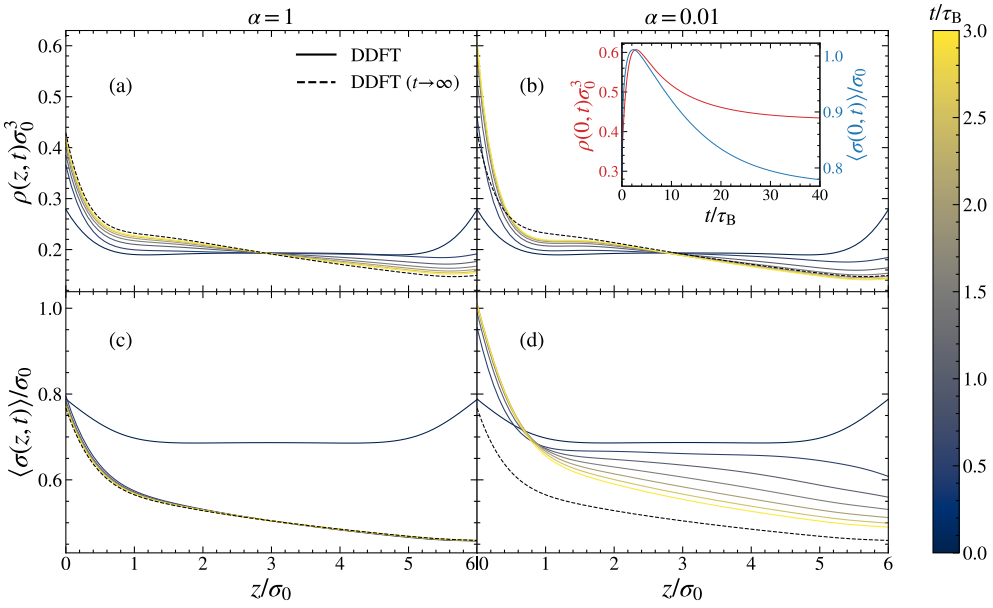

Figure II.5: RC-DDFT results for the time evolution of the system structure for the osmotic field, ϕ_{O}, being switched on at time $t = 0$ for various values of the timescale parameter α. (a), (b) Local density, $\rho(z)$, and (c), (d) local mean size, $\langle\sigma(z)\rangle$, at different times ranging from 0 τ_{B} (blue) to 3 τ_{B} (yellow) with a time interval of 0.5 τ_{B}. The surface density is $N/S = 1.2\sigma_0^{-2}$. The insert in (b) shows the time evolution of the density ρ and the mean size $\langle\sigma\rangle$ on the left wall.

each potential and across both RC-DDFT and BD analyses. This similarity suggests that the complex dynamics of the system are influenced by the interaction between translational and size diffusion processes. The differences in the shapes of macroscopic quantities for various potentials, as shown in Fig. II.4, likely arise from the differing impacts of these time scales. The close match between macroscopic quantities obtained from BD simulations and those predicted by RC-DDFT highlights the effectiveness of the RC-DDFT extension in accurately capturing the dynamics of the system. This concordance further supports the use of RC-DDFT for additional studies.

As summarized in Table II.1, the relaxation time for $\langle z(t)\rangle$ when ϕ_{O} is switched on ($0.24\tau_{\mathrm{B}}$) and off ($1.33\tau_{\mathrm{B}}$) or the relaxation time for $\langle\sigma(t)\rangle$ when ϕ_{G} is switched on ($1.08\tau_{\mathrm{B}}$) and off ($0.61\tau_{\mathrm{B}}$) is a clear signature of irreversible relaxation pathway. In addition, the difference in relaxation time for $\langle z(t)\rangle$ when switching on ϕ_{O} and ϕ_{G} reveals that the nature of the perturbation has a important effect on the relaxation process (see Fig. II.4).

Table II.1: Relaxation times obtained by fitting Eq. (II.25) to mean size, $\langle\sigma(t)\rangle$, and mean position, $\langle z(t)\rangle$ predicted by RC-DDFT during the activation (on) and deactivation (off) of the external potentials, $\phi_{\mathrm{G}}(z)$ and $\phi_{\mathrm{O}}(z,\sigma)$. The corresponding times for BD simulations are shown inside the parenthesis.

	τ	ϕ_{G} (on)	ϕ_{G} (off)	ϕ_{O} (on)	ϕ_{O} (off)
$\langle z\rangle$	τ_1	0.90 (0.91)	1.38 (1.47)	0.24 (0.25)	1.33 (1.46)
	τ_2	1.97 (1.95)	1.38 (1.47)	1.23 (1.23)	1.33 (1.46)
$\langle\sigma\rangle$	τ_1	1.08 (1.15)	0.61 (0.72)	0.30 (0.31)	0.28 (0.27)
	τ_2	1.69 (1.83)	1.50 (1.55)	1.20 (1.42)	1.48 (1.61)

II.4.4. Competition of time scales: the α-study

Having evaluated the effects of the activation and deactivation process of the external field, we now focus on the assessment of the influence of the time scale ratio, $\alpha = D_\sigma/D_0$, on the non-equilibrium relaxation dynamics of our confined system of soft RCs. As mentioned earlier, α modulates the interplay between size diffusion and translational diffusion. For such a study, we select the osmotic external potential and consider only the activation process. Fig. II.5 shows the time evolution of $\rho(z;t)$ and $\langle\sigma(z;t)\rangle$ for $\alpha = 1$ (plots (a) and (c)) and $\alpha = 0.01$ (plots (b) and (d)), representing two limiting dynamic condition for which the σ-diffusion is very fast and very slow compared to the translational diffusion. The particle surface concentration is fixed in all cases to $N/S = 1.2\sigma_0^{-2}$. Considering the close alignment between RC-DDFT and BD observed in previous sections, we only depict the results obtained with RC-DDFT.

For $\alpha = 1$, the particle size rapidly adjusts to the new environmental conditions during the initial relaxation stage, and the system approaches full structural equilibrium within $3\tau_{\mathrm{B}}$. Decreasing α to 0.01 results in a slower response of particle size to the activation of the external potential. In this regime, our findings reveal the presence of a transient dynamic state: initially, particles accumulate on the left wall for $t < 3\tau_{\mathrm{B}}$, followed by a subsequent decrease in concentration towards the final equilibrium state for $t > 3\tau_{\mathrm{B}}$. This dynamic reentrance is clearly depicted in the inset of Fig. II.5(b), illustrating the time dependence of the particle density in contact with the left hard wall, $\rho(z=0,t)$, which exhibits a maximum at $t \approx 3\tau_B$. A similar trend is observed for the mean size of colloids in contact with the left wall ($\langle\sigma(z=0,t)\rangle$), initially increasing with time before eventually decreasing again (see again the inset of Fig. II.5(b)).

It is important to highlight that this transient dynamic state observed at intermediate times arises directly from the disparity in time scales between translation and swelling, evident for $\alpha = 0.01$ and absent for $\alpha = 1$. Initially, colloids diffuse towards the left under the external field without altering their size, which evolves 100 times slower. The observed increase in $\langle\sigma(z=0,t)\rangle$ is primarily

attributed to the selective motion of larger colloids driven by the applied external force $f_{\text{ext}} = -d\phi_{\text{O}}/dz = -A\sigma^3$. Over longer timescales, compression effects lead to a gradual (slower) reduction in particle size, consequently inducing a decrease in $\rho(z = 0, t)$ until the new equilibrium state is attained. In essence, this observation signifies a transition from translationally driven to size-driven relaxation dynamics as α decreases from 1 to 0.01, a characteristic exclusive to responsive colloids.

This rich interplay between structural and size relaxation is further illustrated in Fig. II.6(a) and (b), which explore, respectively, the impact of α on the center of mass position ($\langle z(t)\rangle$) and on the mean particle size ($\langle\sigma(t)\rangle$) across a wide range of α values from 0.01 to 2. In cases where $\alpha < 0.04$, a non-monotonic curve with a pronounced minimum appears in $\langle z(t)\rangle$, signifying that responsive colloids initially migrate towards the left wall due to the applied external force before subsequently reversing direction due to gradual size reduction. Conversely, for $\alpha > 0.25$, the opposing trend is found: the particle size undergoes rapid reduction attributed to the compression induced by the osmotic field during the initial stages of evolution, yet the colloids have not traversed the necessary distance to achieve structural relaxation. For longer times, the progressive redistribution of colloids towards the left wall through spatial diffusion allows $\langle\sigma(t)\rangle$ to exhibit a slight increase, driven by the swelling of colloids near $z = 0$.

This transient behavior observed for dissimilar values of D_{T} and D_σ becomes evident in Fig. II.7, where $\langle z(t)\rangle$ is plotted against $\langle\sigma(t)\rangle$ for different values of α, from 0.01 to 3. Indeed, for $\alpha = 0.01$ we find that $\langle z(t)\rangle$ shows a dynamic reentrance induced by the slow σ-response, leading to a minimum in the curve. Conversely, for $\alpha = 3$. the curve depicts a shoulder on the left, indicating the reentrance of the center of mass location caused by the slow translational diffusion. These phenomena controlled by α demonstrate the dynamic competition between translational and size diffusion. At very low or high α values, the dynamics of mean size and position appear closely coupled, depicting a scenario where one aspect of the system's behavior must "wait" for the other to stabilize.

The fitting of mean size and mean position according to the double exponential function given by Eq. (II.25) yields relaxation times and prefactors as functions of α, as shown in Figure II.8. This analysis confirms the presence of two distinct time scales. Examining the mean position, as depicted in Fig. II.8(a), enables us to classify τ_1 as the translational relaxation time and τ_2 as the size relaxation time. Notably, τ_1 remains relatively unchanged across different values of α. In scenarios where α is high, the prefactor A_1 is always significantly larger then A_2 (please not that in this regime A_2 is very close to 0.), indicating that size adjusts swiftly, and the mean position is predominantly governed by translational relaxation. Conversely, at lower α values, the significance of A_2 elevates, taking negative values. In this regime the translational relaxation transpires swiftly following a change in size, suggesting that the mean position, $\langle z\rangle$, is driven by size adjustments. Taking a look to the relaxation

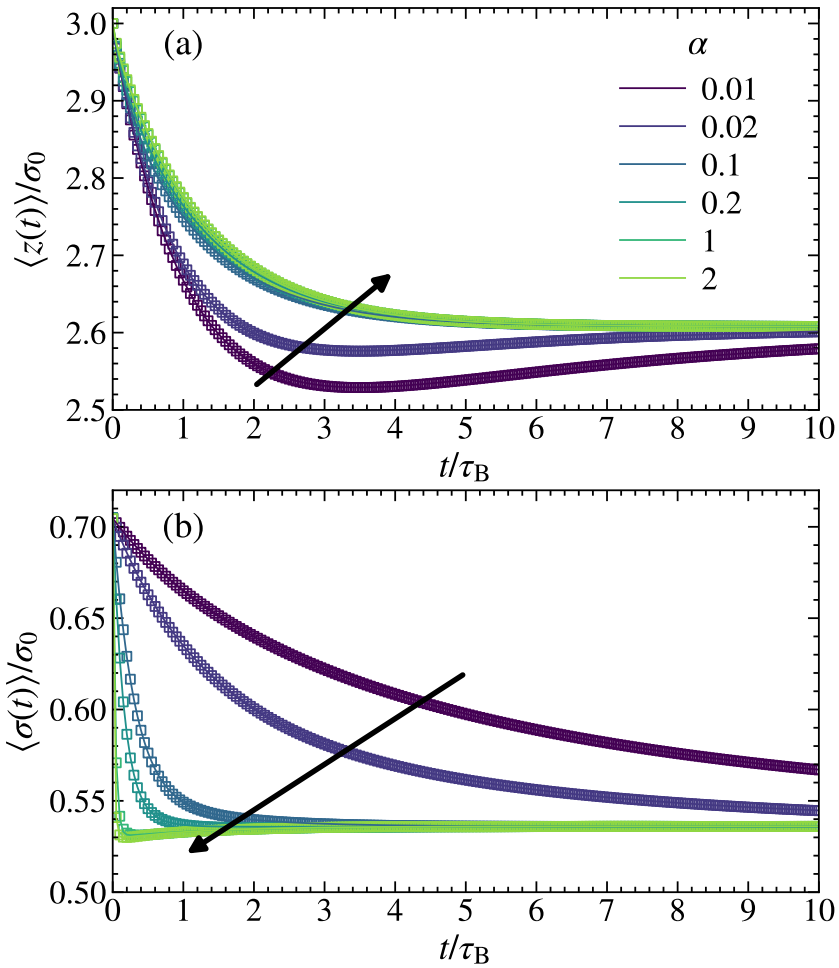

Figure II.6: Time evolution of (a) the center of mass position ($\langle z(t)\rangle$) and (b) the mean size of the colloids ($\langle\sigma(t)\rangle$) predicted by RC-DDFT (symbols) during the activation of the osmotic external potential, obtained for different values of α from 0.01 to 2. Solid lines are the result of the fitting of the data using Eq. (II.25). In all cases $N/S = 1.2\sigma_0^{-2}$.

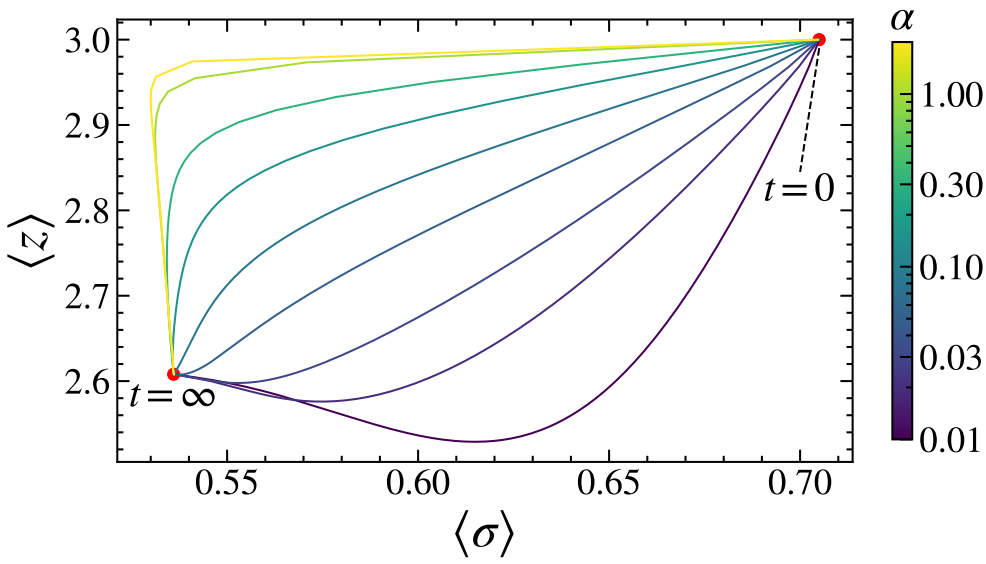

Figure II.7: Transition pathways: Center of mass location $\langle z \rangle$ versus the mean particle size $\langle \sigma \rangle$ of the system during the relaxation process after activation of the osmotic external potential, plotted for different values of α. The red point on the right-top represents the initial equilibrium state ($t = 0$), whereas the one located on the left-bottom corresponds to the new equilibrium state ($t \to \infty$). Results are obtained using RC-DDFT with $N/S = 1.2\sigma_0^{-2}$.

times of the mean size, depicted in Fig. II.8(b), we can conversely identify τ_1 as the size relaxation, since it follows a power law with α, and τ_2 as the translational or density relaxation. For high α the relaxation in size is mainly dominated by size diffusion, since $A_1 \gg A_2$.

The conspicuous discontinuities observed in Figs. II.8(a) and (b) might be interpreted, from a physical perspective, as indicative of a behavioral transition in the dynamical relaxation. Specifically, the domain characterized by high α values can be conceptualized as a conventional liquid-like phase where translational relaxation predominates as the chief mechanism. Conversely, the domain with low α values mirrors a more glassy/amorphous phase, with size relaxation emerging as the primary mechanism and a linked localized cage relaxation. This delineation hints at a fundamental shift in the system's behavior, transitioning from one dominated by translational dynamics to one where size relaxations play a more critical role.

II.5. Concluding remarks

In this work, we have developed and combined a dynamic density-functional theory (RC-DDFT) framework and Brownian dynamics (BD) simulations to

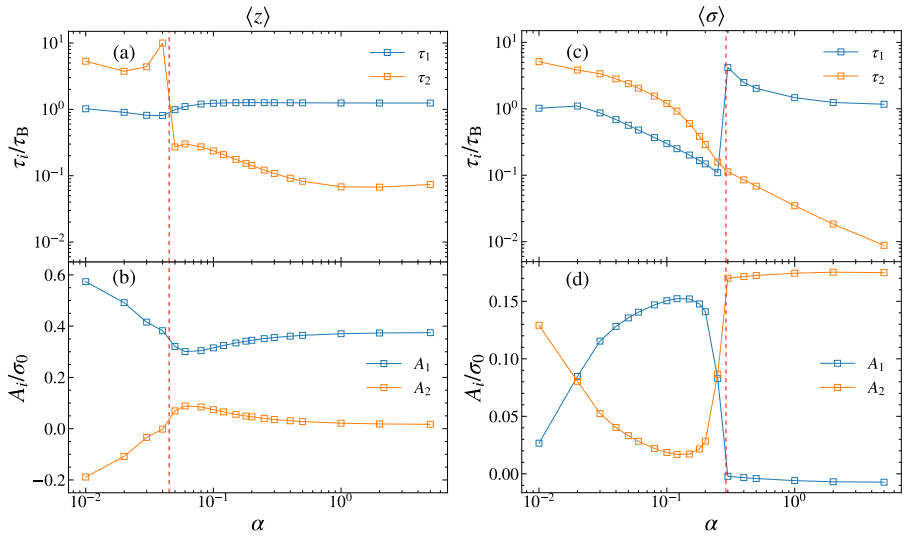

Figure II.8: Relaxation times, τ_i, and prefactors, A_i, as a function of α. They are obtained by fitting $\langle z(t)\rangle$ (plots (a) and (c)) and$\langle \sigma(t)\rangle$ (plots (b) and (d)) predicted by RC-DDFT to Eq. (II.25), during the activation process of the osmotic external potential, for $N/S = 1.2\sigma_0^{-2}$. The data corresponds to the structural time evolution shown in Figs. II.6.

investigate the full time-dependent non-equilibrium relaxation dynamics of confined systems of soft responsive colloids (RCs) after activation/deactivation of external potentials. In contrast to conventional models of soft colloids, in our model the size dynamics of the colloids is explicitly resolved and the influence of its relaxation behavior and timescale on the full system could be explored for the first time. The results showed a complex interplay between the translational diffusion and particle swelling/shrinking, leading to interesting non-equilibrium structuring as well as reentrant transient states when the typical spatial and size relaxation times scales are very different. We also demonstrated that the modification of intrinsic timescales of the system lead to tuneable macroscopic relaxation times and pathways in systems with many relaxing degrees of freedom. The excellent agreement between DDFT and BD showed that DDFT can also be faithfully used to study the nonequilibrium behavior of soft, weakly correlated colloids with additional internal degrees of freedom, if the systems are not too slaved by dissipative mechanisms [II.92]. Hence, our study constitutes a big step forward for the modeling and description of the full nonequilibrium structuring of soft complex fluids.

In future, it would be interesting to extend the RC-DDFT method to responsive (intrinsically polydisperse) systems of stiffer systems, e.g., microgels modeled by Hertizan potentials [II.7, II.40]. For these systems, we expect to find marked oscillations of the density profiles that will become strongly affected by particle stiffness. Also the dynamical properties can lead to the formation of interesting transient, e.g., highly structured while full nonequilibrium regions that finally relax

when the colloids adapt their size to the new environmental conditions. These transients may have interesting new properties. Finally, one could also envision to add more internal degrees of freedom to the colloids with a more complex hierarchy of timescales, or even add internal chemical activity to the colloids, e.g., as used in catalytically active nanoreactors where the bistable size response is crucial for complex self-dynamics [II.93].

Acknowledgements

This work was supported by the Deutsche Forschungsgemeinschaft (DFG) via the Research Unit FOR 5099 “Reducing complexity of nonequilibrium systems” and Project No. 430195928. The authors also acknowledge support by the state of Baden-Württemberg through bwHPC and the DFG through grant no INST 39/963-1 FUGG (bwForCluster NEMO). Further support was provided by grant PID2022-136540NB-I00 funded by MCIN/AEI/10.13039/501100011033, ERDF *A way of making Europe*, the Spanish Ministerio de Ciencia e Innovación, Programa Estatal de Investigación Científica, Técnica y de Innovación 2021–2023 (Project No. PID2022-136540NB-00) and program Visiting Scholars funded by the Plan Propio of the University of Granada (Project No. PPVS2018-08). J.L.M. thanks the Ph.D. student fellowship (FPU21/03568) supported by the Spanish *Ministerio de Universidades*.

Bibliography

[II.1] Martien A. Cohen Stuart, Wilhelm T. S. Huck, Jan Genzer, Marcus Müller, Christopher Ober, Manfred Stamm, Gleb B. Sukhorukov, Igal Szleifer, Vladimir V. Tsukruk, Marek Urban, Françoise Winnik, Stefan Zauscher, Igor Luzinov, and Sergiy Minko. Emerging applications of stimuli-responsive polymer materials. *Nat. Mater.*, 9(2):101–113, 2010.

[II.2] José Nelson Onuchic, Zaida Luthey-Schulten, and Peter G. Wolynes. Theory of protein folding: The energy landscape perspective. *Annu. Rev. Phys. Chem.*, 48(1):545–600, 1997.

[II.3] Chi Wu and Xiaohui Wang. Globule-to-coil transition of a single homopolymer chain in solution. *Phys. Rev. Lett.*, 80:4092–4094, May 1998.

[II.4] Samuel S. Cho, Yaakov Levy, and Peter G. Wolynes. *P* versus *Q*: Structural reaction coordinates capture protein folding on smooth landscapes. *Proc. Natl. Acad. Sci. U.S.A.*, 103(3):586–591, 2006.

[II.5] Ucheor B. Choi, James J. McCann, Keith R. Weninger, and Mark E. Bowen. Beyond the random coil: Stochastic conformational switching in intrinsically disordered proteins. *Structure*, 19(4):566 – 576, 2011.

[II.6] Alan R Denton and Matthias Schmidt. Colloid-induced polymer compression. *J. Phys.-Condes. Matter*, 14(46):12051–12062, nov 2002.

[II.7] Matthew Urich and Alan R. Denton. Swelling, structure, and phase stability of compressible microgels. *Soft Matter*, 12:9086–9094, 2016.

[II.8] J. Brijitta and P. Schurtenberger. Responsive hydrogel colloids: Structure, interactions, phase behavior, and equilibrium and nonequilibrium transitions of microgel dispersions. *Curr. Opin. Colloid Interface Sci.*, 40:87–103, 2019.

[II.9] Upayan Baul and Joachim Dzubiella. Structure and dynamics of responsive colloids with dynamical polydispersity. *J. Phys.-Condes. Matter*, 33(17):174002, apr 2021.

[II.10] Upayan Baul, Nils Göth, Michael Bley, and Joachim Dzubiella. Modulating internal transition kinetics of responsive macromolecules by collective crowding. *J. Chem. Phys.*, 155(24), 2021.

[II.11] Yi-Chen Lin, Benjamin Rotenberg, and Joachim Dzubiella. Structure and position-dependent properties of inhomogeneous suspensions of responsive colloids. *Phys. Rev. E*, 102:042602, Oct 2020.

[II.12] Harper Meng and Guoqiang Li. Reversible switching transitions of stimuli-responsive shape changing polymers. *J. Mater. Chem. A*, 1:7838–7865, 2013.

[II.13] Junhyuk Lee, Kang Hee Ku, Chan Ho Park, Young Jun Lee, Hongseok Yun, and Bumjoon J. Kim. Shape and color switchable block copolymer particles by temperature and ph dual responses. *ACS Nano*, 13(4):4230–4237, April 2019.

[II.14] Wei Kang Lim and Alan R. Denton. Polymer crowding and shape distributions in polymer-nanoparticle mixtures. *J. Chem. Phys.*, 141(11):114909, 2014.

[II.15] Wei Kang Lim and Alan R. Denton. Depletion-induced forces and crowding in polymer-nanoparticle mixtures: Role of polymer shape fluctuations and penetrability. *J. Chem. Phys.*, 144(2):024904, 2016.

[II.16] Wei Kang Lim and Alan R. Denton. Influence of polymer shape on depletion potentials and crowding in colloid–polymer mixtures. *Soft Matter*, 12:2247–2252, 2016.

[II.17] Johannes Harrer, Marcel Rey, Simone Ciarella, Hartmut Löwen, Liesbeth M. C. Janssen, and Nicolas Vogel. Stimuli-responsive behavior of pnipam microgels under interfacial confinement. *Langmuir*, 35(32):10512–10521, August 2019.

[II.18] Giovanni Del Monte and Emanuela Zaccarelli. Numerical study of neutral and charged microgel suspensions: from single-particle to collective behavior. *arXiv preprint arXiv:2404.04032*, 2024.

[II.19] Rajam Elancheliyan, Giovanni Del Monte, Edouard Chauveau, Simona Sennato, Emanuela Zaccarelli, and Domenico Truzzolillo. Role of charge content in the two-step deswelling of poly (n-isopropylacrylamide)-based microgels. *Macromolecules*, 55(17):7526–7539, 2022.

[II.20] Tyler J. Weyer and Alan R. Denton. Concentration-dependent swelling and structure of ionic microgels: simulation and theory of a coarse-grained model. *Soft Matter*, 14:4530–4540, 2018.

[II.21] Jianshu Cao and B. J. Berne. Theory and simulation of polar and nonpolar polarizable fluids. *J. Chem. Phys.*, 99(9):6998–7011, 1993.

[II.22] Daniel F Calef and Peter G Wolynes. Smoluchowski–vlasov theory of charge solvation dynamics. *J. Chem. Phys.*, 78(6):4145–4153, 1983.

[II.23] Amalendu Chandra and Biman Bagchi. Collective orientational relaxation in a dense liquid of ellipsoidal molecules. *Physica A*, 169(2):246–262, 1990.

[II.24] Amalendu Chandra and Biman Bagchi. The role of translational diffusion in the polarization relaxation in dense polar liquids. *Chem. Phys. Lett.*, 151(1-2):47–53, 1988.

[II.25] Mikhail Motornov, Roman Sheparovych, Robert Lupitskyy, Emily MacWilliams, and Sergiy Minko. Responsive colloidal systems: Reversible aggregation and fabrication of superhydrophobic surfaces. *J. Colloid Interface Sci.*, 310(2):481–488, 2007.

[II.26] Mikhail Motornov, Halyna Royter, Robert Lupitskyy, Yuri Roiter, and Sergiy Minko. Stimuli-responsive hydrogel hollow capsules by material efficient and robust cross-linking-precipitation synthesis revisited. *Langmuir*, 27(24):15305–15311, 2011.

[II.27] Kyriaki Kalaitzidou and Alfred J. Crosby. Adaptive polymer particles. *Appl. Phys. Lett.*, 93(4):041910, 2008.

[II.28] Margaret S. Cheung, Dmitri Klimov, and D. Thirumalai. Molecular crowding enhances native state stability and refolding rates of globular proteins. *Proc. Natl. Acad. Sci. U.S.A.*, 102(13):4753–4758, 2005.

[II.29] Huan-Xiang Zhou, Germán Rivas, and Allen P. Minton. Macromolecular crowding and confinement: Biochemical, biophysical, and potential physiological consequences. *Annu. Rev. Biophys.*, 37(1):375–397, 2008.

[II.30] Jiang Hong and Lila M. Gierasch. Macromolecular crowding remodels the energy landscape of a protein by favoring a more compact unfolded state. *J. Am. Chem. Soc.*, 132(30):10445–10452, August 2010.

[II.31] Nicholas F. Dupuis, Erik D. Holmstrom, and David J. Nesbitt. Molecular-crowding effects on single-molecule rna folding/unfolding thermodynamics and kinetics. *Proc. Natl. Acad. Sci. U.S.A.*, 111(23):8464–8469, 2014.

[II.32] Jaeoh Shin, Andrey G. Cherstvy, and Ralf Metzler. Kinetics of polymer looping with macromolecular crowding: effects of volume fraction and crowder size. *Soft Matter*, 11:472–488, 2015.

[II.33] Upayan Baul, Nils Götth, Michael Bley, and Joachim Dzubiella. Modulating internal transition kinetics in responsive macromolecules by collective crowding. *J. Chem. Phys.*, 155:244902, 2021.

[II.34] Shilin Huang, Kornelia Gawlitza, Regine von Klitzing, Laurent Gilson, Johannes Nowak, Stefan Odenbach, Werner Steffen, and Gu¨nter K Auernhammer. Microgels at the water/oil interface: In situ observation of structural aging and two-dimensional magnetic bead microrheology. *Langmuir*, 32(3):712–722, 2016.

[II.35] Valeria Garbin, Ian Jenkins, Talid Sinno, John C Crocker, and Kathleen J Stebe. Interactions and stress relaxation in monolayers of soft nanoparticles at fluid-fluid interfaces. *Phys. Rev. Lett.*, 114(10):108301, 2015.

[II.36] Thomas Vettorel, Gerhard Besold, and Kurt Kremer. Fluctuating soft-sphere approach to coarse-graining of polymer models. *Soft Matter*, 6:2282–2292, 2010.

[II.37] Roland G. Winkler, Dmitry A. Fedosov, and Gerhard Gompper. Dynamical and rheological properties of soft colloid suspensions. *Curr. Opin. Colloid Interface Sci.*, 19(6):594–610, 2014.

[II.38] Arturo Moncho-Jordá and Joachim Dzubiella. Swelling of ionic microgel particles in the presence of excluded-volume interactions: a density functional approach. *Phys. Chem. Chem. Phys.*, 18(7):5372–5385, 2016.

[II.39] Matthias Karg, Andrij Pich, Thomas Hellweg, Todd Hoare, L. Andrew Lyon, J. J. Crassous, Daisuke Suzuki, Rustam A. Gumerov, Stefanie Schneider, Igor. I. Potemkin, and Walter Richtering. Nanogels and microgels: From model colloids to applications, recent developments, and future trends. *Langmuir*, 35(19):6231–6255, May 2019.

[II.40] Lorenzo Rovigatti, Nicoletta Gnan, Andrea Ninarello, and Emanuela Zaccarelli. Connecting elasticity and effective interactions of neutral microgels: The validity of the hertzian model. *Macromolecules*, 52(13):4895–4906, July 2019.

[II.41] A. Scotti, S. Bochenek, M. Brugnoni, M. A. Fernandez-Rodriguez, M. F. Schulte, J. E. Houston, A. P. H. Gelissen, I. I. Potemkin, L. Isa, and W. Richtering. Exploring the colloid-to-polymer transition for ultra-low crosslinked microgels from three to two dimensions. *Nat. Commun.*, 10(1):1418, 2019.

[II.42] Andrea Scotti, Alan R. Denton, Monia Brugnoni, Judith E. Houston, Ralf Schweins, Igor I. Potemkin, and Walter Richtering. Deswelling of microgels in crowded suspensions depends on cross-link density and architecture. *Macromolecules*, 52(11):3995–4007, June 2019.

[II.43] Andrea Scotti. Characterization of the volume fraction of soft deformable microgels by means of small-angle neutron scattering with contrast variation. *Soft Matter*, 17:5548–5559, 2021.

[II.44] M.J. Murray and M.J. Snowden. The preparation, characterisation and applications of colloidal microgels. *Adv. Colloid Interface Sci.*, 54:73 – 91, 1995.

[II.45] Brian R. Saunders and Brian Vincent. Microgel particles as model colloids: Theory, properties and applications. *Adv. Colloid Interface Sci.*, 80(1):1 – 25, 1999.

[II.46] Alberto Fernandez-Nieves, Hans Wyss, Johan Mattsson, and David A Weitz. *Microgel suspensions: fundamentals and applications*. John Wiley & Sons, 2011.

[II.47] Yuanyuan Zhou, Hui Tang, and Peiyi Wu. Volume phase transition mechanism of poly [oligo (ethylene glycol) methacrylate] based thermo-responsive microgels with poly (ionic liquid) cross-linkers. *Physical Chemistry Chemical Physics*, 17(38):25525–25535, 2015.

[II.48] Steffen Bochenek, Fabrizio Camerin, Emanuela Zaccarelli, Armando Maestro, Maximilian M. Schmidt, Walter Richtering, and Andrea Scotti. In-situ study of the impact of temperature and architecture on the interfacial structure of microgels. *Nature Communications*, 13(1):3744, 2022.

[II.49] Svetoslav V. Nikolov, Alberto Fernandez-Nieves, and Alexander Alexeev. Behavior and mechanics of dense microgel suspensions. *Proc. Natl. Acad. Sci. U.S.A.*, 117(44):27096–27103, 2020.

[II.50] Nicoletta Gnan and Emanuela Zaccarelli. The microscopic role of deformation in the dynamics of soft colloids. *Nat. Phys.*, 15(7):683–688, 2019.

[II.51] Rafael Roa, Won Kyu Kim, Matej Kanduč, Joachim Dzubiella, and Stefano Angioletti-Uberti. Catalyzed bimolecular reactions in responsive nanoreactors. *ACS Catal.*, 7(9):5604–5611, September 2017.

[II.52] Rafael Roa, Stefano Angioletti-Uberti, Yan Lu, Joachim Dzubiella, Francesco Piazza, and Matthias Ballauff. Catalysis by metallic nanoparticles in solution: Thermosensitive microgels as nanoreactors. *Z. Phys. Chem.*, 232(5-6):773–803, 2018.

[II.53] Matej Kanduč, Won Kyu Kim, Rafael Roa, and Joachim Dzubiella. Modeling of stimuli-responsive nanoreactors: rational rate control towards the design of colloidal enzymes. *Mol. Syst. Des. Eng.*, 5:602–619, 2020.

[II.54] Mehrdad Hamidi, Amir Azadi, and Pedram Rafiei. Hydrogel nanoparticles in drug delivery. *Adv. Drug Deliv. Rev.*, 60(15):1638–1649, 2008. 2008 Editors' Collection.

[II.55] Brian R. Saunders, Nadiah Laajam, Emma Daly, Stephanie Teow, Xinhua Hu, and Robert Stepto. Microgels: From responsive polymer colloids to biomaterials. *Adv. Colloid Interface Sci.*, 147-148:251 – 262, 2009.

[II.56] Serguei V Vinogradov. Nanogels in the race for drug delivery. *Nanomedicine*, 5(2):165–168, 2010.

[II.57] Arturo Moncho-Jordá, Alicia Germán-Bellod, Stefano Angioletti-Uberti, Irene Adroher-Benítez, and Joachim Dzubiella. Nonequilibrium uptake kinetics of molecular cargo into hollow hydrogels tuned by electrosteric interactions. *ACS Nano*, 13(2):1603–1616, February 2019.

[II.58] Arturo Moncho-Jordá, Ana B. Jódar-Reyes, Matej Kanduč, Alicia Germán-Bellod, Juan M. López-Romero, Rafael Contreras-Cáceres, Francisco Sarabia, Miguel García-Castro, Héctor A. Pérez-Ramírez, and Gerardo Odriozola. Scaling laws in the diffusive release of neutral cargo from hollow hydrogel nanoparticles: Paclitaxel-loaded poly(4-vinylpyridine). *ACS Nano*, 14(11):15227–15240, November 2020.

[II.59] I. Pagonabarraga, M. E. Cates, and G. J. Ackland. Local size segregation in polydisperse hard sphere fluids. *Phys. Rev. Lett.*, 84:911–914, Jan 2000.

[II.60] Matteo Buzzacchi, Ignacio Pagonabarraga, and Nigel B. Wilding. Polydisperse hard spheres at a hard wall. *J. Chem. Phys.*, 121(22):11362–11373, 11 2004.

[II.61] I Pagonabarraga and ME Cates. A practical density functional for polydisperse polymers. *Europhysics Letters*, 55(3):348, 2001.

[II.62] Arturo Moncho-Jordá, Sebastien Groh, and Joachim Dzubiella. External field-driven property localization in liquids of responsive macromolecules. *J. Chem. Phys.*, 160(2):024904, 2024.

[II.63] Arturo Moncho-Jordá, Nils Göth, and Joachim Dzubiella. Liquid structure of bistable responsive macromolecules using mean-field density-functional theory. *Soft Matter*, 19(15):2832–2846, 2023.

[II.64] Michael te Vrugt, Hartmut Löwen, and Raphael Wittkowski. Classical dynamical density functional theory: from fundamentals to applications. *Adv. Phys.*, 69(2):121–247, 2020.

[II.65] Umberto Marini Bettolo Marconi and Pedro Tarazona. Dynamic density functional theory of fluids. *J. Chem. Phys.*, 110(16):8032–8044, 1999.

[II.66] Andrew J Archer and Robert Evans. Dynamical density functional theory and its application to spinodal decomposition. *J. Chem. Phys.*, 121(9):4246–4254, 2004.

[II.67] C Patrick Royall, Joachim Dzubiella, Matthias Schmidt, and Alfons van Blaaderen. Nonequilibrium sedimentation of colloids on the particle scale. *Phys. Rev. Lett.*, 98(18):188304, 2007.

[II.68] Michael te Vrugt, Hartmut Löwen, and Raphael Wittkowski. Classical dynamical density functional theory: from fundamentals to applications. *Adv. Phys.*, 69(2):121–247, 2020.

[II.69] Michael te Vrugt, Jens Bickmann, and Raphael Wittkowski. Effects of social distancing and isolation on epidemic spreading modeled via dynamical density functional theory. *Nat. Commun.*, 11(1):5576, 2020.

[II.70] Arturo Moncho-Jordá and Joachim Dzubiella. Controlling the microstructure and phase behavior of confined soft colloids by active interaction switching. *Phys. Rev. Lett.*, 125:078001, Aug 2020.

[II.71] Michael Bley, Joachim Dzubiella, and Arturo Moncho-Jordá. Active binary switching of soft colloids: stability and structural properties. *Soft Matter*, 17:7682–7696, 2021.

[II.72] Michael Bley, Pablo I. Hurtado, Joachim Dzubiella, and Arturo Moncho-Jordá. Active interaction switching controls the dynamic heterogeneity of soft colloidal dispersions. *Soft Matter*, 18:397–411, 2022.

[II.73] Eriko Sato Matsuo and Toyoichi Tanaka. Kinetics of discontinuous volume-phase transition of gels. *J. Chem. Phys.*, 89(3):1695–1703, 1988.

[II.74] A. Suzuki and H. Suzuki. Hysteretic behavior and irreversibility of polymer gels by ph change. *J. Chem. Phys.*, 103(11):4706–4710, 1995.

[II.75] Kevin W. Plaxco, Kim T. Simons, Ingo Ruczinski, and David Baker. Topology, stability, sequence, and length: Defining the determinants of two-state protein folding kinetics. *Biochemistry*, 39(37):11177–11183, 09 2000.

[II.76] Hannah K. Murnen, Alexei R. Khokhlov, Pavel G. Khalatur, Rachel A. Segalman, and Ronald N. Zuckermann. Impact of hydrophobic sequence patterning on the coil-to-globule transition of protein-like polymers. *Macromolecules*, 45(12):5229–5236, 06 2012.

[II.77] Xiangze Zeng, Kiersten M. Ruff, and Rohit V. Pappu. Competing interactions give rise to two-state behavior and switch-like transitions in charge-rich intrinsically disordered proteins. *Proc. Natl. Acad. Sci. U. S. A.*, 119(19):e2200559119, 2022.

[II.78] Ucheor B. Choi, James J. McCann, Keith R. Weninger, and Mark E. Bowen. Beyond the random coil: Stochastic conformational switching in intrinsically disordered proteins. *Structure*, 19(4):566 – 576, 2011.

[II.79] Shikha Dhiman, Ankit Jain, and Subi J. George. Transient helicity: Fuel-driven temporal control over conformational switching in a supramolecular polymer. *Angew. Chem. Int. Ed.*, 56(5):1329–1333, 2017.

[II.80] Hongsuk Kang, Philip A. Pincus, Changbong Hyeon, and D. Thirumalai. Effects of macromolecular crowding on the collapse of biopolymers. *Phys. Rev. Lett.*, 114:068303, Feb 2015.

[II.81] Arturo Moncho-Jordá, Nils Göth, and Joachim Dzubiella. Liquid structure of bistable responsive macromolecules using mean-field density-functional theory. *Soft Matter*, 19:2832–2846, 2023.

[II.82] Christos N. Likos. Effective interactions in soft condensed matter physics. *Phys. Rep.*, 348(4):267–439, 2001.

[II.83] P. G. Bolhuis, A. A. Louis, J. P. Hansen, and E. J. Meijer. Accurate effective pair potentials for polymer solutions. *J. Chem. Phys.*, 114(9):4296–4311, 03 2001.

[II.84] James Dautenhahn and Carol K. Hall. Monte carlo simulation of off-lattice polymer chains: Effective pair potentials in dilute solution. *Macromolecules*, 27(19):5399–5412, 1994.

[II.85] A. A. Louis, P. G. Bolhuis, and J. P. Hansen. Mean-field fluid behavior of the gaussian core model. *Phys. Rev. E*, 62:7961–7972, Dec 2000.

[II.86] R. Finken, J. P. Hansen, and A. A. Louis. Phase separation of penetrable core mixtures. *J. Stat. Phys.*, 110(4):1015–1037, 2003.

[II.87] A. J. Archer and R. Evans. Binary gaussian core model: Fluid-fluid phase separation and interfacial properties. *Phys. Rev. E*, 64:041501, Sep 2001.

[II.88] A J Archer. Dynamical density functional theory: binary phase-separating colloidal fluid in a cavity. *J. Phys.-Condes. Matter*, 17(10):1405–1427, feb 2005.

[II.89] A. J. Archer and R. Evans. Dynamical density functional theory and its application to spinodal decomposition. *J. Chem. Phys.*, 121(9):4246–4254, 2004.

[II.90] A J Archer, C N Likos, and R Evans. Soft-core binary fluid exhibiting a λ-line and freezing to a highly delocalized crystal. *J. Phys.-Condes. Matter*, 16(23):L297, may 2004.

[II.91] A J Archer. Dynamical density functional theory: phase separation in a cavity and the influence of symmetry. *J. Phys.-Condes. Matter*, 17(45):S3253–S3258, oct 2005.

[II.92] Matthias Schmidt. Power functional theory for many-body dynamics. *Rev. Mod. Phys.*, 94(1):015007, 2022.

[II.93] Sebastian Milster, Abeer Darwish, Nils Göth, and Joachim Dzubiella. Synergistic chemomechanical dynamics of feedback-controlled microreactors. *Phys. Rev. E*, 108(4):L042601, oct 2023.

Publication III

Diffusion and interaction effects on molecular release kinetics from collapsed microgels

Escañuela-Copado, A.[1], López-Molina, J.[1], Kanduč, M.[2], Jódar-Reyes, A. B.[1], Tirado-Miranda, M.[1], Bastos-González, D.[1], Peula-García, J.[3], Adroher-Benítez, I.[1], Moncho-Jordá, A. [1,4]

[1]*Departamento de Física Aplicada, Universidad de Granada, Campus Fuentenueva S/N, 18071 Granada, Spain*

[2]*Jožef Stefan Institute, SI-1000 Ljubljana, Slovenia*

[3]*Departamento of Física Aplicada II, Facultad de Ciencias, Universidad of Málaga, 29071 Málaga, Spain*

[4]*Institute Carlos I for Theoretical and Computational Physics, Facultad de Ciencias, Universidad de Granada, Campus Fuentenueva S/N, 18071 Granada, Spain*

Published in

ACS APPLIED POLYMER MATERIALS

ACS Applied Polymer Materials, **2024**, *6(15)*, 8905-8917.

Abstract

The efficient transport of small molecules through dense hydrogel networks is crucial for various applications, including drug delivery, biosensing, catalysis, nanofiltration, water purification, and desalination. In dense polymer matrices, such as collapsed microgels, molecular transport follows the solution-diffusion principle: Molecules dissolve in the polymeric matrix and subsequently diffuse due to a concentration gradient. Employing Dynamical Density Functional Theory (DDFT), we investigate the non-equilibrium release kinetics of non-ionic subnanometer-sized molecules from a microgel particle, using parameters derived from prior molecular simulations of a thermoresponsive hydrogel. The kinetics is primarily governed by the microgel radius and two intensive parameters: the diffusion coefficient and solvation free energy of the molecule. Our results reveal two limiting regimes: a diffusion-limited regime for large, slowly diffusing, and poorly soluble molecules within the hydrogel, and a reaction-limited regime for small, rapidly diffusing, and highly soluble molecules. These principles allow us to derive an analytical equation for release time, demonstrating excellent quantitative agreement with the DDFT results—a valuable and straightforward tool for predicting release kinetics from microgels.

III.1. Introduction

Microgels, cross-linked polymer networks of sizes ranging from hundreds of nanometers to around a micrometer, remain an active area of research in disciplines like nanotechnology [III.1], materials science [III.2], environmental sciences [III.3], and biomedical sciences [III.4]. These colloidal particles are recognized for their stimuli-responsive behavior, which is characterized by reversible volume phase transitions in response to environmental stimuli such as changes in temperature [III.5], pH [III.6], ionic strength [III.7], or solvent properties [III.8]. This unique adaptability and functional versatility enable microgels to serve in a wide range of applications, from surface coating [III.9] to optoelectronic switches [III.10]. In particular, their responsiveness to environmental changes further broadens their utility in medicine. They can act as effective containers for various molecules, such as proteins, polysaccharides, enzymes, nucleic acids and drugs, providing a foundation for advancements in drug accumulation, release, and targeted delivery [III.11, III.12, III.13]. Such capabilities underscore the significant promise of microgels in driving the evolution of drug delivery systems and further developments in nanotechnology and nanomedicine [III.14].

Poly(N-isopropylacrylamide) (PNIPAM) is one of the most extensively studied thermoresponsive polymers, mainly because it exhibits a volume transition in water from a swollen to collapsed state at temperatures closely approximating the human body temperature [III.15,III.16]. Given its versatility, PNIPAM microgels have served as fundamental model systems, paving the way for numerous advancements in the field of soft responsive materials [III.17].

The control over the uptake and release kinetics of molecules from nanoparticulate systems is crucial for realizing their full potential in a range of applications. For targeted drug delivery, the precise modulation of the kinetics is key to achieving desired therapeutic outcomes [III.18,III.19]. Properly tuned release rates can ensure consistent drug concentrations in the systemic circulation, while efficient uptake directly impacts drug loading capacity, influencing overall therapeutic efficacy. In industrial contexts, control over uptake and release kinetics can directly influence process efficiency in catalysis or chemical separation, where the kinetics can dictate reaction rates and separation performance [III.20]. When utilized as nanoreactors, the responsive network structure of microgel particles allows for modulation of the permeability of reactants, thereby determining the reaction rate [III.17, III.21]. Therefore, understanding and manipulating these kinetics is a central aspect of nanocarrier optimization, providing a solid foundation for more predictable and reliable system performance across various applications. This understanding is essential not only for the practical implementation of these systems but also for the development of accurate theoretical models.

In most of the aforementioned applications, the hydrogel matrix exhibits high

density [III.22, III.23]. In such regimes, the interplay between the molecule and the polymer matrix, as well as its transport through a densely crowded environment, becomes notably complex owing to polymer-water interactions and obstruction effects [III.24]. Many traditional size-exclusion theories fail to accurately predict the solvation free energy and, consequently, the resulting partition ratio in these scenarios. They often predict lower values for the concentration ratio of cargo within the microgel compared to its bulk concentration. Notably, the partition ratio of hydrophobic molecules (such as drugs) within the microgel can be significantly higher, sometimes exceeding theoretical predictions by several orders of magnitude [III.25, III.26]. This phenomenon has been further corroborated by atomistic computer simulations, which have shown that the calculated solvation free energies (i.e., transfer free energies from the bulk solution to the interior of a collapsed polymer gel) can be considerably negative [III.27, III.28, III.29]. This suggests a tendency for molecules to remain inside the gel.

The diffusive transport of cargo molecules across a collapsed microgel is also a complex process [III.30], intrinsically different from diffusion in simple liquids and dilute systems [III.31, III.32, III.33]. Atomistic computer simulations offer valuable insights into the behavior of molecules within dense polymer networks at a microscopic scale. Studies reveal various distributions of water molecules—either evenly dispersed [III.34] or forming clusters [III.35]. For hydrophobic collapsed PNIPAM networks, a combination of atomistic simulations [III.36, III.28] and experimental data [III.37] suggests that water molecules form disconnected, fractal-like clusters absorbed within voids created by polymeric chains. In these dense systems, where free-volume elements within the polymer network emerge due to thermal fluctuations at a similar timescale as molecule movements, the collapsed microgel functions as a non-porous membrane. Molecular transport in collapsed microgels follows a solution–diffusion mechanism [III.38]. Here, cargo molecules dissolve within the densely packed polymeric matrix and subsequently diffuse due to concentration gradients. At this level of description, these dense microgels can often be regarded as a continuum.

In this work, we make use of Dynamical Density Functional Theory (DDFT) to model the release of molecules previously encapsulated inside a collapsed microgel [III.39, III.40, III.41]. DDFT is a theoretical framework that has evolved as an effective tool for studying the dynamics of many-body systems in the field of condensed matter physics and soft matter science. This technique extends classical Density Functional Theory (DFT) to incorporate time-dependent phenomena, thereby enabling the investigation of out-of-equilibrium states.

It is important to emphasize that DDFT serves as a coarse-grained, macroscopic framework for describing non-equilibrium processes. In the context of drug release, DDFT offers insights into the spatio-temporal evolution of the density profile of molecules, $\rho(\mathbf{r}, t)$, throughout the release process. The method takes into account the

actual sterically-obstructed diffusion coefficient of the molecules inside the microgel. Furthermore, it incorporates the effects of both the microgel-molecule and molecule-molecule interactions. DDFT has been successfully applied to similar problems, namely the prediction of protein adsorption into nanoparticles [III.42, III.43] and the encapsulation/release kinetics of neutral and charged molecules in hollow microgel particles [III.44, III.29, III.45].

In the literature, various coarse-grained free energy functionals describe a cross-linked polymer network of microgels as a quenched mobile random matrix composed of hard or soft core particles. Within this matrix, molecules diffuse under the influence of an effective external potential [III.46, III.47]. However, in this work, we construct our DDFT framework following a more macroscopic description by considering the effective diffusion coefficient, D^*, and the transfer free energy, ΔG, obtained from previous atomistic molecular dynamics simulations of different neutral molecules within collapsed PNIPAM polymer networks [III.27, III.36, III.28]. Thus, although our DDFT approach is intrinsically macroscopic, it incorporates microscopic details regarding the complex interactions of the molecules with the polymer network, which may become extremely important in the case of collapsed networks.

The novelty of this work is twofold. Firstly, we demonstrate that the time evolution of the fraction of released molecules can be effectively scaled into a master curve that only depends on the half-release time, $\tau_{1/2}$. This finding suggests a potential universal behavior in the release dynamics of different molecules, indicating that $\tau_{1/2}$ alone is sufficient to fully describe the release kinetics of any molecule. Secondly, we derive an analytical expression for the half-release time, incorporating the key parameters that rule the non-equilibrium kinetics of the release process, namely the microgel radius, the solvation free energy of the cargo molecules, and their diffusion coefficients. This result not only provides a conceptual framework for understanding release kinetics but also facilitates preliminary predictions that can guide subsequent experimental work. To the best of our knowledge, such a simple yet powerful mathematical expression has not been reported in the existing literature for collapsed microgels.

This paper is organized as follows. After this introduction, we describe our Theoretical methods, detailing the model for cargo release from a collapsed microgel and explaining the theoretical framework applied in our study. In the following Results and discussion section we present our findings, exploring the release kinetics of molecular cargo from collapsed microgels solving the DDFT equation. We analyze the time-dependent density profile of cargo molecules as they diffuse through the polymer network, and discuss the time evolution of the fraction of released molecules. This is followed by a comprehensive study of the influence of the diffusion coefficient and the molecule–microgel interaction free energy on release dynamics. We also analyze the role of microgel size in the release behavior. One of the main contributions of this study is to show that, solving the stochastic differential equation for mean-

first passage time, allows the full set of results to be gathered into a single analytical expression that correctly describes the release kinetics for any particular situation. In the Conclusions section, we summarize our primary findings and discuss their broader implications.

III.2. Theoretical methods

III.2.1. Model for cargo release from a collapsed microgel

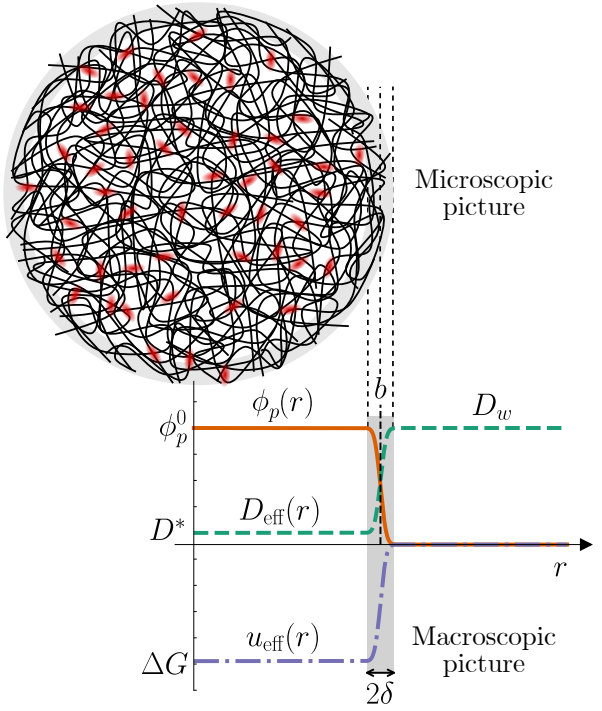

Figure III.1: Representation of a collapsed microgel of radius b with a narrow interface of width $2\delta \ll b$ carrying cargo molecules. The plot illustrates the radial dependence of the polymer volume fraction ($\phi_{\rm p}(r)$), the effective diffusion coefficient of the cargo molecule ($D_{\rm eff}(r)$), which switches from D^* inside the microgel to D_w in bulk, and the effective microgel–molecule interaction ($u_{\rm eff}(r)$), which is given by the ΔG inside the microgel and decays to 0 at the interface with the bulk.

To theoretically investigate the release of molecular cargo from a collapsed microgel, we model our system by considering a single spherical microgel particle of radius b immersed in an aqueous solution, treated as a uniform background. Fig. III.1 shows a schematic illustration of the microgel particle. Although the interior of the

particle exhibits localized fluctuations in polymer density, it is still possible to define an average local polymer volume fraction, ϕ_{p}. For a collapsed microgel, ϕ_{p} is roughly constant inside the microgel, and abruptly declines to zero at the external interface. This radial dependence can be approximated as $\phi_{\mathrm{p}}(r) = \phi_{\mathrm{p}}^0 f(r)$, with

$$f(r) = \frac{1}{2}\Big[1 - \mathrm{erf}(2(r - b - \delta)/\delta)\Big], \tag{III.1}$$

where r represents the distance to the microgel center, $\mathrm{erf}(x)$ is the error function, 2δ is the thickness of the interface and $\phi_{\mathrm{p}}^0 \approx 0.5$ is the accepted value of polymer volume fraction inside a collapsed microgel [III.48]. This functional dependence leads to the required polymer distribution: It is roughly uniform inside the microgel with $\phi_{\mathrm{p}}(r) \approx \phi_{\mathrm{p}}^0$ for $r < b$, and decays to zero near the external interface, spanning from $r = b$ to $r = b + 2\delta$. For collapsed microgels, the experimental data report a very sharp interface, with a value for the interface half-thickness of about $\delta = 1$ nm [III.48]. We will set the system temperature at 340 K, well above the lower critical solution temperature of PNIPAM, where microgel particles, composed of this thermo-responsive polymer, are in their collapsed state. This relatively high temperature was chosen to utilize parameters from a previous simulation study [III.28], where the elevated temperature facilitated the dynamics and sampling.

In the initial stage, the microgel is loaded with a certain amount of cargo molecules. Our model does not specify a particular molecule, thus making it broadly applicable to a wide range of non-ionic encapsulated entities, including chemical reactants, biomolecules, and pharmaceutical compounds. It should be noted that charged molecules may involve long-range electrostatic interactions, leading to a very different behavior. As corroborated by a recent simulation study [III.28], the size and shape of the non-ionic molecule contribute to its diffusion coefficient. We proceed under the assumption of a generic cargo molecule, characterized by a hydrodynamic (Stokes) radius a_w. This radius is determined from the diffusion coefficient of the molecule in water, D_w, using the Stokes–Einstein relation,

$$a_w = \frac{k_{\mathrm{B}}T}{6\pi\eta D_w}. \tag{III.2}$$

Here, T is the absolute temperature, k_{B} is the Boltzmann constant, and $\eta = 4.206 \times 10^{-4}$ Pa·s is the viscosity of water at $T = 340$ K.

The two key parameters that strongly control the release kinetics are the effective diffusion coefficient of the cargo molecule inside the microgel, D_{eff}, and the effective interaction between the molecule and the collapsed polymeric network, u_{eff}. On the one hand, D_{eff} determines the time the molecule needs to diffuse from the initial position inside the microgel to its external interface. This time scales as $\tau \sim l^2/D_{\mathrm{eff}}$, where l is a characteristic length of the system, included for dimensional consistency and related to the size of the microgel. On the other hand, u_{eff} represents the free

energy difference that the molecule must overcome in order to escape to the bulk solution. According to the Arrhenius law [III.49], the typical time implied by the molecule to surpass this energy barrier is expected to scale as $\exp(-u_{\text{eff}}/(k_{\text{B}}T))$. Since both quantities describe local properties of the polymer matrix, they depend on the distance to the center of the microgel, r. Given the great importance of both functions, we discuss them in detail in the following two sections.

Effective diffusion coefficient

The effective diffusion coefficient varies from inside the microgel, denoted by D^*, to the corresponding value outside (i.e., in bulk water), given by D_w. The switch between these two values at the interface is modeled as

$$D_{\text{eff}}(r) = D_w + (D^* - D_w)f(r), \tag{III.3}$$

where $f(r)$ is given by Eq. III.1. This dependence is illustrated in Fig. III.1, featuring a sharp increase at the interface.

A key feature of collapsed hydrogels is fluctuating free-volumes formed between the polymer chains, which allows the molecules to diffuse through the solution–diffusion mechanism [III.38, III.50]. Experiments [III.51, III.52] and computer simulations [III.31, III.32, III.53] on these systems have demonstrated that molecular diffusion is significantly influenced by this characteristic of the polymer network. The diffusion coefficient within such dense polymer networks can be orders of magnitude lower than in bulk water, $D^*/D_w \approx 10^{-4}$–10^{-2}, as shown by other studies [III.54, III.36]. In addition, D^* decreases exponentially with the molecule Stokes radius [III.27, III.28]:

$$D^* = D_0 e^{-a_w/\lambda}, \tag{III.4}$$

where D_0 is a reference diffusion constant and λ is a characteristic length scale that exclusively depends on the shape of the diffusing molecule. Schweizer and coworkers [III.55, III.56] have offered a theoretical explanation for the exponential relationship between D^* and the size of the molecule, grounded in the coupled dynamics in dense liquids.

It is important to emphasize that D^* for non-ionic molecules is not affected by the polymer-molecule affinity [III.28]. For instance, the value of D^* is the same for polar and non-polar cargo molecules, provided that the size and shape of both molecules are the same in both cases. This is a singular feature of collapsed polymer networks, for which the diffusion of the cargo only depends on its geometrical properties through the steric exclusion effects induced by the polymer chains [III.27, III.28]. The reason for that relies on the fact that, during a jump of the molecule inside such a dense polymer network, the coordination of its solvation shell and the number of contacts with the

surrounding polymers are not significantly altered, so the free energy change between the old and the new position is very small compared to obstruction effects caused by the local trapping, which only depends on the size and shape of the molecule [III.27, III.28].

Relative shape anisotropy

The stringent constraints imposed by a dense polymer matrix on the motion of cargo molecules lead to preferential diffusion directions dictated by the geometry of the cargo molecule. Employing a simple qualitative geometric criterion, molecules can be categorized into linear, planar, and spherical groups, as demonstrated in a previous atomistic study [III.28]. This classification was employed to examine the dynamics of the diffusion coefficient and the depth of potential barriers. It was revealed that, for molecules with the same Stokes radii (see Eq. III.2), linear molecules have the most favorable diffusion, as their shape allows easy penetration through narrow channels between polymer chains. Planar molecules, displaying intermediate diffusion efficiency, use their shape to diffuse in a sideways manner. Conversely, spherical molecules encounter the greatest difficulty during diffusion. Consequently, for a given Stokes radius, the diffusion coefficient follows the order $D^*_{\text{linear}} > D^*_{\text{planar}} > D^*_{\text{spherical}}$.

In this work, we adopt a slightly different approach using quantitative criteria to determine diffusion coefficients based on molecular shape. We compute the cargo radius of gyration tensor, $\mathbf{G}$, a method frequently used to characterize the shape of polymers [III.57]. Performing the diagonalization of the gyration tensor yields three eigenvalues, $(\alpha_1, \alpha_2, \alpha_3)$. This intuitively evokes the representation of an ellipsoidal shape, where the eigenvalues correspond to the semiaxes of the ellipsoid. To identify the molecule shape, we calculate a shape descriptor derived from the gyration tensor, called relative shape anisotropy [III.58, III.59]:

$$\kappa \equiv \frac{3}{2}\frac{\mathrm{Tr}\mathbf{G}^2}{(\mathrm{Tr}\mathbf{G})^2} = 1 - 3\frac{\alpha_1\alpha_2 + \alpha_1\alpha_3 + \alpha_2\alpha_3}{(\alpha_1 + \alpha_2 + \alpha_3)^2}, \tag{III.5}$$

which can range from 0 to 1. A linear arrangement of atoms corresponds to $\kappa = 1$, a regular planar geometry corresponds to $\kappa = 0.25$, and structures of tetrahedral symmetry or higher, such as spheres, correspond to $\kappa = 0$ [III.58]. We computed the relative shape anisotropy for each molecule in Table III.2, classifying those within a tolerance of $\Delta\kappa = 0.1$.

Fig. III.2 plots the diffusion coefficient prefactor, D_0, and decay length, λ, from Eq. III.4, as functions of the relative shape anisotropy, κ. The diffusion coefficients were taken from a previous simulation work of a collapsed PNIPAM hydrogel [III.28]. Molecules are categorized into spherical, planar, or linear groups based on their κ values, and within each group, average values $\langle D_0 \rangle$ and $\langle \lambda \rangle$ are calculated. The data

are then fitted using the following functions:

$$\lambda = m_1\kappa + n_1, \tag{III.6}$$

$$D_0 = n_2\, \mathrm{e}^{m_2\kappa}. \tag{III.7}$$

The left panel of Fig. III.2, employing a linear-log scale, reveals an exponential relationship between D_0 and κ, outlined in Eq. III.7. The right panel displays a linear correlation between λ and κ, as described by Eq. III.6. The values of the fitting parameters for each plot are compiled in Table III.1. These parameters allow us to compute D_0 and λ, and therefore the value of D^* for every non-ionic molecule by using Eq. III.4, just by computing the corresponding shape anisotropy, κ.

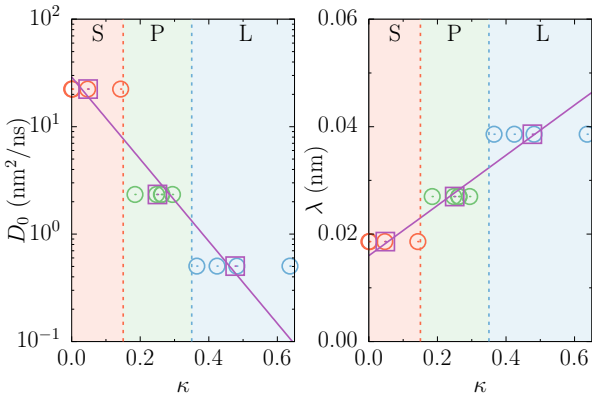

Figure III.2: Diffusion coefficient prefactor (D_0) and decay length (λ) as a function of relative shape anisotropy (κ). Each panel is divided into three sections corresponding, from left to right, to the spherical (S), planar (P), and linear (L) shapes of the molecules, respectively.

Table III.1: Numerical values for the fitting parameters obtained from the fits in Fig. III.2. Parameters (m_1, n_1) are derived from the linear fit of λ as a function of κ. Parameters (m_2, n_2) result from the linear-log fit of D_0 as a function of κ.

Fitting parameter	Value	Standard error
m_1 (nm)	0.047	0.003
n_1 (nm)	0.0160	0.0009
m_2	-8.8	1.3
n_2 (nm^2/ns)	3.37	0.39

Effective molecule-microgel interaction

Transferring the molecule from the bulk solution (water phase) into the microgel (polymer phase) is characterized by the free energy difference, ΔG. In a similar fashion as we modeled $\phi_{\mathrm{p}}(r)$ and $D^*(r)$, we assume the radial variation of the effective interaction as $u_{\mathrm{eff}}(r) = \Delta G f(r)$. In contrast to the diffusion coefficient, ΔG depends not only on the size and shape of the molecule but also on its chemical nature, particularly its polarity. Thus, the molecule's affinity to the polymer matrix is strongly influenced by its hydrophobic or hydrophilic nature. In a simple phenomenological approach, this energetic contribution scales very well with the molecule's surface area and can be written as [III.36, III.28]

$$\Delta G = \Delta G_0 + \gamma_0 4\pi a_{\mathrm{AS}}^2. \tag{III.8}$$

In the second term, $4\pi a_{\mathrm{AS}}^2$ is the solvent-accessible surface area of the molecule, expressed with an equivalent spherical radius, a_{AS}. Note that a_{AS} is strongly linked to the Stokes radius, and for a wide range of diverse molecules, it can be expressed as $a_{\mathrm{AS}} = a_w + 0.233$ nm [III.28]. The coefficient γ_0 can be interpreted as the disparity between the surface tensions of the molecule with the polymer and the molecule with water. The first term in Eq. III.8, ΔG_0, reflects the chemical nature of the molecule, correlating with the number of polar groups present within it.

We emphasize that for a specific molecule, the values of D^* and ΔG provided by Eqs. (III.4) and (III.8) are not mutually independent. Indeed, varying the size or shape of the molecule will affect both parameters. Therefore, they are interconnected for each microgel-molecule pair. However, in this work, we systematically explore different values of these two parameters, treating them as independent to understand the role of each in the release kinetics.

III.2.2. Dynamical Density Functional Theory

To investigate the non-equilibrium diffusive release of cargo molecules, we make use of classical Dynamical Density Functional Theory (DDFT) [III.39, III.40, III.60, III.41]. DDFT is a theoretical framework for the time evolution of the one-body density of a fluid. It extends the original framework of the density functional theory (DFT), which was designed for equilibrium systems [III.61, III.62, III.63, III.64], to address non-equilibrium cases. This method can be used to describe how an initial non-equilibrium density profile of molecules evolves in time in the presence of an external potential exerted by the microgel. In particular, it provides the local concentration of the cargo on position $\mathbf{r}$ at time t during the release process, $\rho_{\mathrm{c}}(\mathbf{r}, t)$, starting from an initial distribution, $\rho_{\mathrm{c}}(\mathbf{r}, 0)$.

In contrast to the usually employed diffusion equation, DDFT has three important improvements. First, the diffusion of the cargo takes into account the interaction of

Table III.2: Transfer free energies and diffusion coefficients, taken from a previous simulation work [III.28], which are investigated in this study. Molecules have been classified based on the relative shape anisotropy, as defined by Eq. III.5.

Molecule	Symbol	κ	$\beta\Delta G$	$D^*/D_w \times 10^4$
Linear				
Nitrophenol	NP	0.365102	-7.90	1.5
Pentane	Pe	0.481603	-6.22	4
Pentanol	PeOH	0.424164	-4.44	3.2
Planar				
Nitrobenzene	NB	0.294118	-7.54	3.6
Phenol	Ph	0.263224	-6.19	2.4
Benzene	B	0.247294	-4.88	3.7
Propanol	PrOH	0.261749	-2.07	6.3
Methanol	MeOH	0.184735	-0.36	27
Spherical				
Tetraclhoromethane	CCl_4	0.046486	-8.75	1.12
Neopentane	NPe	0.000002	-8.43	0.77
Ethane	Et	0.142804	-3.44	17
Methane	Me	0.002383	-1.88	71
Argon	Ar	0.000000	-1.51	135
Neon	Ne	0.000000	-0.20	810
Helium	He	0.000000	0.19	1970

the molecule with the external field exerted by the polymer network of the microgel, $u_{\text{eff}}(r)$. Second, the method also considers the position dependence of the diffusion coefficient, $D_{\text{eff}}(r)$. Indeed, this is precisely the case when the molecule travels from the interior of the microgel to the bulk solution, where the diffusion constant changes from D^* to D_w. Third, DDFT also incorporates the effect of the molecule–molecule interactions by means of the corresponding excess free energy.

Within the DDFT approach, the cargo concentration obeys the following continuity equation [III.39, III.60]:

$$\frac{\partial \rho_{\text{c}}(\mathbf{r},t)}{\partial t} = -\nabla \cdot J_{\text{c}}(\mathbf{r},t), \tag{III.9}$$

where $J_{\text{c}}(\mathbf{r},t)$ denotes the space and time-dependent diffusive current density, given by

$$J_{\text{c}} = -D_{\text{c}}(\mathbf{r})\Big[\nabla\rho_{\text{c}} + \rho_{\text{c}}\beta\nabla\big(u_{\text{eff}}(\mathbf{r}) + \mu_{\text{c}}^{\text{ex}}(\mathbf{r},t)\big)\Big], \tag{III.10}$$

where $\beta = 1/(k_{\text{B}}T)$. The excess non-equilibrium chemical potential, $\mu_{\text{c}}^{\text{ex}}(\mathbf{r},t)$,

gathers the effect of molecule–molecule interactions. In general, it is obtained from the functional derivative of the equilibrium excess free energy of the molecules [III.62, III.61]. Here, we use a simple mean-field prescription to account for excluded-volume interactions, given by the Carnahan–Starling expression [III.61]:

$$\beta\mu_{\mathrm{c}}^{\mathrm{ex}}(\mathbf{r},t) = \phi_{\mathrm{c}}(\mathbf{r},t)\frac{8-9\phi_{\mathrm{c}}(\mathbf{r},t)+3\phi_{\mathrm{c}}(\mathbf{r},t)^2}{[1-\phi_{\mathrm{c}}(\mathbf{r},t)]^3}, \tag{III.11}$$

where $\phi_{\mathrm{c}}(r,t) = \frac{4}{3}\pi a_w^3 \rho_{\mathrm{c}}(r,t)$ is the local volume fraction of molecules. We remark here that this model does not introduce attraction between molecules, which may lead to phase separation of the diffusing molecules inside the microgel. For weak attractions, this effect can be effectively included in the model by simply renormalizing ΔG [III.65, III.66].

Eqs. III.9 and III.10 have to be solved numerically for spherical symmetry. Three boundary conditions are required. The first one establishes the initial distribution of cargo molecules. In this regard, there are two possibilities for the passive release experiments. One possibility is to initially load the microgel with the cargo molecules until equilibrium is reached. After that, the supernatant is replaced by fresh solvent (e.g., pure water), so that the encapsulated molecules are in a non-equilibrium state and the release process begins. The other option is to use microgels in a lyophilized and collapsed state with the molecules trapped inside, which is a common procedure in many release experiments. When these lyophilized microgels are rehydrated by immersion in a solvent (e.g., water), the release process begins. In both scenarios, the cargo molecules are initially uniformly distributed inside the microgel particle, whereas their concentration outside the microgel is zero,

$$\rho_{\mathrm{c}}(r,t=0) = \begin{cases} \rho_{\mathrm{c}}^0 & r \le b \\ 0 & r > b \end{cases}. \tag{III.12}$$

Second, the diffusive current density in the center of the microgel must be zero due to the spherical symmetry of the system,

$$J_{\mathrm{c}}(r=0,t) = 0 \quad \forall t. \tag{III.13}$$

Finally, for a very diluted suspension of microgel particles, we can assume that the volume of the bulk solution surrounding the microgel is very large, such that the cargo concentration far away from the microgel is zero. This implies the following absorbing boundary condition:

$$\rho_{\mathrm{c}}(r\to\infty,t) = 0 \quad \forall t. \tag{III.14}$$

For practical reasons, we consider that a distance $R = 20b$ is large enough to apply this boundary condition, such that $\rho_{\mathrm{c}}(r=R,t) = 0$.

We emphasize again that, although the DDFT framework provides a macroscopic description for the diffusive release of cargo molecules, it effectively encapsulates microscopic details linked to the complex diffusion and interactions of the cargo molecule within the crowded environment of a collapsed microgel. Namely, our macroscopic description considers the microscopic complexity through parameters D^* and ΔG obtained from atomistic MD simulations (see Eqs. III.4 and III.8).

In our calculations, cargo molecules are assumed to be released to the bulk solution when they reach the outer interface of the microgel, that is, when $r > b + 2\delta$. With this prescription, the fraction of released cargo is given by

$$f_{\text{rel}}(t) = 1 - \frac{4\pi}{N_0} \int_0^{b+2\delta} r^2 \rho_{\text{c}}(r,t) \mathrm{d}r, \tag{III.15}$$

where N_0 is the number of molecules encapsulated inside the microgel in the initial state, $N_0 = \frac{4}{3}\pi b^3 \rho_{\text{c}}^0$. We define the half-release time, $\tau_{1/2}$, as the time required to release 50% of the encapsulated cargo, i.e. $f_{\text{rel}}(\tau_{1/2}) = 0.5$. As we will see later, $\tau_{1/2}$ holds immense significance as it consolidates the most pertinent details regarding the release kinetics into a singular parameter. In fact, the knowledge of the scaling $\tau_{1/2}$ with D^* and ΔG is especially of vital help to estimate extremely slow release kinetics where the integration of the DDFT equation can involve prohibitively long calculations.

In addition to $\tau_{1/2}$, we can define the mean release time of the encapsulated molecules, given by

$$\bar{\tau} = \int_0^{\infty} t \Big(\frac{\mathrm{d}f_{\text{rel}}}{\mathrm{d}t} \Big) \mathrm{d}t. \tag{III.16}$$

To solve the time-dependent DDFT differential equation, distances were scaled by $l_0 = 1$ nm, and time by $\tau_0 = l_0^2/D_w$. In order to shorten the computation time of the numerical resolution, a non-uniform spatial grid was used to sample the distance r. We used a very narrow grid size of $\Delta r_{\text{min}} = 0.02 l_0$ at the microgel interface, where the gradients of $D_{\text{eff}}(r)$ and $u_{\text{eff}}(r)$ are larger, whereas a thicker size intervals $\Delta r_{\text{min}} = 0.5 l_0$ were employed in the regions inside and outside the microgels. On the other hand, a time step of $\Delta t = 10^{-4}\tau_0$ was used in all the calculations. This value is smaller than $(\Delta r_{\text{min}})^2/(2D_0)$, thus preventing the occurrence of non-physical sawtooth instabilities.

III.3. Results and discussion

In this section, we make use of the DDFT theoretical framework described above to study the release kinetics of the molecules encapsulated within the collapsed microgel. This technique provides the time evolution of the cargo's density profiles,

enabling us to determine the fraction of released molecules and the characteristic release time. In all the cases studied here, the initial encapsulated cargo concentration contained inside the microgel is $\rho_c^0 = 0.01$ M.

III.3.1. Spatio-temporal evolution of cargo molecules

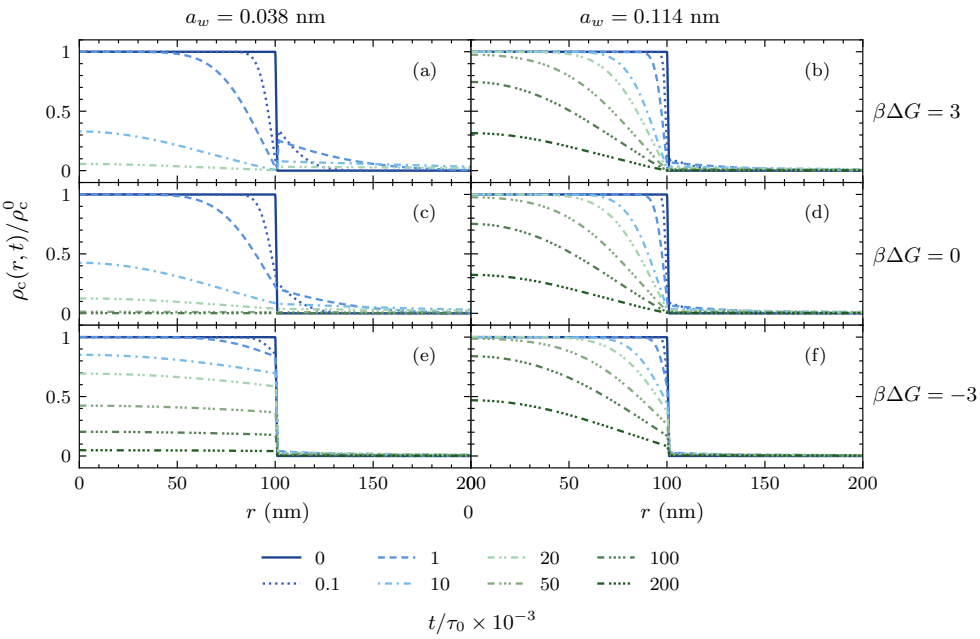

Figure III.3: Spatial evolution of the density of cargo molecules normalized by their initial density inside the microgel; different lines represent different snapshots in time. Each column depicts the results for a given diffusion coefficient (or molecular size). In panels (a), (c), and (e), the Stokes radius corresponds to that of helium, that is $a_w = 0.038$ nm. Additionally, in panels (b), (d), and (f) the cargo molecular size is restricted to the methane Stokes radius, which is $a_w = 0.114$ nm. Every row of panels represents a specific value of the potential barrier $\beta\Delta G$: (a) and (b) to $\beta\Delta G = 3$, (c) and (d) to $\beta\Delta G = 0$, and (e) and (f) to $\beta\Delta G = -3$. In all cases, the geometry of the molecule is spherical, $\rho_c^0 = 0.01$ M, and $\delta = 1$ nm.

Fig. III.3 shows the time evolution of the local density of cargo molecules normalized by the initial density inside the microgel, $\rho_c(r,t)/\rho_c^0$, for two molecular sizes and three molecule–microgel interaction free energies, covering attractive, neutral, and repulsive polymer networks ($\beta\Delta G = -3$, 0 and 3, respectively). We consider the particular case of spherical molecules ($\kappa = 0$), although similar results are found for other shapes. The results are organized so that each column represents a specific molecule size. From these graphs, it becomes clear that the larger molecules are released at a slower rate than their smaller counterparts. This inverse relation

between molecular size and release rate can be attributed to the exponential decay of the diffusion coefficient with the molecule size, a_w.

Fig. III.3 also shows the influence of various free energy values on the release process. Each row of panels corresponds to a specific value of $\beta\Delta G$. We observe that attractive microgels remarkably slow down the release process, which can be observed in the difference between concentration profiles over time when comparing $\beta\Delta G = -3$ to other potential barriers. Important differences are observed between the time-dependent density profiles in repulsive and attractive polymer networks. For repulsive networks, such as $\beta\Delta G = +3$, the cargo molecules are energetically expelled from the microgel, leading to a dynamic depletion of molecules near the microgel interface (see Fig. III.3(a) and (b)). However, when comparing these profiles with those from the no potential barrier case ($\beta\Delta G = 0$), we observe no significant differences. This indicates that a positive energy barrier has minimal impact on the release dynamics. Conversely, for attractive networks ($\beta\Delta G = -3$), molecules are retained inside the microgel because they need to overcome a free energy step-edge barrier to escape from the interior of the microgel to the bulk solution, giving rise to a more uniform distribution of molecules, especially for small cargo molecules, as seen in Fig. III.3(e).

III.3.2. Time evolution of the fraction of released molecules

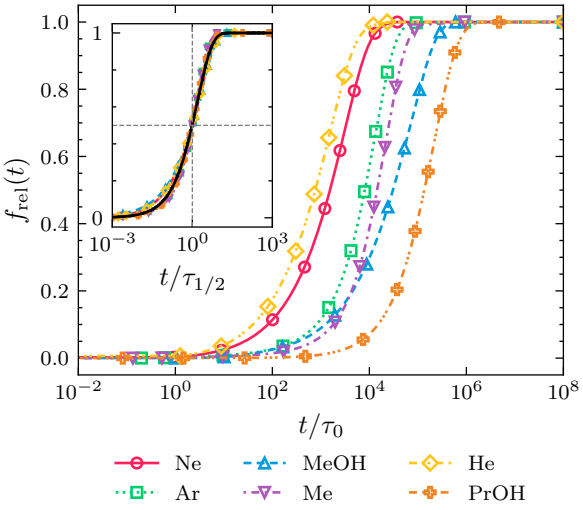

Figure III.4: Time evolution of the fraction of released cargo for different molecules. The inset represents the same dataset, with the time axis normalized by the half-release time. A reference grid helps emphasize how all the renormalized curves align at $(1, 0.5)$. In all cases, the used parameters are $\rho_c^0 = 0.01$ M, $\delta = 1$ nm, and $b = 50$ nm. The black solid line shows the fit provided by Eq. III.17.

Integrating the density profiles $\rho_c(r,t)$ in Eq. III.15 leads to the time-dependent fraction of release cargo, $f_{\text{rel}}(t)$. In Fig. III.4 we depict $f_{\text{rel}}(t)$ for a specific set of molecules, covering small and large sizes and different molecule–microgel interaction free energies. As observed, $f_{\text{rel}}(t)$ exhibits a profile consistent with a cumulative distribution function. As previously mentioned, a very important quantity that characterizes the release process is the half-release time, $\tau_{1/2}$, defined as the time at which 50% of the molecules have been released. Notably, while all the curves exhibit analogous profiles, the primary variance among them is attributed to the $\tau_{1/2}$ value, arising from the particular release dynamics of each molecule. Indeed, the curve corresponding to the diffusive release of large-sized molecules that are strongly attracted to the microgel is shifted to longer times compared to small molecules weakly attracted to the microgel, because the former ones diffuse slower and also need to surpass a higher free energy barrier to reach the bulk solution.

Normalizing the time by the respective half-release times for each molecule allows all these curves to converge into a master curve, as shown in the inset of Fig. III.4. The overlap of all of the release profiles upon this normalization suggests a potential universal feature of the release process, which is scalable across different molecular types. In addition, this scaling demonstrates that $\tau_{1/2}$ is enough to fully predict the release kinetics of any molecule. The percentage of released cargo molecules, of various shapes and sizes can be described by a common Weibull cumulative distribution function [III.67, III.68]

$$f_{\text{rel}}(t) = 1 - \exp\left[-\left(\chi t/\tau_{1/2}\right)^{\nu}\right], \tag{III.17}$$

where χ and ν are the fitting parameters controlling the shape of the function, with values $\chi = 0.64 \pm 0.04$ and $\nu = 0.79 \pm 0.13$, as determined from fitting the DDFT results. From this cumulative distribution, the mean release time of the molecules can be calculated using Eq. III.16, resulting in

$$\bar{\tau} = 1.787\tau_{1/2}. \tag{III.18}$$

III.3.3. Effect of the diffusion coefficient and molecule–microgel interaction free energy

Recognizing $\tau_{1/2}$ as the inherent time scale of the release, it becomes imperative to thoroughly explore its dependency on D^* and ΔG as the main material parameters of our system. The goal is to find an analytical expression $\tau_{1/2}(D^*, \Delta G)$ capable of universally characterizing the release kinetics of any non-ionic molecule from collapsed microgels.

Fig. III.5 illustrates how the half-release time, derived from solving the DDFT equation, correlates with the effective diffusion coefficient D^* for different ΔG values, including both repulsive and attractive interactions. For molecules with a small

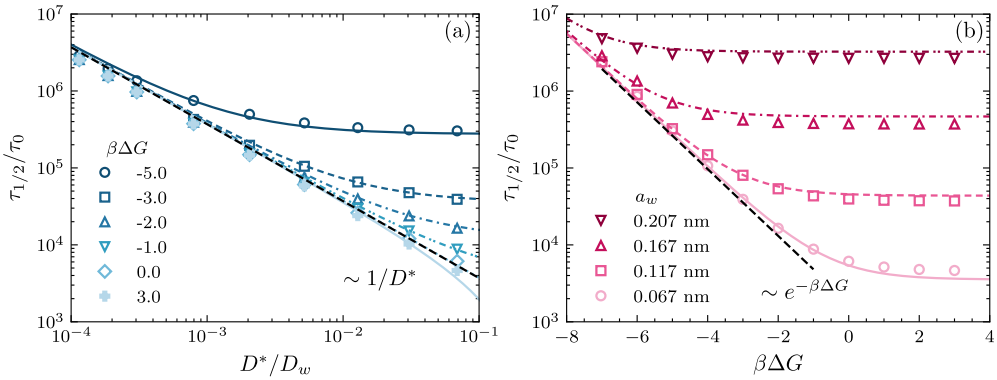

Figure III.5: Normalized half-release time as a function of the diffusion coefficient and the molecule–microgel interaction free energy. Symbols represent results obtained from DDFT, while lines correspond to theoretical predictions from Eqs. III.22 and III.23. Fig. III.5(a) displays $\tau_{1/2}/\tau_0$ plotted against the diffusion coefficient inside the microgel D^* normalized by the value in bulk, D_w, for various values of the microgel-molecule interaction free energy, $\beta\Delta G = \{-5, -3, -2, -1, 0, 3\}$. Conversely, Fig. III.5(b) illustrates $\tau_{1/2}/\tau_0$ as a function of $\beta\Delta G$ for different molecular sizes, given by $a_w = \{0.067, 0.117, 0.167, 0.208\}$ nm. For all presented cases, the molecule has a spherical geometry, with $\rho_c^0 = 0.01$ M, $b = 100$ nm, and $\delta = 1$ nm.

diffusion coefficient the release of cargo is primarily governed by diffusion. This observation aligns with well-established diffusion principles of Brownian particles, which state that the mean time to travel a fixed distance is inversely proportional to the diffusion coefficient, i.e. $\tau \sim 1/D^*$. We emphasize that, in this diffusion-limited regime, the effect of ΔG is negligible because the release kinetics are completely controlled by the time the molecules need to diffuse to the external interface of the microgel. The time to surpass the microgel interface is only a minor correction in this case. Consequently, all curves with different ΔG collapse onto a common form in this regime. The use of a normalized release time $\tau_{1/2}/\tau_0$ enhances the visibility of this collapse since it removes the dependence of the half-release time on D_w.

As D^* increases, indicative of smaller particle sizes, we observe a departure from the law $\tau_{1/2} \sim 1/D^*$ when examining attractive microgels. Indeed, beyond a certain point, the effects of negative ΔG over small cargo become significant in determining their release time. The reason for this relies on the fact that, for such fast molecules, the diffusive time inside the microgel becomes smaller. Therefore, the role played by the interaction free energy starts to be relevant, as the molecule needs to spend a significant time to overcome the step-edge free energy barrier at the microgel external surface in the case of attractive polymer networks. In other words, the molecule release becomes a reaction-limited process.

This is closely related to the dependence of the release time with the effective potential, shown as symbols in Fig. III.5(b). When considering negative values of

ΔG, we find that the release time increases as $\tau_{1/2} \sim \exp(-\beta\Delta G) = \exp(\beta|\Delta G|)$ (see black dashed line), suggesting that the release kinetics follows an Arrhenius law. However, when the free energy is positive, its effects become negligible, indicating a saturation or threshold effect, beyond which the energetic profile exerted by the microgel does not affect the release time, leading to the diffusion-limited regime, in which $\tau_{1/2}$ is independent of ΔG. In this realm of interactions, the $\tau_{1/2} \sim 1/D^*$ tendency is manifested through the logarithmic shifts for different molecular sizes (see Eq. III.4).

Clearly, the existence of these two kinetic regimes indicates the presence of two major processes involved in the release kinetics: the diffusion through the microgel and the crossing of the free energy barrier. Later, we will delve into the role of these two contributions and propose an analytical model for $\tau_{1/2}$ in terms of both physical parameters.

It is important to remark that, as indicated by Eqs. III.4 and III.8, the value of D^* and ΔG are not independent for a particular molecule. In other words, it is not possible to fix a_w (i.e., D^*) and then arbitrarily vary ΔG and vice versa. In this sense, the plots in Fig. III.5 do not precisely represent results for a particular cargo molecule. Instead, they provide general physical insights useful for understanding the overall dependence of $\tau_{1/2}$ with our model parameters.

III.3.4. Effect of the microgel size

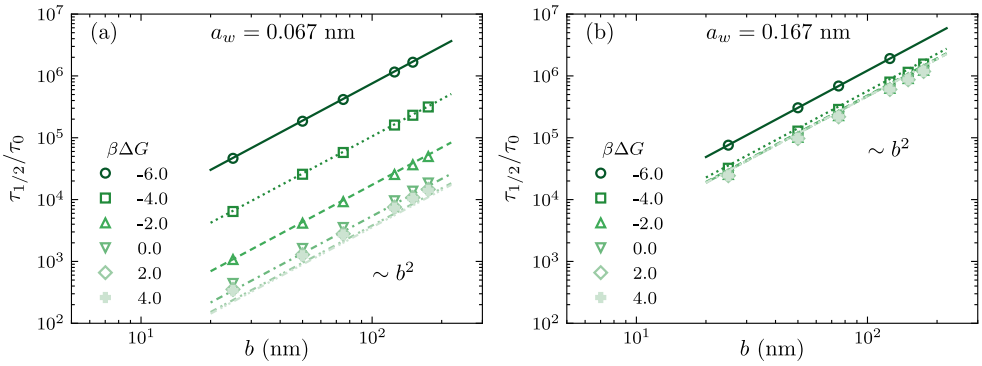

Figure III.6: Half-release time, $\tau_{1/2}$, against the radius of the microgel b. The symbols represent data obtained by numerical integration of the DDFT equations, whereas the lines correspond to the theoretical predictions given by Eqs. III.22 and III.23. The left panel (Fig. III.6(a)) displays the case in which $a_w = 0.067$ nm, a value that is identified with Neon. The right panel (Fig. III.6(b)) plots the same results, but for $a_w = 0.167$ nm. Each plot shows results for several values of $\beta\Delta G$, which extend from -6 to 4. In all cases, the geometry of the molecule is spherical, $\rho_c^0 = 0.01$ M, and $\delta = 1$ nm.

Fig. III.6 dives into the relationship between the half-release time $\tau_{1/2}$ and the

radius of the collapsed microgel, b. The data obtained for different values of a_w and ΔG (shown as symbols) reveals that there is a direct proportionality between the release time and the square of the microgel's radius, $\tau_{1/2} \sim b^2$. Clearly, a larger microgel requires a longer release time, since the encapsulated molecules have to diffuse a larger distance to reach the interface and escape to the bulk solution. This correlation is, in fact, related to a fundamental equation in diffusion studies known as the mean square displacement equation, $\langle \Delta \mathbf{r}^2 \rangle = 6Dt$. Interestingly, the square radius dependence observed for the characteristic release time of cargo molecules from dense microgels mirrors the same dependence reported for the characteristic swelling time of microgels in water [III.69, III.70]. Both phenomena—cargo release and water molecule uptake—are governed by diffusion processes. As such, our findings are consistent with previously reported behaviors in diffusion-controlled systems.

We can also appreciate the effect that different molecular sizes and free energy potential depths have on the release time. Repulsive and non-interacting microgels ($\Delta G \geq 0$) behave in somewhat the same way: the transfer free energy has a very weak effect on the release time. However, for attractive microgels ($\Delta G < 0$) the release time scales exponentially with the attraction strength, as observed in the log-scaled constant shifts of the release time in Fig. III.6(a). In addition, Fig. III.6(b) shows that the influence that cargo size has over the kinetics is to universalize the release time all across the potential range once the molecular radii become sufficiently large. That is, diffusion through the microgel becomes a matter of size and not interaction. This is something that has been already noted in Fig. III.5(a), where larger cargo shared a common $\tau_{1/2}$ regardless of the value of ΔG.

III.3.5. Analytical expression for the half-release time

In order to gather all the scaling trends into a unique analytical expression and provide a physical interpretation of the DDFT results, we calculate the mean-first passage time (MFPT), defined as the mean time that the molecules contained inside the microgel reach the bulk solution for the first time [III.71, III.72, III.73]. Since the concentration of cargo molecules considered in our DDFT calculations is low everywhere, as a first approximation the molecule–molecule interactions can be neglected, so the release process can be modeled as a diffusion problem of molecules through the effective potential induced by the microgel, $u_{\text{eff}}(r)$. In this limit, the DDFT equations simplify to the well-known Smoluchowski equation. We consider a suspension of microgels, in which each microgel occupies, on average, a volume V. This volume V is the total system volume divided by the number of microgel particles. We approximate, as in our DDFT calculations, this volume V as a sphere of radius R, such that the volume fraction of microgels in the suspension is $\varphi = (b/R)^3$. We apply an absorbing boundary condition at $r = R$, which means that the molecules that

reach this distance disappear from the system. We now turn our attention to a molecule initially located at a distance $r = s$ from the center of the microgel. We are interested in determining the average time spent by this molecule to exit the designated volume, essentially reaching the surface of the spherical cell. The derivation, shown in detail in the Appendix, leads to the following expression for the MFPT [III.72, III.73]:

$$\bar{\tau}(s) = \int_s^R \mathrm{d}r \frac{e^{\beta u_{\mathrm{eff}}(r)}}{r^2 D_{\mathrm{eff}}(r)} \int_0^r \mathrm{d}r' r'^2 e^{\beta u_{\mathrm{eff}}(r')}. \tag{III.19}$$

In order to perform the integrals and obtain an analytical expression for $\bar{\tau}(s)$, we approximate the interface of the microgel as a sharp boundary, such that $u_{\mathrm{eff}}(r) = \Delta G$ for $r \leq b$, and $u_{\mathrm{eff}}(r) = 0$ for $r > b$. Analogously, the effective diffusion coefficient is simplified to $D_{\mathrm{eff}}(r) = D^*$ for $r \leq b$ and $D_{\mathrm{eff}}(r) = D_w$ for $r > b$. Both assumptions are fully justified since collapsed microgels have a very narrow interface. With all these simplifications, we find the MFPT of a molecule located at $r = s$ as

$$\bar{\tau}(s) = \frac{b^2 - s^2}{6D^*} + \frac{b^3}{3D_w}\Big(\frac{1}{b} - \frac{1}{R}\Big)(e^{-\beta\Delta G} - 1) + \frac{R^2 - b^2}{6D_w}. \tag{III.20}$$

To calculate the average MFPT of all the encapsulated molecules, we have to perform a second averaging, accounting for the uniform distribution of molecules within the microgel in the initial stage, so $\bar{\tau} = \int_0^b s^2 \bar{\tau}(s)\mathrm{d}s / \int_0^b s^2 \mathrm{d}s$, leading to

$$\bar{\tau} = \frac{b^2}{15D^*} + \frac{b^3}{3D_w}\Big(\frac{1}{b} - \frac{1}{R}\Big)(e^{-\beta\Delta G} - 1) + \frac{R^2 - b^2}{6D_w}. \tag{III.21}$$

Each term on the right-hand side of Eq. III.21 has a clear interpretation. The first term is the average time of diffusion of the molecules inside the microgel to reach the microgel interface at $r = b$. The second term represents the time to overcome the free energy well ΔG. Finally, the third term is the time spent by the molecules to diffuse from $r = b$ to reach the bulk at $r = R$.

For the comparison between this theoretical prediction and the DDFT calculations we only need to retain the first two terms of Eq. III.21, as they provide the time spent by the molecules to escape outside the microgel. Then, taking a very diluted suspension of microgels ($R \gg b$) we obtain the MFPT for the molecules to escape from the microgel:

$$\bar{\tau} = \frac{b^2}{15D^*} + \frac{b^2}{3D_w}(e^{-\beta\Delta G} - 1). \tag{III.22}$$

Finally, the corresponding half release time will be given by

$$\tau_{1/2} = \bar{\tau}/1.787. \tag{III.23}$$

Eq. III.22 gathers all the expected scalings of the release time with b, D^*, and ΔG. Our equation aims to capture the intricate dynamics involved in the release kinetics

of molecular cargo from collapsed microgels. This formula includes two terms that highlight the two fundamental forces at play. The first term mirrors the influence of pure diffusion on the release kinetics. This term embodies the classic principles of diffusive transport, suggesting that the larger the microgel, the longer the release time, while faster diffusion coefficients lead to shorter release times. The second term introduces the influence of the free energy profile of the microgel-cargo system.

As observed in Fig. III.5 and III.6, the analytical estimate given by Eq. III.22, represented by lines, demonstrates remarkable predictive accuracy across diverse conditions in our study. Particularly, this finding enables us to predict the release of cargo $f_{\mathrm{rel}}(t)$ portrayed in Fig. III.4 by fusing Eq. III.17 with Eq. III.22. Consequently, the fraction of released cargo can be accurately solved at any given time upon knowing the diffusion coefficient, the interaction microgel-molecule interaction free energy, and the radius of the microgel. We believe that this equation presents a powerful tool for researchers. It not only offers a conceptual framework for contemplating release kinetics but also provides a way for making preliminary predictions that can be refined using experimental data. We also believe that the equation can serve as a catalyst for further advancements in the field, fostering a more profound understanding of microgel behavior and potentially contributing to progress in applications such as drug delivery systems.

III.4. Conclusions

In this study, we have methodically elucidated the non-equilibrium diffusive release kinetics of small molecules from spherical microgel particles, extending our understanding from insights gained in previous all-atom simulation studies involving subnanometer-sized molecules within collapsed PNIPAM polymers in water. Molecular geometry emerged as a defining factor influencing the preferred directions of molecular motion, with linearly-shaped molecules demonstrating more efficient transport through the microgel compared to their spherical counterparts. We employed Dynamical Density Functional Theory to integrate the properties of transport molecules into a robust theoretical framework for evaluating the release kinetics from a spherical microgel particle. Notably, we have uncovered a universal behavior in the release dynamics of different molecules, characterized by a single parameter: the half-release time, $\tau_{1/2}$. This parameter incorporates all the essential system parameters: the diffusion coefficient within the polymer network, D^*, and in water, D_w, the interaction free energy of the molecule with the microgel, ΔG, as well as the microgel radius, b.

Finally, we have unified these key variables into a single analytical expression for $\tau_{1/2}$ (given by Eq. III.22), which has demonstrated excellent agreement with our DDFT calculations. The formula provides a comprehensive understanding of

the physics governing the release kinetics. The release process manifests into two distinct limiting regimes: For large, slowly diffusing, and poorly soluble molecules within the hydrogel (exhibiting large ΔG), the diffusion-limited regime prevails, where the release time inversely scales with their diffusion coefficient within the gel ($\tau_{1/2} \sim b^2/D^*$). Conversely, small, rapidly diffusing, and highly soluble molecules (with small or negative ΔG) tend toward the reaction-limited regime. In this scenario, the bottleneck becomes the overcoming of the free-energy step-edge barrier to escape the microgel, resulting in the release time scaling exponentially with the free energy ($\tau_{1/2} \sim b^2 \exp(-\Delta G/k_{\mathrm{B}}T)$). In both cases, the relationship between the microgel particle size and $\tau_{1/2}$ strictly adheres to a well-known power law ($\tau_{1/2} \sim b^2$).

To the best of our knowledge, the simple mathematical expression for the release time (Eq. III.22) has not been previously reported in the literature. Notably, the theoretical framework we employed is applicable not only to microgels but also to a wider range of hydrogel structures and other porous materials. Assuming that the diffusion coefficient and the interaction free energy between the molecule and the polymer network are known, the diffusion-solution principles at the macroscopic level remain applicable. While we specifically designed the model for PNIPAM microgels in their collapsed state, our theory has a broader scope, particularly for particles with clearly defined and sharp interfaces.

However, it is important to note the limitations of our current model. In this regard, while the absorbing boundary condition is appropriate for very dilute solutions, we acknowledge that for more concentrated suspensions and longer times, reflective boundaries are more accurate. Indeed, for a non-dilute suspension of microgel particles, the final equilibrium concentration of cargo molecules in bulk tends to a non-zero constant value, which is achieved by imposing reflective boundary conditions at the external boundary of the spherical cell ($r = R$). In this case, the release kinetics becomes strongly dependent on the microgel volume fraction, adding an additional parameter to consider in the analysis. As many experiments and applications of drug release are performed under highly diluted conditions, the correction introduced by the reflective boundary conditions only affects the very late stages of the release process, leaving the estimate of the half-release time almost unaffected. The study of release kinetics in concentrated microgel suspensions is out of the scope of this paper and will be part of our future work.

Despite this limitation, our research provides valuable insights and establishes a foundation for further studies. We aim to explore the release kinetics from swollen microgels in our future work, anticipating differences in diffusion compared to collapsed states. Ultimately, our goal is to develop a comprehensive theoretical framework capable of predicting cargo diffusion within microgel particles in various swelling conditions.

III.5. Appendix. Calculation of the mean first passage time

In the limit of negligible molecule–molecule interactions, the DDFT formalism converges to the Smoluchowski equation for the time-dependent probability density, $\rho(\mathbf{r},t)$, defined as the probability density of finding a Brownian particle (molecule) at position $\mathbf{r}$ at time t [III.72, III.73]

$$\frac{\partial \rho}{\partial t} = \nabla \cdot \left[D(\mathbf{r}) \nabla \rho + D(\mathbf{r}) \rho \beta \nabla u(\mathbf{r}) \right], \tag{III.24}$$

where $D(\mathbf{r})$ is the position-dependent diffusion coefficient and $u(\mathbf{r})$ is the external interaction potential acting on the Brownian molecules. If at time $t = 0$ the molecules are localized in a very small region at position $\mathbf{r}$, the probability density can be denoted as $\rho(\mathbf{r}', t|\mathbf{r}, 0)$, which satisfies the initial condition $\rho(\mathbf{r}', 0|\mathbf{r}, 0) = \delta(\mathbf{r} - \mathbf{r}')$.

We assume that the molecules are contained within a volume V. The molecules can escape from this volume by reaching its surface Σ. This means that the system has an absorbing surface, with $\rho(\mathbf{r} \in \Sigma, t)$. The probability that a given molecule initially located at position $\mathbf{r}$ inside V at $t = 0$ escapes outside this volume at time t will be denoted by $W(r,t)$, given by

$$W(\mathbf{r},t) = 1 - \int_V \rho(\mathbf{r}', t|\mathbf{r}, 0) \mathrm{d}\mathbf{r}'. \tag{III.25}$$

This new function W satisfies several conditions. On the one hand, if the point $\mathbf{r}$ is located at the surface of V, then $W(\mathbf{r},t) = 1$. On the other hand, if $\mathbf{r}$ is a point inside of V, then $W(\mathbf{r},0) = 0$ and $W(\mathbf{r},\infty) = 1$. $W(\mathbf{r},t)$ obeys the following partial differential equation [III.72, III.73]:

$$\frac{\partial W}{\partial t} = \nabla \cdot \left[D(\mathbf{r}) \nabla W \right] - D(\mathbf{r}) \beta \nabla u(\mathbf{r}) \cdot \nabla W. \tag{III.26}$$

The probability that a molecule located at $\mathbf{r}$ at time $t = 0$ arrives at the surface of the volume and escapes outside between t and $t + \mathrm{d}t$ is

$$W(\mathbf{r}, t + \mathrm{d}t) - W(\mathbf{r},t) = \frac{\partial W(\mathbf{r},t)}{\partial t} \mathrm{d}t. \tag{III.27}$$

Therefore, the average time for a molecule located at $\mathbf{r}$ at time $t = 0$ to arrive at the surface is given by the following integral,

$$\bar{\tau}(\mathbf{r}) = \int_0^\infty t \frac{\partial W(\mathbf{r},t)}{\partial t} \mathrm{d}t. \tag{III.28}$$

This is precisely the so-called mean first passage time (MFPT). We can deduce the differential equation that satisfies the MFPT by applying a second-time derivative in Eq. III.26, multiplying by t and then integrating over t:

$$\int_0^\infty t\frac{\partial^2 W}{\partial t^2}\mathrm{d}t = \nabla\cdot\left[D(\mathbf{r})\nabla\bar{\tau}(\mathbf{r})\right] - D(\mathbf{r})\beta\nabla u(\mathbf{r})\cdot\nabla\bar{\tau}(\mathbf{r}). \tag{III.29}$$

Integrating by parts the left-hand side of this equation leads to

$$\begin{aligned}\int_0^\infty t\frac{\partial^2 W}{\partial t^2}\mathrm{d}t &= t\frac{\partial W}{\partial t}\bigg|_0^\infty - \int_0^\infty \frac{\partial W}{\partial t}\mathrm{d}t \\ &= W(\mathbf{r},0) - W(\mathbf{r},\infty) = -1.\end{aligned} \tag{III.30}$$

The resulting differential equation for the MFPT is

$$\nabla\cdot\left[D(\mathbf{r})\nabla\bar{\tau}(\mathbf{r})\right] - D(\mathbf{r})\beta\nabla u(\mathbf{r})\cdot\nabla\bar{\tau}(\mathbf{r}) = -1. \tag{III.31}$$

Rewriting this equation to the particular case of the spherical geometry, with the volume V representing a sphere of radius R, we obtain

$$\frac{1}{r^2}\frac{\mathrm{d}}{\mathrm{d}r}\left[r^2 D(r)\frac{\mathrm{d}\bar{\tau}}{\mathrm{d}r}\right] - D(r)\frac{\mathrm{d}(\beta u)}{\mathrm{d}r}\frac{\mathrm{d}\bar{\tau}}{\mathrm{d}r} = -1, \tag{III.32}$$

which can be expressed as

$$\frac{\mathrm{d}}{\mathrm{d}r}\left[r^2 D(r)e^{-\beta u(r)}\frac{\mathrm{d}\bar{\tau}}{\mathrm{d}r}\right] = -r^2 e^{-\beta u(r)}. \tag{III.33}$$

This differential equation can be integrated analytically, using the fact that the MFPT is finite for any point within the volume V, and equals zero if the molecule is located at the external surface of radius R, $\bar{\tau}(r=R)=0$. Performing the first integration gives

$$\frac{\mathrm{d}\bar{\tau}}{\mathrm{d}r} = -\frac{e^{\beta u(r)}}{r^2 D(r)}\int_0^r \mathrm{d}r' r'^2 e^{-\beta u(r')}. \tag{III.34}$$

Finally, the MFPT for a molecule located at a distance $r=s$ from the center of spherical volume is obtained through the second integration

$$\bar{\tau}(s) = \int_s^R \mathrm{d}r\frac{e^{\beta u(r)}}{r^2 D(r)}\int_0^r r'^2 e^{-\beta u(r')}\mathrm{d}r'. \tag{III.35}$$

Acknowledgements

The authors thank the financial support provided by *Junta de Andalucía* and European Regional Development Fund - *Consejería de Conocimiento, Investigación*

y Universidad, Junta de Andalucía (Projects PY20-00241, A-FQM-90-UGR20) and the Spanish *Ministerio de Ciencia e Innovación, Plan Estatal de Investigación Científica, Técnica y de Innovación* (Project PID2022-136540NB-I00). I.A.B. acknowledges grant A-EXP-359-UGR23 funded by *Consejería de Universidad, Investigación e Innovación* and by ERDF Andalusia Program 2021-2027, grant María Zambrano funded by MCIN/AEI and NextGenerationEU/PRTR, and the Precompetitive Research Projects Program of the UGR Research Plan (PPJIA2022-46). J.L.M. thanks the Ph.D. student fellowship (FPU21/03568) funded by *Gobierno de España, Ministerio de Universidades*. M.K. acknowledges financial support from the Slovenian Research and Innovation Agency ARIS (contracts P1-0055 and J1-4382). Finally, we thank Prof. Gerardo Odriozola (UAM, México City) for inspiring discussions and useful comments, and the computational resources and assistance provided by PROTEUS, the supercomputing center of Institute Carlos I for Theoretical and Computational Physics at the University of Granada, Spain.

Author Contributions

A.E.C. and J.L.M. contributed equally to the investigation, formal analysis, methodology, visualization, and writing of the manuscript. M.K. was responsible for conceptualization, methodology, resources, software, validation, and editing of the draft. A.B.J.R., M.T.M., J.M.P.G. and D.B.G. contributed to the conceptualization, funding acquisition, resources, validation and editing of the draft. I.A.B. contributed to the formal analysis, methodology, supervision, and writing and editing of the manuscript. A.M.J. was responsible for conceptualization, formal analysis, funding acquisition, project administration, resources, software, supervision, and writing and editing of the manuscript.

Bibliography

[III.1] Shuang Wu, Joachim Dzubiella, Julian Kaiser, Markus Drechsler, Xuhong Guo, Matthias Ballauff, and Yan Lu. Thermosensitive au-pnipa yolk–shell nanoparticles with tunable selectivity for catalysis. *Angew. Chem. - Int. Ed.*, 51(9):2229–2233, 2012.

[III.2] Jian-Tao Zhang, Gang Wei, Thomas F. Keller, Hilary Gallagher, Christian Stötzel, Frank A. Müller, Michael Gottschaldt, Ulrich S. Schubert, and Klaus D. Jandt. Responsive hybrid polymeric/metallic nanoparticles for catalytic applications. *Macromol. Mater. Eng.*, 295(11):1049–1057, 2010.

[III.3] Deepika Parasuraman and Michael J. Serpe. Poly (n-isopropylacrylamide) microgel-based assemblies for organic dye removal from water. *ACS Appl. Mater. Interfaces*, 3(12):4714–4721, 2011.

[III.4] Rakesh Banerjee, Sheetal Parida, Chiranjit Maiti, Mahitosh Mandal, and Dibakar Dhara. ph-degradable and thermoresponsive water-soluble core cross-linked polymeric nanoparticles as potential drug delivery vehicle for doxorubicin. *RSC Adv.*, 5:83565–83575, 2015.

[III.5] Tao Ding and Jeremy J. Baumberg. Thermo-responsive plasmonic systems: Old materials with new applications. *Nanoscale Adv.*, 2:1410–1416, 2020.

[III.6] G. Kocak, C. Tuncer, and V. Bütün. ph-responsive polymers. *Polym. Chem.*, 8:144–176, 2017.

[III.7] Xiao-Qiao Wang, Shengyang Yang, Cai-Feng Wang, Li Chen, and Su Chen. Multifunctional hydrogels with temperature, ion, and magnetocaloric stimuli-responsive performances. *Macromol. Rapid Commun.*, 37(9):759–768, 2016.

[III.8] Maddalena Bertolla, Lucia Cenci, Andrea Anesi, Emmanuele Ambrosi, Franco Tagliaro, Lia Vanzetti, Graziano Guella, and Alessandra Maria Bossi.

Solvent-responsive molecularly imprinted nanogels for targeted protein analysis in maldi-tof mass spectrometry. *ACS Appl. Mater. Inter.*, 9(8):6908–6915, March 2017.

[III.9] Kunlin Chen, Shuxue Zhou, and Limin Wu. Self-healing underwater superoleophobic and antibiofouling coatings based on the assembly of hierarchical microgel spheres. *ACS Nano*, 10(1):1386–1394, January 2016.

[III.10] Chotiros Dokkhan, Muhamad Z. Mokhtar, Qian Chen, Brian R. Saunders, Nigel W. Hodson, and Bruce Hamilton. Using microgels to control the morphology and optoelectronic properties of hybrid organic–inorganic perovskite films. *Phys. Chem. Chem. Phys.*, 20:27959–27969, 2018.

[III.11] Veronika Kozlovskaya, Jenolyn F. Alexander, Yun Wang, Thomas Kuncewicz, Xuewu Liu, Biana Godin, and Eugenia Kharlampieva. Internalization of red blood cell-mimicking hydrogel capsules with ph-triggered shape responses. *ACS Nano*, 8(6):5725–5737, June 2014.

[III.12] James McMasters, Scott Poh, Jenny B. Lin, and Alyssa Panitch. Delivery of anti-inflammatory peptides from hollow pegylated poly(nipam) nanoparticles reduces inflammation in an ex vivo osteoarthritis model. *J. Controlled Release*, 258:161 – 170, 2017.

[III.13] Yue Qiao, Jian He, Weiyu Chen, Yinhui Yu, Wanlin Li, Zhen Du, Tingting Xie, Yang Ye, Shi Yuan Hua, Danni Zhong, Ke Yao, and Min Zhou. Light-activatable synergistic therapy of drug-resistant bacteria-infected cutaneous chronic wounds and nonhealing keratitis by cupriferous hollow nanoshells. *ACS Nano*, 14(3):3299–3315, March 2020.

[III.14] Takuma Kureha and Daisuke Suzuki. Nanocomposite microgels for the selective separation of halogen compounds from aqueous solution. *Langmuir*, 34(3):837–846, 2018.

[III.15] Robert Pelton. Temperature-sensitive aqueous microgels. *Adv. Colloid Interface Sci.*, 85(1):1–33, 2000.

[III.16] Avraham Halperin, Martin Kröger, and Françoise M. Winnik. Poly(n-isopropylacrylamide) phase diagrams: Fifty years of research. *Angew. Chem. - Int. Ed.*, 54(51):15342–15367, 2015.

[III.17] Yan Lu, Yu Mei, Markus Drechsler, and Matthias Ballauff. Thermosensitive core–shell particles as carriers for ag nanoparticles: Modulating the catalytic activity by a phase transition in networks. *Angew. Chem. - Int. Ed.*, 45(5):813–816, 2006.

[III.18] Allan S. Hoffman. Applications of thermally reversible polymers and hydrogels in therapeutics and diagnostics. *J. Control. Release*, 6(1):297–305, 1987.

[III.19] S. H. Gehrke, J. P. Fisher, M. Palasis, and M. E. Lund. Factors determining hydrogel permeability. *Ann. New York Acad. Sci.*, 831:179–207, 1997.

[III.20] Pablo Hervés, Moisés Pérez-Lorenzo, Luis M. Liz-Marzán, Joachim Dzubiella, Yan Lu, and Matthias Ballauff. Catalysis by metallic nanoparticles in aqueous solution: Model reactions. *Chem. Soc. Rev.*, 41:5577–5587, 2012.

[III.21] Rafael Roa, Won Kyu Kim, Matej Kanduč, Joachim Dzubiella, and Stefano Angioletti-Uberti. Catalyzed bimolecular reactions in responsive nanoreactors. *ACS Catal.*, 7(9):5604–5611, September 2017.

[III.22] Tsai-Wei Lin and Charles E Sing. Effect of penetrant–polymer interactions and shape on the motion of molecular penetrants in dense polymer networks. *J. Chem. Phys.*, 160(11), 2024.

[III.23] Tsai-Wei Lin, Baicheng Mei, Kenneth S Schweizer, and Charles E Sing. Simulation study of the effects of polymer network dynamics and mesh confinement on the diffusion and structural relaxation of penetrants. *J. Chem. Phys.*, 159(1), 2023.

[III.24] Edward W. Merrill, Kathleen A. Dennison, and Cynthia Sung. Partitioning and diffusion of solutes in hydrogels of poly(ethylene oxide). *Biomaterials*, 14(15):1117–1126, 1993.

[III.25] Maria Palasis and Stevin H. Gehrke. Permeability of responsive poly (n-isopropylacrylamide) gel to solutes. *Journal of Controlled Release*, 18(1):1 – 11, 1992.

[III.26] M.A. Molina, C.R. Rivarola, and C.A. Barbero. Study on partition and release of molecules in superabsorbent thermosensitive nanocomposites. *Polymer*, 53(2):445–453, 2012.

[III.27] Matej Kanduc, Won Kyu Kim, Rafael Roa, and Joachim Dzubiella. Selective molecular transport in thermoresponsive polymer membranes: Role of nanoscale hydration and fluctuations. *Macromolecules*, 51(13):4853–4864, 2018.

[III.28] Matej Kanduč, Won Kyu Kim, Rafael Roa, and Joachim Dzubiella. How the shape and chemistry of molecular penetrants control responsive hydrogel permeability. *ACS Nano*, 15(1):614–624, 2021.

[III.29] Arturo Moncho-Jordá, Ana B. Jódar-Reyes, Matej Kanduč, Alicia Germán-Bellod, Juan M. López-Romero, Rafael Contreras-Cáceres, Francisco

Sarabia, Miguel García-Castro, Héctor A. Pérez-Ramírez, and Gerardo Odriozola. Scaling laws in the diffusive release of neutral cargo from hollow hydrogel nanoparticles: Paclitaxel-loaded poly(4-vinylpyridine). *ACS Nano*, 14(11):15227–15240, 2020.

[III.30] Florian Müller-Plathe. Diffusion of water in swollen poly(vinyl alcohol) membranes studied by molecular dynamics simulation. *J. Membr. Sci.*, 141(2):147–154, 1998.

[III.31] Hisao Takeuchi. A jump motion of small molecules in glassy polymers: A molecular dynamics simulation. *J. Chem. Phys.*, 93(3):2062–2067, 08 1990.

[III.32] Florian Müller-Plathe. Diffusion of penetrants in amorphous polymers: A molecular dynamics study. *J. Chem. Phys.*, 94(4):3192–3199, 02 1991.

[III.33] Baicheng Mei and Kenneth S Schweizer. Penetrant shape effects on activated dynamics and selectivity in polymer melts and networks based on self-consistent cooperative hopping theory. *Soft Matter*, 19(45):8744–8763, 2023.

[III.34] G.E. Karlsson, U.W. Gedde, and M.S. Hedenqvist. Molecular dynamics simulation of oxygen diffusion in dry and water-containing poly(vinyl alcohol). *Polymer*, 45(11):3893–3900, 2004.

[III.35] Mitsuhiro Fukuda. Clustering of Water in Polyethylene: A Molecular-Dynamics Simulation. *J. Chem. Phys.*, 109(15):6476–6485, October 1998.

[III.36] Matej Kanduč, Won Kyu Kim, Rafael Roa, and Joachim Dzubiella. Transfer free energies and partitioning of small molecules in collapsed pnipam polymers. *J. Phys. Chem. B*, 123(3):720–728, 2019.

[III.37] Shigeo Sasaki, Shogo Koga, and H. Maeda. Dielectric properties of collapsing hydrogels. *Macromolecules*, 32(14):4619–4624, July 1999.

[III.38] J.G. Wijmans and R.W. Baker. The solution-diffusion model: A review. *J. Membr. Sci.*, 107(1):1–21, 1995.

[III.39] Umberto Marini Bettolo Marconi and Pedro Tarazona. Dynamic density functional theory of fluids. *J. Chem. Phys.*, 110(16):8032–8044, 1999.

[III.40] A. J. Archer and R. Evans. Dynamical density functional theory and its application to spinodal decomposition. *J. Chem. Phys.*, 121(9):4246–4254, 2004.

[III.41] Michael te Vrugt and Raphael Wittkowski. Perspective: New directions in dynamical density functional theory. *J. Phys.: Condens. Matter*, 35(4):041501, December 2022.

[III.42] Stefano Angioletti-Uberti, Matthias Ballauff, and Joachim Dzubiella. Dynamic density functional theory of protein adsorption on polymer-coated nanoparticles. *Soft Matter*, 10:7932–7945, 2014.

[III.43] Stefano Angioletti-Uberti. Theory, simulations and the design of functionalized nanoparticles for biomedical applications: A soft matter perspective. *npj Comput. Mater.*, 3(1):48, November 2017.

[III.44] Arturo Moncho-Jordá, Alicia Germán-Bellod, Stefano Angioletti-Uberti, Irene Adroher-Benítez, and Joachim Dzubiella. Nonequilibrium uptake kinetics of molecular cargo into hollow hydrogels tuned by electrosteric interactions. *ACS Nano*, 13(2):1603–1616, February 2019.

[III.45] H. A. Pérez-Ramírez, A. Moncho-Jordá, and G. Odriozola. Phenol release from pnipam hydrogels: Scaling molecular dynamics simulations with dynamical density functional theory. *Soft Matter*, 18:8271–8284, 2022.

[III.46] Andrew J Archer, Matthias Schmidt, and Robert Evans. Soft core fluid in a quenched matrix of soft core particles: A mobile mixture in a model gel. *Phys. Rev. E*, 73(1):011506, 2006.

[III.47] Matthias Schmidt, Hartmut Löwen, Joseph M Brader, and Robert Evans. Density functional theory for a model colloid–polymer mixture: bulk fluid phases. *Journal of Physics: Condensed Matter*, 14(40):9353, sep 2002.

[III.48] Ingo Berndt, Jan Skov Pedersen, and Walter Richtering. Structure of multiresponsive intelligent coreshell microgels. *J. Am. Chem. Soc.*, 127(26):9372–9373, 2005.

[III.49] Keith J. Laidler. The development of the arrhenius equation. *J. Chem. Educ.*, 61(6):494, 1984.

[III.50] R. M. Sok, H. J. C. Berendsen, and W. F. van Gunsteren. Molecular dynamics simulation of the transport of small molecules across a polymer membrane. *J. Chem. Phys.*, 96(6):4699–4704, 03 1992.

[III.51] Shivkumar V. Ghugare, Ester Chiessi, Mark T. F. Telling, Antonio Deriu, Yuri Gerelli, Joachim Wuttke, and Gaio Paradossi. Structure and dynamics of a thermoresponsive microgel around its volume phase transition temperature. *J. Phys. Chem. B*, 114(32):10285–10293, August 2010.

[III.52] Martine Philipp, Konstantinos Kyriakos, Luca Silvi, Wiebke Lohstroh, Winfried Petry, Jan K. Krüger, Christine M. Papadakis, and Peter Müller-Buschbaum. From molecular dehydration to excess volumes of phase-separating pnipam solutions. *J. Phys. Chem. B*, 118(15):4253–4260, April 2014.

[III.53] Florian Müller-Plathe. Permeation of polymers — a computational approach. *Acta Polym.*, 45(4):259–293, 1994.

[III.54] Weimin Zhang, Irina Gaberman, and Malgorzata Ciszkowska. Diffusion and concentration of molecular probes in thermoresponsive poly(n-isopropylacrylamide) hydrogels: Effect of the volume phase transition. *Anal. Chem.*, 74(6):1343–1348, March 2002.

[III.55] Kaihuan Zhang, Xueling Feng, Chongnan Ye, Mark A. Hempenius, and G. Julius Vancso. Hydrogels with a memory: Dual-responsive, organometallic poly(ionic liquid)s with hysteretic volume-phase transition. *J. Am. Chem. Soc.*, 139(29):10029–10035, July 2017.

[III.56] Baicheng Mei and Kenneth S. Schweizer. Activated penetrant dynamics in glass forming liquids: Size effects, decoupling, slaving, collective elasticity and correlation with matrix compressibility. *Soft Matter*, 17(9):2624–2639, 2021.

[III.57] Karel Šolc and Walter H. Stockmayer. Shape of a random-flight chain. *J. Chem. Phys.*, 54(6):2756–2757, 09 1971.

[III.58] Doros N. Theodorou and Ulrich W. Suter. Shape of unperturbed linear polymers: Polypropylene. *Macromolecules*, 18(6):1206–1214, 1985.

[III.59] Handan Arkın and Wolfhard Janke. Gyration tensor based analysis of the shapes of polymer chains in an attractive spherical cage. *J. Chem. Phys.*, 138(5):054904, 02 2013.

[III.60] Jianzhong Wu and Zhidong Li. Density-functional theory for complex fluids. *Annu. Rev. Phys. Chem.*, 58(1):85–112, 2007.

[III.61] J-P. Hansen and I.R. McDonald. *Theory of Simple Liquids, Fourth Edition*. Academic Press, 4th edn, 2013.

[III.62] R. Evans. *Fundamentals in Inhomogeneous Fluids*. Marcel Derrer, Inc., 1992.

[III.63] C. Ebner, W. F. Saam, and D. Stroud. Density-functional theory of simple classical fluids. i. surfaces. *Phys. Rev. A*, 14:2264–2273, December 1976.

[III.64] W. F. Saam and C. Ebner. Density-functional theory of classical systems. *Phys. Rev. A*, 15:2566–2568, June 1977.

[III.65] John D. Weeks. Connecting local structure to interface formation: A molecular scale van der waals theory of nonuniform liquids. *Annu. Rev. Phys. Chem.*, 53(Volume 53, 2002):533–562, 2002.

[III.66] Andrew J Archer and Robert Evans. Relationship between local molecular field theory and density functional theory for non-uniform liquids. *J. Chem. Phys.*, 138(1), 2013.

[III.67] Sébastien Casault and Gary W. Slater. Systematic characterization of drug release profiles from finite-sized hydrogels. *Phys. A: Stat. Mech. Appl*, 387(22):5387–5402, 2008.

[III.68] Yiming Wang, Jie Wang, Zhenyu Yuan, Haoya Han, Tao Li, Li Li, and Xuhong Guo. Chitosan cross-linked poly(acrylic acid) hydrogels: Drug release control and mechanism. *Colloids Surf. B*, 152:252–259, 2017.

[III.69] Matz Andersson, Anders Axelsson, and Guido Zacchi. Swelling kinetics of poly (n-isopropylacrylamide) gel. *J. Control. Release*, 50(1-3):273–281, 1998.

[III.70] Ivan J Suarez, Alberto Fernandez-Nieves, and Manuel Marquez. Swelling kinetics of poly (n-isopropylacrylamide) minigels. *J. Phys. Chem. B*, 110(51):25729–25733, 2006.

[III.71] G. Klein and Max Born. Mean first-passage times of brownian motion and related problems. *Proc. R. Soc. A: Math. Phys. Eng. Sci.*, 211(1106):431–443, 1952.

[III.72] Shneior Lifson and Julius L. Jackson. On the Self-Diffusion of Ions in a Polyelectrolyte Solution. *J. Chem. Phys.*, 36(9):2410–2414, 07 1962.

[III.73] Attila Szabo, Klaus Schulten, and Zan Schulten. First passage time approach to diffusion controlled reactions. *J. Chem. Phys.*, 72(8):4350–4357, 07 1980.

Publication IV

Measuring Absolute Velocities from Nonequilibrium Oscillations via Single-Detector 3D Dynamic Light Scattering

López-Molina, J.[1], Moncho-Jordá, A.[1,2] and Tirado-Miranda, M.[1]

[1]*Departamento de Física Aplicada, Universidad de Granada, Campus Fuentenueva S/N, 18071 Granada, Spain*

[2]*Institute Carlos I for Theoretical and Computational Physics, Facultad de Ciencias, Universidad de Granada, Campus Fuentenueva S/N, 18071 Granada, Spain*

Published in

Physical Review Letters, **2024** *133(19)*, 198202.

Abstract

Single-detector 3D dynamic light scattering (3D DLS) emerges as a reliable technique to determine the drift velocity of out-of-equilibrium colloidal particles. In particular, our investigation reveals the appearance of oscillations of a well-defined frequency in the autocorrelation function of the scattered intensity when particles are immersed in a medium exposed to thermally induced convection. These oscillations arise as a consequence of the directed motion of particles due to the convection of the fluid. The experimental results obtained for different colloidal systems are corroborated by a theoretical model and thoroughly validated with fluid dynamics and Brownian dynamics simulations. The excellent agreement between experimental, theoretical and simulation data allows us to provide a solid and comprehensive explanation of the observed physical phenomena. This Letter, using an advanced dynamic light scattering technique, offers insights into the field of nonequilibrium particle dynamics, applicable not only to colloidal suspensions affected by steady-state diffusion-convection but also to other nonequilibrium scenarios, such as systems driven by external fields (e.g., gravitational, electric or magnetic fields).

Dynamic light scattering (DLS) is a powerful tool for measuring dynamic properties over a wide range of systems. Recently, this technique has been employed to study acousto-responsive microgels under ultrasonic influence [IV.1], flow-induced dynamics s [IV.2], and 3D imaging of heterogeneous diffusion [IV.3]. Similar techniques such as x-ray photon correlation spectroscopy has also been refined to observe ballistic dynamics in magnetic fields [IV.4], direction-dependent diffusion [IV.5], noninvasive studies in living cells [IV.6], or in colloidal palladium [IV.7]. So, the techniques that have yielded valuable insights into the dynamic behaviors of mesoscopic systems are now being adapted to more complex scenarios such as colloidal systems out of equilibrium.

A common phenomenon in many particle systems exposed to external fields is the emergence of a particle drift velocity. Traditionally, these velocities have been obtained with the heterodyne dynamic light scattering (HeDLS) method, which builds the intensity autocorrelation function $g^{(2)}(\mathbf{q},\tau)$ by mixing scattered light from particles with an unscattered reference beam in a detector. Particles velocity is derived from the time oscillations that appear in $g^{(2)}(\mathbf{q},\tau)$ [IV.8, IV.9, IV.10, IV.11, IV.12]. Alternatively, in a classical homodyne dynamic light scattering setup (HoDLS), which uses a single incident beam and a single detector to analyze only the scattered light from particles, theory predicts no oscillatory behavior [IV.8, IV.9]. However, several studies have observed oscillations using HoDLS, leading a considerable discussion about its physical interpretation [IV.13, IV.14, IV.15].

The 3D DLS setup is a standard device widely used in many laboratories to characterize dense colloidal suspensions [IV.16, IV.17]. In this Letter, we expand its conventional application to include the detection of particle drift velocities induced by external fields using this setup with a single detector that collects the scattered light from two intersecting laser beams within the sample (see Fig. IV.1). Based on light scattering theory, we provide a formal justification for the observed oscillatory behavior of $g^{(2)}(\mathbf{q},\tau)$ arising in nonequilibrium steady-state colloidal fluids, and connect this phenomenon to the existence of a drift velocity. This method enables the precise quantification of drift velocities from the intensity autocorrelation function. We illustrate this procedure by studying fluid-induced thermal-convective systems, while emphasizing its applicability to other nonequilibrium scenarios. Our experimental findings and theoretical description are fully validated by Brownian dynamics (BD) and fluid dynamic simulations.

Before presenting the experimental results, we provide the theoretical framework required to understand the behavior of $g^{(2)}(\mathbf{q},\tau)$ when the particles not only move by Brownian diffusion, but also due to an imposed drift velocity. We start with the simplest HoDLS device, namely, the one with a single beam and a single detector. The field autocorrelation function of a monodisperse system of spherical particles with diffusion coefficient D and drift velocity $\mathbf{v}$ is given by [IV.8, IV.13, IV.15, IV.18]

$$g^{(1)}(\mathbf{q},\tau) = e^{i\mathbf{q}\cdot\mathbf{v}}e^{-Dq^2\tau}, \tag{IV.1}$$

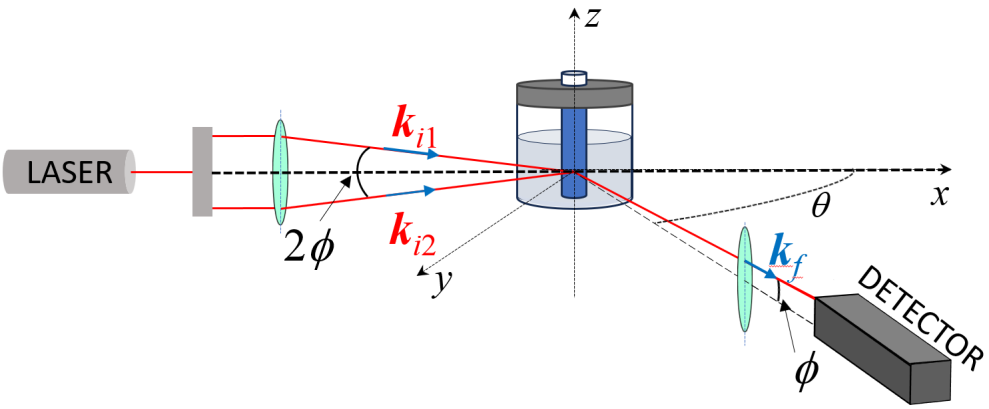

Figure IV.1: Experimental scattering setup. The incident laser beam is split into two beams that converge at the center of a sample cell. The angle between each beam and the scattering plane is denoted by ϕ. The scattered light is collected by a detector positioned at an angle θ relative to the initial laser direction and ϕ above the plane.

where $\mathbf{q}$ is the scattering vector of the monochromatic laser beam. With the traditional one-beam HoDLS it is only possible to measure the intensity correlation function, given by [IV.19, IV.20, IV.9, IV.8]

$$g^{(2)}(\mathbf{q},\tau) = 1 + \beta|g^{(1)}(\mathbf{q},\tau)|^2 = 1 + e^{-2Dq^2\tau}, \tag{IV.2}$$

where β is the coherence factor. In the following equations, we set $\beta = 1$ for simplicity although in experiments it is a number $0 < \beta < 1$. As observed, $\mathbf{v}$ does not explicitly appear in $g^{(2)}$ [IV.21, IV.22]. However, in the study of driven systems, a nonequilibrium anomaly is observed in the correlation function that is not captured by Eq. (IV.2). In particular, the diffusion coefficient derived from the experimental decay of $g^{(2)}(\tau)$ consistently exceeds the value predicted by the Stokes-Einstein equation, $D_{\text{st}} = k_B T/(6\pi\eta a)$ (where k_B is the Boltzmann constant, T the absolute temperature, η is the solvent viscosity and a denotes the radius of the colloidal particles). In other words, $g^{(2)}(\tau)$ decays faster with time than expected for this particle size. This phenomenon has been previously attributed to an enhancement of the diffusion coefficient due to reduced friction caused by the convective flow [IV.18] or discussed as superdiffusion [IV.23]. In this Letter, we show that the rapid decay of $g^{(2)}(\tau)$ is provoked by particles systematically escaping the scattering volume due to the drift velocity, resulting in a loss of correlation.

A proposed correction involves an exponential term dependent on velocity and time squared, based on a Gaussian laser beam intensity profile [IV.24, IV.25, IV.26, IV.27, IV.28]. However, this approach fails to accurately measure the diffusion coefficient for low drift velocities in our experiments. We reconsidered the laser beam profile's shape, focusing on the scattering volume defined by the intersection of laser beams and the detector's pinhole projection. This led us to treat the beam's intensity as uniform within the scattering region and 0 outside it.

The amplitude of the scattered electric field is thus considered constant across the beam thickness h, i.e., $P(z) = E_0$ for $-\frac{h}{2} < z < \frac{h}{2}$. This revised model introduces a new factor into the correlation function $\langle P(z(0))P(z(t))\rangle g^{(1)}(\mathbf{q},\tau)$, where $g^{(1)}(\mathbf{q},\tau)$ is given by Eq. (IV.1) and $z(t) = vt + z_0$. The modified field correlation function for a single-beam device is expressed as

$$g^{(1)}(\mathbf{q},\tau) = e^{i\mathbf{q}\cdot\mathbf{v}}e^{-Dq^2\tau}\left(1 - \frac{v\tau}{h}\right) \qquad \tau \leq h/v, \tag{IV.3}$$

and $g^{(1)}(\mathbf{q},\tau) = 0$ if $\tau > h/v$. The term $1 - \frac{v\tau}{h}$ embodies the rate at which particles drift out of the scattering volume.

Having studied the single-beam device, we describe our setup with one detector but two beams with scattering vectors $\mathbf{q}_1$ and $\mathbf{q}_2$, respectively, that interfere inside the sample volume (see Fig. IV.1). Here, only the most relevant equations are shown. The full theoretical demonstration is available in Sec. A of Supplemental Material (SM) IV.1. Using that photons scattered by particles from different beams are not intercorrelated, $g^{(2)}$ is generalized to [IV.16, IV.29, IV.30, IV.31]

$$g^{(2)}(\mathbf{q}_1,\mathbf{q}_2,\tau) - 1 = |A_1 g^{(1)}(\mathbf{q}_1,\tau) + A_2 g^{(1)}(\mathbf{q}_2,\tau)|^2, \tag{IV.4}$$

where A_1 and A_2 are constants related to each beam intensity and alignment. Combining Eqs. (IV.3) and (IV.4), a new expression arises that gathers both the oscillatory behavior and the enhanced loss of correlation for the two-beams arrangement:

$$\begin{aligned} g^{(2)}(\mathbf{q}_1,\mathbf{q}_2,\tau) - 1 = & \\ = e^{-2D\bar{q}^2\tau} & \left[(1-C) + C\cos(\Delta\mathbf{q}\cdot\mathbf{v}\tau)\right]\left(1 - \tfrac{v\tau}{h}\right)^2 \end{aligned} \tag{IV.5}$$

for $\tau < h/v$ and $g^{(2)}(\mathbf{q}_1,\mathbf{q}_2,\tau) - 1 = 0$ for $\tau > h/v$, where $\bar{q} = |\mathbf{q}_1 + \mathbf{q}_2|/2$ represents the modulus of the mean of both scattering vectors, $\Delta\mathbf{q} = \mathbf{q}_1 - \mathbf{q}_2$ is the scattering vectors' difference, and $0 \leq C \leq 0.5$ represents the relative intensity of each beam. Crucially, this model reveals an oscillatory component with a characteristic frequency given by $\omega = \Delta\mathbf{q}\cdot\mathbf{v}$. As ω depends on $\mathbf{v}$ through this scalar product, it is only possible to access the projection of the velocity along the $\Delta\mathbf{q}$ vector. In our experimental setup $\Delta\mathbf{q}$ has only a z-component (i.e. z corresponds to the vertical direction)), so this measurement technique will only allow us to obtain v_z.

In our experiments, we study the oscillatory behavior and anomalous loss of correlation of $g^{(2)}$ for a colloidal system affected by a thermally induced convective flow. For this purpose, we use a 3D DLS setup from LS instruments. This device divides an incoming laser beam of wavelength $\lambda = 632.8\,\mathrm{nm}$ into two, slightly shifted above and below the scattering plane (see Fig.. IV.1). As mentioned, our method involves using just one detector, enabling it to capture scattered light from both beams

that intersect inside the colloidal sample, resulting in two distinct scattering vectors. As colloidal systems, we use monodisperse polystyrene spheres (from microparticles GmbH, Berlin, Germany) and microgel pNIPAM-co-3BA@ particles [IV.32] in water. Measurements took place in a cylindrical glass cell by LS-Instruments, 0.8 cm in diameter and 7.5 cm height with the sample filling up to 4 cm height. To induce thermal convection, only the lower 1 cm portion of the cell was immersed in a temperature-controlled bath, with the upper part in contact with metal. Measurements are performed at the center of the cell, 0.5 cm from the bottom, where the beams of the dual-laser setup intersect. Because of the axial symmetry of our cylindrical cell, fluid velocity in the center of the cell has only a z-component, meaning $\mathbf{v} = v_z\hat{\mathbf{k}}$. In all measurements the duration is 60 s and the room temperature is $T_{\text{room}} = 23°\text{C}$.

Figure IV.2(a) presents a comparison between single and dual-beam laser measurements with a bath temperature $T_{\text{bath}} = 38°\text{C}$.. In the single-beam setup, $g^{(2)}(\tau)$ decays exponentially, as predicted by Eq. IV.2. In contrast, the dual-beam setup reveals clear oscillations of a well-defined frequency [see inset of Fig. IV.2(a)], confirming that the simultaneous use of two laser beams is essential for observing this phenomenon.

The oscillations observed in our experiments are not a particular result tied to specific particle types; rather, it is a general behavior evident across a range of systems, including $a = 406$ nm and 30 nm radius monodisperse polystyrene particles, a mixture of them, and significantly larger pNIPAM microgels, as illustrated in Fig. IV.2(b). Particularly notable are the pronounced oscillations in the microgel system, attributable to its larger size. Examining the size dependence of these oscillations reveals that, as particle size decreases, the amplitude of the oscillations dampens. Indeed, $g^{(2)}(\tau)$ decays faster for particles with a larger diffusion coefficient (i.e., particles of smaller size), thus smoothing out the oscillations.

Although convection and oscillations are usually reported as issues related to particle light absorption [IV.33, IV.13, IV.15, IV.34], we see that thermal gradients inducing convection and oscillations can be externally imposed and measured also in non-light-absorbing colloids, regardless of particle composition. We observe this phenomenon in both monodisperse and bidisperse systems, indicating that all particles, regardless of size, move at a common velocity induced by the convective flow of the solvent. The study by Moulin et al. [IV.13] also reported oscillations in the correlation function of a system consisting of bidisperse light-absorbing particles. These oscillations were attributed to the existence of two distinct velocities for large and small particles. We propose that the cause of these oscillations aligns with our findings: a single drift induced by the convective solvent flow with two laser beams incident on the system $\Delta\mathbf{q} \cdot \mathbf{v}$. However, if the system exhibits two distinct velocities and only one laser beam is employed, it is plausible that oscillations with a frequency of $\mathbf{q} \cdot \Delta\mathbf{v}$ will emerge, thereby enabling the measurement of the velocity difference between both species (see Sec. B of SM IV.1). This two-velocity scenario may

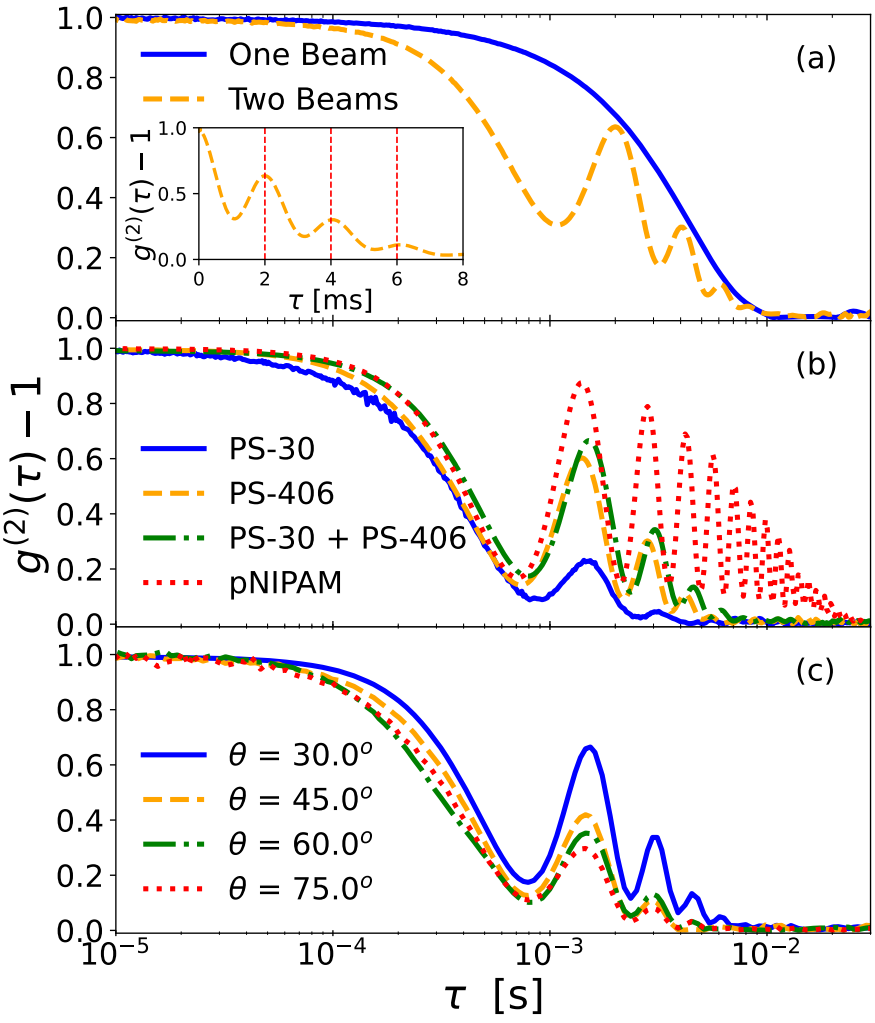

Figure IV.2: Intensity autocorrelation functions, $g^{(2)}(\tau) - 1$, obtained via 3D-DLS setup with one detector. Plot (a) shows the effect of the number of beams for $T_{\mathrm{bath}} = 38°\mathrm{C}$ and $\theta = 30°$. Plot (b) depicts the oscillatory effect for different kind of colloidal particles and sizes, for $T_{\mathrm{bath}} = 40°\mathrm{C}$ and $\theta = 30°$. Panel (c) shows that the oscillation frequency does not depend on θ, for $T_{\mathrm{bath}} = 40°\mathrm{C}$. In all cases $T_{\mathrm{room}} = 23°\mathrm{C}$.

occur in cases involving sedimentation with two types of particles, or if two charged particles move in the presence of an electric field and have different responses to the field.

The influence of the scattering angle θ on the autocorrelation function is illustrated in Fig. IV.2(c), for a system composed of polystyrene particles of radius $a = 406\,\text{nm}$. As observed, the oscillation amplitude decreases when increasing θ, but the frequency remains totally unaffected by changes in θ. To elucidate both effects, we calculate $\Delta\mathbf{q} = \mathbf{q}_1 - \mathbf{q}_2$, where $\mathbf{q}$ is the scattering vector defined by $\mathbf{q} = \mathbf{k}_i - \mathbf{k}_f$ and its modulus is $\bar{q} = \frac{4\pi n}{\lambda}\sin\left(\frac{\theta}{2}\right)$. The configuration setup of our 3D DLS device results in $\Delta\mathbf{q} = (2\pi n/\lambda)(0, 0, 2\sin(\phi))$, where $\phi = 0.052$ rad. As observed, $\Delta\mathbf{q}$ only has a z-component (perpendicular to the scattering plane) and does not depend on θ. This invariance in frequency with the detection angle aligns with our theoretical model, which posits that $\omega = \Delta\mathbf{q} \cdot \mathbf{v}$. In addition, according to Eq. IV.5 the amplitude of the oscillations is modulated by $\exp\left(-2D\bar{q}^2\tau\right)$, so increasing θ increases $\bar{q}$, reducing the observable oscillations. Therefore, to detect small drift velocities, low angles are preferable.

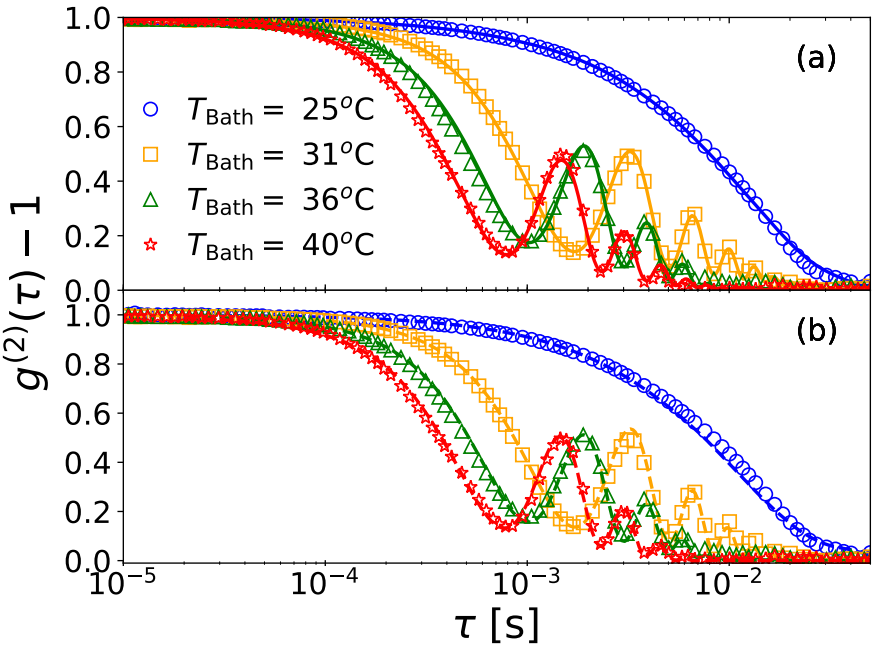

Figure IV.3: $g^{(2)}(\tau) - 1$ as a function of τ for particles with a radius of $a = 406$ nm, illuminated by two beams at different T_{bath}. Symbols represent the experimental measurements obtained with the 3D-DLS device with only one detector. In plot (a), solid lines depict fits of the experimental data to the theoretical model (Eq. (IV.5)). In plot (b), dashed lines represent correlation functions derived from BD simulations at velocities determined by the respective fits. In both panels $\theta = 40°$, and $T_{\text{room}} = 23°\text{C}$.

Figure IV.3(a) shows the experimental correlation function (symbols) for different T_{Bath}. When T_{Bath} is close to T_{Room}, $g^{(2)}$ does not show oscillations. This observation indicates that the convective currents are indeed driven by the thermal gradient. As $\Delta T_{\text{BR}} = T_{\text{Bath}} - T_{\text{Room}}$ is increased, we observe the emergence of oscillations, which shift toward the left. This shift signifies a growth of the vertical velocity of the particles v_z.

T_{bath} [°C]	D_{st} [μm²/s]	D_{fit} [μm²/s]	v_z [mm/s]	C
25	0.596	0.56	0.07	0.41
31	0.693	0.71	1.36	0.40
36	0.780	0.86	2.30	0.36
40	0.901	0.97	2.95	0.39

Table IV.1: Values of D_{fit}, v_z and C obtained by fitting the experimental data from Fig. (IV.3) using Eq. (IV.5) for different T_{bath}. The corresponding Stokes-Einstein diffusion coefficients, D_{st}, are also included for comparison.

The experimental results are compared with theoretical prediction as outlined by Eq. (IV.5), depicted by solid lines in Fig. IV.3(a). The fitting procedure is performed as follows. First, we extract the drift velocity from the oscillation using the relation $v_z = \omega/|\Delta\mathbf{q}|$, which allows a very accurate determination of v_z. Then, this value is fixed to fit the whole autocorrelation function using the diffusion coefficient (D_{fit}) and constant C as fitting parameters, with the beam thickness set at $h = 30\mu$m. The resulting values of v_z, D_{fit} and C are presented in Table IV.1. This table also lists the expected Stokes-Einstein diffusion coefficients, D_{st}, calculated for different temperatures. As observed, Eq. (IV.5) captures the experimental data in all cases. The fitted D_{fit} values closely match the expected D_{st}, with discrepancies ranging from 5% to 8%. Crucially, neglecting the correction for particle drifting out the dispersion volume $\left(1 - \frac{v\tau}{h}\right)$ leads to D_{fit} values inaccurately increasing with temperature T_{bath}, deviating from D_{st} values and significantly elevating the error over 100% at high drift velocities. The velocities obtained align with typical values for such measurement cells [IV.35]. The parameter C was observed to stay consistently around 0.4, indicating the reliability of the theoretical framework. It was not possible to reproduce velocity measurements for $T_{\text{Bath}} > 40$°C, since the system reaches unsteady convection.

To further validate the proposed explanations, we conduct Brownian dynamics simulations on an ideal system with $N = 10^4$ colloidal particles, in which particles possess the expected diffusion coefficient D_{st}. The simulation employs a time step of 10^{-5} s during a total time of 10 s and is set in a simulation cubic box with side $h = 30$ μm representing the scattering volume. A vertical upward flow is imposed along the z-axis representing the fluid velocity due to thermal convection. The associated values of v_z are extracted from our fits presented in Table IV.1. Periodic boundary conditions are applied on the x and y directions.

When a particle exits the simulation box through the top, another one is randomly introduced at the bottom, maintaining constant the number of particles. The total scattered electric field of the system at each time step is calculated using $E_s(t) = \sum_{i=1}^{N} [C \exp(i\mathbf{q}_1 \cdot \mathbf{r}_i(t)) + (1-C)\exp(i\mathbf{q}_2 \cdot \mathbf{r}_i(t))]$. The correlation function of $E_s(t)$ is then determined and normalized. To account for our particular experimental setup, $C = 0.4$ is used in the calculation of the autocorrelation function.

Figure IV.3(b) presents the simulated correlation functions (dashed lines) alongside the experimental data (symbols), showing a remarkable agreement, thus confirming that our simulation accurately captures the loss of correlation arising when particles escape from the scattering volume due to the convective flow. BD simulations also reproduce correctly the oscillation frequency obtained experimentally for all T_{Bath}. This evidence supports the full validation of our procedure for measuring drift velocities in colloidal systems.

Although our DLS method has been used to characterize the dynamics of colloidal suspensions affected by thermal convection, it can also be applied to other nonequilibrium colloidal systems where a vertical velocity appears, such as colloidal sedimentation or electrophoresis. In addition, it can be used for accessing solvent characteristics including viscosity and relevant dimensionless numbers of the fluid, such as Reynolds, Péclet, and Rayleigh numbers. Moreover, the proposed dual-beam setup allows a very accurate particle velocity determination through the oscillation frequency. We use it to characterize the correlation loss due to the escape of particles from the scattering volume, which is something very difficult to perform from the fitting of $g^{(2)}(\tau)$ for small velocities in ordinary light scattering setups [IV.28].

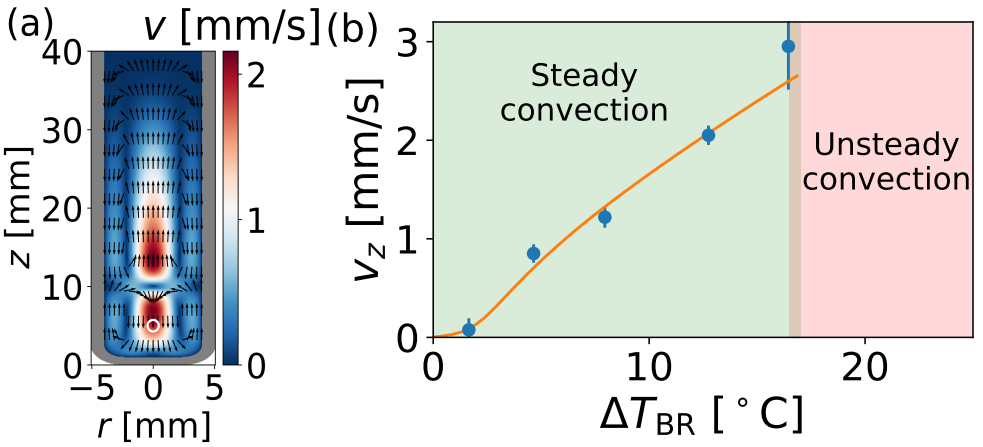

Figure IV.4: Predictions obtained by COMSOL simulations. (a) Velocity profile in stationary conditions, for a temperature difference given by $\Delta T_{\text{BR}} = 10°\text{C}$. The white circle denotes the measurement point in our DLS device. (b) v_z at the measurement point as a function of the temperature difference , ΔT_{BR} (line). Symbols represent the experimental data, obtained from the average over ten independent DLS measurements using Eq. (IV.5).

Using the nonisothermal flow interface in comsol, free convection was modeled in water. We use this simulation technique to explore the system response over time for different temperature differences, from $\Delta T_{\mathrm{BR}} = 0°\mathrm{C}$ to $\Delta T_{\mathrm{BR}} = 25°\mathrm{C}$. For $\Delta T_{\mathrm{BR}} \leq 17°\mathrm{C}$, fluid dynamics simulations reveal that both the velocity and temperature profiles inside the cell eventually reach a steady state. The stationary velocity field for $\Delta T_{\mathrm{BR}} = 10°\mathrm{C}$ is illustrated in Fig. IV.4(a). We notice two convective regions above and below the bath level that arise as a consequence of the different boundary temperatures, T_{Room} and T_{Bath}, respectively. The experimental measurement point is highlighted by a circle, inside which magnitudes vary less than 1%, and the drift velocities are completely vertical. The temperature in this region is lower than T_{bath} due to the convection currents.

Figure IV.4(b) shows v_z at the measurement point obtained both experimentally and from fluid simulations, as a function of the ΔT_{BR}. We clearly identify two distinct dynamic regimes of convective behavior, delineated by the value of ΔT_{BR}. In the first regime, corresponding to $\Delta T_{\mathrm{BR}} \leq 17°\mathrm{C}$, the flow eventually reaches a laminar steady state. We see excellent quantitative agreement in v_z between simulations and experiments underscoring the robustness of our DLS method for measuring velocities. For $\Delta T_{\mathrm{BR}} > 17°\mathrm{C}$, the obtained experimental $g^{(2)}(\tau)$ shows huge temporal fluctuations that make it impossible to identify the oscillations. Through COMSOL simulations we confirm that, in this dynamical regime, the system keeps on an unsteady state [IV.36, IV.37, IV.38, IV.39], in which the fluid velocity at the measurement point is not constant anymore and fluctuates over time (see Fig. S2 of SM IV.1). This nonsteady regime has associated Rayleigh numbers larger than the critical Rayleigh number for this cell geometry (see Sec. C of SM IV.1) [IV.40]. Therefore, comsol simulations not only reproduce the experimental drift velocities without any fitting parameter, but also capture the transition temperature separating the steady and nonsteady dynamic regimes.

In summary, this Letter extends the conventional applications of 3D DLS setups using a single detector for measuring drift velocities in nonequilibrium colloidal systems where particles do not only diffuse by Brownian motion, but also possess a drift velocity imposed by thermal or concentration gradients and/or applied external fields. A notable finding is the elucidation of the underlying physical mechanisms driving the oscillatory behavior of the autocorrelation function. Additionally, our research provides a correction methodology for the loss of correlation observed in these types of systems via HoDLS, and enriches the understanding of nonequilibrium particle dynamics, contributing to a broader application of 3D DLS as a valuable tool in exploring complex fluid dynamics.

Acknowledgements

We are grateful to Prof. Antonio M. Puertas-Lopez (University of Almería)

and Prof. Alberto Fernández-Nieves (University of Barcelona) for their insightful comments. The authors acknowledge grant PID2022-136540NB-I00 funded by MICIU/AEI/10.13039/501100011033 and ERDF *A way of making Europe*. J.L.M. thanks the Ph.D. student fellowship (FPU21/03568) supported by the Spanish *Ministerio de Universidades*.

IV.1. Appendix. Supplementary Material

IV.1.1. Two-Laser Single-Detector Correlation Function in Dynamic Light Scattering with One Drift Velocity

Dynamic Light Scattering (DLS) experiments invariably encompass three integral elements positioned within a plane: a light source, a colloidal system inducing light scattering and a detector situated at an angle θ relative to the incident beam. The detector quantifies the intensity of the system-scattered light as a function of time, denoted as $I(\mathbf{q}, t)$. To elucidate pertinent information from this signal, the intensity autocorrelation function $g^{(2)}(\mathbf{q}, \tau)$ is employed [IV.9, IV.8]:

$$g^{(2)}(\mathbf{q}, \tau) = \frac{\langle I(\mathbf{q}, 0) I(\mathbf{q}, \tau) \rangle}{\langle I(\mathbf{q}, 0) \rangle^2} \tag{IV.6}$$

Here, τ represents the correlation time, and $\mathbf{q}$ signifies the scattering vector, defined as $\mathbf{q} = \mathbf{k}_i - \mathbf{k}_f$, with $\mathbf{k}_i$ and $\mathbf{k}_f$ being the wave vectors of the incident and scattered waves, respectively. The angular brackets denote ensemble averaging.

This research centers on colloidal systems with monodisperse, non-interacting particles, thereby satisfying the Siegert relation which connects the intensity correlation function $g^{(2)}(\mathbf{q}, \tau)$ with the electric field correlation function $g^{(1)}(\mathbf{q}, \tau)$ [IV.16, IV.29, IV.30, IV.31]:

$$g^{(2)}(\mathbf{q}, \tau) = 1 + |g^{(1)}(\mathbf{q}, \tau)|^2 \tag{IV.7}$$

This relationship facilitates the model development by considering the electric field. The correlation function of the electric field is expressed as:

$$g^{(1)}(\mathbf{q}, \tau) = \frac{G^{(1)}(\mathbf{q}, \tau)}{G^{(1)}(\mathbf{q}, 0)} \tag{IV.8}$$

where $G^{(1)}(\mathbf{q}, \tau)$ is the non-normalized correlation function of the scattered electric field $E_s(\mathbf{q}, t)$

$$G^{(1)}(\mathbf{q}, \tau) = \langle E_s(\mathbf{q}, 0) E_s^*(\mathbf{q}, \tau) \rangle \tag{IV.9}$$

We start by considering a flat monochromatic electromagnetic wave, described by the electric field $\mathbf{E}_i(\mathbf{r}, t)$ at a point $\mathbf{r}$ and time t. This wave has a wavelength λ_i, frequency ω_i, polarization $\mathbf{n}_i$ perpendicular to the plane, with amplitude E_0. The wave also has a wave vector $\mathbf{k}_i$ pointing in the direction of propagation of the incident

wave, defined as:

$$\mathbf{k}_i = \left(\frac{\omega_i}{c}\right)\hat{\mathbf{k}}_i$$

where c is the speed of light. The electric field of the incident wave is given by:

$$\mathbf{E}_i(\mathbf{r},t) = \mathbf{n}_i E_0 e^{i(\mathbf{k}_i\cdot\mathbf{r}-\omega_i t)} \tag{IV.10}$$

This incident wave arrives at the dispersion of colloidal particles, each of which scatters without changing the frequency of the incident wave. A detector is placed at an angle θ to the incident direction as shown in Fig. IV.5. It collects the scattered radiation, which has the same polarization as the incident beam, $\mathbf{n}_f = \mathbf{n}_i$. We consider the scattering induced by a single colloidal particle α located at position $\mathbf{r}_\alpha(t)$ that arrives at the light detector placed at position $\mathbf{R}$, both with respect to the light source. The wave travels from the source to the particle position $\mathbf{r}_\alpha(t)$ with a wave vector $\mathbf{k}_i$, is scattered by the particle, and then travels a distance $\mathbf{R}-\mathbf{r}_\alpha(t)$ to reach the detector with a wave vector $\mathbf{k}_f$. We denote by θ the angle formed between the incident and scattered light.

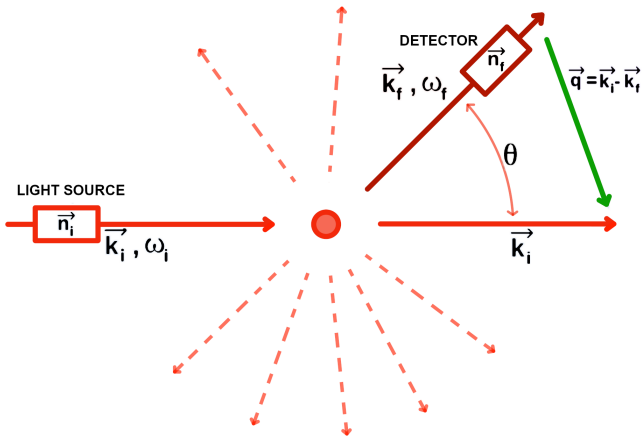

Figure IV.5: Electromagnetic wave with wave vector $\mathbf{k}_i$ strikes a particle and is scattered. At an angle θ, the scattered wave with wave vector $\mathbf{k}_f$ and polarization $\mathbf{n}_f$ reaches the detector.

The electric field from laser l scattered by particle α and arriving at the detector can be expressed as:

$$\mathbf{E}_{l,\alpha}(\mathbf{q},t) = \mathbf{n}_i E_{l,\alpha}(\mathbf{q}) e^{i[\mathbf{k}_i\cdot\mathbf{r}_\alpha(t)+\mathbf{k}_f\cdot(\mathbf{R}-\mathbf{r}_\alpha(t))-\omega_i t]} \tag{IV.11}$$

where $E_{l,\alpha}(\mathbf{q})$ is the amplitude of the scattered field.

The scattering vector $\mathbf{q}$ is defined as $\mathbf{q} = \mathbf{k}_i - \mathbf{k}_f$, where $\mathbf{k}_i$ and $\mathbf{k}_f$ are the wave vectors of the incident and scattered waves, respectively. The modulus of these wave vectors can be expressed as $k_i = 2\pi n/\lambda_i$ and $k_f = 2\pi n/\lambda_f$, where λ_i and λ_f are

the wavelengths of the incident and scattered waves and n is the refractive index of the medium. It is generally assumed that the wavelength does not undergo significant changes during scattering, so we can approximate $|\mathbf{k}_i| \cong |\mathbf{k}_f|$.

With this expression for $\mathbf{q}$, we can rewrite the equation for the field scattered by a particle Eq. (IV.11) as follows:

$$\mathbf{E}_{l,\alpha}(\mathbf{q},t) = \mathbf{n}_i E_{l,\alpha}(\mathbf{q}) e^{i\mathbf{q}\cdot\mathbf{r}_\alpha(t)}\, e^{i(\mathbf{k}_f\cdot\mathbf{R}-\omega_i t)} \tag{IV.12}$$

When calculating correlation functions, the phase term of the electric field is discarded because it does not depend on particle position. Therefore, it is convenient to work only with the amplitude of the electric field. Once the field scattered by a single colloidal particle is known, it is straightforward to find the field scattered by colloidal particle system.

Consider a volume V containing a large number of particles N in suspension that do not interfere with each other (that is, their positions are mutually independent). The total scattered electric field at a given $\mathbf{q}$, will be the sum of the fields scattered by each individual particle at that $\mathbf{q}$. Therefore, the amplitude of the total field can be expressed as:

$$\mathbf{E}_l(\mathbf{q},t) = \sum_{\alpha=1}^{N} E_{l,\alpha}(\mathbf{q}) e^{i\mathbf{q}\cdot\mathbf{r}_\alpha(t)} \tag{IV.13}$$

As we can see, the fluctuations of the amplitude of the scattered electric field with time depend on the movement of each particle in suspension [IV.9, IV.8].

In this section, we will focus on monodisperse systems, in which all particles are identical. Therefore, we can set $E_{l,1}(q) = E_{l,2}(q) = ... = E_l(q)$ and rewrite the Eq. (IV.13) as:

$$\mathbf{E}_l(\mathbf{q},t) = \sum_{\alpha=1}^{N} E_l(\mathbf{q}) e^{i\mathbf{q}\cdot\mathbf{r}_\alpha(t)} \tag{IV.14}$$

Our experiment enhances a standard DLS setup by introducing a design where two beams target the same sample, though at slightly different angles as shown in Fig. 1 of the main text. A detector measures the scattered intensity from these beams. Consequently, the electric field amplitude at the detector is formulated as [IV.16,IV.29, IV.30, IV.31]:

$$E(t) = E_1(\mathbf{q}_1,t) + E_2(\mathbf{q}_2,t) \tag{IV.15}$$

Here, $\mathbf{q}_l$ is each beam's scattering vector, and $E_l(\mathbf{q}_l,t)$ denotes the scattered amplitude each beam directs to the detector for $l = \{1,2\}$. Using this expression

for the scattered field, it is possible to define the electric field autocorrelation function in the case that there is a sum of electric fields $G^{(1)}(\mathbf{q}_1, \mathbf{q}_2, \tau)$. Inserting expression (IV.15) into (IV.9) we obtain:

$$\begin{aligned} G^{(1)}(\mathbf{q}_1, \mathbf{q}_2, \tau) &= \langle E(0)E^*(\tau)\rangle \\ &= \langle E_1(\mathbf{q}_1, 0)E_1^*(\mathbf{q}_1, \tau)\rangle + \langle E_1(\mathbf{q}_1, 0)E_2^*(\mathbf{q}_2, \tau)\rangle + \\ &\quad + \langle E_2(\mathbf{q}_2, 0)E_1^*(\mathbf{q}_1, \tau)\rangle + \langle E_2(\mathbf{q}_2, 0)E_2^*(\mathbf{q}_2, \tau)\rangle \end{aligned} \tag{IV.16}$$

Using the definition of $G^{(1)}(\mathbf{q}, \tau)$ given by Eq. (IV.9):

$$G^{(1)}(\mathbf{q}_1, \mathbf{q}_2, \tau) = G^{(1)}(\mathbf{q}_1, \tau) + \langle E_1(\mathbf{q}_1, 0)E_2^*(\mathbf{q}_2, \tau)\rangle + \langle E_2(\mathbf{q}_2, 0)E_1^*(\mathbf{q}_1, \tau)\rangle + G^{(1)}(\mathbf{q}_2, \tau) \tag{IV.17}$$

In this expression, the terms where $l = m$ refer to $G^{(1)}(\mathbf{q}_1, \tau)$ and $G^{(1)}(\mathbf{q}_2, \tau)$. The cross terms where $l \neq m$ equate to zero due to the absence of correlation between $E_1(\mathbf{q}_1, t)$ and $E_2(\mathbf{q}_2, t)$.

To see this, the terms where $l \neq m$ are expanded, following a similar approach to cross-correlation derivations [IV.16]. If we introduce the expression for the scattered electric field of each beam (IV.13) and by defining $\Delta\mathbf{q} = \mathbf{q}_l - \mathbf{q}_m$ we arrive at the following expression:

$$\langle E_l(\mathbf{q}_l, 0)E_m^*(\mathbf{q}_m, \tau)\rangle = \sum_{\alpha,\beta=1}^{N} \left\langle E_{l,\alpha}E_{m,\beta}e^{i\mathbf{q}_l(\mathbf{r}_\alpha - \mathbf{r}'_\beta)}e^{-i\Delta\mathbf{q}\mathbf{r}'_\beta}\right\rangle \tag{IV.18}$$

Particle coordinates with a prime refer to time τ, while others are at time 0. It is assumed here that each beam illuminates an identical scattering volume.

For small values of $\Delta\mathbf{q}$ the last exponential varies slowly. This allows us to separate the expected value of the product into the product of expected values. Moreover, since the system is monodisperse, the electric field amplitude solely depends on the magnitude of the scattering vector $\mathbf{q}$ [IV.8]. Given the small nature of $\Delta\mathbf{q}$, we can approximate $E_{l,\alpha} = E_{m,\beta} = E_0$:

$$\langle E_l(\mathbf{q}_l, 0)E_m^*(\mathbf{q}_m, \tau)\rangle = \sum_{\alpha,\beta=1}^{N} \left\langle E_0^2 e^{-i\Delta\mathbf{q}\mathbf{r}'_\beta}\right\rangle \left\langle e^{i\mathbf{q}_1(\mathbf{r}_\alpha - \mathbf{r}'_\beta)}\right\rangle \tag{IV.19}$$

The last expected value matches the typical expression of $g^{(1)}(\mathbf{q}_1, \tau)$ [IV.8, IV.9]. This allows us to solve the spatial average, assuming our scattering volume is represented by a 3-D Gaussian with a $1/e^2$-radius R [IV.16]:

$$\begin{aligned}\langle E_l(\mathbf{q}_l,0)E_m^*(\mathbf{q}_m,\tau)\rangle &= ng^{(1)}(\mathbf{q}_l,\tau)\int d^3r E_l^2 e^{-2\mathbf{r}^2/R^2}e^{-i\Delta\mathbf{q}\cdot\mathbf{r}} \\ &= n\,E_l^2(\pi/2)^{3/2}e^{-\Delta\mathbf{q}^2R^2/8}g^{(1)}(\mathbf{q}_l,\tau) \qquad \text{(IV.20)}\end{aligned}$$

By comparing the relative weight of each term in expression (IV.17), we observe the following: In the case of $l = m$ we get $nE_l^2(q)(\pi/2)^{3/2}g^{(1)}(\mathbf{q}_l,\tau)$. Conversely, for $l \neq m$, we see a difference factor of $e^{-\Delta\mathbf{q}^2R^2/8}$.

This leads us to deduce that, for cross terms to vanish, the subsequent condition must be satisfied:

$$|\Delta\mathbf{q}|^{-1} < R \qquad \text{(IV.21)}$$

Knowing that our wavelength is $\lambda = 632.8\,\mathrm{nm}$ and $\Delta\mathbf{q} = (2\pi n/\lambda)(0,0,2\sin(\phi))$ with refraction index $n = 1.33$ and $\phi = 0.052\,\mathrm{rad}$, we obtain $|\Delta\mathbf{q}|^{-1} \approx 7\cdot10^{-7}\,\mathrm{m}$, which is much lower than our beam radius $R \in \left[10^{-5}\,\mathrm{m} - 10^{-4}\,\mathrm{m}\right]$.

Given this context, the electric field correlation function simplifies to:

$$g^{(1)}(\mathbf{q}_1,\mathbf{q}_2,\tau) \approx \frac{G^{(1)}(\mathbf{q}_1,\tau)+G^{(1)}(\mathbf{q}_2,\tau)}{G^{(1)}(\mathbf{q}_1,0)+G^{(1)}(\mathbf{q}_2,0)} = A_1g^{(1)}(\mathbf{q}_1,\tau)+A_2g^{(1)}(\mathbf{q}_2,\tau) \qquad \text{(IV.22)}$$

where A_1 and A_2 are positive constants that take into account the relative field amplitude of each beam and possible misalignment of the scattering volumes and $A_1 + A_2 = 1$. The Siegert relation (IV.7) is altered by substituting Equation (IV.22), obtaining:

$$g^{(2)}(\mathbf{q}_1,\mathbf{q}_2,\tau) - 1 = \left|g^{(1)}(\mathbf{q}_1,\mathbf{q}_2,\tau)\right|^2 \qquad \text{(IV.23)}$$

With the acknowledgment that the function $g^{(1)}(\mathbf{q},\tau)$ with a drift velocity is given by expression $g^{(1)}(\mathbf{q},\tau) = e^{i\mathbf{q}\cdot\mathbf{v}}e^{-Dq^2\tau}$ [IV.8, IV.13, IV.15, IV.18]:

$$g^{(2)}(\mathbf{q}_1,\mathbf{q}_2,\tau) - 1 = \left|A_1e^{i\mathbf{q}_1\cdot\mathbf{v}\tau}e^{-Dq_1^2\tau} + A_2e^{i\mathbf{q}_2\cdot\mathbf{v}\tau}e^{-Dq_2^2\tau}\right|^2 \qquad \text{(IV.24)}$$

Since $\Delta\mathbf{q}$ is very small, $q_1 \approx q_2 \approx \bar{q} = |\mathbf{q}_1 + \mathbf{q}_2|/2$, so the last expression can be approximated to:

$$g^{(2)}(\mathbf{q}_1,\mathbf{q}_2,\tau)-1\approx\left|e^{-D\bar{q}^2\tau}\left(A_1e^{i\mathbf{q}_1\cdot\mathbf{v}\tau}+A_2e^{i\mathbf{q}_2\cdot\mathbf{v}\tau}\right)\right|^2 \tag{IV.25}$$

and solving the square:

$$g^{(2)}(\mathbf{q}_1,\mathbf{q}_2,\tau)-1=e^{-2D\bar{q}^2\tau}\left(A_1^2+A_2^2+2A_1A_2\cos(\Delta\mathbf{q}\cdot\mathbf{v}\tau)\right) \tag{IV.26}$$

In an experimental case in which the intensities of both beams are not the same, the previous expression turns to:

$$g^{(2)}(\mathbf{q}_1,\mathbf{q}_2,\tau)-1=e^{-2D\bar{q}^2\tau}\left[(1-C)+C\cos(\Delta\mathbf{q}\cdot\mathbf{v}\tau)\right] \tag{IV.27}$$

where $C\in[0-0.5]$ is a constant.

Lastly we want to take into account the effect of particles leaving the scattering volume. To do so, a position-dependent field amplitude is defined. Since in our experiment the velocity is completely vertical, it is assumed that particles only exit the volume through the z direction. The position-dependent field amplitude is:

$$P(z)=\begin{cases}\frac{1}{h} & \text{if } -h/2\le z\le h/2\\ 0 & \text{otherwise}\end{cases} \tag{IV.28}$$

Where h is the beam thickness. We go back to equation (IV.19), using $l=m$ so $\Delta\mathbf{q}=0$ and taking into account that different particles do not interact:

$$G^{(1)}(\mathbf{q},\tau)=\langle E(\mathbf{q},0)E^*(\mathbf{q},\tau)\rangle=\sum_{\alpha=1}^{N}\left\langle E_0^2P(z_\alpha(0))P(z_\alpha(\tau))\right\rangle\left\langle e^{i\mathbf{q}(\mathbf{r}_\alpha-\mathbf{r}'_\alpha)}\right\rangle \tag{IV.29}$$

where $z_\alpha(t)=z_0+vt$ is the z-coordinate of the particle α. Assuming that the particles are equally distributed, the first average is straightforward and the normalized correlation function is:

$$g^{(1)}(\mathbf{q},\tau)=\left(1-\frac{v\tau}{h}\right)\left\langle e^{i\mathbf{q}(\mathbf{r}_\alpha-\mathbf{r}'_\alpha)}\right\rangle=\left(1-\frac{v\tau}{h}\right)e^{i\mathbf{q}\cdot\mathbf{v}}e^{-Dq^2\tau} \tag{IV.30}$$

with $\tau\le h/v$ and using this expression into Eqs. (IV.22,IV.23):

$$g^{(2)}(\mathbf{q}_1,\mathbf{q}_2,\tau)-1=e^{-2D\bar{q}^2\tau}\left[(1-C)+C\cos(\Delta\mathbf{q}\cdot\mathbf{v}\tau)\right]\left(1-\frac{v\tau}{h}\right)^2 \tag{IV.31}$$

IV.1.2. Two-Velocity One-Laser Single-Detector Correlation Function in Dynamic Light Scattering

We now consider a new configuration with respect to the one described in section A: a single laser, a single detector and two distinct velocities. In this configuration, we employ a single scattering vector $\mathbf{q}$ but allow for two distinct drift velocities $\mathbf{v}_1$ and $\mathbf{v}_2$. This scenario is relevant when the colloidal system contains two populations of particles moving at different velocities, either due to different driving forces or differing interactions with the medium.

The intensity autocorrelation function $g^{(2)}(\mathbf{q}, \tau)$ is given by the same fundamental definition:

$$g^{(2)}(\mathbf{q}, \tau) = \frac{\langle I(\mathbf{q}, 0) I(\mathbf{q}, \tau) \rangle}{\langle I(\mathbf{q}, 0) \rangle^2} \tag{IV.32}$$

Using the Siegert relation, we connect $g^{(2)}(\mathbf{q}, \tau)$ with the electric field correlation function $g^{(1)}(\mathbf{q}, \tau)$:

$$g^{(2)}(\mathbf{q}, \tau) = 1 + |g^{(1)}(\mathbf{q}, \tau)|^2 \tag{IV.33}$$

Given the two distinct drift velocities, the total scattered electric field at the detector can be expressed as the sum of the fields corresponding to each velocity:

$$E(t) = E_1(\mathbf{q}, t) + E_2(\mathbf{q}, t) \tag{IV.34}$$

Inserting this into the definition of the electric field correlation function $G^{(1)}(\mathbf{q}, \tau)$ Eq. (IV.9) and assuming there is no correlation between E_1 and E_2, the cross terms $\langle E_1(\mathbf{q}, 0) E_2^*(\mathbf{q}, \tau) \rangle$ and $\langle E_2(\mathbf{q}, 0) E_1^*(\mathbf{q}, \tau) \rangle$ vanish. Thus, the correlation function simplifies to:

$$G^{(1)}(\mathbf{q}, \tau) = G_1^{(1)}(\mathbf{q}, \tau) + G_2^{(1)}(\mathbf{q}, \tau) \tag{IV.35}$$

Utilizing the normalized electric field correlation function $g^{(1)}(\mathbf{q}, \tau) = \frac{G^{(1)}(\mathbf{q}, \tau)}{G^{(1)}(\mathbf{q}, 0)}$, we can express:

$$g^{(1)}(\mathbf{q}, \tau) = B_1 g_1^{(1)}(\mathbf{q}, \tau) + B_2 g_2^{(1)}(\mathbf{q}, \tau) \tag{IV.36}$$

Here, B_1 and B_2 are the weighting factors corresponding to the proportion of particles with each velocity component, satisfying $B_1 + B_2 = 1$.

The electric field correlation function for particles with drift velocity is given by $g^{(1)}(\mathbf{q},\tau) = e^{i\mathbf{q}\cdot\mathbf{v}\tau}e^{-Dq^2\tau}$ [IV.8, IV.13, IV.15, IV.18]. For the system with two velocities, this becomes:

$$g_1^{(1)}(\mathbf{q},\tau) = e^{i\mathbf{q}\cdot\mathbf{v}_1\tau}e^{-D_1q^2\tau}, \quad g_2^{(1)}(\mathbf{q},\tau) = e^{i\mathbf{q}\cdot\mathbf{v}_2\tau}e^{-D_2q^2\tau} \tag{IV.37}$$

Substituting these into Equation (IV.36), we get:

$$g^{(1)}(\mathbf{q},\tau) = B_1e^{i\mathbf{q}\cdot\mathbf{v}_1\tau}e^{-D_1q^2\tau} + B_2e^{i\mathbf{q}\cdot\mathbf{v}_2\tau}e^{-D_2q^2\tau} \tag{IV.38}$$

Using the Siegert relation (IV.33), we obtain:

$$g^{(2)}(\mathbf{q},\tau) - 1 = \left|B_1e^{i\mathbf{q}\cdot\mathbf{v}_1\tau}e^{-D_1q^2\tau} + B_2e^{i\mathbf{q}\cdot\mathbf{v}_2\tau}e^{-D_2q^2\tau}\right|^2 \tag{IV.39}$$

Simplifying further, we have:

$$g^{(2)}(\mathbf{q},\tau) - 1 = B_1^2e^{-2D_1q^2\tau} + B_2^2e^{-2D_2q^2\tau} + 2B_1B_2\cos(\mathbf{q}\cdot\Delta\mathbf{v}\tau)e^{-(D_1+D_2)q^2\tau} \tag{IV.40}$$

where $\Delta\mathbf{v} = \mathbf{v}_1 - \mathbf{v}_2$.

This final expression provides the intensity autocorrelation function for a system with one scattering vector and two distinct drift velocities, extending the model developed in the previous section. It is important to notice that for obtaining oscillations, the dot product must not be 0, so in the case of a vertical velocity the scattering vector must not be in the scattering plane.

IV.1.3. Technical Details of Fluid Dynamics Simulations

Using the Nonisothermal Flow interface in COMSOL, free convection was modeled in water, taking into account both momentum and energy balances. The simulations aimed to provide insights into heat transfer through convection and conduction within the setup. The initial conditions were set as $T_{\text{room}} = 23°\text{C}$ for both the cell and water. The cylindrical glass cell's base was positioned in a thermostated bath that heated only its bottom-most 1 cm. This section of the external surface of the cell maintained a constant temperature, mirroring the bath's temperature. The remaining cell's side walls, which were not submerged in the bath, were in direct contact with a metal component maintained at room temperature, leading to a constant lateral temperature boundary for the cell. Internally, the boundary between the water and glass adhered to a no-slip condition, while the open surface of the water, subject to ambient conditions, was characterized by a slip condition.

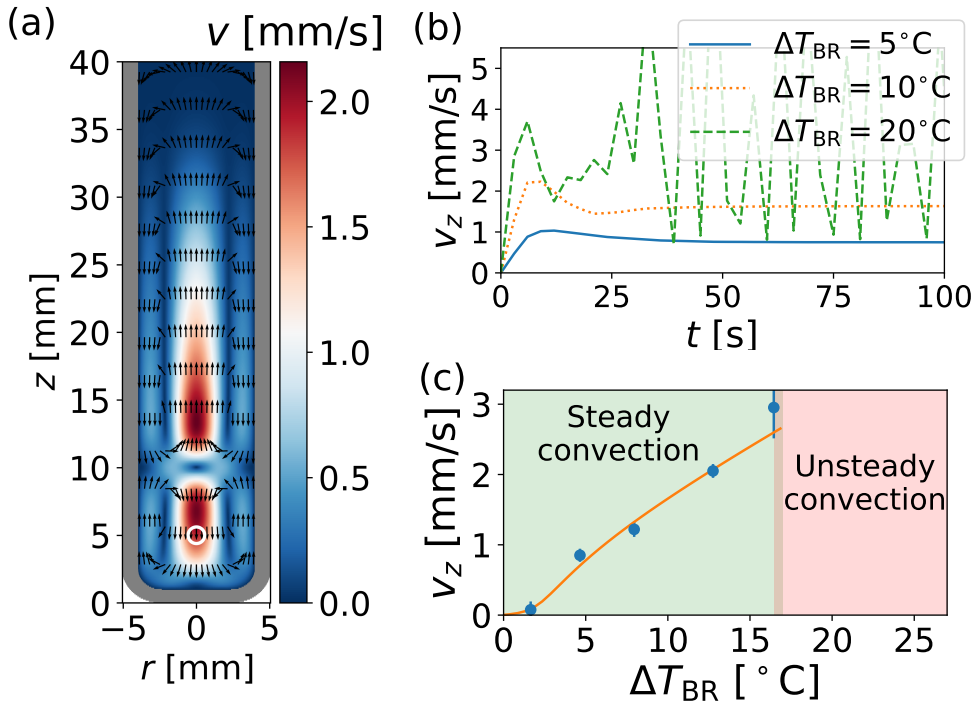

Figure IV.6: Predictions obtained by COMSOL simulations. (a) Velocity profile in stationary conditions, for a temperature gradient given by $\Delta T_{\mathrm{BR}} = 10°\mathrm{C}$. The white circle denotes the measurement point in our DLS device. (b) Time evolution of v_z at the measurement point for different temperature gradients. (c) v_z at the measurement point as a function of the temperature difference, ΔT_{BR} (line). Symbols represent the experimental data, obtained from the average over ten independent DLS measurements using Eq. (IV.31).

This model was used to explore the system response over time to a temperature difference between the bath and the room of $\Delta T_{\mathrm{BR}} = 10°\mathrm{C}$, at which oscillatory behavior in the correlation function was observed in our experiments. For this condition, the fluid dynamics simulation revealed that both the velocity and temperature profiles within the cell eventually reach a steady state. The stationary velocity profile is depicted in Fig. IV.6(a), with the experimental measurement point highlighted by a circle, inside which magnitudes vary less than 1%, and the drift velocities are completely vertical. The temperature there is lower than the bath temperature as an effect of the convection currents. We observe two convective regions above and below the bath level.

However, when ΔT_{BR} becomes significantly large, the system dynamics undergo significant alterations. This is evident from Figure IV.6(b), where the time evolution of vertical velocity at the measuring point for different ΔT_{BR} is presented. For ΔT_{BR} of $5°\mathrm{C}$ and $10°\mathrm{C}$, the system stabilizes between 30 and 40 s. However, at $\Delta T_{\mathrm{BR}} = 20°\mathrm{C}$, a steady state is unattainable, indicating a transition to a non-stationary regime. This behavior entirely aligns with the experimental observations, which identify two regimes based on the ΔT_{BR}.

A physical description of the stationary to non-stationary transition observed in both experiments and fluid dynamics simulations can be explained in terms of the Rayleigh number ($\mathrm{Ra} = \frac{g\beta\Delta T L^3}{\nu\alpha}$), which compares the time scales for thermal transport via diffusion and via convection. According to the literature, there is a critical value, $\mathrm{Ra_c}$, at which the fluid transits from a laminar steady convection state towards a laminar but unsteady convection regime that depends on the geometry [IV.36, IV.37, IV.38, IV.39]. Using the experimental values of the height of the measurement cell ($L = 3.0$ cm), thermal diffusivity of water ($\alpha = 1.43 \cdot 10^{-7}\mathrm{m}^2/\mathrm{s}$), kinematic viscosity ($\nu = 8 \cdot 10^{-7}\mathrm{m}^2/\mathrm{s}$), gravity ($g = 9.81\mathrm{m}/\mathrm{s}^2$), thermal expansion coefficient ($\beta = 4 \cdot 10^{-4}\mathrm{K}^{-1}$), and temperature difference at the transition, we find that $\mathrm{Ra_c} \approx 1.5 \cdot 10^7$, which agrees with the value reported in the literature for a similar cell geometry using adiabatic walls [IV.40].

Bibliography

[IV.1] Sebastian Stock, Regine von Klitzing, and Amin Rahimzadeh. Impact of ultrasound on the motion of compact particles and acousto-responsive microgels. *arXiv preprint arXiv:2307.12696*, 2023.

[IV.2] Xiaobing Feng, Guiqiong Huang, Jian Qiu, Li Peng, Kaiqing Luo, Dongmei Liu, and Peng Han. Dynamic light scattering in flowing dispersion. *Optics Communications*, 531:129225, 2023.

[IV.3] Jonghwan Lee, Weicheng Wu, James Y Jiang, Bo Zhu, and David A Boas. Dynamic light scattering optical coherence tomography. *Optics express*, 20(20):22262–22277, 2012.

[IV.4] Alexander Schavkan. *Dynamics of colloidal systems of magnetic nanoparticles under influence of magnetic fields investigated by XPCS*. PhD thesis, Staats-und Universitätsbibliothek Hamburg Carl von Ossietzky, 2017.

[IV.5] Joachim Wagner, Christian Märkert, Birgit Fischer, and Leonard Müller. Direction dependent diffusion of aligned magnetic rods by means of x-ray photon correlation spectroscopy. *Physical review letters*, 110(4):048301, 2013.

[IV.6] Yuriy Chushkin, Alessandro Gulotta, Felix Roosen-Runge, Antara Pal, Anna Stradner, and Peter Schurtenberger. Probing cage relaxation in concentrated protein solutions by x-ray photon correlation spectroscopy. *Physical Review Letters*, 129(23):238001, 2022.

[IV.7] T. Thurn-Albrecht, W. Steffen, A. Patkowski, G. Meier, Erhard W. Fischer, G. Grübel, and D.L. Abernathy. Photon correlation spectroscopy of colloidal palladium using a coherent x-ray beam. *Physical Review Letters*, 77(27):5437, 1996.

[IV.8] Robert Pecora. *Dynamic light scattering: applications of photon correlation spectroscopy*. Springer Science & Business Media, 1985.

[IV.9] Bruce J Berne and Robert Pecora. *Dynamic light scattering: with applications to chemistry, biology, and physics*. Courier Corporation, 2000.

[IV.10] Takashi Ito, Li Sun, Michael A Bevan, and Richard M Crooks. Comparison of nanoparticle size and electrophoretic mobility measurements using a carbon-nanotube-based coulter counter, dynamic light scattering, transmission electron microscopy, and phase analysis light scattering. *Langmuir*, 20(16):6940–6945, 2004.

[IV.11] Manuel Medrano, Laurent Lobry, Francois Peters, and Alberto T Perez. Measuring the electrophoretic mobility in semi-diluted suspensions by dynamic light scattering. In *2008 IEEE International Conference on Dielectric Liquids*, pages 1–4. IEEE, 2008.

[IV.12] Ekaterina A Savchenko, Alexey N Skvortsov, Elena N Velichko, and Savchenko Elena. Determination of electrophoretic mobilities by dls: homodyne vs heterodyne setup. In *2019 IEEE International Conference on Electrical Engineering and Photonics (EExPolytech)*, pages 315–317. IEEE, 2019.

[IV.13] Emilie Moulin, Irina A Nyrkova, Nicolas Giuseppone, Alexander N Semenov, and Eric Buhler. Homodyne dynamic light scattering in supramolecular polymer solutions: anomalous oscillations in intensity correlation function. *Soft Matter*, 16(12):2971–2993, 2020.

[IV.14] J Josefowicz and FR Hallett. Homodyne electrophoretic light scattering of polystyrene spheres by laser cross-beam intensity correlation. *Applied Optics*, 14(3):740–742, 1975.

[IV.15] Amit Sehgal and Thomas AP Seery. Anomalous dynamic light scattering from solutions of light absorbing polymers. *Macromolecules*, 32(23):7807–7814, 1999.

[IV.16] Klaus Schätzel. Suppression of multiple scattering by photon cross-correlation techniques. *Journal of modern optics*, 38(9):1849–1865, 1991.

[IV.17] Claus Urban and Peter Schurtenberger. Characterization of turbid colloidal suspensions using light scattering techniques combined with cross-correlation methods. *Journal of colloid and interface science*, 207(1):150–158, 1998.

[IV.18] Kenji Katayama, Hiroko Nomura, Hiroki Ogata, and Takeshi Eitoku. Diffusion coefficients for nanoparticles under flow and stop-flow conditions. *Physical Chemistry Chemical Physics*, 11(44):10494–10499, 2009.

[IV.19] Jan KG Dhont. *An introduction to dynamics of colloids*. Elsevier, 1996.

[IV.20] Walter I Goldburg. Dynamic light scattering. *American Journal of Physics*, 67(12):1152–1160, 1999.

[IV.21] GG Fuller, JM Rallison, RL Schmidt, and LG Leal. The measurement of velocity gradients in laminar flow by homodyne light-scattering spectroscopy. *Journal of Fluid Mechanics*, 100(3):555–575, 1980.

[IV.22] D Bicout and G Maret. Multiple light scattering in taylor-couette flow. *Physica A: Statistical Mechanics and its Applications*, 210(1-2):87–112, 1994.

[IV.23] Nico Carl, Julian Sindram, Markus Gallei, Stefan U Egelhaaf, and Matthias Karg. From normal diffusion to superdiffusion: Photothermal heating of plasmonic core-shell microgels. *Physical Review E*, 100(5):052605, 2019.

[IV.24] DP Chowdhury, Christopher M Sorensen, TW Taylor, JF Merklin, and TW Lester. Application of photon correlation spectroscopy to flowing brownian motion systems. *Applied optics*, 23(22):4149–4154, 1984.

[IV.25] Yanwen Sun, Gabriella Carini, Matthieu Chollet, Franz-Josef Decker, Mike Dunne, Paul Fuoss, Stephan O Hruszkewycz, Thomas J Lane, Kazutaka Nakahara, Silke Nelson, et al. Nonuniform flow dynamics probed by nanosecond x-ray speckle visibility spectroscopy. *Physical Review Letters*, 127(5):058001, 2021.

[IV.26] Alfred B Leung, Kwang I Suh, and Rafat R Ansari. Particle-size and velocity measurements in flowing conditions using dynamic light scattering. *Applied optics*, 45(10):2186–2190, 2006.

[IV.27] Sebastian Busch, Torben Haugaard Jensen, Yuriy Chushkin, and Andrei Fluerasu. Dynamics in shear flow studied by x-ray photon correlation spectroscopy. *The European Physical Journal E*, 26:55–62, 2008.

[IV.28] Luis MG Torquato, Nelson Hélaine, Yufan Cui, Roisin O'Connell, Jérémie Gummel, Eric SJ Robles, David Jacob, and João T Cabral. Microfluidic in-line dynamic light scattering with a commercial fibre optic system. *Lab on a Chip*, 23(11):2540–2552, 2023.

[IV.29] Lisa B Aberle, Peter Hülstede, Simone Wiegand, Wolffram Schröer, and Wilfried Staude. Effective suppression of multiply scattered light in static and dynamic light scattering. *Applied Optics*, 37(27):6511–6524, 1998.

[IV.30] George DJ Phillies. Suppression of multiple scattering effects in quasielastic light scattering by homodyne cross-correlation techniques. *The Journal of Chemical Physics*, 74(1):260–262, 1981.

[IV.31] PN Pusey. Suppression of multiple scattering by photon cross-correlation techniques. *Current opinion in colloid & interface science*, 4(3):177–185, 1999.

[IV.32] Beatriz Garcia-Pinel, Alicia Ortega-Rodríguez, Cristina Porras-Alcalá, Laura Cabeza, Rafael Contreras-Cáceres, Raul Ortiz, Amelia Díaz, Ana Moscoso, Francisco Sarabia, José Prados, et al. Magnetically active pnipam nanosystems as temperature-sensitive biocompatible structures for controlled drug delivery. *Artificial Cells, Nanomedicine, and Biotechnology*, 48(1):1022–1035, 2020.

[IV.33] Olga D Parashchuk, Tatyana V Laptinskaya, Maria S Ananieva, and Dmitry Yu Paraschuk. Hyperdiffusive dynamics in conjugated polymer blends and fullerene absorbing solutions. *Soft Matter*, 7(12):5585–5594, 2011.

[IV.34] Wolfgang Schaertl and Christopher Roos. Convection and thermodiffusion of colloidal gold tracers by laser light scattering. *Physical Review E*, 60(2):2020, 1999.

[IV.35] V Ruseva, M Lyons, J Powell, J Austin, A Malm, and J Corbett. Capillary dynamic light scattering: continuous hydrodynamic particle size from the nano to the micro-scale. *Colloids and Surfaces A: Physicochemical and Engineering Aspects*, 558:504–511, 2018.

[IV.36] Subrahmanyan Chandrasekhar. *Hydrodynamic and hydromagnetic stability*. Courier Corporation, 2013.

[IV.37] RM Clever and FH Busse. Transition to time-dependent convection. *Journal of Fluid Mechanics*, 65(4):625–645, 1974.

[IV.38] John Patterson and Jorg Imberger. Unsteady natural convection in a rectangular cavity. *Journal of Fluid Mechanics*, 100(1):65–86, 1980.

[IV.39] P Oresta, G Stringano, and R Verzicco. Transitional regimes and rotation effects in rayleigh–bénard convection in a slender cylindrical cell. *European Journal of Mechanics-B/Fluids*, 26(1):1–14, 2007.

[IV.40] P Le Quéré. Transition to unsteady natural convection in a tall water-filled cavity. *Physics of Fluids A: Fluid Dynamics*, 2(4):503–515, 1990.

Publication V

Device and method for characterizing relative drift velocities in colloidal salmples

López-Molina, J.[1] and Tirado-Miranda, M. [1]

[1]*Departamento de Física Aplicada, Universidad de Granada, Campus Fuentenueva S/N, 18071 Granada, Spain*

Published in

Oficina Española de Patentes y Marcas

Spanish Patent and Trademark Office

The research that led to the publication presented in Chapter IV also resulted in the development of a patent proyect. After observing that the use of two intersecting beams produces oscillations in the correlation function, we realized that we could measure relative velocities of particle populations using a single beam. Furthermore, we could explore the accessible velocity range by modifying the beam's inclination relative to the vertical axis. This insight led us to propose a patent for a device capable of controlling the incident angle of the beam on the sample.

Given that patent documents are typically written in highly technical and legal language, we present here a summary of the invention proposal and its capabilities. The complete technical details and specifications can be found in the Spanish Patent and Trademark Office database under reference number P202330112 [V.1].

V.1. Device Description

Our proposal extends traditional Dynamic Light Scattering capabilities by introducing a variable incident angle configuration. Figure (V.1) shows the experimental setup of our device. The setup consists of a laser source ($\lambda = 632$ nm) and an optical system that allows precise control of the incident beam angle while maintaining measurement consistency.

The key component of our design is the optical arrangement that ensures the beam always passes through the same point in the sample, regardless of its incident angle. This is achieved through a parabolic convergent lens positioned so that its focus coincides with the center of the sample cell. We control the incident angle by adjusting the vertical position of a mobile mirror, which modifies the beam's inclination relative to the vertical axis.

When particles in the sample move with different velocities due to any external field, their relative motion can be detected through the scattered light. The incident beam, entering at a controlled angle to the vertical, interacts with these moving particles and produces characteristic patterns in the intensity correlation function. Figure (V.2) demonstrates this effect through simulated correlation functions for two cases: a sample without relative motion between particles and a sample where one population moves relative to the other.

For a system with particles in motion, the intensity correlation function takes the form (see Appendix Publication IV):

$$g^{(2)}(\mathbf{q},\tau) - 1 = A_1^2 e^{-2D_1 q^2 \tau} + A_2^2 e^{-2D_2 q^2 \tau} + A_{12} \cos(\mathbf{q}\cdot\Delta\mathbf{v}\tau) e^{-(D_1+D_2)q^2\tau} \quad \text{(V.1)}$$

where D_1 and D_2 are the diffusion coefficients of the two particle populations, A_1 and A_2 are their respective amplitudes, and $\Delta\mathbf{v}$ is their relative velocity. The scattering

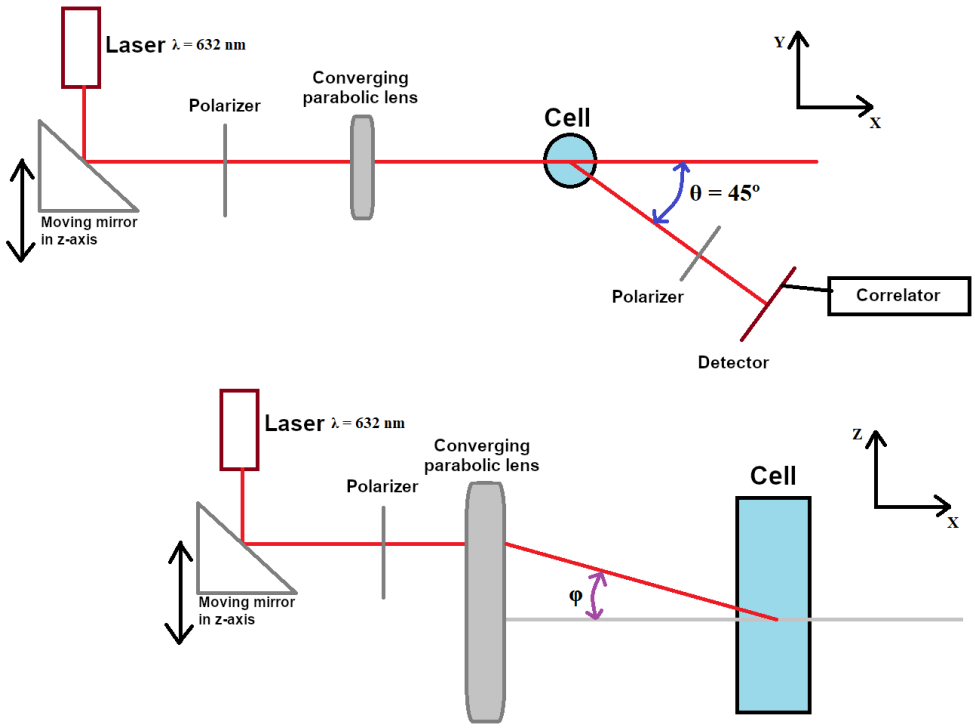

Figure V.1: Schematic representation of the experimental setup. Top: XY plane view showing the scattering angle $\theta = 45°$. Bottom: XZ plane view showing the incident angle φ that can be modified by moving the mirror along the Z axis.

vector $\mathbf{q}$ depends on both the scattering angle θ and the incident angle φ:

$$\mathbf{q} = \mathbf{k_s} - \mathbf{k_i} \tag{V.2}$$

where $\mathbf{k_i}$ and $\mathbf{k_s}$ are the incident and scattered wave vectors, respectively. The magnitude of $\mathbf{q}$ is given by:

$$q = \frac{4\pi n}{\lambda} \sin(\theta/2) \tag{V.3}$$

When the incident beam enters at an angle φ relative to the horizontal plane, the vertical component of $\mathbf{q}$ becomes:

$$q_z = \frac{2\pi n}{\lambda} \sin(\varphi) \tag{V.4}$$

The frequency of the oscillations in the correlation function is determined by the dot product $\mathbf{q} \cdot \Delta\mathbf{v}$. By adjusting the incident angle φ, we can modify q_z and thus control our sensitivity to vertical velocity differences. Larger values of φ increase

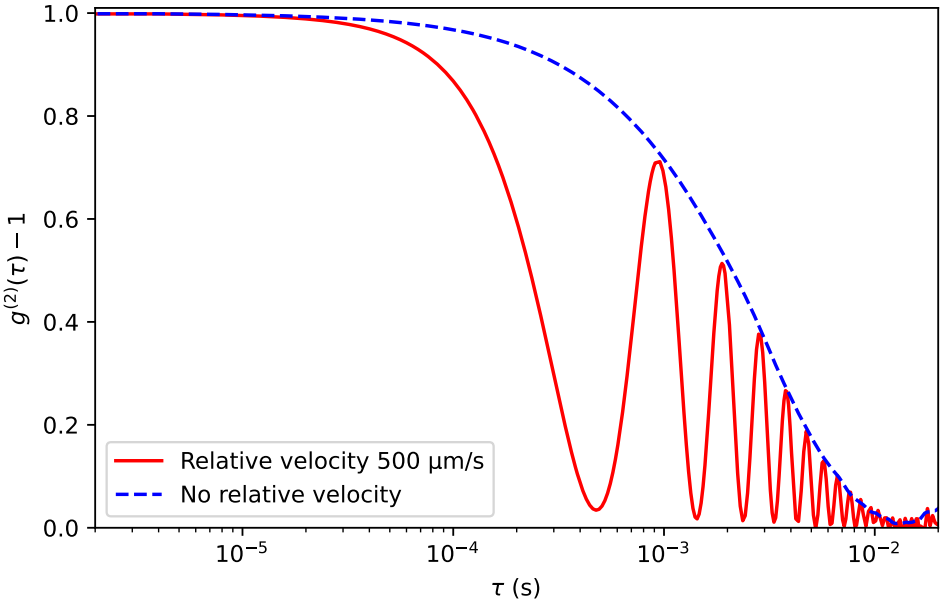

Figure V.2: Simulated intensity correlation functions. (a) Sample without relative motion between particles, showing a simple exponential decay. (b) Sample with two populations with different velocities, showing characteristic oscillations in the correlation function.

the vertical component of $\mathbf{q}$, allowing us to detect smaller velocity differences. This control over the incident angle therefore provides a way to tune the measurement sensitivity and access a wider range of measurable relative velocities.

V.2. Applications and Significance

The variable incident angle configuration provides significant advantages in studying particle dynamics. When particles in a sample move at different velocities, the correlation function exhibits oscillations whose frequency depends on their relative velocity. By adjusting the incident angle, we can optimize the detection conditions for different velocity ranges, making the technique adaptable to various experimental requirements.

This innovation proves particularly valuable in several research contexts. For instance, when studying particle sedimentation, where particles of different sizes move at different velocities, our device can help characterize these velocity differences with high precision. Similarly, in systems where external fields induce differential particle motion, the ability to adjust the incident angle allows us to optimize the

measurement conditions for the specific velocity range of interest.

The proposed device introduces a new approach to measuring relative velocities between particle populations through control of the incident beam angle. The optical configuration allows for adjustment of the scattering vector's vertical component, enabling measurements of different velocity ranges. The device can be used to study systems where particle populations exhibit differential motion, regardless of the mechanism inducing this motion. Its applications extend to both research and industrial settings where characterization of relative particle velocities is needed.

Bibliography

[V.1] J. López-Molina and M. Tirado-Miranda. Dispositivo y mÉtodo de caracterizaciÓn de una muestra con partÍculas, 2023. URL: https://consultas2.oepm.es/InvenesWeb/detalle?referencia=P202330112.

Publication VI

Recovery of Size Distributions from Dynamic Light Scattering using Convolutional Neural Networks

López-Molina, J.[1], Tirado-Miranda, M. [1] and Moncho-Jordá, A.[1,2]

[1]*Departamento de Física Aplicada, Universidad de Granada, Campus Fuentenueva S/N, 18071 Granada, Spain*

[2]*Institute Carlos I for Theoretical and Computational Physics, Facultad de Ciencias, Universidad de Granada, Campus Fuentenueva S/N, 18071 Granada, Spain*

Not published

UNIVERSIDAD DE GRANADA

This paper proposes a convolutional neural network (CNN) to recover the particle size distribution $P(R)$ from the intensity autocorrelation function measured in Dynamic Light Scattering (DLS). The inverse Laplace transform involved in this process is traditionally addressed by methods such as CONTIN, which can be sensitive to noise and to the choice of regularization parameters. To assess the effectiveness of the proposed approach, we synthetically generated one-, two- and three-peak Gaussian distributions, computed the corresponding autocorrelation functions, and added noise to simulate realistic DLS data. We then trained a CNN with these noisy signals. The model performance was evaluated against CONTIN using mean squared error (MSE), mean absolute error (MAE), Kullback–Leibler divergence (KL), the match in the number of peaks with respect to the ground truth, and a human visual validation. We also extend the analysis to additional simulated conditions and varying noise levels. The results suggest that the proposed CNN is a robust and competitive alternative to CONTIN for determining $P(R)$ in DLS measurements.

VI.1. Introduction

Dynamic Light Scattering (DLS) has emerged as an indispensable technique for characterizing the size distribution of colloidal systems through the analysis of time-dependent fluctuations in scattered light intensity [VI.1, VI.2, VI.3, VI.4, VI.5]. At its core, DLS measurements yield an intensity autocorrelation function, $g^{(2)}(\tau)$, which encodes crucial information about particle diffusivities and, consequently, particle size distributions. Accurate recovery of particle size distributions is crucial for applications ranging from quality control in pharmaceutical formulations to monitoring nanoparticle synthesis and studying protein aggregation. However, the extraction of size distribution information from $g^{(2)}(\tau)$ presents a significant challenge, as it constitutes a non-trivial inverse problem that is inherently ill-posed.

The scientific community has traditionally relied on two principal approaches to address this problem. The first approach, known as the cumulant method, [VI.6] approximates the correlation function through a series expansion. While this method proves effective for monomodal distributions exhibiting low polydispersity, it fails to adequately characterize systems that are either polydisperse or multimodal [VI.5]. The second approach, embodied in the CONTIN algorithm developed by Provencher [VI.7], treats the correlation function as a Laplace transform of the size distribution and attempts to solve the inverse problem through the application of regularization constraints. Although CONTIN offers greater flexibility than the cumulant method, it still imposes specific conditions such as non-negativity and smoothness, and often struggles when confronted with closely overlapping multiple modes. Several studies have documented CONTIN's limitations, particularly its sensitivity to noise and difficulty in resolving closely spaced peaks. [VI.8, VI.9] These limitations become especially pronounced when analyzing complex mixtures or when working with experimental data affected by measurement noise.

It is important to note that noise in correlation functions is inherent to the measurement process in DLS experiments. This inherent noise arises from various sources in real systems, including the finite number of particles in the scattering volume, limited temporal averaging during measurements, statistical uncertainties in ensemble averages, and thermal fluctuations in the detection system. In simulations, additional noise can emerge from insufficient statistical sampling in the averaging process. Since noise is always present to some degree in experimental data, it becomes imperative to develop inversion methods capable of working with noise-affected correlation functions while still accurately recovering the underlying particle size distribution. [VI.5, VI.2]

Recent advances in Machine Learning (ML) have opened new avenues for addressing this inverse problem, with several pioneering studies demonstrating its potential across different applications. Early work by Chicea [VI.10] showed that ML could effectively predict average particle diameters from autocorrelation

functions in monomodal systems. Wang et al. [VI.11] extended this approach to bimodal distributions using generalized regression neural networks, though limited to well-separated peaks. In the pharmaceutical domain, Shrivastava et al. [VI.12] applied ML to quantify size-based heterogeneity in monoclonal antibodies, while other researchers have explored ML for specific applications such as cancer subtype classification from DLS microscopy [VI.13] and aerosol characterization [VI.14]. Despite these advances, existing ML approaches have primarily focused on simple distributions or specific use cases, leaving open the need of developing a general-purpose solution capable of handling complex multimodal distributions where peaks significantly overlap under realistic measurement conditions.

In this context, we present a ML-based approach utilizing convolutional neural networks (CNNs) to enhance the robustness of size distribution retrieval from noisy autocorrelation functions. Our approach is specifically designed to handle mono-, bi-, and trimodal distributions with arbitrary peak separations and widths, addressing a significant limitation of existing methods that typically struggle with closely spaced or overlapping modes. We incorporate noise conditions directly in the training process, ensuring robust performance in practical applications. Unlike previous work that has focused on specific distribution types or idealized conditions, our method provides a comprehensive solution that maintains high accuracy across a broad spectrum of distribution complexities.

The present work aims to advance DLS analysis through several complementary objectives. Our primary focus is the development and implementation of a CNN architecture specifically optimized for predicting particle size distributions from autocorrelation functions under realistic conditions. Through comprehensive evaluation, we conduct systematic comparisons between our CNN approach and CONTIN, with particular emphasis on performance across different noise levels and distribution complexities. The robustness of the proposed model is evaluated through multiple quantitative metrics supplemented by human visual validation, while its generalization capabilities are assessed through extended testing under various simulated conditions. Through this comprehensive approach, we demonstrate that deep learning can provide a more reliable and efficient solution for DLS analysis, particularly for complex multimodal distributions.

VI.2. Methodology

This section presents our methodological approach for developing and validating a neural network solution to analyze DLS data, as illustrated in Figure (VI.1). Our methodology comprises three main stages: data generation, network training, and comparative validation. In the first stage, we generate a comprehensive synthetic dataset of particle size distributions ranging from monomodal to trimodal

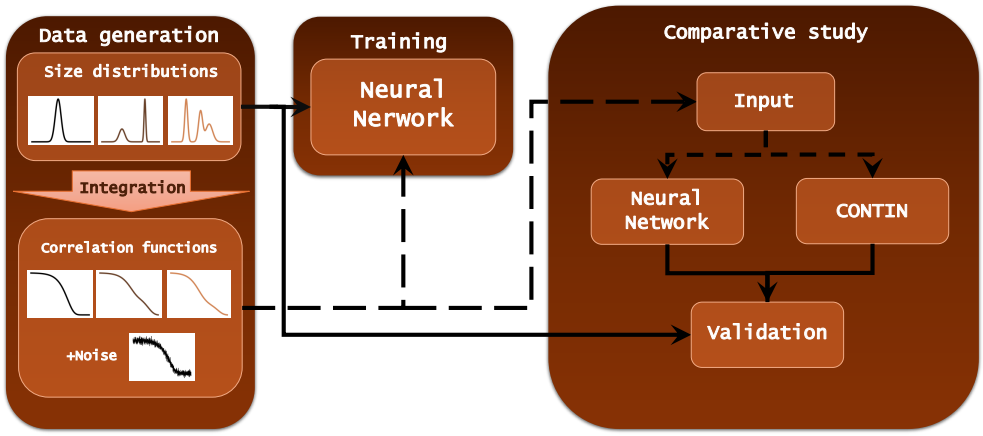

Figure VI.1: Overview of the methodology. The workflow consists of three main components: (1) synthetic data generation, where particle size distributions are created and transformed into correlation functions with optional noise addition, (2) neural network training using the generated dataset, and (3) comparative validation study between our neural network approach and the traditional CONTIN method.

configurations, which are then transformed into correlation functions through numerical integration, with optional noise addition. The second stage involves training a specially designed neural network architecture to learn the inverse transformation from correlation functions to size distributions. Finally, we conduct a comparative study to evaluate our neural network's performance against the established CONTIN method, providing a thorough validation of our approach's effectiveness in analyzing DLS data.

VI.2.1. Synthetic Data Generation

To train and validate our network, we generated synthetic size distributions $P(R)$ based on Gaussian peaks, assuming spherical particles throughout all simulations. We begin by selecting the number of peaks in the particle size distribution, randomly choosing between one (monomodal), two (bimodal) and three peaks (trimodal). For each chosen number of modes M, we construct the size distribution as a sum of M distinct Gaussian-like peaks:

$$P(R) = \sum_{i=1}^{M} A_i \exp\left(-\frac{(R - R_i)^2}{2\sigma_i^2}\right), \tag{VI.1}$$

where A_i, R_i, and σ_i represent the amplitude, mean radius, and standard deviation of each mode, respectively. The amplitudes A_i are randomly selected from a uniform distribution in the interval [0.5,1] and then normalized to ensure that $P(R)$ satisfies

the normalization condition:

$$\int_0^\infty P(R)dR = 1. \tag{VI.2}$$

The mean size R_i of each mode is drawn from a uniform distribution over the interval [10 nm, 1000 nm], capturing a broad spectrum that includes both relatively small and large colloids. The standard deviation σ_i of each mode is sampled from 0.5% to 5% of the corresponding mean R_i, representing varying degrees of polydispersity within each subpopulation.

We model the intensity autocorrelation function $g_2(\tau)$ via an integral expression analogous to a Laplace transform:

$$g_2(\tau) = \int P(R)\, e^{-2D(R)q^2\tau}\, dR, \tag{VI.3}$$

where $D(R)$ denotes the diffusion coefficient and q is the scattering wave vector. In all simulations, we considered a detection angle $\theta = 30^\circ$ and a laser wavelength $\lambda = 632.8$ nm, which determines the scattering wave vector through $q = (4\pi n/\lambda)\sin(\theta/2)$, where n is the refractive index of the medium (in our case, water). While this work could be generalized to analyze decay rate distributions directly, we chose to work in the particle size space for its more immediate physical interpretation. For spherical particles, the diffusion coefficient is given by the Stokes-Einstein relation $D(R) = k_B T/(6\pi\eta R)$, where k_B is the Boltzmann constant, T is the absolute temperature, and η is the solvent viscosity. For each synthetic $P(R)$, the function $g_2(\tau)$ was computed for 400 delay times τ sampled logarithmically in the range $[10^{-6} - 10^{-1}]$ s. This integral is performed numerically. The result is a synthetic correlation function $g_2(\tau)$ paired with its known ground-truth distribution $P(R)$. By repeating this process for $5 \cdot 10^5$ of randomly generated distributions, we create a large, heterogeneous dataset that spans from simple monomodal cases to more intricate bimodal and trimodal scenarios.

To train a model robust to variations in signal-to-noise ratio, gaussian noise with standard deviation 0.005 was added to half of the generated $g_2(\tau)$.

VI.2.2. Neural Network Architecture and Training

The neural network architecture developed for this work transforms DLS correlation data into particle size distributions through a combination of convolutional and dense layers. Before delving into the specific details, we present a high-level overview of our design approach: the network first identifies characteristic patterns in the correlation function using convolutional layers, then processes these patterns through dense layers to reconstruct the size distribution. These patterns include both local features (such as decay rates at specific time scales) and global characteristics

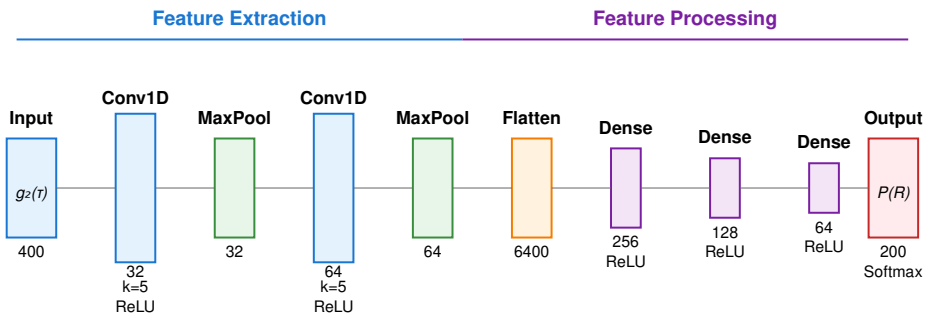

Figure VI.2: Schematic representation of the neural network architecture. The network processes the input autocorrelation function $g_2(\tau)$ through multiple convolutional and dense layers to predict the particle size distribution $P(R)$. The architecture combines feature extraction through convolutional layers with feature processing through dense layers to achieve accurate distribution prediction.

(like the overall shape of the correlation function). Detailed information about the architecture selection can be found in Appendix VI.5. Figure (VI.2) presents a schematic overview of the network structure, which can be divided into feature extraction and feature processing stages.

The network accepts as input the autocorrelation function $g_2(\tau)$, which contains the temporal correlation information from DLS functions. The feature extraction stage begins with a one-dimensional convolutional layer (Conv1D) containing 32 filters with a kernel size of 5 and 'same' padding. Each filter is designed to detect specific temporal patterns in the correlation function, such as rapid decay characteristics (indicating small particles), gradual decay patterns (suggesting larger particles), or mixed decay behaviors (implying multiple size populations). These filters, activated by a Rectified Linear Unit (ReLU) function, effectively create a set of pattern detectors that respond to different correlation function features. A MaxPooling layer with pool size 2 follows, reducing dimensionality while preserving essential features and effectively increasing the receptive field of subsequent layers.

A second convolutional block, comprising 64 filters of the same kernel size, processes the downsized feature maps to capture more complex patterns. While the first layer identifies basic decay characteristics, this second layer combines these primary features to recognize more sophisticated patterns, such as the presence of multiple decay rates (indicating multiple particle populations) or subtle variations in decay profiles (suggesting size distribution widths). This hierarchical pattern recognition is crucial for distinguishing between monomodal, bimodal, and more complex distributions. Another MaxPooling layer further reduces the spatial dimensions, completing the feature extraction phase.

The feature processing stage begins with a Flatten operation that transforms the two-dimensional feature maps into a one-dimensional vector. This flattened representation feeds into a sequence of densely connected layers with decreasing sizes of 256, 128, and 64 neurons, each employing ReLU activation functions. The progressive reduction in layer size creates a bottleneck architecture that distills the most relevant information for size distribution prediction. These dense layers learn the non-linear mapping between the extracted features and the desired output distribution.

The output layer consists of a dense layer with dimension 400, followed by a softmax activation function. This activation ensures that the network's output, representing the discretized probability density function $P(R)$, satisfies the appropriate normalization conditions. Specifically, if we denote the network's output at discrete radius values R_i as $P_d(R_i)$, this represents the integral of the continuous probability density function $P(R)$ over a small interval ΔR_i around R_i:

$$P(R_i) = \int_{R_i - \Delta R_i/2}^{R_i + \Delta R_i/2} P(R) dR \tag{VI.4}$$

The softmax activation ensures:

$$\sum_i P(R_i) = 1 \quad \text{and} \quad P(R_i) \geq 0 \quad \forall i \tag{VI.5}$$

The network is trained using the Adam optimizer [VI.15], which adaptively adjusts learning rates for efficient convergence. The Kullback-Leibler (KL) divergence serves as the loss function:

$$\mathcal{L}_{\text{KL}} = \sum_i P_{\text{true}}(R_i) \log \left(\frac{P_{\text{true}}(R_i)}{P_{\text{pred}}(R_i)} \right) \tag{VI.6}$$

where $P_{\text{true}}(R_i)$ represents the discretized ground truth distribution and $P_{\text{pred}}(R_i)$ is the network's predicted distribution. This choice of loss function is particularly appropriate for distribution prediction tasks, as it naturally handles the comparison between probability distributions and is sensitive to distribution shape differences [VI.16].

The architecture's design reflects key considerations specific to DLS data processing: the convolutional layers capture temporal patterns at multiple scales, the MaxPooling layers manage computational complexity while preserving essential features, and the dense layers enable non-linear mapping to the final size distribution. This combination creates a robust architecture capable of learning the complex relationship between correlation functions and particle size distributions.

A large dataset of 500000 functions was generated, composed of single-, double-, and triple-peak distributions, each at varying noise levels. Approximately 70% of the

data was used for training, 15% for validation, and 15% for testing. The network was trained using batches of 128 correlation functions with learning rate scheduling to prevent overfitting. During training, we monitored the Kullback–Leibler divergence on both the training and validation sets to gauge convergence. The training process was terminated when the validation loss showed no improvement for 20 consecutive epochs, ensuring optimal model performance while preventing overfitting.

VI.2.3. CONTIN Method

The analysis of Dynamic Light Scattering (DLS) data to obtain particle size distributions requires solving an inverse Laplace transform problem, which is inherently ill-posed [VI.7]. To address this challenge, we employed the CONSTRAINED REGULARIZATION (CONTIN) method developed by Provencher, implementing it with Tikhonov regularization [VI.17, VI.18]. This approach provides a framework for extracting particle size distributions from intensity autocorrelation functions while maintaining physical meaningfulness and statistical reliability.

The measured intensity autocorrelation function $g_2(\tau)$ and the particle size distribution are related through the electric field autocorrelation function $g_1(\tau)$ via the Siegert relation [VI.5]:

$$g_2(\tau) = 1 + \beta|g_1(\tau)|^2 \tag{VI.7}$$

where β is an instrumental parameter depending on the experimental geometry and coherence conditions. The electric field autocorrelation function is expressed as a continuous distribution of exponential decays:

$$g_1(\tau) = \int_0^\infty P(R)\exp(-\Gamma(R)\tau)dR \tag{VI.8}$$

Here, $P(R)$ represents the size distribution function, and $\Gamma(R)$ is the decay rate for particles of hydrodynamic radius R. The decay rate relates to the diffusion coefficient $D(R)$ through:

$$\Gamma(R) = 2D(R)q^2 \tag{VI.9}$$

where q is the scattering vector magnitude. The Stokes-Einstein equation connects the diffusion coefficient to the hydrodynamic radius:

$$D(R) = \frac{k_B T}{6\pi\eta R} \tag{VI.10}$$

with k_B as the Boltzmann constant (1.38×10^{-23} J/K), T as the absolute temperature (298 K in our implementation), and η as the solvent viscosity (0.001 Pa·s for water).

Our implementation of the CONTIN method utilizes Tikhonov regularization with discretization of the size distribution using logarithmically spaced bins [VI.19]. This spacing allows effective capture of the particle size range typically present in colloidal systems. The algorithm minimizes a functional combining data fidelity and regularization terms while enforcing non-negativity constraints:

$$\min_{x \geq 0} \{\|Ax - y\|^2 + \alpha \|x\|^2\} \tag{VI.11}$$

The vector x represents the discretized size distribution, y contains the measured autocorrelation data, and A is the kernel matrix containing the theoretical decay functions. We employ zero-order Tikhonov regularization, using the identity matrix as the regularization operator.

The numerical implementation begins with the discretization of the size range into logarithmically spaced bins according to $R_i = R_{\min}(R_{\max}/R_{\min})^{i/N}, \quad i = 0, \ldots, N-1$, where $N = 200$ is the number of bins, with R_{min} and R_{max} defining the size range boundaries. For each size bin, we calculate the corresponding diffusion coefficient and decay rate using the Stokes-Einstein equation. The kernel matrix elements are then constructed as:

$$A_{ij} = \exp(-\tau_i \Gamma(R_j)) \tag{VI.12}$$

where τ_i represents the correlation delay times.

The system is solved using non-negative least squares optimization [VI.20], ensuring the physical requirement of non-negative size distributions. The regularization parameter α is set to 10^{-4}, providing an appropriate balance between resolution and stability.

This implementation of the CONTIN method with Tikhonov regularization maintains computational efficiency while ensuring physically meaningful results through the combination of logarithmic size binning, zero-order regularization, and non-negative constraints.

VI.3. Results

VI.3.1. Representative Examples

Figure (VI.3) presents a comparative analysis of particle size distributions obtained through different methods. Each of the six subplots displays three

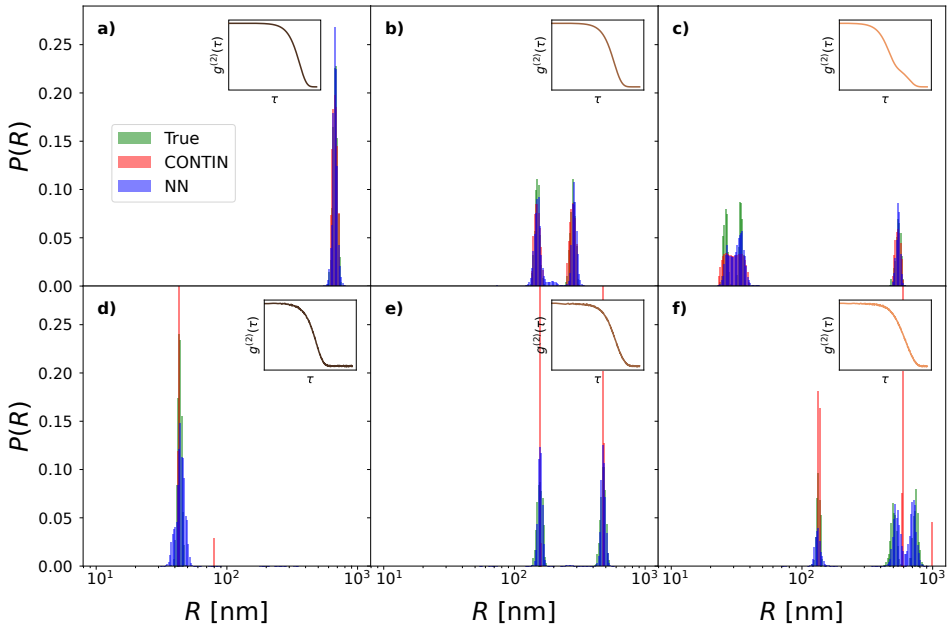

Figure VI.3: Comparison of particle size distributions obtained through different methods. Each subplot shows the true distribution (green) used to generate the correlation function (shown in inset), along with distributions recovered using CONTIN (red) and our Neural Network approach (blue). Top row (a-c) shows results without added noise, while bottom row (d-f) shows results with gaussian noise of 0.005 amplitude added to the correlation functions. The columns represent increasing complexity: monomodal (a,d), bimodal (b,e), and trimodal (c,f) distributions.

distributions: the true (ground truth) distribution used to generate the correlation function (shown in the inset of each subplot), and the reconstructed distributions using both the CONTIN method and our Neural Network (NN) approach. The figure is organized in two rows, where the top row (subplots a-c) represents cases without added noise, while the bottom row (subplots d-f) shows distributions with gaussian noise of 0.005 amplitude added to the correlation functions. As evident from the insets, the added noise produces minimal visual changes in the correlation functions.

It is important to note that while this figure provides valuable insights into the performance of both methods, definitive conclusions cannot be drawn from these six cases alone. A comprehensive statistical analysis over a larger dataset will be presented later to establish robust conclusions about the relative performance of each method.

Examining the monomodal distributions (subplots a and d), we observe that in the noise-free case (a), both CONTIN and NN methods accurately reproduce the true distribution, with their predictions largely overlapping the ground truth. However, when noise is introduced (subplot d), significant differences emerge. While CONTIN

captures the peak position, it fails to preserve the distribution width, producing an artificially narrow peak. Moreover, it generates a spurious secondary peak that could lead to misinterpretation of the particle size distribution. In contrast, our NN approach maintains better fidelity to the true distribution shape, albeit with a slight overestimation of the distribution width, and notably avoids the generation of spurious peaks.

For the bimodal case (subplots b and e), both methods perform effectively in the noise-free scenario (b), accurately reproducing the true distribution. Our NN approach generates a small artificial peak between the main peaks, which led us to implement a 0.01 threshold to filter out such artifacts. When noise is introduced (subplot e), we observe behavior similar to the monomodal case: CONTIN captures the peak positions but produces artificially narrow distributions. In contrast, our NN method demonstrates remarkable robustness, producing a reconstruction that closely matches the true distribution.

The trimodal distributions (subplots c and f) present the most challenging test cases. In the noise-free scenario (c), both methods accurately capture the rightmost peak but struggle to fully resolve the two leftmost peaks. However, the NN approach provides better peak definition compared to CONTIN, preserving more information about the underlying distribution structure. The addition of noise (subplot f) highlights the superior performance of our NN method. While CONTIN only accurately captures the leftmost peak's position and generates spurious peaks near the other true peak locations, our NN approach maintains excellent fidelity to the true distribution, demonstrating its robustness even in this complex scenario.

These results suggest that our NN-based approach offers improved resilience to noise compared to CONTIN, particularly in cases involving multiple peaks. However, a more comprehensive statistical analysis is necessary to quantify these improvements and establish their significance across a broader range of distribution types and noise levels.

VI.3.2. Quantitative Performance Analysis

To rigorously evaluate the performance of our Neural Network approach compared to the CONTIN method, we conducted a comprehensive statistical analysis using three different error metrics: Mean Square Error (MSE), Mean Absolute Error (MAE), and Kullback-Leibler (KL) divergence. For each metric, we analyzed the performance across different noise levels and distribution types (monomodal, bimodal, and trimodal), with each data point representing an average over 10000 samples. It is important to note that our Neural Network was specifically trained using only two noise conditions: noise-free data and data with a noise amplitude of 0.005.

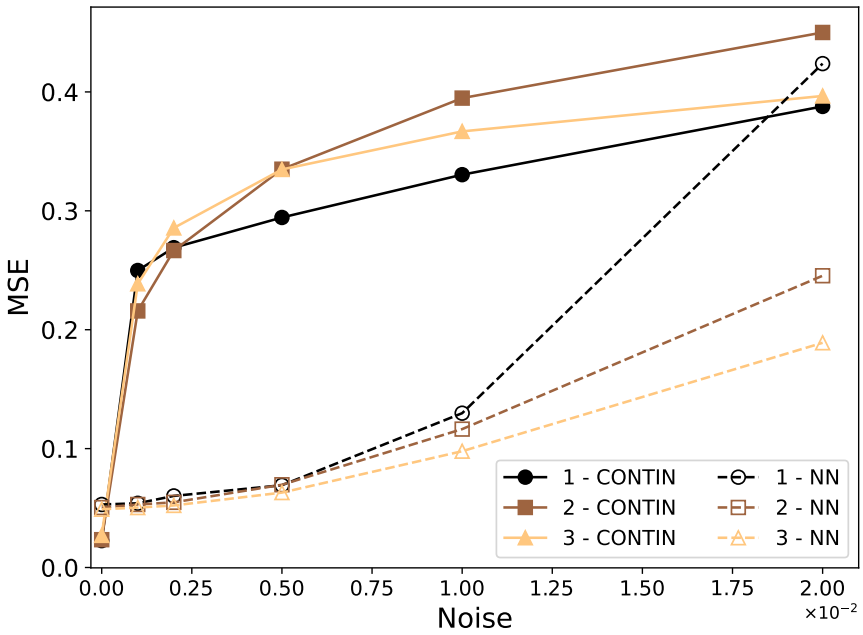

Figure VI.4: Mean Square Error (MSE) as a function of noise amplitude for both CONTIN (solid lines and filled symbols) and Neural Network (dashed lines and empty symbols) methods. Results are shown for monomodal (circles), bimodal (squares), and trimodal (triangles) distributions. Each point represents the average over 10000 samples.

Figure (VI.4) presents the MSE analysis, where the error is calculated as $\sum(P_{true} - P_{pred})^2$. This metric ranges from 0 for perfect overlap to 2 in the extreme case where the predicted and true distributions have no overlap and all probability is concentrated in single, different bins. At zero noise, CONTIN demonstrates superior performance with near-zero MSE for all distribution types, slightly outperforming our Neural Network. However, a striking feature appears with the introduction of even minimal noise (0.001): CONTIN exhibits a sharp increase in MSE that continues to grow with increasing noise amplitude. This abrupt degradation can be attributed to CONTIN's tendency to produce delta-function-like distributions under noisy conditions, as previously observed in the qualitative analysis.

In contrast, our Neural Network maintains relatively stable and low MSE values up to noise levels of 0.005 (corresponding to its training condition). Beyond this noise threshold, the MSE increases more gradually than CONTIN, while maintaining better overall performance. Interestingly, at high noise levels (0.02, four times the training noise), we observe a counterintuitive trend where monomodal distributions show higher MSE than bimodal and trimodal cases. This behavior can be explained

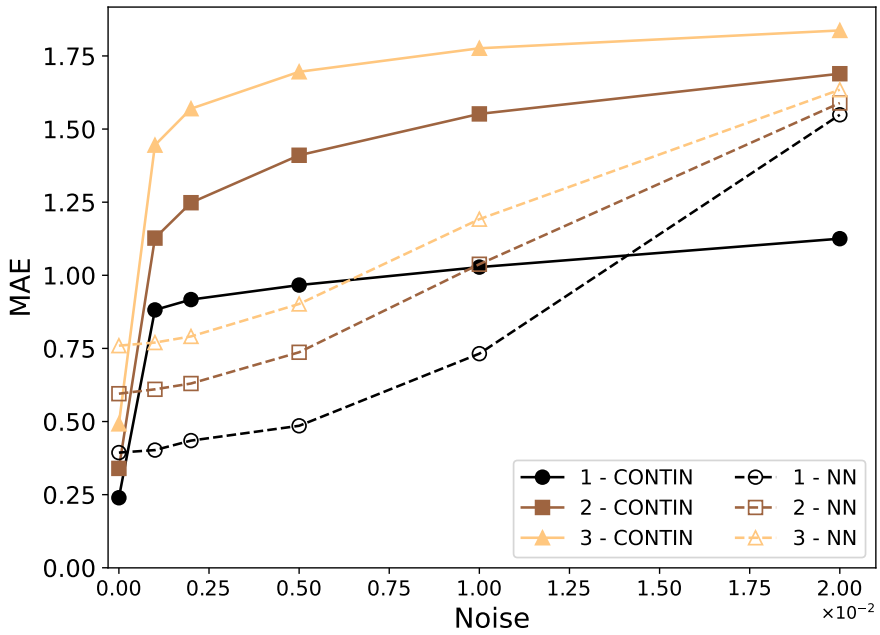

Figure VI.5: Mean Absolute Error (MAE) as a function of noise amplitude for both CONTIN (solid lines and filled symbols) and Neural Network (dashed lines and empty symbols) methods. Results are shown for monomodal (circles), bimodal (squares), and trimodal (triangles) distributions. Each point represents the average over 10000 samples.

by the distribution of probability mass: in multimodal distributions, the total probability is divided among multiple peaks, resulting in lower individual bin values. Since MSE is particularly sensitive to large deviations, the lower amplitudes in multimodal distributions lead to smaller squared errors despite potentially poorer overall distribution recovery, making it seem that the one-peak performance is worse than the three-peak performance.

Figure (VI.5) shows the MAE results, calculated as $\sum |P_{true} - P_{pred}|$, which ranges from 0 for perfect overlap to 2 for completely non-overlapping distributions. This metric provides a less restrictive measure of error compared to MSE, as it does not disproportionately penalize large deviations. The general trends mirror those observed in the MSE analysis: CONTIN shows superior performance under noise-free conditions but experiences a sharp performance degradation with minimal noise introduction.

For monomodal distributions, CONTIN's MAE stabilizes around 1 after the initial jump, consistent with the loss of distribution width information while maintaining

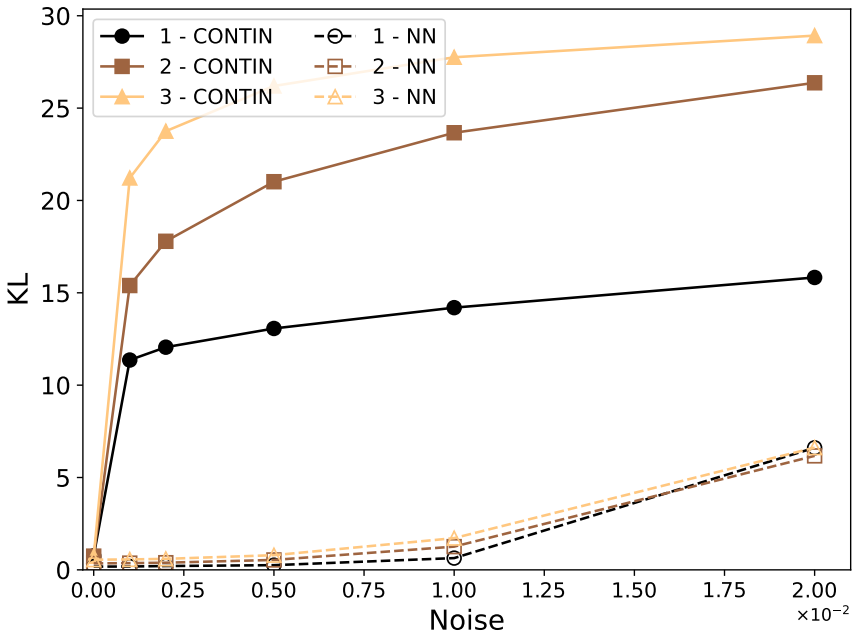

Figure VI.6: Kullback-Leibler divergence as a function of noise amplitude for both CONTIN (solid lines and filled symbols) and Neural Network (dashed lines and empty symbols) methods. Results are shown for monomodal (circles), bimodal (squares), and trimodal (triangles) distributions. Each point represents the average over 10000 samples.

accurate peak position. The performance deterioration is more severe for multimodal distributions, with MAE reaching 1.6 and 1.8 for bimodal and trimodal cases, respectively. This suggests that CONTIN's regularization approach, while effective at preventing noise overfitting, may overconstrain the solution space for complex distributions under noisy conditions.

Our Neural Network demonstrates superior noise resilience, maintaining lower MAE values even at twice its training noise level (0.01). However, at very high noise (0.02), its performance converges with CONTIN for multimodal cases, while showing worse performance for monomodal distributions, highlighting the limitations of extrapolating beyond training conditions.

Figure (VI.6) presents the KL divergence analysis obtained via Eq.(VI.6), which provides a more nuanced measure of distribution similarity by capturing relative differences between distributions. This metric is particularly valuable for DLS analysis as it better handles cases where distributions are slightly shifted or have partial overlap, situations where MAE and MSE might indicate poor performance

despite qualitatively reasonable results.

The KL divergence results reveal that our Neural Network consistently outperforms CONTIN across all noise levels and distribution types. CONTIN exhibits the familiar pattern of sharp performance degradation with noise introduction, with performance decreasing monotonically from monomodal to trimodal cases. In contrast, our Neural Network maintains remarkably consistent and low KL divergence values across all distribution types up to 0.01 noise amplitude, demonstrating robust performance even beyond its training noise level. Even at 0.02 noise, while showing increased error, the Neural Network maintains significantly better performance than CONTIN.

The superior performance under the KL divergence metric, particularly in preserving distribution width information, suggests that our Neural Network approach better maintains the overall shape and information content of the particle size distributions, even under challenging noise conditions.

While traditional error metrics provide valuable insights into the overall quality of distribution reconstruction, they may not fully capture the ability to identify and locate distinct particle populations, which is often the primary goal in DLS analysis. To address this specific aspect, we developed two complementary metrics focused on peak detection and localization: a peak counting metric and a peak distance metric. These metrics provide direct insight into how well each method identifies and positions the modes of the particle size distribution.

Figure (VI.7) presents the performance of the methods in correctly identifying the number of peaks present in the distribution. For monomodal distributions, both CONTIN and our Neural Network demonstrate great peak detection across all noise levels, consistently identifying a single peak correctly in over a 75% of the cases. This robust performance confirms that both methods excel at handling simple, single-population systems, even under significant noise conditions.

The more challenging cases of bimodal and trimodal distributions reveal interesting dynamics. Under noise-free conditions, both methods achieve comparable performance, successfully identifying over 80% of the true peaks. Notably, unlike the sharp performance degradation observed in traditional error metrics, CONTIN's peak detection capability shows a more gradual decline with increasing noise. This observation suggests that while CONTIN may lose information about distribution width (as evidenced by earlier metrics), it maintains the ability to identify distinct particle populations, albeit with decreasing accuracy at higher noise levels.

Our Neural Network exhibits stable peak detection performance up to its training noise level (0.005), maintaining a clear plateau region for all distribution types. Beyond this threshold, performance decreases more rapidly, though remaining superior to CONTIN up to approximately 0.01 noise amplitude. This behavior demonstrates the network's ability to generalize beyond its training conditions, while

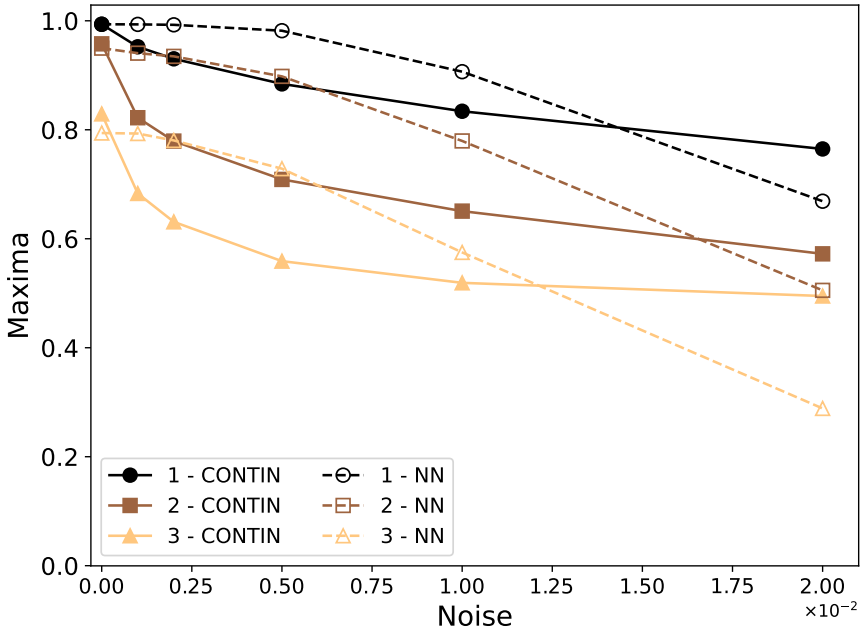

Figure VI.7: Performance comparison of peak detection capabilities as a function of noise amplitude. Results shown for both CONTIN (solid lines and filled symbols) and Neural Network (dashed lines and empty symbols) methods across monomodal (circles), bimodal (squares), and trimodal (triangles) distributions. The vertical axis represents the fraction of correctly identified peaks relative to the true distribution. Each point represents an average over 10000 samples.

also highlighting the limitations of this generalization.

Figure (VI.8) complements the peak detection analysis by quantifying how accurately each method positions the identified peaks. CONTIN demonstrates remarkable stability in peak positioning for monomodal distributions, maintaining excellent accuracy across all noise levels. Even in the most challenging noise conditions, CONTIN's peak position error for bimodal and trimodal case remains limited to 5-6 bins from the true position, indicating robust localization capability even if the number of peaks are not matching.

The Neural Network shows more complex behavior in peak positioning. For noise levels within or near its training range (up to 0.005), it maintains competitive performance across all distribution types. However, at higher noise levels, particularly for monomodal distributions, the network shows increased positioning error. This seemingly counterintuitive result—worse performance for simpler distributions—can be understood through the metric's construction: in multimodal distributions, even if

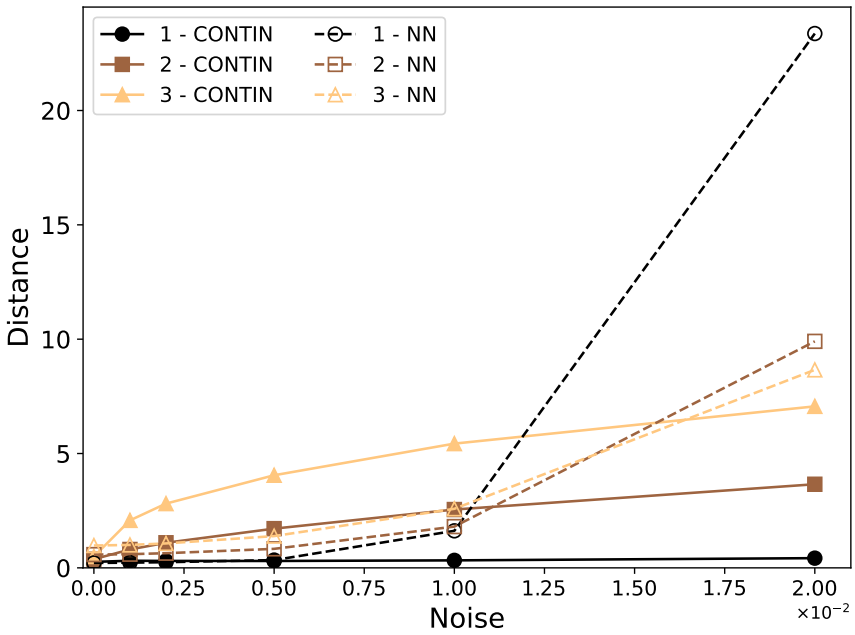

Figure VI.8: Mean distance between predicted and true maxima positions as a function of noise amplitude. Results shown for both CONTIN (solid lines and filled symbols) and Neural Network (dashed lines and empty symbols) methods across monomodal (circles), bimodal (squares), and trimodal (triangles) distributions. The vertical axis represents the average minimum distance in bin units between predicted and true peak positions. Each point represents an average over 10000 samples.

peak positions are somewhat randomized, the probability of a predicted peak being close to any true peak is higher simply due to the presence of multiple targets. In this monomodal and high noise case, the Neural Networks seems that is able to detect that there should be one peak but position it at random.

When considered together, these metrics reveal important complementary aspects of each method's performance. CONTIN exhibits remarkable stability in peak positioning for simple distributions but struggles increasingly with peak identification as distribution complexity increases. Our Neural Network demonstrates more balanced performance across distribution types within its training regime and maintains this advantage even slightly beyond, though with clear degradation at much higher noise levels.

These findings suggest that while CONTIN may produce artificially narrow distributions (as shown by traditional error metrics), it can still provide valuable information about the number and approximate positions of distinct particle

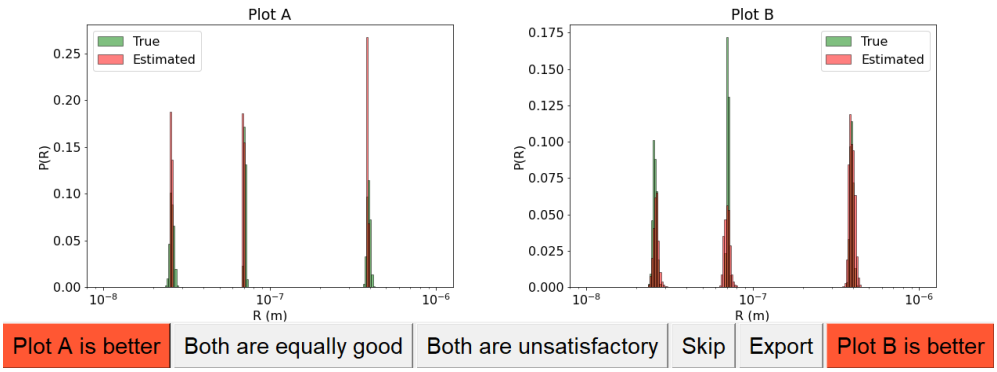

Figure VI.9: Interface used for expert validation of reconstruction methods. The platform presents two plots (A and B) showing different reconstructions of the same particle size distribution. Each plot displays both the true distribution (solid line) and a reconstructed distribution (dashed line) obtained from either CONTIN or the Neural Network approach. Experts were asked to evaluate which reconstruction they would prefer in practice, without knowing which method generated each result.

populations, particularly for simpler distributions. The Neural Network, on the other hand, offers more robust overall performance within and slightly beyond its training conditions, but its reliability decreases more uniformly across all aspects (detection and positioning) at very high noise levels.

VI.3.3. Human Expert Validation Study

While quantitative metrics provide valuable insights into method performance, the ultimate test of any analytical technique lies in its practical utility as judged by domain experts. To this end, we conducted an human validation study, engaging 10 researchers with extensive experience in DLS measurements and analysis.

We developed an interface that presented experts with paired comparisons of reconstruction results, shown in Figure (VI.9). For each trial, the interface displayed two plots (labeled A and B) showing the true particle size distribution alongside either the CONTIN or Neural Network reconstruction. The presentation order was randomized to eliminate potential bias. Importantly, the participating researchers had no prior exposure to either method's results to ensure unbiased evaluation.

For each comparison, experts were asked: "If you were working with a system having the known size distribution shown, which reconstruction would you prefer to obtain from your measurement method?" They could select from four options:

- Plot A is better
- Plot B is better

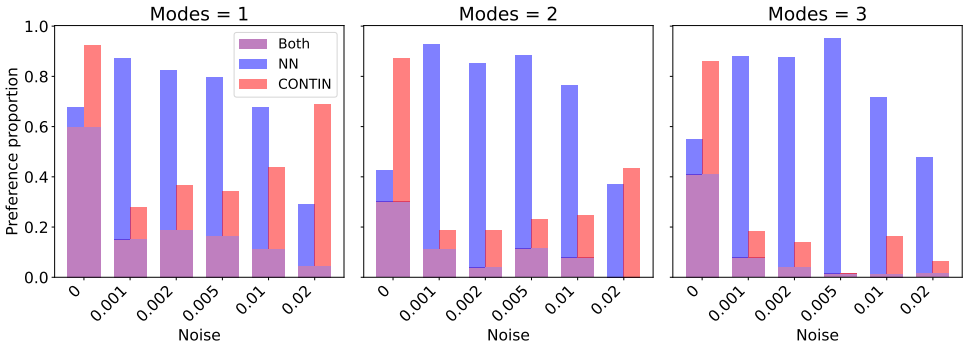

Figure VI.10: Results of human validation study comparing CONTIN and Neural Network performance across different noise levels and distribution modalities. Each subplot represents a different modality: monomodal, bimodal, and trimodal distributions. For each noise level, the stacked bars show the fraction of cases where experts deemed both methods equally good (purple), preferred the Neural Network (blue), or preferred CONTIN (red). Each noise level represents at least 100 independent evaluations by DLS experts. The total height of each stacked bar (sum of all fractions) may be less than 1 as cases where experts deemed both methods unsatisfactory are not shown.

- Both reconstructions are equally good
- Both reconstructions are unsatisfactory

The system recorded each choice along with metadata about the distribution type (monomodal, bimodal, or trimodal) and the noise level of the corresponding correlation function. Each combination of noise level and modality was evaluated at least 100 times, ensuring statistical significance of the results.

Figure (VI.10) presents the results of this human validation study. The data is organized into three subplots corresponding to monomodal, bimodal, and trimodal distributions. For each noise level, we display stacked bars showing the fraction of cases where experts deemed both methods equally good (purple), preferred the Neural Network reconstruction (blue) or preferred the CONTIN reconstruction (red).

The results reveal a clear pattern: for noise levels up to 0.01 and across all modalities, the Neural Network approach equals or outperforms CONTIN in approximately 70% of cases. This strong preference for Neural Network reconstructions is particularly noteworthy given that it represents the unbiased judgment of experienced DLS practitioners.

Under noise-free conditions, CONTIN maintains an edge across all modalities, consistent with our earlier quantitative metrics. However, the introduction of even minimal noise leads to a dramatic shift in expert preference. This transition is particularly pronounced for multimodal distributions, where CONTIN's performance

degradation is reflected in diminishing expert approval rates as the number of modes increases. For trimodal distributions under noise, CONTIN's acceptance becomes negligible.

At very high noise levels (0.02), an interesting pattern emerges. CONTIN regains some advantage for mono- and bidisperse systems, aligning with our earlier quantitative analyses that showed poor Neural Network performance under these conditions. However, surprisingly, the Neural Network maintains superior performance for tridisperse systems even at this extreme noise level, suggesting particular robustness in handling complex distributions despite noise levels well beyond its training regime.

Combining insights from traditional error metrics, peak detection analysis, and human expert validation provides a comprehensive understanding of each method's strengths and limitations. The Neural Network approach, while not achieving the perfect accuracy of CONTIN under ideal conditions, demonstrates remarkable consistency across a practical range of noise levels. This robustness to noise, particularly evident in the human validation study, suggests that the Neural Network approach may be better suited for real-world applications where some level of measurement noise is inevitable.

The consistent preference for Neural Network reconstructions by domain experts, especially for multimodal distributions under realistic noise conditions, provides strong validation of our approach. This preference aligns well with our quantitative metrics, particularly the KL divergence results that showed better preservation of distribution characteristics. The human validation study thus confirms that the improvements observed in our numerical metrics translate to practically meaningful benefits as judged by experienced practitioners.

These findings suggest that while CONTIN remains valuable for ideal or near-ideal conditions, the Neural Network approach offers a more robust alternative for practical DLS analysis, particularly when dealing with multimodal distributions or noisy data. The combination of consistent performance across noise levels and strong expert endorsement indicates that this approach represents a significant advancement in the practical application of DLS analysis.

VI.3.4. Computational Performance Analysis

Beyond accuracy and reliability, computational efficiency represents an increasingly important consideration in modern analytical methods. To evaluate this aspect, we conducted a systematic comparison of processing times between CONTIN and our Neural Network approach across varying numbers of samples. All measurements were performed on a standardized test system featuring an AMD Radeon 7 4800H processor with 8 cores and 16 threads, 15.37 GB of RAM, running

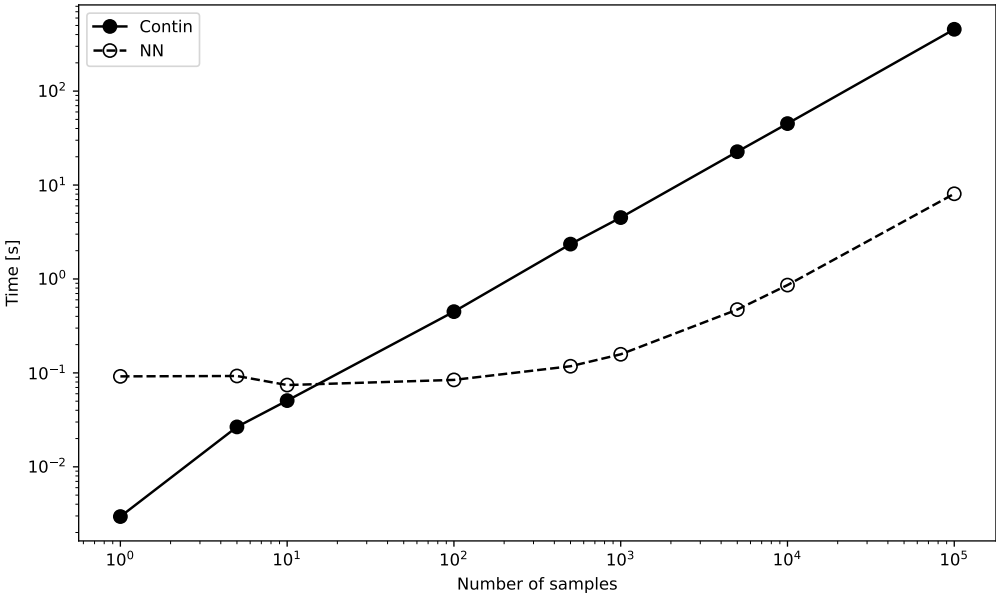

Figure VI.11: Computational time comparison between CONTIN and Neural Network approaches as a function of the number of samples processed. Measurements were performed on an AMD Radeon 7 4800H system with 8 cores, 16 threads, and 15.37 GB RAM, running Windows and Python 3.12.4 with TensorFlow 2.18.0. The plot shows how processing time scales with batch size for both methods, highlighting the efficiency advantages of Neural Network batch processing for larger datasets.

Windows and Python 3.12.4 with TensorFlow 2.18.0 and NumPy 1.26.4.

As shown in Figure (VI.11), the computational demands of these methods exhibit markedly different scaling behaviors. CONTIN demonstrates a strictly linear relationship between processing time and the number of samples from the outset, reflecting its sequential processing nature where each correlation function must be analyzed independently. This linear scaling begins with the very first sample and maintains a consistent slope throughout the tested range.

In contrast, our Neural Network approach shows more complex scaling behavior that can be divided into two distinct regimes. For small sample sizes (below approximately 500 samples), the processing time remains nearly constant, showing minimal increase with additional samples. This behavior stems from the Neural Network's ability to leverage batch processing capabilities, effectively parallelizing the computation across multiple samples. Beyond this threshold, the processing time begins to scale linearly with the number of samples, albeit with a much shallower slope than CONTIN.

The practical implications of these scaling behaviors are significant. For individual or very small numbers of samples (less than 10-15), CONTIN maintains

a slight speed advantage, making it potentially preferable for one-off analyses. However, as the sample size increases beyond this modest threshold, our Neural Network approach demonstrates increasingly superior performance. In the linear scaling regime, where both methods show proportional growth in processing time with sample size, the Neural Network processes samples 50-60 times faster than CONTIN.

This performance advantage becomes particularly relevant in the context of emerging trends in scientific research. As artificial intelligence and automation technologies become more prevalent in laboratory settings, the ability to process large datasets efficiently becomes increasingly crucial. High-throughput experimental setups, automated quality control systems, and large-scale research studies all benefit from faster processing capabilities. The significant speed advantage of our Neural Network approach in processing larger datasets positions it well for these emerging applications, enabling more comprehensive studies and faster turnaround times for large-scale analyses.

VI.4. Conclusions

This work presents a novel neural network-based approach for analyzing Dynamic Light Scattering data, demonstrating significant improvements over traditional CONTIN analysis in both accuracy and computational efficiency under noisy conditions. Our comprehensive evaluation, combining quantitative metrics, peak detection analysis, and human expert validation, reveals several key findings that address longstanding limitations in DLS analysis, particularly the difficult problem of resolving multimodal distributions.

The ability to accurately characterize multimodal distributions has been a persistent challenge in DLS analysis, with traditional methods like CONTIN often struggling to reliably distinguish and characterize multiple particle populations. Our neural network approach represents a significant step forward in addressing this difficulty, demonstrating robust performance in identifying and characterizing multiple peaks even in cases with overlapping distributions. This advancement is particularly noteworthy, as it opens new possibilities for studying complex colloidal systems where multiple particle populations coexist.

While CONTIN maintains superior performance under ideal, noise-free conditions, our neural network approach demonstrates remarkable resilience to correlation function noise, particularly for complex multimodal distributions. This robustness is evidenced by consistently lower Kullback-Leibler divergence values across all distribution types up to noise levels double that of the training conditions. The network's ability to preserve distribution characteristics, especially width information and peak separation in multimodal cases, represents a significant advancement over CONTIN's tendency to produce artificially narrow distributions

under noisy conditions.

The success of our CNN architecture in learning the mapping from autocorrelation functions to size distributions suggests that deep learning approaches can effectively reduce reliance on explicit regularization heuristics, which have historically been a limiting factor in DLS analysis. This reduction in dependence on predetermined constraints allows for more flexible and potentially more accurate distribution recovery, particularly in complex cases where traditional regularization assumptions might be overly restrictive.

However, our study also reveals important limitations that warrant further investigation. The current implementation relies on synthetic training data composed of Gaussian mixture distributions, which may not fully capture the complexity of real experimental systems. Additionally, the model's training is confined to a specific range of particle sizes, and its performance for distributions outside this range remains to be validated. These limitations, combined with the lack of experimental validation in this initial phase, suggest clear directions for future development. The computational efficiency of our approach, particularly in batch processing scenarios where it runs 50-60 times faster than CONTIN, makes it especially suitable for high-throughput applications and automated analysis systems. This speed advantage, coupled with the robust handling of multimodal distributions, positions the method as a valuable tool for characterization and quality control applications.

Extension to more realistic noise models and experimental data represents a crucial next step, as does the potential application to non-spherical scattering and multi-angle DLS measurements. These developments could significantly expand the method's practical utility while maintaining its core advantages in speed and accuracy.

Moreover, the successful application of deep learning to this challenging inverse problem suggests broader implications for related fields in scattering and spectroscopy. The demonstrated ability to handle multimodal distributions more effectively than traditional methods could inspire similar approaches in other areas where multiple population characterization remains challenging.

In conclusion, our neural network approach represents a significant advancement in DLS analysis, particularly in addressing the longstanding problem of multimodal distribution characterization. While acknowledging current limitations, the method's improved robustness and efficiency for practical applications, combined with its strong performance across a range of distribution complexities, suggest it could become a valuable tool for routine DLS analysis. These improvements, validated by both quantitative metrics and domain experts, point toward a promising future where deep learning methods complement and enhance traditional analysis techniques in physical characterization.

VI.5. Appendix

One-dimensional Convolutional Layers

One-dimensional convolutional layers form the foundation of our neural network architecture. To understand their operation, consider how we might manually analyze a time series signal. When examining such data, we often look for specific patterns by focusing on small segments of the signal at a time, sliding our attention from start to finish. A one-dimensional convolutional layer automates this process, systematically scanning through the input data to detect important features.

The key insight is that these layers act as automated pattern detectors. Just as a human expert might recognize characteristic shapes in a correlation function—such as exponential decays, sudden drops, or plateau regions—each convolutional filter learns to identify specific patterns in the data. The layer achieves this by applying a sliding window known as a kernel across the input signal, performing the same mathematical operation at each position.

Consider our input correlation function $g_2(\tau)$, which represents the temporal correlation of scattered light intensity. A convolutional layer processes this signal by applying multiple filters, each designed to detect different features. The operation of a single filter can be expressed mathematically as:

$$y(i) = \sum_{k=1}^{K} w(k) \cdot x(i+k) + b \tag{VI.13}$$

where $y(i)$ is the output value at position i, $w(k)$ represents the learned weights of the filter, $x(i)$ is the input signal, K is the kernel size (5 in our architecture) and b is a learned bias term.

To illustrate this operation, let us examine a specific example. Consider a segment of our correlation function containing five consecutive points:

$$x = [0.8, 0.7, 0.5, 0.3, 0.2]$$

This sequence shows a decreasing trend, typical of the decay in correlation over time that we observe in DLS measurements. A convolutional filter specialized in detecting such declining trends might have weights:

$$w = [-2, -1, 0, 1, 2]$$

When this filter is applied to our data segment, the convolution computes:

$$\begin{aligned} y &= (0.8 \times -2) + (0.7 \times -1) + (0.5 \times 0) + (0.3 \times 1) + (0.2 \times 2) + b \\ &= -1.6 - 0.7 + 0 + 0.3 + 0.4 + b \\ &= -1.6 + b \end{aligned}$$

The negative output value indicates that this filter has detected a declining trend in the signal. This makes intuitive sense: the filter weights are arranged to give a strong negative response when aligned with a decreasing pattern.

Multiple Filters and Pattern Detection

In our architecture, the first convolutional layer employs 32 different filters, each potentially specializing in different patterns. For example, some filters could be:

$$\begin{aligned} \text{Sharp decline filter: } w_1 &= [-0.2, -0.1, 0, 0.1, 0.2] \\ \text{Peak detection filter: } w_2 &= [-0.1, 0.1, 0.2, 0.1, -0.1] \\ \text{Plateau detection filter: } w_3 &= [-0.1, -0.1, 0.4, -0.1, -0.1] \end{aligned}$$

For the m-th filter in the first layer, the output at position i is given by:

$$y_1^m(i) = \sum_{k=1}^{K} w_1^m(k) \cdot g_2(i+k) + b_1^m \tag{VI.14}$$

The second convolutional layer, containing 64 filters, processes these initial feature maps to detect more complex patterns. For the n-th filter in the second layer:

$$y_2^n(i) = \sum_{k=1}^{K} \sum_{m=1}^{M} w_2^{nm}(k) \cdot y_1^m(i+k) + b_2^n \tag{VI.15}$$

This hierarchical structure allows the network to recognize increasingly sophisticated features. While the first layer might detect simple trends, the second layer can identify more complex patterns such as the combination of a decay followed by a plateau, or multiple decay rates characteristic of polydisperse samples.

To preserve the signal length and ensure we don't lose information at the boundaries, we employ 'same' padding, which adds zeros at the edges of our input data. This ensures that the convolution operation produces an output of the same length as the input signal.

By training the neural network, it learns the filters that detect the features of the correlation function that allow to reconstruct the size distribution.

Non-linear Activation: The ReLU Function

The Rectified Linear Unit (ReLU) is a crucial component that introduces non-linearity into our neural network. While its mathematical formulation is simple, its impact on the network's capability to learn complex patterns is profound. To understand why non-linearity is essential, consider that most physical phenomena in DLS, such as the relationship between particle size and diffusion coefficient, are inherently non-linear. The ReLU function is defined mathematically as:

$$\text{ReLU}(x) = \max(0, x) = \begin{cases} x & \text{if } x > 0 \\ 0 & \text{if } x \leq 0 \end{cases} \tag{VI.16}$$

This piecewise linear function has a simple derivative:

$$\frac{d}{dx}\text{ReLU}(x) = \begin{cases} 1 & \text{if } x > 0 \\ 0 & \text{if } x < 0 \\ \text{undefined} & \text{if } x = 0 \end{cases} \tag{VI.17}$$

Consider the output from the kernel of our previously defined convolutional layer. Suppose we have a sequence of values:

$$x = [1.2, -0.5, 0.8, -0.3, 0.0, 2.1, -1.4]$$

After applying the ReLU function, we get:

$$\text{ReLU}(x) = [1.2, 0.0, 0.8, 0.0, 0.0, 2.1, 0.0]$$

This transformation accomplishes two important objectives. First, it introduces non-linearity by creating a sharp bend at x = 0, and second, it promotes sparsity in the network by setting negative values to zero.

The combination of convolution and ReLU enables our network to learn complex, non-linear relationships. For instance, when processing DLS data, we might want to detect:

$$y = \begin{cases} \text{strong signal} & \text{if correlation } > \text{threshold} \\ \text{no signal} & \text{otherwise} \end{cases} \tag{VI.18}$$

The ReLU function naturally implements this type of threshold behavior, allowing the network to focus on significant features while suppressing noise or weak correlations.

Dimensionality Reduction: MaxPooling Layers

MaxPooling layers serve as a form of non-linear downsampling, reducing the spatial dimensions of our feature maps while preserving the most salient information. This operation helps make the network more computationally efficient and focuses attention on the strongest detected features. For a window size of 2 and stride of 2, the MaxPooling operation is defined as:

$$p(i) = \max\{z(2i), z(2i+1)\} \tag{VI.19}$$

where $p(i)$ is the output at position i, $z(j)$ is the input at position j, the window size of 2 means we consider pairs of adjacent values and the stride of 2 means we move the window by 2 positions each time.

Consider a feature map after ReLU activation containing the following sequence:

$$z = [0.5, 0.3, 0.8, 0.4, 0.2, 0.6, 0.1, 0.3]$$

The MaxPooling operation processes this sequence in pairs:

$$\begin{aligned}
p(0) &= \max\{z(0), z(1)\} = \max\{0.5, 0.3\} = 0.5 \\
p(1) &= \max\{z(2), z(3)\} = \max\{0.8, 0.4\} = 0.8 \\
p(2) &= \max\{z(4), z(5)\} = \max\{0.2, 0.6\} = 0.6 \\
p(3) &= \max\{z(6), z(7)\} = \max\{0.1, 0.3\} = 0.3
\end{aligned}$$

Resulting in the reduced sequence: $p = [0.5, 0.8, 0.6, 0.3]$.

In our DLS application, MaxPooling provides several benefits:

1. **Dimensionality Reduction:** Each MaxPooling layer halves the spatial dimension of its input, reducing computational complexity
2. **Translation Invariance:** The operation helps make feature detection more robust to small shifts in the input signal
3. **Feature Emphasis:** By selecting maximum values, MaxPooling emphasizes the strongest responses from the convolutional filters

For example, if a convolutional filter detects a characteristic decay pattern in the correlation function, MaxPooling helps ensure this pattern is recognized regardless of its exact temporal position and preserves its peak response while discarding weaker, potentially noise-related responses.

Feature Integration through Dense Layers

Following the convolutional stages of our network, dense layers perform the crucial task of integrating extracted features into a coherent representation suitable for particle size distribution prediction. These layers, also known as fully connected layers, implement a complete set of learnable connections between their inputs and outputs. For a dense layer with n inputs and m outputs, the transformation can be expressed mathematically as:

$$\mathbf{h} = \text{ReLU}(\mathbf{W}\mathbf{x} + \mathbf{b}) \tag{VI.20}$$

where $\mathbf{W}$ represents an $m \times n$ weight matrix, $\mathbf{x}$ is the n-dimensional input vector, $\mathbf{b}$ is an m-dimensional bias vector, and $\mathbf{h}$ is the resulting m-dimensional output.

Our architecture implements a sequence of three dense layers with progressively decreasing sizes: 256, 128, and 64 neurons. This deliberate reduction in dimensionality creates an information bottleneck that forces the network to learn increasingly compact and relevant representations of the particle size distribution features. The first dense layer, with its 256 neurons, has sufficient capacity to represent many different combinations of the convolutional features. The subsequent layers with 128 and 64 neurons must learn to combine these representations efficiently, distilling the essential information required for accurate size distribution prediction.

Probability Distribution Output through Softmax Activation

The network's final layer transforms its raw outputs into a proper probability distribution through the softmax activation function. For a set of raw outputs $\{x_1, \ldots, x_n\}$, the softmax function computes:

$$P(R_i) = \frac{\exp(x_i)}{\sum_{j=1}^{n} \exp(x_j)} \tag{VI.21}$$

This transformation ensures that all probabilities are positive and sum to unity, producing a mathematically valid probability distribution for the particle sizes.

Training through Kullback-Leibler Divergence Loss

The network learns by minimizing the Kullback-Leibler (KL) divergence between predicted and true distributions. The KL divergence provides a measure of the difference between two probability distributions and is defined as:

$$D_{\text{KL}}(P_{\text{true}} \parallel P_{\text{pred}}) = \sum_i P_{\text{true}}(R_i) \log \left(\frac{P_{\text{true}}(R_i)}{P_{\text{pred}}(R_i)} \right) \tag{VI.22}$$

To understand the behavior of this loss function, let us examine a specific example where we compare two distributions over three size ranges:

$$P_{\text{true}} = [0.7, 0.2, 0.1]$$
$$P_{\text{pred}} = [0.6, 0.3, 0.1]$$

The KL divergence computation proceeds term by term:

$$\begin{aligned} D_{\text{KL}} &= 0.7 \log(0.7/0.6) + 0.2 \log(0.2/0.3) + 0.1 \log(0.1/0.1) \\ &= 0.7 \log(1.167) + 0.2 \log(0.667) + 0.1 \log(1) \\ &= 0.7 \times 0.154 - 0.2 \times 0.405 + 0 \\ &= 0.108 - 0.081 \\ &= 0.027 \end{aligned}$$

The positive result indicates a discrepancy between the distributions, with larger values suggesting greater divergence. This example demonstrates how the KL divergence penalizes differences between the predicted and true distributions, providing a suitable objective function for training our network.

Parameter Optimization through Adam Algorithm

The training of neural networks fundamentally relies on finding the optimal set of parameters that minimize the loss function, in our case, the Kullback-Leibler divergence between predicted and true particle size distributions. This optimization process presents several challenges specific to our DLS analysis application. The relationship between the correlation function and particle size distribution is inherently complex, leading to a loss landscape with multiple local minima, saddle points, and regions of varying curvature. Furthermore, different parameters in our network may require different scales of updates – for instance, the weights in the early convolutional layers processing the raw correlation function might need different treatment compared to the weights in the final layers producing the probability distribution.

Gradient descent forms the foundational principle for optimizing these parameters. The basic idea is to iteratively adjust each parameter in the direction

that reduces the loss function, using the gradient (derivative) as a guide. However, simple gradient descent faces several limitations. The choice of learning rate becomes crucial: too large a value can cause overshooting and instability, while too small a value leads to slow convergence. Moreover, the same learning rate may not be appropriate for all parameters, particularly given the diverse roles they play in our network architecture.

The Adam (Adaptive Moment Estimation) optimizer addresses these challenges through a sophisticated parameter update strategy that combines two key ideas: momentum and adaptive learning rates. The momentum aspect, implemented through exponentially decaying averages of past gradients, helps overcome local minima and saddle points that are particularly prevalent in our DLS analysis problem due to the complex relationship between correlation functions and size distributions. Mathematically, this first moment estimate is expressed as:

$$\mathbf{m}_t = \beta_1 \mathbf{m}_{t-1} + (1 - \beta_1) \nabla L_t \tag{VI.23}$$

where β_1 controls how much past gradients influence the current update.

The adaptive learning rate aspect, implemented through exponentially decaying averages of squared past gradients, allows each parameter to have its own effective learning rate based on the history of its gradients. This second moment estimate is given by:

$$\mathbf{v}_t = \beta_2 \mathbf{v}_{t-1} + (1 - \beta_2)(\nabla L_t)^2 \tag{VI.24}$$

The parameter update then combines these moments:

$$\theta_t = \theta_{t-1} - \alpha \frac{\hat{\mathbf{m}}_t}{\sqrt{\hat{\mathbf{v}}_t} + \epsilon} \tag{VI.25}$$

The Adam optimizer requires minimal manual tuning of learning rates, as it automatically adapts them based on the observed gradients. This property is especially valuable in our context, where the relationship between network parameters and the final particle size distribution prediction is highly non-linear and potentially varies across different regions of the parameter space. The default values of the hyperparameters ($\beta_1 = 0.9$, $\beta_2 = 0.999$, $\epsilon = 10^{-8}$) have proven robust across a wide range of deep learning applications, including our specific case of DLS analysis.

Bibliography

[VI.1] P. N. Pusey and W. van Megen. Phase behaviour of concentrated suspensions of nearly hard colloidal spheres. *Nature*, 320(6060):340–342, 1986.

[VI.2] Robert Pecora. *Dynamic light scattering: applications of photon correlation spectroscopy*. Springer Science & Business Media, 1985.

[VI.3] Jan KG Dhont. *An introduction to dynamics of colloids*. Elsevier, 1996.

[VI.4] Walter I Goldburg. Dynamic light scattering. *American Journal of Physics*, 67(12):1152–1160, 1999.

[VI.5] Bruce J Berne and Robert Pecora. *Dynamic light scattering: with applications to chemistry, biology, and physics*. Courier Corporation, 2000.

[VI.6] Dennis E Koppel. Analysis of macromolecular polydispersity in intensity correlation spectroscopy: the method of cumulants. *The Journal of Chemical Physics*, 57(11):4814–4820, 1972.

[VI.7] S. W. Provencher. A constrained regularization method for inverting data represented by linear algebraic or integral equations. *Computer Physics Communications*, 27(3):213–227, 1982.

[VI.8] Narasimha Sreerama and Robert W Woody. Estimation of protein secondary structure from circular dichroism spectra: comparison of contin, selcon, and cdsstr methods with an expanded reference set. *Analytical biochemistry*, 287(2):252–260, 2000.

[VI.9] Thomas Antony, Anita Saxena, KB Roy, and HB Bohidar. Laser light scattering immunoassay: an improved data analysis by contin method. *Journal of biochemical and biophysical methods*, 36(2-3):75–85, 1998.

[VI.10] Dan Chicea and Silviu Mihai Rei. A fast artificial neural network approach for dynamic light scattering time series processing. *Measurement Science and Technology*, 29(10):105201, 2018.

[VI.11] Zongzheng Wang, Yajing Wang, Jin Shen, Wei Liu, Xi Yuan, Xiaojun Fu, and Gaoge Zhang. Dynamic light scattering inversion based on tikhonov regularization and parameter-optimized generalized regression neural network. *Powder Technology*, 409:117802, 2022.

[VI.12] Anuj Shrivastava, Shyamapada Mandal, Sudip K Pattanayek, and Anurag S Rathore. Rapid estimation of size-based heterogeneity in monoclonal antibodies by machine learning-enhanced dynamic light scattering. *Analytical Chemistry*, 95(21):8299–8309, 2023.

[VI.13] Meiai Lin, Ting Liu, Yixiong Zheng, and Xiangyuan Ma. Dynamic light scattering microscopy sensing mitochondria dynamics for label-free detection of triple-negative breast cancer enhanced by deep learning. *Biomedical Optics Express*, 14(10):5048–5059, 2023.

[VI.14] Jin Zeng and Jingjing Xia. Light scattering method for aerosol sizing based on machine learning. *ACS sensors*, 9(3):1208–1217, 2024.

[VI.15] Diederik P Kingma and Jimmy Ba. Adam: A method for stochastic optimization. *arXiv preprint arXiv:1412.6980*, 2014.

[VI.16] Ian Goodfellow, Yoshua Bengio, and Aaron Courville. *Deep learning*. MIT press, 2016.

[VI.17] Andrey Nikolayevich Tikhonov. Solutions of ill-posed problems. *VH Winston and Sons*, 1977.

[VI.18] Per Christian Hansen. Regularization tools: A matlab package for analysis and solution of discrete ill-posed problems. *Numerical algorithms*, 6(1):1–35, 1994.

[VI.19] Per Christian Hansen. *Discrete inverse problems: insight and algorithms*. SIAM, 2010.

[VI.20] Charles L Lawson and Richard J Hanson. *Solving least squares problems*. SIAM, 1995.

Part III

Conclusions and summary

Conclusions and Future Work

This thesis has explored different aspects of responsive colloids through various theoretical and computational approaches. The work began with the development of a generalized **Density Functional Theory** for responsive colloids, where the particle size (R) was explicitly resolved and allowed to fluctuate according to a unimodal distribution. The results showed that particle softness substantially affects the size distribution of bulk systems. As the particle concentration increases, softer colloids exhibit a more pronounced reduction in their mean size compared to stiffer ones. This behavior leads to lower particle volume fractions and pressures under identical concentration conditions.

The study of inhomogeneous systems revealed several key features of responsive colloids near surfaces and under external fields. Near a planar hard wall, increasing particle softness reduces the amplitude of density oscillations that arise from hard-sphere repulsions. While the density profile shows strong oscillations at high volume fractions, the mean local particle size does not display such pronounced oscillatory behavior. However, there is a marked decrease in particle size near the wall due to steric constraints, as only smaller colloids can approach the surface closely.

When subjected to gravitational fields, these systems showed distinct behavior patterns. Under a size-independent gravitational field, colloids accumulate at the bottom through sedimentation. In soft systems, this leads to local size segregation due to the higher concentration causing particle size reduction. The addition of an Archimedes buoyant field intensifies this effect and creates significant structuring near the upper wall, where larger colloids tend to accumulate. This effect becomes particularly pronounced at high values of the softness parameter (τ).

The investigation then moved to studying the dynamic properties of these systems through a combined approach using **Dynamic Density Functional Theory** and **Brownian dynamics simulations**. This work revealed that the relaxation dynamics of confined responsive colloids involves a complex interplay between

translational diffusion and particle size changes. When the typical spatial and size relaxation timescales differ significantly, the system can exhibit interesting non-equilibrium structuring and reentrant transient states. The modification of these intrinsic timescales leads to adjustable macroscopic relaxation times and pathways.

Regarding molecular transport, the thesis examined the non-equilibrium diffusive release kinetics of small molecules from spherical microgel particles. The work identified that molecular geometry plays a crucial role in transport efficiency, with linear molecules showing more effective transport compared to spherical ones. A universal behavior in release dynamics was found, characterized by the half-release time $\tau_{1/2}$. This parameter incorporates the diffusion coefficients within the polymer network (D^*) and in water (D_w), the interaction free energy between the molecule and microgel (ΔG), and the microgel radius (b).

The release process operates in two distinct regimes. For large, slowly diffusing molecules with poor solubility in the hydrogel (large ΔG), the process is diffusion-limited, with release time scaling as $\tau_{1/2} \sim b^2/D^*$. Conversely, small, rapidly diffusing, and highly soluble molecules (small or negative ΔG) operate in a reaction-limited regime, where the release time scales as $\tau_{1/2} \sim b^2 \exp(-\Delta G/k_{\mathrm{B}}T)$. In both cases, the relationship between microgel size and release time follows a quadratic scaling law.

The thesis expanded experimental characterization methods through the extension of **3D dynamic light scattering (DLS) techniques** for measuring drift velocities in nonequilibrium colloidal systems. This work developed a theoretical framework that describes the physical mechanisms driving oscillatory behavior in autocorrelation functions and establishes methods to correct for correlation loss homodyne DLS measurements. This theoretical development enables the characterization of particle dynamics in systems with drift velocities, regardless of the underlying mechanism.

The theoretical framework was then implemented in a device for dynamic light scattering measurements, which is currently in the patent application process. The device uses a variable incident angle configuration to measure relative velocities between particle populations. By adjusting the incident beam angle, the optical configuration controls the scattering vector's vertical component, allowing optimization of detection conditions for different velocity ranges. This configuration allows the study of systems where particles move at different velocities, such as during sedimentation processes or under external fields. The device can characterize these velocity differences with high precision by adjusting the measurement conditions to the specific velocity range of interest. The integration of the theoretical framework with the hardware design provides a method for characterizing particle dynamics in complex colloidal systems.

A **neural network approach** was developed for analyzing DLS data, showing particular strength in handling noisy conditions. The method demonstrated superior

performance in resolving multimodal distributions compared to traditional CONTIN analysis when noise is present. While CONTIN maintains better performance under ideal conditions, the neural network approach showed consistent accuracy with correlation function noise levels up to twice that of the training conditions. The method proved especially effective at preserving distribution characteristics, including width information and peak separation in multimodal cases, avoiding the tendency of traditional methods to produce artificially narrow distributions under noisy conditions

Future work in this field should address several aspects. For responsive colloids, investigation of more complex size-dependent pair potentials and their behavior at very high volume fractions would be valuable. The dynamic properties of stiffer systems, such as those modeled by Hertzian potentials, deserve attention, particularly regarding their transient structuring during size adaptation. The release kinetics studies could be extended to concentrated microgel suspensions and swollen states. The theoretical framework developed for DLS analysis could be applied to systems driven out of equilibrium by external fields such as magnetic or electric fields, building upon the developed methodology. For characterization methods, the neural network approach would benefit from validation with experimental data and extension to non-spherical scattering and multi-angle measurements.

Resumen

Introducción

Las suspensiones coloidales, que consisten en pequeñas partículas dispersas en un solvente, [1–3] representan un ejemplo fundamental de la materia blanda, donde los materiales se deforman fácilmente debido a las débiles interacciones entre sus componentes [4, 5]. La comprensión de sus propiedades estructurales y dinámicas, tanto en equilibrio como fuera de él, ha sido de interés central en física, química y ciencia de materiales [6, 7].

En el ámbito de la materia blanda, los conceptos de *blandura* y *capacidad de respuesta* son particularmente relevantes. La blandura se refiere a la flexibilidad y adaptabilidad intrínseca de estos materiales, que surge de un delicado equilibrio entre contribuciones entrópicas y energéticas [8–12]. Por otro lado, la capacidad de respuesta describe la habilidad de estos materiales para experimentar cambios significativos y reversibles en sus propiedades físicas cuando se exponen a estímulos externos como temperatura, pH, fuerza iónica, luz o fuerzas mecánicas [13, 14].

Los sistemas coloidales responsivos incluyen coloides y macromoléculas que pueden detectar y adaptarse a cambios ambientales mediante la modificación de su conformación interna, tamaño, forma, densidad de carga, dipolo eléctrico y orientación [15–24]. Estos ajustes afectan tanto a las propiedades de partículas individuales como a las colectivas, dando lugar frecuentemente a comportamientos dinámicos complejos con múltiples tiempos de relajación [7, 25]. Esta capacidad de respuesta es particularmente atractiva en aplicaciones donde la adaptación en tiempo real a estímulos externos es crucial, por ejemplo, en la administración de fármacos (donde cambios en el pH o la temperatura pueden desencadenar la liberación del fármaco).

Los **microgeles** constituyen una clase particularmente versátil de partículas

coloidales responsivas [26,27]. A diferencia de las nanopartículas rígidas, un microgel está formado por una *red polimérica entrecruzada* que mantiene su integridad como partícula individual [14, 26]. Este entrecruzamiento evita que la red polimérica se disgregue, confiriéndole un carácter "tipo esponja" que permite a los microgeles incorporar una cantidad significativa de solvente dentro de su estructura [27, 28].

Una característica distintiva de los microgeles es la *transición de fase volumétrica*: el hinchamiento o colapso reversible de la red polimérica en respuesta a estímulos externos. Esta capacidad única hace que los microgeles sean candidatos ideales para aplicaciones como la administración dirigida de fármacos, la nanocatálisis y la biodetección [29, 30].

Entre los diversos polímeros utilizados en microgeles, el **poli(N-isopropilacrilamida) (PNIPAM)** exhibe un comportamiento termorresponsivo inusual. En soluciones acuosas, el PNIPAM tiene una temperatura de transición de fase volumétrica (VPTT) cerca de 32–34 °C [26, 31], por debajo de la cual se encuentra expandido y por encima de ella colapsado. Esta respuesta inversa a la temperatura se debe a la naturaleza anfifílica del PNIPAM: por debajo de la VPTT, los grupos amida forman una extensa red de enlaces de hidrógeno con las moléculas de agua, superando los efectos hidrofóbicos de los grupos isopropilo y haciendo que esté expandido.

La naturaleza dinámica de los sistemas responsivos constituye una característica fundamental que sustenta su funcionalidad y adaptabilidad. A diferencia de los materiales clásicos, estos sistemas experimentan cambios continuos y reversibles en respuesta a estímulos externos, lo que hace crucial el estudio de sus procesos dinámicos. La comprensión de esta dinámica permite alcanzar varios objetivos fundamentales: facilita un control preciso sobre la capacidad de respuesta del sistema, permitiendo el diseño de materiales que adaptan sus propiedades en tiempo real [11, 12]; optimiza aplicaciones como la administración de fármacos, donde la cinética de liberación es crítica para la eficacia terapéutica [32, 33]; contribuye a la comprensión fundamental de la termodinámica y la mecánica estadística fuera del equilibrio [34, 35]; y permite el diseño de nuevos materiales con propiedades adaptadas para aplicaciones en biotecnología, catálisis e ingeniería de materiales [36, 37].

Los **microgeles** se han establecido como un sistema modelo ideal para examinar fenómenos fuera del equilibrio, gracias a sus transiciones de fase volumétricas reversibles [28, 38]. El transporte de moléculas dentro y a través de los microgeles está íntimamente ligado a su estado de hinchamiento. En el estado colapsado, las interacciones hidrofóbicas dominan y el agua es expulsada para formar una estructura más compacta. Las simulaciones atomísticas han revelado que el agua atrapada en redes colapsadas puede formar grupos desconectados tipo fractal, lo que resulta en un comportamiento de membrana no porosa [39, 40]. Para moléculas hidrofóbicas, los microgeles colapsados actúan como reservorios con una partición mejorada en

comparación con las predicciones tradicionales de exclusión por tamaño [41,42].

El estudio del comportamiento fuera del equilibrio en sistemas responsivos presenta desafíos significativos que requieren una combinación de estrategias computacionales, teóricas y experimentales. Las simulaciones computacionales, aunque proporcionan información detallada sobre los mecanismos microscópicos, enfrentan limitaciones debido a su alto costo computacional y la necesidad de promediar resultados sobre múltiples ejecuciones [43, 44]. Para abordar estas limitaciones, se han desarrollado marcos teóricos como la Teoría Funcional de la Densidad Dinámica (DDFT), que extiende los principios de la Teoría Funcional de la Densidad (DFT) a condiciones fuera del equilibrio [34,43]. La DDFT ha demostrado ser particularmente útil para modelar sistemas blandos y estudiar fenómenos como la liberación de fármacos [45,46].

Las mediciones experimentales, aunque representan el método más directo para estudiar el comportamiento fuera del equilibrio, también enfrentan desafíos considerables. La Dispersión Dinámica de Luz (DLS), una técnica ampliamente utilizada para caracterizar partículas coloidales en suspensión [47,48], puede verse afectada por fenómenos como la convección, que interfiere con la interpretación correcta de los datos [41, 42]. Estas dificultades han impulsado el desarrollo de configuraciones experimentales más sofisticadas que pueden distinguir entre diferentes tipos de movimiento de partículas.

La comprensión y el control de estos sistemas dinámicos responsivos no solo incrementa nuestro conocimiento fundamental de la materia blanda, sino que también tiene implicaciones directas para numerosas aplicaciones tecnológicas, desde la administración controlada de fármacos hasta el desarrollo de materiales inteligentes adaptativos [49,50].

Procedimiento y metodología

La investigación presentada en esta tesis aborda los desafíos en el estudio de sistemas coloidales responsivos, particularmente en microgeles, mediante un enfoque integral que combina desarrollos teóricos, implementaciones computacionales y validaciones experimentales. El trabajo se estructura en una serie de estudios que progresan desde los fundamentos teóricos hasta las aplicaciones prácticas.

En la Publicación I, se desarrolla una extensión de DFT para fluidos de esferas duras responsivas, donde se introduce el tamaño como un grado adicional de libertad. Este desarrollo teórico fundamental permite modelar sistemas donde las partículas pueden modificar su tamaño en respuesta a estímulos externos, una característica esencial de los microgeles [34, 35]. La extensión teórica proporciona el marco necesario para comprender cómo la polidispersidad y la capacidad de respuesta afectan las propiedades estructurales y termodinámicas del sistema.

El trabajo continúa en la Publicación II con el estudio de sistemas fuera del equilibrio mediante la extensión de DDFT. Este desarrollo resulta crucial para comprender la dinámica acoplada entre el movimiento traslacional de las partículas y sus cambios de tamaño [51, 52]. La teoría extendida permite estudiar fenómenos como la respuesta de microgeles a campos externos y gradientes de concentración, aspectos fundamentales para aplicaciones en liberación controlada de fármacos.

En la Publicación III, se desarrolla el estudio de la cinética de liberación molecular desde microgeles colapsados. El marco teórico desarrollado se aplica para modelar y calcular perfiles de liberación, considerando tanto los efectos de difusión como las interacciones dentro de la matriz polimérica [39,40]. Este estudio tiene implicaciones directas para la optimización de sistemas de administración de fármacos, donde la comprensión y el control de la cinética de liberación son cruciales.

En el ámbito experimental, la Publicación IV presenta una metodología innovadora para la medición de velocidades absolutas mediante Dispersión Dinámica de Luz 3D (3D-DLS) [47, 48]. Esta técnica, basada en el análisis de oscilaciones fuera del equilibrio, proporciona una herramienta para caracterizar el comportamiento dinámico de sistemas coloidales. La metodología se valida en sistemas termo-convectivos, demostrando su capacidad para medir velocidades absolutas de arrastre de sistemas coloidales.

El desarrollo metodológico incluye, en la Publicación V, la propuesta de un dispositivo en proceso de ser patentado para la medición de velocidades relativas de dos poblaciones de partículas en el mismo volumen de dispersión. Esta innovación técnica amplía las capacidades de caracterización experimental de sistemas coloidales dinámicos, permitiendo mediciones más precisas y versátiles que con las técnicas convencionales [53, 54].

La investigación se completa en la Publicación VI con la implementación de técnicas de aprendizaje automático para mejorar el análisis de datos de DLS en sistemas altamente polidispersos. Este enfoque complementa los métodos tradicionales como CONTIN y el análisis de cumulantes, permitiendo una caracterización más precisa de las distribuciones de tamaño en sistemas complejos. La integración de aprendizaje automático representa un avance en la interpretación de datos experimentales, especialmente relevante para el estudio de sistemas responsivos donde la polidispersidad es una característica inherente.

Conclusiones

Esta tesis explora diferentes aspectos de los coloides responsivos a través de diversos enfoques teóricos y computacionales. En la Publicación I, se desarrolla una teoría funcional de la densidad generalizada para coloides responsivos, donde el tamaño de partícula (R) se resuelve explícitamente y se permite fluctuar según una distribución unimodal. Los resultados muestran que la blandura de las partículas

afecta sustancialmente la distribución de tamaños en el volumen del sistema. A medida que aumenta la concentración de partículas, los coloides más blandos exhiben una reducción más pronunciada en su tamaño medio en comparación con los más rígidos, lo que conduce a fracciones de volumen y presiones más bajas en condiciones de concentración idénticas.

El estudio de sistemas inhomogéneos revela características clave de los coloides responsivos cerca de superficies y bajo campos externos. Se observa que cerca de una pared dura plana, el aumento de la blandura de las partículas reduce la amplitud de las oscilaciones de densidad que surgen de las repulsiones de esferas duras. Mientras que el perfil de densidad muestra fuertes oscilaciones a altas fracciones de volumen, el tamaño medio local de las partículas no presenta un comportamiento oscilatorio tan pronunciado, aunque sí se observa una marcada disminución en el tamaño de las partículas cerca de la pared debido a restricciones estéricas.

En la Publicación II, se investiga la dinámica de relajación de coloides responsivos confinados mediante una combinación de Teoría Funcional de la Densidad Dinámica y simulaciones de dinámica browniana. Este trabajo revela que la dinámica de relajación involucra una interacción compleja entre la difusión traslacional y los cambios de tamaño de las partículas. Cuando las escalas de tiempo típicas de relajación espacial y de tamaño difieren significativamente, el sistema puede exhibir estructuración fuera del equilibrio y estados transitorios reentrantes interesantes.

La Publicación III se centra en la cinética de liberación difusiva fuera del equilibrio de moléculas pequeñas desde partículas de microgel esféricas. El trabajo identifica que la geometría molecular juega un papel crucial en la eficiencia del transporte, con moléculas lineales mostrando un transporte más efectivo en comparación con las esféricas. Se encuentra un comportamiento universal en la dinámica de liberación, caracterizado por el tiempo de media liberación $\tau_{1/2}$, que incorpora los coeficientes de difusión dentro de la red polimérica (D^*) y en agua (D_w), la energía libre de interacción entre la molécula y el microgel (ΔG), y el radio del microgel (b).

En la Publicación IV, se propone una extensión de la técnica de dispersión dinámica de luz 3D (DLS) para medir velocidades de deriva en sistemas coloidales fuera del equilibrio. Este trabajo desarrolla un marco teórico que describe los mecanismos físicos que impulsan el comportamiento oscilatorio en las funciones de autocorrelación y establece métodos para corregir la pérdida de correlación en mediciones DLS homodinas.

Este desarrollo teórico se implementa en un dispositivo para mediciones de dispersión dinámica de luz, descrito en la Publicación V, que actualmente se encuentra en proceso de patente. El dispositivo utiliza una configuración de ángulo de incidencia variable para medir velocidades relativas entre poblaciones de partículas, permitiendo optimizar las condiciones de detección para diferentes rangos de velocidad.

Finalmente, en la Publicación VI, se desarrolla un enfoque de red neuronal para analizar datos de DLS, mostrando particular fortaleza en el manejo de condiciones de alto ruido. El método demuestra un rendimiento superior en la resolución de distribuciones multimodales en comparación con el análisis tradicional realizado con CONTIN. La red neuronal muestra una precisión que se mantiene a distintos niveles de ruido en la función de correlación de hasta el doble de las condiciones de entrenamiento.

El trabajo futuro en este campo abordará varios aspectos. Para los coloides responsivos, se investigarán potenciales de par más complejos dependientes del tamaño y se analizará su comportamiento a fracciones de volumen muy altas. Asimismo, se estudiarán las propiedades dinámicas de sistemas más rígidos, como aquellos modelados por potenciales hertzianos, particularmente en relación con su estructuración transitoria durante la adaptación de tamaño. Los estudios de cinética de liberación se ampliarán a suspensiones concentradas de microgeles y estados hinchados, mientras que el marco teórico desarrollado para el análisis DLS se aplicará a sistemas impulsados fuera del equilibrio por campos externos, como campos magnéticos o eléctricos. En cuanto a los métodos de caracterización, el enfoque de red neuronal se validará con datos experimentales y se explorará su extensión a la dispersión por partículas no esféricas y a mediciones multiángulo.

Bibliography

[1] William B. Russel, D. A. Saville, and W. R. Schowalter. *Colloidal Dispersions*. Cambridge University Press, Cambridge, UK, 1989.

[2] R. J. Hunter. *Foundations of Colloid Science*. Oxford University Press, Oxford, UK, 2001.

[3] P. N. Pusey and W. van Megen. Phase behaviour of concentrated suspensions of nearly hard colloidal spheres. *Nature*, 320(6060):340–342, 1986.

[4] Ronald G Larson. *The structure and rheology of complex fluids*, volume 150. Oxford university press New York, 1999.

[5] Jacob N. Isralachvili. *Intermolecular and Surface Forces, Third Edition*. Academic Press, 3rd edn, 2011.

[6] Todd M Squires and Stephen R Quake. Microfluidics: Fluid physics at the nanoliter scale. *Reviews of modern physics*, 77(3):977–1026, 2005.

[7] Michael E. Cates and Julien Tailleur. Motility-induced phase separation. *Annu. Rev. Condens. Matter Phys.*, 6(1):219–244, March 2015.

[8] José Nelson Onuchic, Zaida Luthey-Schulten, and Peter G. Wolynes. Theory of protein folding: The energy landscape perspective. *Annu. Rev. Phys. Chem.*, 48(1):545–600, 1997.

[9] Chi Wu and Xiaohui Wang. Globule-to-coil transition of a single homopolymer chain in solution. *Phys. Rev. Lett.*, 80:4092–4094, May 1998.

[10] Samuel S. Cho, Yaakov Levy, and Peter G. Wolynes. P versus Q: Structural reaction coordinates capture protein folding on smooth landscapes. *Proc. Natl. Acad. Sci. U.S.A.*, 103(3):586–591, 2006.

[11] Alan R Denton and Matthias Schmidt. Colloid-induced polymer compression. *J. Phys.-Condes. Matter*, 14(46):12051–12062, nov 2002.

[12] Matthew Urich and Alan R. Denton. Swelling, structure, and phase stability of compressible microgels. *Soft Matter*, 12:9086–9094, 2016.

[13] Martien A. Cohen Stuart, Wilhelm T. S. Huck, Jan Genzer, Marcus Müller, Christopher Ober, Manfred Stamm, Gleb B. Sukhorukov, Igal Szleifer, Vladimir V. Tsukruk, Marek Urban, Françoise Winnik, Stefan Zauscher, Igor Luzinov, and Sergiy Minko. Emerging applications of stimuli-responsive polymer materials. *Nat. Mater.*, 9(2):101–113, 2010.

[14] Matthias Karg and Thomas Hellweg. Smart inorganic/organic hybrid microgels: Synthesis and characterisation. *Journal of Materials Chemistry*, 19(46):8714–8727, 2009.

[15] Mikhail Motornov, Roman Sheparovych, Robert Lupitskyy, Emily MacWilliams, and Sergiy Minko. Responsive colloidal systems: Reversible aggregation and fabrication of superhydrophobic surfaces. *J. Colloid Interface Sci.*, 310(2):481–488, 2007.

[16] Mikhail Motornov, Halyna Royter, Robert Lupitskyy, Yuri Roiter, and Sergiy Minko. Stimuli-responsive hydrogel hollow capsules by material efficient and robust cross-linking-precipitation synthesis revisited. *Langmuir*, 27(24):15305–15311, 2011.

[17] Kyriaki Kalaitzidou and Alfred J. Crosby. Adaptive polymer particles. *Appl. Phys. Lett.*, 93(4):041910, 2008.

[18] Huan-Xiang Zhou, Germán Rivas, and Allen P. Minton. Macromolecular crowding and confinement: Biochemical, biophysical, and potential physiological consequences. *Annu. Rev. Biophys.*, 37(1):375–397, 2008.

[19] Jiang Hong and Lila M. Gierasch. Macromolecular crowding remodels the energy landscape of a protein by favoring a more compact unfolded state. *J. Am. Chem. Soc.*, 132(30):10445–10452, August 2010.

[20] Nicholas F. Dupuis, Erik D. Holmstrom, and David J. Nesbitt. Molecular-crowding effects on single-molecule rna folding/unfolding thermodynamics and kinetics. *Proc. Natl. Acad. Sci. U.S.A.*, 111(23):8464–8469, 2014.

[21] Jaeoh Shin, Andrey G. Cherstvy, and Ralf Metzler. Kinetics of polymer looping with macromolecular crowding: effects of volume fraction and crowder size. *Soft Matter*, 11:472–488, 2015.

[22] Upayan Baul, Nils Götth, Michael Bley, and Joachim Dzubiella. Modulating internal transition kinetics in responsive macromolecules by collective crowding. *J. Chem. Phys.*, 155:244902, 2021.

[23] Shilin Huang, Kornelia Gawlitza, Regine von Klitzing, Laurent Gilson, Johannes Nowak, Stefan Odenbach, Werner Steffen, and Gu˜nter K Auernhammer. Microgels at the water/oil interface: In situ observation of structural aging and two-dimensional magnetic bead microrheology. *Langmuir*, 32(3):712–722, 2016.

[24] Valeria Garbin, Ian Jenkins, Talid Sinno, John C Crocker, and Kathleen J Stebe. Interactions and stress relaxation in monolayers of soft nanoparticles at fluid-fluid interfaces. *Phys. Rev. Lett.*, 114(10):108301, 2015.

[25] Margaret S. Cheung, Dmitri Klimov, and D. Thirumalai. Molecular crowding enhances native state stability and refolding rates of globular proteins. *Proc. Natl. Acad. Sci. U.S.A.*, 102(13):4753–4758, 2005.

[26] Robert Pelton. Temperature-sensitive aqueous microgels. *Adv. Colloid Interface Sci.*, 85(1):1–33, 2000.

[27] L Andrew Lyon and Alberto Fernandez-Nieves. The polymer/colloid duality of microgel suspensions. *Annual review of physical chemistry*, 63(1):25–43, 2012.

[28] Shuang Wu, Joachim Dzubiella, Julian Kaiser, Markus Drechsler, Xuhong Guo, Matthias Ballauff, and Yan Lu. Thermosensitive au-pnipa yolk–shell nanoparticles with tunable selectivity for catalysis. *Angew. Chem. - Int. Ed.*, 51(9):2229–2233, 2012.

[29] Deepika Parasuraman and Michael J. Serpe. Poly (n-isopropylacrylamide) microgel-based assemblies for organic dye removal from water. *ACS Appl. Mater. Interfaces*, 3(12):4714–4721, 2011.

[30] Rakesh Banerjee, Sheetal Parida, Chiranjit Maiti, Mahitosh Mandal, and Dibakar Dhara. ph-degradable and thermoresponsive water-soluble core cross-linked polymeric nanoparticles as potential drug delivery vehicle for doxorubicin. *RSC Adv.*, 5:83565–83575, 2015.

[31] Avraham Halperin, Martin Kröger, and Françoise M. Winnik. Poly(n-isopropylacrylamide) phase diagrams: Fifty years of research. *Angew. Chem. - Int. Ed.*, 54(51):15342–15367, 2015.

[32] Allan S. Hoffman. Applications of thermally reversible polymers and hydrogels in therapeutics and diagnostics. *J. Control. Release*, 6(1):297–305, 1987.

[33] S. H. Gehrke, J. P. Fisher, M. Palasis, and M. E. Lund. Factors determining hydrogel permeability. *Ann. New York Acad. Sci.*, 831:179–207, 1997.

[34] Michael te Vrugt, Hartmut Löwen, and Raphael Wittkowski. Classical dynamical density functional theory: from fundamentals to applications. *Adv. Phys.*, 69(2):121–247, 2020.

[35] Umberto Marini Bettolo Marconi and Pedro Tarazona. Dynamic density functional theory of fluids. *J. Chem. Phys.*, 110(16):8032–8044, 1999.

[36] Pablo Hervés, Moisés Pérez-Lorenzo, Luis M. Liz-Marzán, Joachim Dzubiella, Yan Lu, and Matthias Ballauff. Catalysis by metallic nanoparticles in aqueous solution: Model reactions. *Chem. Soc. Rev.*, 41:5577–5587, 2012.

[37] Yan Lu, Yu Mei, Markus Drechsler, and Matthias Ballauff. Thermosensitive core–shell particles as carriers for ag nanoparticles: Modulating the catalytic activity by a phase transition in networks. *Angew. Chem. - Int. Ed.*, 45(5):813–816, 2006.

[38] Jian-Tao Zhang, Gang Wei, Thomas F. Keller, Hilary Gallagher, Christian Stötzel, Frank A. Müller, Michael Gottschaldt, Ulrich S. Schubert, and Klaus D. Jandt. Responsive hybrid polymeric/metallic nanoparticles for catalytic applications. *Macromol. Mater. Eng.*, 295(11):1049–1057, 2010.

[39] Matej Kanduč, Won Kyu Kim, Rafael Roa, and Joachim Dzubiella. Transfer free energies and partitioning of small molecules in collapsed pnipam polymers. *J. Phys. Chem. B*, 123(3):720–728, 2019.

[40] Matej Kanduč, Won Kyu Kim, Rafael Roa, and Joachim Dzubiella. How the shape and chemistry of molecular penetrants control responsive hydrogel permeability. *ACS Nano*, 15(1):614–624, 2021.

[41] Maria Palasis and Stevin H. Gehrke. Permeability of responsive poly (n-isopropylacrylamide) gel to solutes. *Journal of Controlled Release*, 18(1):1 – 11, 1992.

[42] M.A. Molina, C.R. Rivarola, and C.A. Barbero. Study on partition and release of molecules in superabsorbent thermosensitive nanocomposites. *Polymer*, 53(2):445–453, 2012.

[43] Umberto Marini Bettolo Marconi and Pedro Tarazona. Dynamic density functional theory of fluids. *J. Chem. Phys.*, 110(16):8032–8044, 1999.

[44] C Patrick Royall, Joachim Dzubiella, Matthias Schmidt, and Alfons van Blaaderen. Nonequilibrium sedimentation of colloids on the particle scale. *Phys. Rev. Lett.*, 98(18):188304, 2007.

[45] Michael te Vrugt, Jens Bickmann, and Raphael Wittkowski. Effects of social distancing and isolation on epidemic spreading modeled via dynamical density functional theory. *Nat. Commun.*, 11(1):5576, 2020.

[46] Arturo Moncho-Jordá and Joachim Dzubiella. Controlling the microstructure and phase behavior of confined soft colloids by active interaction switching. *Phys. Rev. Lett.*, 125:078001, Aug 2020.

[47] Sebastian Stock, Regine von Klitzing, and Amin Rahimzadeh. Impact of ultrasound on the motion of compact particles and acousto-responsive microgels. *arXiv preprint arXiv:2307.12696*, 2023.

[48] Xiaobing Feng, Guiqiong Huang, Jian Qiu, Li Peng, Kaiqing Luo, Dongmei Liu, and Peng Han. Dynamic light scattering in flowing dispersion. *Optics Communications*, 531:129225, 2023.

[49] Mehrdad Hamidi, Amir Azadi, and Pedram Rafiei. Hydrogel nanoparticles in drug delivery. *Adv. Drug Deliv. Rev.*, 60(15):1638–1649, 2008. 2008 Editors' Collection.

[50] Brian R. Saunders, Nadiah Laajam, Emma Daly, Stephanie Teow, Xinhua Hu, and Robert Stepto. Microgels: From responsive polymer colloids to biomaterials. *Adv. Colloid Interface Sci.*, 147-148:251 – 262, 2009.

[51] Arturo Moncho-Jordá, Sebastien Groh, and Joachim Dzubiella. External field-driven property localization in liquids of responsive macromolecules. *J. Chem. Phys.*, 160(2):024904, 2024.

[52] Arturo Moncho-Jordá, Nils Göth, and Joachim Dzubiella. Liquid structure of bistable responsive macromolecules using mean-field density-functional theory. *Soft Matter*, 19(15):2832–2846, 2023.

[53] Robert Pecora. *Dynamic light scattering: applications of photon correlation spectroscopy*. Springer Science & Business Media, 1985.

[54] Bruce J Berne and Robert Pecora. *Dynamic light scattering: with applications to chemistry, biology, and physics*. Courier Corporation, 2000.